POLITECNICO DI MILANO

School of Industrial and Information Engineering
Department of Chemistry, Materials and Chemical Engineering "Giulio Natta"
Master of science in
Materials Engineering and Nanotechnology

PULLULAN AS RELEASE ENHANCER
FOR CONTROLLED RELEASE CAPSULAR DEVICE:
PERFORMANCE ASSESSMENT
AND PREPARATION METHODS

Supervisor:
Prof. Francesco BRIATICO VANGOSA

Flavia DI STEFANO 864202

Academic Year 2016 – 2017

Contents

List of Figures

List of Tables

Abstract

Nel corso degli ultimi anni si è assistito ad un crescente interesse nei confronti di nuove tecnologie per la realizzazione di dispositivi per il rilascio di farmaci, Drug Delivery Systems. I DDS proposti basano il proprio funzionamento su particolari approcci formulativi e si configurano come forme farmaceutiche non convenzionali in quanto capaci di generare profili farmacocinetici diversi da quelli ottenibili con le forme farmaceutiche tradizionali. Il primo e fondamentale vantaggio delle forme farmaceutiche non convenzionali è il miglioramento del profilo terapeutico grazie alla riduzione degli effetti collaterali, al mantenimento di livelli plasmatici efficaci nei modi e nei tempi richiesti dalla terapia e all'aumento della compliance da parte dei pazienti.

Sistemi capsulari per il rilascio del farmaco nel tratto gastrointestinale possono essere realizzati grazie allo stampaggio ad iniezione di polimeri gastroresistenti in grado di imporre una fase di latenza del rilascio, la cui durata è programmabile in funzione della tipologia del polimero utilizzato e dello spessore delle pareti del contenitore. Tuttavia, i polimeri attualmente impiegati, pur essendo in grado di resistere in ambiente acido, una volta raggiunto l'intestino non consentono una pronta disponibilità del farmaco. Per raggiungere l'obiettivo di rilascio si utilizzano delle cariche che agiscono da modificatori di rilasci.

Lo scopo di questo lavoro era di valutare la possibilità di impiegare un nuovo materiale, il Pullulano, per modificare il rilascio di una sistema stampato per iniezione impiegando come matrice una idrossipropil metilcellulosa acetato succinato, HPCMAS. L'effetto del metodo di dispersione e della dimensione del modificatore di rilascio sono stati valutati, ottenendo validi risultati che attestano le interessanti prestazioni del Pullulano. Inoltre, sfruttando la tecnica dello spray drying, è stata investigata con successo la possibilità di modificare la morfologia del Pullulano, da particellare a fibrosa, per creare un percorso di percolazione all'interno della matrice.

Abstract

Over the last few years, there has been a growing interest in new technologies for the production of drug delivery systems, DDS. The proposed DDS base their functioning on particular formulation approaches and are configured as unconventional pharmaceutical forms due to the fact that they are able to generate pharmacokinetic profiles different from those obtainable with traditional pharmaceutical forms. The first and fundamental advantage of the unconventional pharmaceutical forms is the improvement of the therapeutic profile thanks to the reduction of the side effects, the maintenance of plasma levels effective in the ways and times required by the therapy and the increase of patient compliance.

Capsular systems for the release of the drug in the gastrointestinal tract can be realized thanks to the injection moulding of gastro resistant polymers able to impose a lag phase prior to the release, whose duration can be programmed according to the type of polymer used and the container's walls thickness. However, the polymers currently used, despite being able to resist in an acid environment, once they reach the intestine do not allow a ready availability of the drug. To achieve the release target, additives are used that act as release modifiers.

The aim of the present work was to evaluate the feasibility of using a new material, Pullulan, to modify the release of an injection moulded system using as a matrix a hydroxyl propyl methyl cellulose acetate succinate, HPCMAS. The effect of both the dispersion method and the size of the release modifier were evaluated, obtaining valid results that attest the interesting performance of the Pullulan. Furthermore, by exploiting the spray drying technique, the possibility of modifying the morphology of the Pullulan, from particulate to fibrous, in order to create a percolation path within the matrix was successfully investigated.

Summary

New dosage forms and formulations can represent meaningful advances in pharmacotherapeutics, providing both clinical and economic value. To obtain a given therapeutic response, the suitable amount of the active drug must be released to the site of action at the right time. Drug delivery systems able to incorporate a lag phase of pre-established duration in their release patterns are a topic of high current interest, primarily in connection with gastro intestinal targeting.

Injection moulded capsule technology was developed to provide oral delivery with full enteric protection and rapid release in the upper gastrointestinal tract without the use of coatings. However, even if the selected bulk material dissolves at pH typical of the intestinal tract, an immediate drug release is not feasible. Therefore, the aim of the present work was to evaluate the addition of a new release enhancer, the Pullulan, in the capsule matrix in order to improve the performance of the system reducing its lag phase. Moreover, based on the idea of realizing a percolation path, the feasibility of producing Pullulan fibrillary shaped particles was examined.

The present work is developed into 4 sections:

In Part I a Literature review on drug delivery systems and strategies and material to control it is presented. Moreover, a description of the spray drying process, the method selected for the production of Pullulan fibres, and the capillary breakup method, which was exploited to assess the fluid viscoelasticity in free surface extensional flows, are provided.

The Part II deals with the use of Pullulan as a release enhancer in its pristine form. Pullulan was tested to verify its reliability as pore former and its performances were compared to those of a release enhancer already available. A new protocol was set up for the preparation of the capsule matrix and, thus, the influence of pretreatment, dimensions and dispersion route of particles in the matrix was evaluated.

Despite the excellent results achieved, the attainment of a percolation path resulted still necessary to foster even faster release performance, and to modify the HPMCAS release performance in acidic environments.

To this aim, the spray drying technique was applied, and the effect of solution concentration and formulations were studied.

Part III describes the water and hydro alcoholic solutions preparation and their characterization in terms of rheological behaviour, both in shear and in extension, and of evaporation behaviour. Considering that a sufficient viscoelastic behaviour is required to overcome the capillary forces and stabilize the jet during the spray drying process, particular attention was paid to the investigation of the filament diameter evolution, time to breakup and longest relaxation time, getting an indication about the solutions degree of elasticity.

Part IV finally describes the spray drying process and its outcomes, in terms of morphologies and of the distribution in dimensions of the particles. The experimental results were temptatively correlated with the properties of the solution and the processing conditions through adimensional analysis, but the results, even if encouraging, are far from conclusive.

PART I

Literature review

Chapter 1

Drug delivery

Development of new drug molecules is expensive and time consuming. Improving the ratio between safety and efficacy of well established drugs has been attempted using different methods such as personalization of the drug therapy, monitoring of the drug dose and improvement of bioavailability [1][2].

The idea that drug delivery technology, per se, can bring both therapeutic and commercial value to health care products has been widely accepted. Recently, big pharmaceutical companies have been losing their market share to generic competitors with increasing rapidity after their patents expire. This has created an intense need for presenting well established drugs in new formulations and utilizing novel dosage forms or delivery systems. As a result, companies developing new drug delivery systems seem to enjoy a good return on their investment in the form of increased revenues and market share [3].

Drug delivery has now become a multidisciplinary science consisting of biopharmaceutics and pharmacokinetics, which takes into consideration the carrier, the route, and the target, and has evolved into the strategy of designing processes or devices to enhance the efficacy of therapeutics agents through controlled release. This may involve:

- Enhanced bioavailability;
- Improved therapeutic index;
- Improvement of patient compliance [4].

1.1 DRUG DELIVERY SYSTEM

A drug delivery system is described as a device that enables the introduction of a therapeutic substance in the human body and improves its efficacy and safety by controlling the rate, time, or place of its release. This includes the administration of the drug product, the release of the active ingredients that it contains, in such a way that the amount of drug in the site of action can be conceived. Drug delivery system is an interface between the patient and the drug. It may be a formulation of the drug to administer it for a therapeutic purpose or a device used to deliver the drug. The distinction between the drug and the device is important as it is the criterion for regulatory control of the delivery system by the medicine control agency [5].

To obtain a given therapeutic response, the suitable amount of the active drug must be absorbed and transported to the site of action at the right time and the rate of input can then be adjusted to

produce the concentrations required to maintain the level of the effect for as long as necessary. The distribution of the drug to tissues other than the sites of action and organs of elimination is unnecessary, wasteful, and a potential cause of toxicity. The modification of the means of delivering the drug by projecting and preparing new advanced drug delivery devices can improve therapy [6].

Therefore features that should be emphasized in drug delivery are:

- Exclusive delivery to specific areas;
- Access to primarily inaccessible sites;
- Protection of body from unwanted deposition;
- Controlled rate and modality of delivery to pharmacological receptors;
- Reduction in the amount of active principal employed [7].

1.2 DRUG DELIVERY ROUTES

Drug may be introduced into the human body by various anatomical routes. They may be administered directly to the organ affected by disease or given systemically and targeted to the diseased organ. The choice of the route of administration depends on the disease, the desired effect, and the available product.

Historically, the oral route of drug administration has been the one used most for both conventional and novel drug delivery. The reasons for this preference are obvious: ease of administration and widespread acceptance by the patients. Nevertheless the major limitations are:

- Some drugs taken orally for systemic effects have variable absorption rate and variable serum concentrations that may be unpredictable. This has led to the development of sustained release and controlled release systems.
- Some drugs irritate the gastrointestinal tract, and this is partially counteracted by coating.
- The high acid content and ubiquitous digestive enzymes of the digestive tract can degrade some drugs well before they reach the site of absorption into the bloodstream. This is a particular problem for ingested proteins.
- Many drugs become insoluble at the low pH levels encountered in the digestive tract. Since only the soluble form of the drug can dissolve and be available for absorption into the bloodstream, the transition of the drug to the insoluble form can significantly reduce bioavailability.

1.3 MECHANISM OF DRUG RELEASE

Most conventional oral drug products, such as tablets and capsules, are formulated to release the active drug immediately after oral administration. Such immediate release products generally result in relatively rapid drug absorption and onset of accompanying pharmacodynamics effects. In all

cases, this only depends from drug dissolution and permeability through biological membranes at the site of absorption. In the case of conventional oral products containing prodrugs, the pharmacodynamics activity may be slow due to conversion to the active drug by hepatic or intestinal metabolism or by chemical hydrolysis. Alternatively, in conventional oral products containing poorly soluble lipophilic drugs, the drug absorption may be slower due to slow dissolution in or selective absorption across the gastro intestinal tract, also resulting in a delayed onset time. However, after absorption of the drug from the site of release is complete, plasma drug concentrations decline according to the drug's pharmacokinetic profile. Eventually, plasma drug concentrations fall below the minimum effective plasma concentration, resulting in loss of therapeutic activity. Before this point is reached, another dose is usually given if a sustained therapeutic effect is desired [8].

To address the above described limitations in traditional oral delivery forms, the pattern of drug release from modified release dosage forms is deliberately changed from that of a conventional immediate release formulation to achieve a desired therapeutic objective or better patient compliance. The term modified release drug product is used to describe products that alter the timing and/or the rate of release of the drug substance. Several types of modified release oral drug products are recognized [9]:

- Extended release drug products.

Extended release systems allow the drug to be released over prolonged time periods. By extending the release profile of a drug, the frequency of dosing can be reduced. Extended release can be achieved using sustained or controlled release dosage forms. Sustained release systems maintain a constant rate of drug release over a sustained period. Controlled release systems also offer a sustained release profile but are designed to lead to predictably constant plasma concentrations, independently of the biological environment of the application site. This means that they are actually controlling the drug concentration in the body, not just the duration of the release of the drug from the dosage form.

- Delayed release drug products.

Delayed release dosage forms can be defined as systems which are formulated to release the active ingredient at a time other than immediately after administration. When oral delayed release dosage forms are used is possible to control where the drug is released, based on the transit time throught the gastro intestinal tract.

1.4 CAPSULAR DOSAGE FORMS

Two-piece hard capsules filled with a drug preparation are a well established dosage form that provides quicker and simpler formulation approach than tablets, making them increasingly relevant in today’s cost constrained pharmaceutical environment. Capsules may offer better solid dosage form to tablets for drugs with low compressibility, slow dissolution and bitter tasting [10].

While two-piece capsules may be comprised of various materials, the vast majority are still made using high quality gelatin prepared from collagen. Capsules are manufactured under strict environmental conditions by a dipping process on high capacity machines. The gelatin is dissolved with demineralized, filtered, and sterilized water. Entrapped air is removed by vacuum. The gelatin solution is then mixed with adjuvants, i.e. plasticizers and colorants, and transferred to the capsule manufacturing line. Standardized steel pins are arranged in rows on the capsule manufacturing machine. Pins are then dipped into a temperature controlled solution to a precise regulated depth. After dipping, the bars are rotated to evenly distribute the gelatin around the pins. Correct gelatin distribution is critical to ensure a homogenous and precise wall thickness. The pins are then passed through several drying stages to achieve the optimal water content. After drying, the capsule halves are stripped from the pins, cut to the correct length, and in the last process step caps and bodies are joined [11]. Capsular dosage forms are prepared by filling bodies with powders containing the drug or granule formulations.

To prevent the chemical degradation of the active principles in the acidic environment of the stomach and protect the gastric mucosa from irritation phenomena induced by drug assumption, filled hard gelatin capsules are provided with an enteric film coating, which postpone the onset of action via targeted release in the small intestine. These gastro resistant dosage forms can be used to pursue selective release into particular regions of the intestinal tract, either to exploit favorable absorption sites or provide treatment for local disease. Lag time is basically programmed by selecting the appropriate polymer and coating level. According to the agent employed, various release mechanisms can be involved, such as diffusion, swelling, degradation, partitioning, osmosis and dissolution [12].

Enteric coating of hard gelatin capsules combines the advantages of the shell system with the protective properties of the film coating. However, the physicochemical characteristics of the gelatin and capsule shell present significant challenges to the pharmaceutical scientist when film coating hard gelatin capsules with enteric polymers. When aqueous spray formulations are used the gelatin shell softens and becomes sticky due to solubilization. Instead, when drying, because hard gelatin capsules rely solely on residual water in the shell for their mechanical strength, the gelatin shell becomes brittle due to water evaporation. The brittleness causes the capsules to lose their mechanical characteristics and they break under low pressure. In addition, due to the fact that the capsule shell is very smooth and gives little anchorage, the insufficient adhesion of the film provokes splintering and peeling of the coat, especially with organic spray formulations. The influence of moisture induces the film coats and the gelatin wall to swell to a varying extent, which also causes the coat to detach from the gelatin. Moreover, the two-piece design of hard gelatin capsules has caused problems in the film coating process due to the separation of the cap and body, resulting in the polymeric dispersion of the coating to reach the drug contained in the capsule and to contaminate it. Other reported problems encountered during enteric coating of hard gelatin capsules have been related to stability and long term storage [13].

1.4.1 INJECTION MOULDED CAPSULAR DEVICES

Based on the above discussed premises, the possibility of preparing container like enteric soluble devices that could be filled and sealed after manufacturing, using a material different than gelatin and incorporating the performance of the coating, would represent an innovative and advantageous alternative to the design of the coated gastro resistant dosage forms.

Injection moulding, as first suggested by Speiser [14], was recently explored as a manufacturing technique for the preparation of pharmaceutical dosage forms because of the several advantages it may offer with respect to production costs and technological and biopharmaceutical characteristics of the moulded items [15]. Injection moulding is a rapid and versatile manufacturing technique used to produce objects with different size, shape and, if needed, details. The process cycle is very short and consists of the following four stages:

- Mould closure:

Prior to the injection of the material into the mould, the two halves of the mould must first be securely closed by the clamping unit. Each half of the mould is attached to the injection moulding press and one half is allowed to slide. The hydraulically powered clamping unit pushes the mould halves together and exerts sufficient force to keep the mould securely closed while the material is injected.

- Injection:

The molten material is pushed into the mould to fill the cavity. During this process, the material is melted by heat and then injected into the mould very quickly. The build up of pressure packs and holds the material. The amount of material that is injected is referred to as the shot.

- Cooling:

The molten material that is inside the mould begins to cool as soon as it makes contact with the interior mould surfaces. As the material cools, it will solidify into the shape of the desired part. However, during cooling some shrinkage of the part may occur. The packing of material in the injection stage allows additional material to flow into the mould and reduce the amount of visible shrinkage. The mould cannot be opened until the required cooling time has elapsed. In this phase, the shot needed for the following cycle is accumulated by melting a controlled quantity of the material.

- Ejection:

After sufficient time has passed, the cooled part may be ejected from the mould by the ejection system, which is attached to the rear half of the mould. When the mould is opened, a mechanism is used to push the part out of the mould. Force must be applied to eject the part because during cooling the part adheres to the mould. In order to facilitate the ejection of the part, a mould release agent

can be sprayed onto the surfaces of the mould cavity prior to injection of the material. Once the part is ejected, the mould can be closed and the next cycle can start.

The process needs to be thoroughly understood in order to maximize its performance and leads to the achievement of moulded products at the least cost, meeting the performance requirements.

The main reasons of the success of this technique in the pharmaceutical area are related to its scalability and patentability. The versatility of the micro injection moulding technique can be exploited for the production of drug delivery systems with defined shape and or dimensional characteristics. Thus micro components can be defined having typical exterior dimensions and wall thickness in the millimeter and micrometer ranges, respectively, as well as weight of hundred milligrams, which is consistent with requirements of delivery drug products. Moreover, the process does not require the use of solvents, which is advantageous in terms of manufacturing times and costs as well as of preserved stability [16]. Furthermore, the process conditions typically involved, pressure and heat, both reduce microbial contamination (auto sterilization) and promote drug polymer interactions with the possible formation of solid solutions or dispersions [17] [18]. As in hot melt extrusion technique, this would increase the dissolution rate and, possibly, improve the bioavailability of poorly soluble drugs [19].

However when applying the injection moulding technique to drug delivery, the formulation step may especially be challenging. In order to successfully design injection moulded drug delivery systems, the selection of the pharmaceutical grade polymer is critical as it often dictates the processing conditions and drug release characteristics. Strict qualitative and quantitative limitations can be associated with the need for ensuring the quality, efficacy and safety requisites of drug products. These limitations are primarily dictated by the dose, physical and chemical characteristics and stability profile of the active ingredient, which cannot be modified. In particular, the operating temperatures could cause drug degradation phenomena to occur in process or impair the overall stability of the product. Therefore, all components must be thermally stable at the processing temperature during the whole injection moulding cycle and the polymer needs to be processed at relative low temperatures to ensure the stability of the active pharmaceutical ingredient in the final dosage form. The physicochemical properties of the carrier materials, as well as drug substances and other excipients , e.g. formulation additives, processing aids, release modifying agents, must be carefully analysed and characterized since they may have a profound impact on the processability, product stability and performance.

The physical and chemical stability of the injection moulded dosage form is generally influenced by the nature of the polymer and excipients, the physical state of the drug in the final dosage form, and the storage and packaging conditions. Further aspects, such as the release pattern pursued, the tolerability and pharmaceutical acceptability of all excipients as well as the possibility of undergoing sterilization, are also to be considered. However, in the case of capsular devices the drug substance does not need to undergo the hot process, thus limiting stability issues of the formulation.

The selected polymer is expected to fully or partly govern the release performance on the one hand, and possess on the other suitable melt flow index, thermal stability and behaviour upon cooling. Some other excipients may therefore have to be selected in order to influence not only the release pattern but also the processability of the polymeric component itself.

Hydrophilic swellable/erodible polymers are opportune for this formulation. Swellable hydrophilic cellulose derivatives were successfully employed as release delaying barriers agents in the development of oral erodible delivery platform. When in contact with the aqueous fluids, the hydrophilic polymer undergoes a glassy rubbery transition and, in the rubbery state, it becomes more permeable. Therefore, the release of the incorporated drug is deferred through the progressive hydration and erosion of the polymeric barrier. These mechanisms concur to a different extent in delaying drug release for a period of time depending on both the physical and chemical properties and the amount of polymer applied. A lag phase prior to drug release was indeed achieved that could be exploited to obtain a site selective release based on a time dependent strategy [20] [21] [22] [23].

Based on these premises, the aim of the present work was to contribute to the design, the preparation and the evaluation of a novel injection moulded swellable/erodible device intended to convey differing formulations and release a variety of bioactive compounds following programmed lag phases. The peculiar advantages of such a device would lie in the possibility of undergoing an independent pharmaceutical development irrespective of the final contents and the scalability of the relevant manufacturing process. By the use of hydroxyl propyl methylcellulose acetate succinate, HPMC AS, which offered a good balance between release controlling performance and injection moulding processability, capsular devices having good technological and stability characteristics were subsequently prepared.

HPMC AS, which chemical structure is shown in Figure 1.1, is a mixture of acetic acid and monosuccinic acid esters of hydroxyl propyl methylcellulose in the form of a white to off white powder granules. It is a synthetic polymer derived from cellulose, the most abundant polymer in nature. Highly purified cellulose pulp is reacted with methyl chloride and propylene oxide under alkaline conditions to produce hydroxyl propyl methylcellulose. The HPMC is then used in a chemical sequence to produce HPMC AS by reaction with acetic anhydride and succinic anhydride.

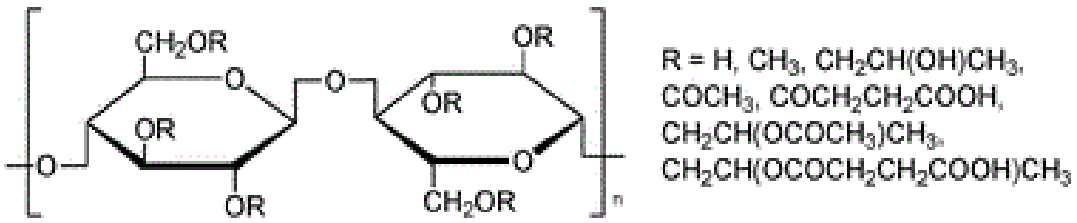

Figure 0.1: HPMC AS chemical structure

HPMC AS has a faint acetic acid like odour and a barely detectable taste. It can be used as a solid dispersion carrier for bioavailability enhancement of poorly soluble compounds. Due to the fact that

it is insoluble in gastric fluid, but will swell and dissolve in the upper small intestine, the release rate of the drug from the matrix is pH dependent. This variable pH solubility is controlled by changing the acetyl and succinoyl content of the polymer. Thus, the release of a pharmaceutical drug in the gastrointestinal tract can be controlled as required by using a suitable grade of the polymer [24].

1.4.2 RELEASE MODIFIERS IN THE CAPSULE MATRIX

Even if designed selecting a bulk material prone to dissolve at pH typical of the intestinal tract, gastro resistant system can take too much time for a complete exposure of the core to the intestinal fluids, thus potentially affecting the drug bioavailability and the efficacy of the therapy. A novel solution, to overcome this lag time limitation and enhance the dissolution rate of the capsular devices at intestinal pH values, is the addition of release modifiers in the capsule shell. Pore formers are typically used to improve the diffusion rate through an insoluble matrix and to achieve the sustained release profile desidered. The channelling action of these fillers could be attributed to their inherent solubility or swelling behaviour.

As investigated in literature [25], a feasible pore former that can be used to tune sustained drug release is Kollicoat® IR. This powder comprises polyethylene glycol and polyvinyl alcohol bound in the ratio of 25:75. A polyethylene glycol chain forms a base onto which side chains of polyvinyl alcohol are grafted. The precise structure is shown in Figure 1.2, as a result of which, the polymer dissolves readily in acidic, neutral and alkaline aqueous media. Indeed KIR is characterized by its exceptional solubility in water as well as by its speed of dissolution, which is particularly aided by its low viscosity [26].

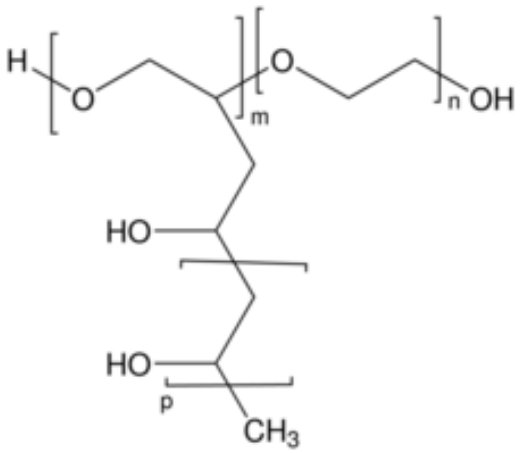

Figure 0.2: KIR chemical structure

The Kollicoat® IR based capsular systems were demonstrated able to withstand the acidic gastric pH values, confirming that the release modifiers were efficiently embedded in the moulded polymeric matrix. At the intestinal pH values a lag time of about 1.5 hours prior to the breakup of capsular devices, based on HPMC AS, and release of the conveyed powder was observed [25].

However, the release time of the drug from this capsular device was not as fast as desired. Therefore, based on these premises, the aim of the present work was to improve the release performance, in order to attain the drug discharge almost immediately after leaving the stomach and entering the small intestine. To achieve this purpose, the idea was to use particles of elongated shape to ensure the creation of percolation paths, allowing the formation of more effective networks throughout the capsule shell thickness. Unlikely, no release modifiers were ready available on the market, thus the fibrillary shape had to be produced by a proper processing method. As KIR demonstrated unfit to the production methods selected, a new material had to be chosen, which:

- Is an adjuvant approved for pharmaceutical use;
- Is stable at HPMC AS process temperature;
- Is expected to be fit for fibrils production.

Based on previous works, Pullulan was chosen as candidate material.

In literature [27], electrospinning was shown to successfully produce uniform and defect free Pullulan fibres. However, mass production of the fibers posed some challenges, due to its time intensiveness and the occurrence of more dense than expected fiber mats. Severe cohesion between the fibers was caused by surface interactions due to high surface to volume ratios. Subsequently separating these fiber mats in small fibrous networks was difficult as application of an ultrasounds and ball mill were unsuccessful and not able to win the strong cohesion forces between the fibers. As to avoid this difficult separation, spray spinning of Pullulan solution was carried out with the purpose of creating short fibers. This method was ineffective as well, the solvent did not evaporate sufficiently and many droplets were collected. This problem could be probably solved by resorting to solvents different than water, but, because the fibrous networks were intended for pharmaceutical applications, this limited the options when looking for alternative solutions to the encountered challenges.

Based on these premises and on Hayashibara, the company that deals with the commercial production of Pullulan, experience, in the present work another experimental technique, the spray drying, was implemented to obtain Pullulan elongated particle.

Chapter 2

A microbial polysaccharide: Pullulan

Pullulan is an extracellular polysaccharide, which was first reported from Aureobasidium Pullulans, synonym Pullularia Pullulans, a yeast like fungus. It is a natural water soluble polysaccharide produced from starch by fermentation. It is an odorless, flavorless, and highly stable white powder [28].

2.1 BIOSYNTHESIS

Most of the functions of exopolysaccharides produced by microorganisms are related to the protection of producer microorganism. Microorganisms would like to surround themselves with a highly hydrated exopolysaccharide layer, which may protect the microorganism from desiccation and against predation by protozoans. The presence of exopolysaccharide around the cell surface may also affect its diffusion properties. Pullulan is synthesized intracellularly at the cell wall membrane and secreted out to the cell surface to form a loose, slimy layer. Despite an intensive investigation on the cytological and physiological characteristics of A. Pullulans, the mechanism of Pullulan biosynthesis is not fully understood yet.

It was suggested that A. Pullulans does not directly convert glucose residues into polysaccharide and may instead be involved in the polymerization of carbohydrate precursors stored inside the cells. It is believed that cells first accumulate sugars and use this carbohydrate reserved for Pullulan production in the late stages of their life cycle. This hypothesis was later proved through an inverse correlation between the concentration of Pullulan and the content of intracellular glycogen [29].

2.2 MANUFACTURE

Pullulan is produced commercially by a batch wise cultivation of A. Pullulans on a medium containing 10±15% of starch hydrolysates. The medium also contains peptone, phosphate, and basal

salts. Cultures are stirred and aerated at 30°C. The initial pH of the culture is adjusted to 6.5, which is decreased, particularly in the first 24h, to a final pH value of about 3.5. The maximum culture growth occurs within 75h while the optimum yields of Pullulan are obtained within about 100h. After completion of fermentation, the fungal cells are removed by microfiltration. The filtrate is sterilized with heat and then treated with activated charcoal for the removal of melanin and other impurities. The decolorized filtrate is cooled and deionized using cation and anion exchange resins. The deionized solution is concentrated to a solid content of about 12% and again treated with activated carbon. Then, it is filtered using diatomaceous earth. The filtrate is concentrated to a solid content of about 30% and dried in a drum dryer. The dried Pullulan is pulverized to a desired particle size and finally packed in sterilized polyethylene bags. More than 70% yields of Pullulan with respect to initial substrate have been reported. The production and molecular weight of Pullulan is dependent on various culture conditions including pH, temperature, substrate, and strain [30].

2.3 STRUCTURE

Pullulan is a linear homopolysaccharide, which consists of maltotriose and maltotetraose units with both $\alpha-(1\rightarrow 6)$ and $\alpha-(1\rightarrow 4)$ linkages in regular alternation, as shown in Figure 2.1. It may also contain a small proportion of $\alpha-(1\rightarrow 3)$ linkages depending on the culture conditions and strain differences.

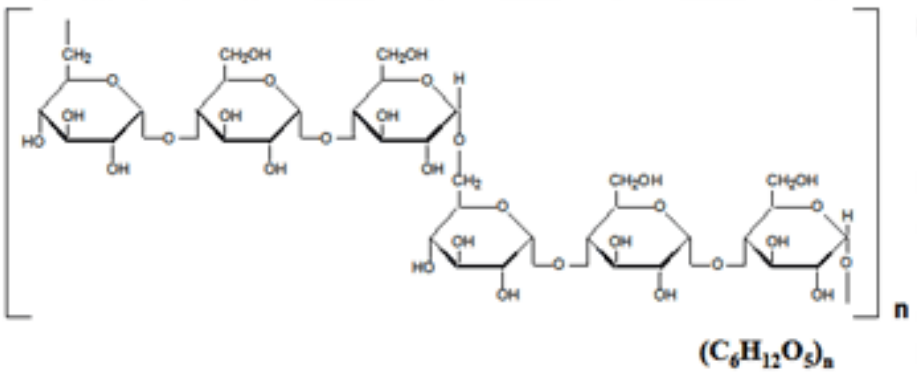

Figure 2.1: Pullulan chemical structure

Pullulan has close structural similarities to starch amylopectin and maltodextrin that, like Pullulan, also consist of glucose units with $\alpha-(1\rightarrow 6)$ and $\alpha-(1\rightarrow 4)$ glucosidic linkages. The major dissimilarity is the difference in the proportion of these linkages. Maltodextrin contains approximately 20% $\alpha-(1\rightarrow 6)$ glucosidic bonds while Pullulan approximately 30%. Similarly, corn starch contains 95% $\alpha-(1\rightarrow 4)$ glucosidic bonds and 5% $\alpha-(1\rightarrow 6)$ glucosidic bonds. Moreover, the tertiary structure of the molecule and the extent and mechanism of degradation of the materials in the human gut is also different in Pullulan and these glucan [31].

2.4 PROPERTIES

The unique linkage pattern, i.e. the regular alternation of glycosidic linkages, provides structural flexibility and enhanced solubility characteristics to the Pullulan molecule. Pullulan yields high viscosity solutions at relatively low concentrations. Due to these properties, Pullulan possesses distinctive physical traits including adhesive properties, mouldability into fibres and capability of formation of strong, oxygen impermeable films, characteristics not exhibited by other polysaccharides. Pullulan is a non toxic, non mutagenic, odourless, tasteless, edible white coloured powder. Pullulan is readily soluble in cold or hot water but is insoluble in organic solvents except for in dimethylformamide and dimethylsulfoxide. It gives clear and viscous solution in water. Although, Pullulan forms viscous aqueous solutions, it does not form gels. The viscosity of Pullulan solutions is not significantly affected by heating, changes in pH, and most metal ions, including sodium chloride [32].

2.5 CHEMICAL MODIFICATIONS

Pullulan can be easily derivatised in order to extend its applications by grafting different chemical structures on the backbone. Nine hydroxyl groups are available for substitution reactions on the repeating unit. They are distinguished by their position on the glucosidic moiety. Moreover, their relative reactivities also depend on the polarity of the solvent and of the reagents. Pullulan hydroxyls were submitted to numerous chemical reactions leading to a large number of derivatives.

Derivatization of Pullulan is carried out mostly to reduce its water solubility or to introduce charged or reactive groups for functionality. Esterification or etherification of Pullulan is performed in order to reduce its water solubility. Similarly, hydrogenation increases the heat stability, and carboxylation enhances its solubility in cold water. Pullulan has been sulfated, chlorinated, sulfinethylated, and chloroalkylated [33].

2.6 APPLICATIONS

Pullulan, as a member of bacterial exopolysaccharides, demonstrates itself a high potential for applications due to its bioactive property. Since the major limitation of Pullulan production, the removal of melanin, has been solved in the early 1990s, the production cost of Pullulan could further reduce and become more competitive to similar products, such as dextran, xanthan, and other microbial produced polysaccharides. Indeed, despite the fact that Pullulan has been in commercial production for more than 25 years, few of these potential uses have been widely adopted. In the past two decades, the major market of Pullulan was mainly in food applications. With the advanced technologies of modification and cultivation skills, production of modified Pullulan derivatives possessing distinctive material properties and Pullulan with specific molecule weight distribution can be achieved. As a result, a boosting number of reports concerning Pullulan applications in

pharmaceutical, medical, electronics and environmental remediation areas have been published [34] [35] [36] [37] [38] [39] [40] [41].

Chapter 3

The spray drying technique

Spray drying is a widely used manufacturing process applied in many areas, including the food, chemical, electronics, pharmaceutical and biopharmaceutical industry. It is a well established technique that has been used for over a century but remains an active field of innovation, driven by the ever increasing demand for more sophisticated particles. In the pharmaceutical industry spray drying is used to manufacture particles that form the basis for dry dosage forms. These particles must be able to stabilize the active pharmaceutical ingredient and provide physical stability for the dosage form on storage. They must have adequate powder flow properties and dispersibility, and, in the case of respiratory delivery, suitable aerodynamic properties. In recent years, particle engineering has been used to design complex particles that meet these demands. Hollow, low density particles with controlled surface morphology, particles with functional layers, or particles comprising smaller subunits such as nanoparticles or defined voids, have been introduced. Because of the complexity of these particles, a sound understanding of the particle formation process is necessary for successful particle engineering. This motivates further research into the physical and chemical mechanisms that control the drying and particle formation process in the aerosol phase [42].

The process, as schematized in Figure 3.1, involves the spraying of a liquid feed formulation into a hot drying medium. The droplets formed by the atomization process are dried through solvent evaporation to form particles that are collected as a dry powder.

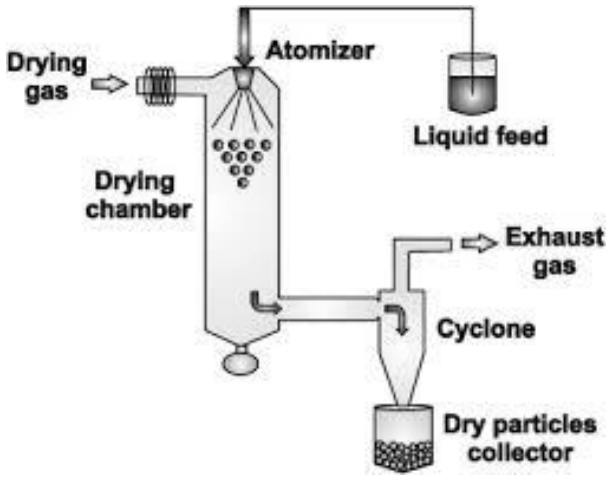

Figure 3.1: Diagram of the equipment and process of conventional spray drying

The variables that affect the characteristics of the product and that can be tuned are:

- Process parameters;
- Properties of the liquid feed;
- Equipment design [43].

The process of particle formation, as described here, together with the control of the droplet size, constitutes the backbone of the thesis that particle size can be controlled by the atomization conditions and morphology can be manipulated by the solids concentration and drying temperature.

3.1 ATOMIZATION

Usually the main reason for atomizing a liquid is to obtain a large and rapid increase in its surface area and thereby a corresponding increase in its rate of evaporation. Although the phenomena behind atomization are difficult to model and fully understand, the atomization of a liquid in practice is fortunately fairly easy to accomplish, since, for most liquids, all that is needed is the existence of a high relative velocity between the liquid to be atomized and the surrounding air or gas [44].

3.1.1 ATOMIZER CLASSIFICATION

There are various nozzle designs and nozzle sizes available to produce optimum conditions of liquid air contact. Some atomizers accomplish this by discharging the liquid at high velocity into a relatively slow moving stream of air or gas. Notable examples include the various forms of pressure atomizers and rotary atomizers, which eject the liquid at high velocity from the periphery of a rotating cup or disk. An alternative approach is to expose the relatively slow moving liquid to a high velocity airstream. The latter method is generally known as twin fluid, air assist, or air blast atomization. Other examples may involve heterogeneous processes in which air bubbles or liquid vapor become involved in disrupting the liquid phase during the spraying process [44].

Two fluid nozzles are usually classified into:

- Internal mixing nozzles:

The contact between the air and the liquid occurs within the nozzle head. These nozzles have the advantage of wide flexibility and are particularly useful for atomizing highly viscous liquids and liquid slurries. However, their aerodynamic and fluid dynamic flow patterns are very complex, due to the intense mixing of gas and liquid within the mixing chamber. A schematization is illustrated in Figure 3.2.

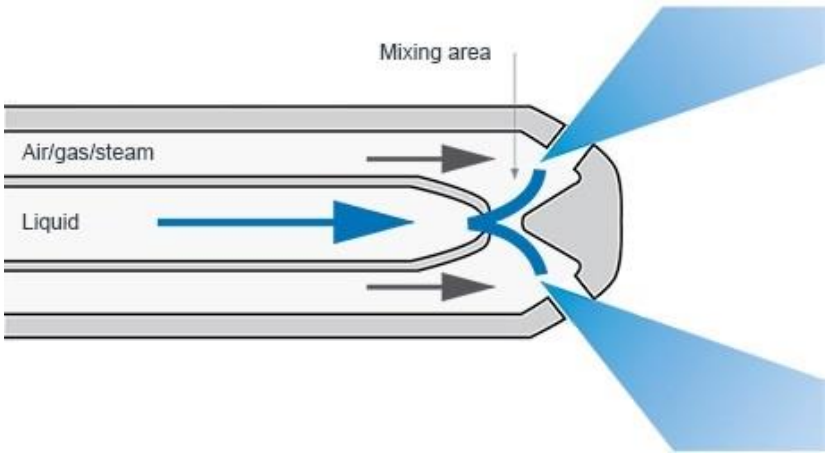

Figure 3.2: Internal mix two fluid spray nozzle

- External mixing atomizers:

The contact between the air and the liquid takes place outside the nozzle head. These nozzles usually employ a high velocity stream of air or steam that flows from an annular nozzle and is arranged to impinge at some angle onto a jet or conical sheet of liquid that is created at the center of the atomizer. An illustration is displayed in Figure 3.3.

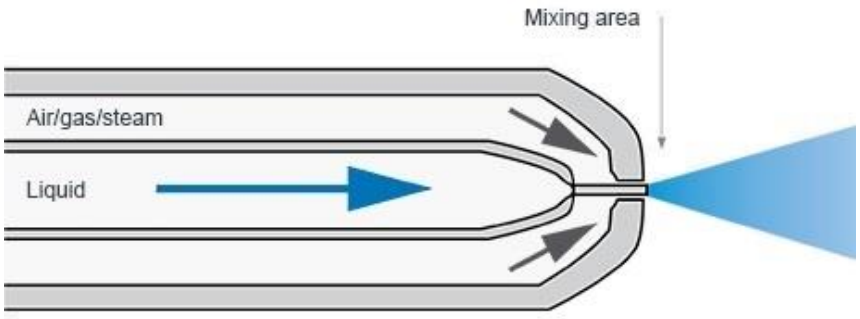

Figure 3.3: External mix two fluid spray nozzle

3.1.2 THE PRINCIPLES OF ATOMIZATION IN TWO FLUID EXTERNAL MIXING NOZZLES

Pneumatic nozzle atomization involves impacting a bulk liquid with high velocity gas, creating high frictional forces over liquid surfaces and causing liquid disintegration into spray droplets. The process can be considered as a disruption of the consolidating influence of surface tension by the action of internal and external forces. In the absence of such disruptive forces, the system is stable and the surface tension tends to maintain it into the cylindrical conformation. However, if a disturbance is applied, instabilities develop. Thus, the surface tension tends to pull the liquid into the form of a sphere, since this has the minimum surface energy. Liquid viscosity exerts a stabilizing influence by opposing any change in system geometry. On the other hand, aerodynamic forces

acting on the liquid surface may promote the disruption process by applying an external distorting force to the bulk liquid. Breakup occurs when the magnitude of the disruptive force just exceeds the consolidating surface tension force.

Therefore, liquid disintegration in the presence of gaseous flow involves complex situations of liquid instability, but, as clarified in Figure 3.4, the overall process can be considered to occur in two phases:

- Tearing of the liquid sheet into ligaments;
- Further breaking of these liquid forms into small droplets [45].

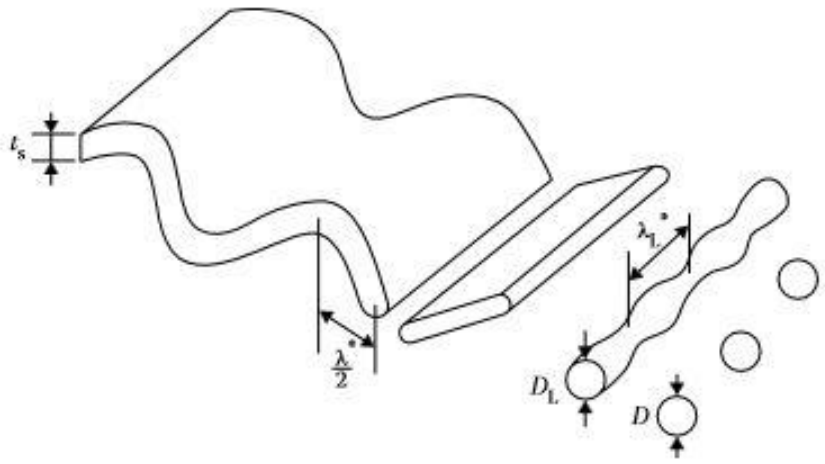

Figure 3.4: The atomization process

3.1.2.1 FORMATION OF THREADS BY DISINTEGRATION OF LIQUID SHEETS

The disruption of the liquid as it is discharged from the orifice of the atomizer is affected by:

- The disturbances in the liquid flow within the atomizer, which may cause turbulence in the liquid;
- The properties of the gaseous medium into which the stream is discharged;
- The physical properties of the liquid itself.

High velocity air can typically readily penetrate a low velocity liquid jet thereby causing the necessary turbulence and energy transfer to form a spray with narrow spray angle. The angle of the spray is normally defined as the angle formed by two straight lines drown from the discharge orifice to the outer periphery of the spray at some specified distance downstream of the nozzle, as illustrated in Figure 3.5. An important aspect of atomizer design, in addition to achieving the desired drop size distribution, is to ensure that the droplets formed in atomization are discharged from the nozzle in the form of a symmetrical uniform spray. In general, an increase in spray cone angle increases the exposure of the droplets to the surrounding air or gas, leading to improved atomization and to higher rates of heat and mass transfer [46].

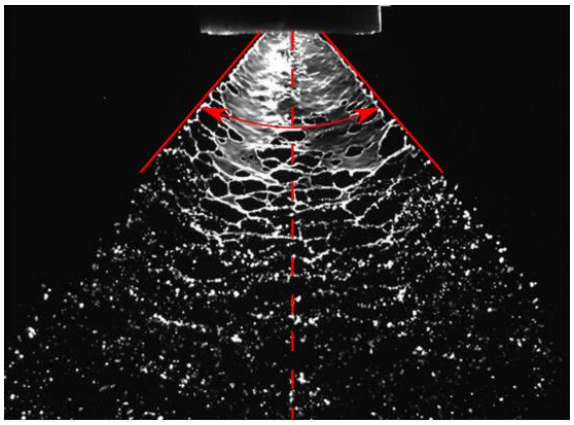

Figure 3.5: Spray cone angle

As the air speed increases, the liquid sheet disintegrates earlier so that ligaments are formed nearer the lip of the atomizer. The size of the ligaments tends to decrease, their life time becomes shorter and, upon their collapse, much smaller drops are formed. Instead high values of liquid viscosity and liquid flow rate result in thicker films. Taking into account that the role of viscosity is to inhibit the growth of instability and tends to generally delay the onset of disintegration, when atomization occurs, it does so well downstream in regions of relatively low velocity, so the liquid is drawn out from the atomizing lip in the form of long ligaments. In consequence, drop sizes tend to be higher. At larger liquid feed rates however, even high velocity air cannot penetrate the thick liquid jets involved. Atomization is thus incomplete, and a wide droplet size distribution results [47]. In most cases, turbulence in the liquid, cavitation in the nozzle, and aerodynamic interaction with the surrounding air, which increases with air density, all contribute to atomization.

Three modes of disintegration in the sheet have been defined by Fraser and Eisenklam [45]:

- Rim contraction, Figure 3.6 (on the left);
- Wavy sheet, Figure 3.6 (in the middle);
- Perforated sheet, Figure 3.6 (on the right).

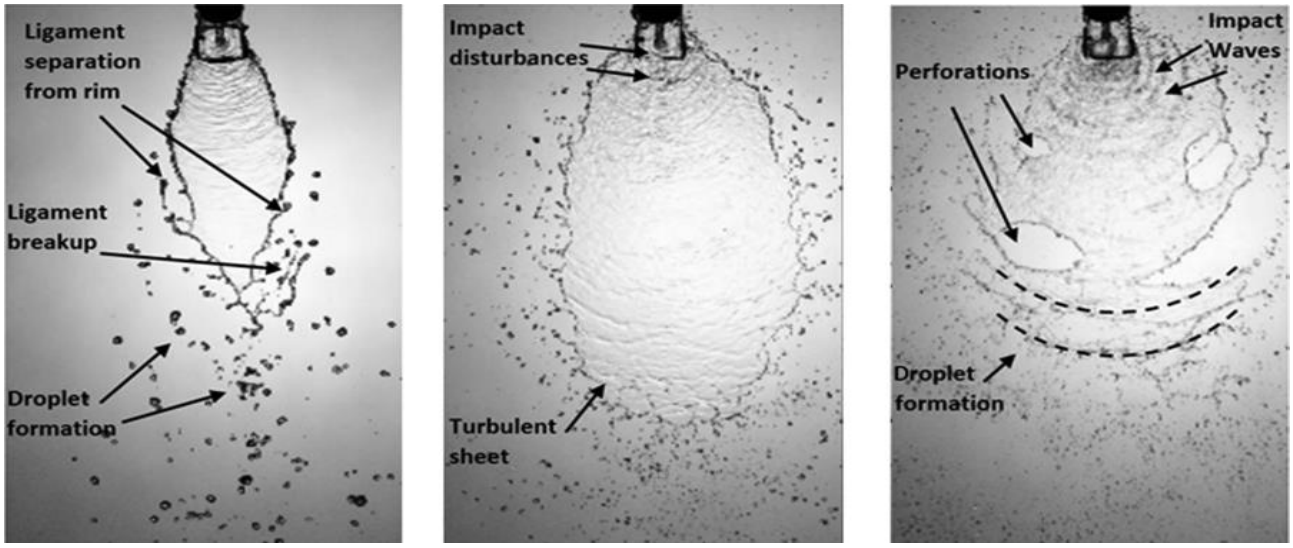

Figure 3.6: Modes of sheet disintegration

Because of surface tension, any liquid boundary is continually contracting and this phenomenon produces rim disintegration. Threads are pulled out from the rim during contraction. This mode is most prominent under conditions of low velocity, high surface tension and high viscosity. In perforated sheet disintegration, the leading edge disintegrates to a network of threads. Disturbances on the sheet puncture it when they have reached a thin enough region and the resulting holes expand regularly by surface tension so that they remain nearly circular until they coalesce, forming long threads. Disintegration can also occur in the absence of perforations through the generation of a wave motion on the sheet. The stability is such that major wave disturbances caused by the atmosphere disintegrate the sheet by tearing whole surfaces away before the leading edge is reached [48].

Clearly, the orderliness of the manner of disintegration of the sheet and the uniformity of production and diameter of threads has a great influence on the drop size distribution. Rim disintegration gives large drops together with numerous small satellite drops. Perforations occurring in the sheet at the same distance from the orifice have a similar life and thus the threads can be uniform, producing uniform drops. Wavy sheet disintegration is highly irregular and thus the drop sizes are very varied [49].

3.1.2.2 DROPLET FORMATION BY DISINTEGRATION OF LIQUID LIGAMENTS

The competition set up on the surface of the ligament between the cohesive and disruptive forces gives rise to oscillations and perturbations. Under favourable conditions, the oscillations are amplified and the liquid body disintegrates into droplets. This process is sometimes referred to as primary atomization. If the droplets so formed exceed the critical size, they further disintegrate into drops of smaller size, a process known as secondary atomization.

The properties of jets of most interest are the continuous length, which provides a measure of the growth rate of the disturbance, and the drop size, which is a measure of the wave number of the most unstable disturbance. Also of interest is the manner in which the jet is disrupted.

In an early mathematical analysis, Rayleigh [50] employed the method of small disturbances to predict the conditions necessary to cause the collapse of a liquid jet. Comparing the surface energy, directly proportional to the product of surface area and surface tension, of the disturbed configuration with that of the undisturbed column, Rayleigh calculated the potential energy of the disturbed configuration, relative to the equilibrium value, as

$$E_S = \frac{\pi\sigma}{2d}(\gamma^2 + n^2 - 1)b_n^2 \qquad \text{Eq(3.1)}$$

where

- E_S: potential surface energy
- d: jet diameter
- b_n: constant in the Fourier series expansion
- γ: dimensionless wave number, defined as

$$\gamma = \frac{2\pi}{\lambda} \quad \text{Eq(3.2)}$$

- λ: wavelength of disturbance
- n: any positive integer (including zero).

For non symmetrical disturbances, $n \gg 1$ and E_S is always positive, indicating that the system is always stable to this class of disturbance. When $n = 0$ and $\gamma < 1$, which is the case for symmetrical disturbances, equation (3.1) shows that E_S is negative and the system is unstable to this class of disturbance. Hence, a liquid jet that is affected by surface tension forces only will become unstable to any axisymmetrical disturbance whose wavelength satisfies the inequality

$$\lambda > \pi d \quad \text{Eq(3.3)}$$

which corresponds to

$$\gamma < 1 \quad \text{Eq(3.4)}$$

The conclusion to be drawn from Rayleigh's analysis of the breakup of non viscous liquid jets under laminar flow conditions is that all disturbances on a jet with wavelengths greater than its circumference will grow. Furthermore, his results show that one class of disturbance will grow fastest and eventually control the breakup. Although actual liquid jets are viscous, turbulent, and subjected to surrounding air influences, the conclusions of Rayleigh have found general acceptance in later theories as a valid first approximation.

Rayleigh's contribution to the mathematical treatment of the breakup of jets stemmed from his recognition that jet breakup is a dynamic problem and that the rate of collapse is important. Assuming in equation (3.1) that

$$b_n \propto e^{qt} \quad \text{Eq(3.5)}$$

where q is the exponential growth rate of disturbance, Rayleigh showed that the exponential growth rate of the fastest growing disturbance is given by

$$q_{max} = 0.97\left(\frac{\sigma}{\rho_L d^3}\right)^{0.5} \quad \text{Eq(3.6)}$$

and λ_{opt} corresponding to q_{max} is

$$\lambda_{opt} = 4.51d \quad \text{Eq(3.7)}$$

After breakup, the cylinder of length $4.51d$ becomes a spherical drop of diameter D, so that

$$4.51d \times \frac{\pi}{4} d^2 = \frac{\pi}{6} D^3 \quad \text{Eq(3.8)}$$

and hence

$$D = 1.89d \quad \text{Eq(3.9)}$$

Thus for the Rayleigh mechanism of breakup the average drop size is nearly twice the diameter of the undisturbed jet.

Tyler [51] later measured the frequency of formation of droplets as a jet disintegrated and related it to the wavelength of the disturbance. By assuming that the volume of the spherical drops formed by disintegration of the jet is equal to the volume of a cylinder, with diameter equal to that of the undisturbed jet and with wavelength equal to the most rapidly growing disturbance, Tyler obtained the following results:

$$\frac{D}{d} = \left(1.5 \frac{\lambda}{d}\right)^{\frac{1}{3}} \quad \text{Eq(3.10)}$$

$$\lambda_{opt} = 4.69d \quad \text{Eq(3.11)}$$

$$D = 1.92d \quad \text{Eq(3.12)}$$

In view of the close agreement between his experimental results and the predictions of Rayleigh's mathematical analysis, Tyler concluded that cylindrical jets do break up under the conditions required for maximum instability, as predicted by Rayleigh's theory.

A more general theory for disintegration at low jet velocities was developed by Weber [52], who extended Rayleigh's analysis to include viscous liquids. He assumed that any disturbance causes rotationally symmetrical oscillations of the jet, as illustrated in Figure 3.7.

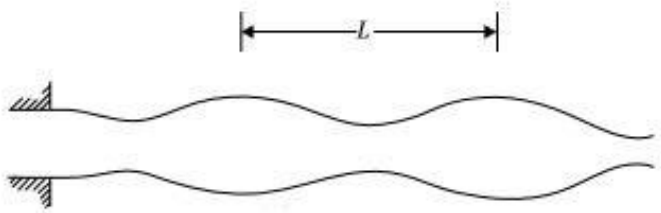

Figure 3.7: Jet with rotationally symmetric disturbance

If the wavelength of the initial disturbance is less than λ_{min} the surface forces tend to damp out the disturbance. If λ is greater than λ_{min} the surface tension forces tend to increase the disturbance, which eventually leads to disintegration of the jet. There is, however, one particular wavelength λ_{opt} that is most favourable for drop formation.

For non viscous liquids:

$$\lambda_{min} = \pi d \quad \text{Eq(3.13)}$$

$$\lambda_{opt} = \sqrt{2\pi d} = 4.44d \quad \text{Eq(3.14)}$$

For viscous liquids:

$$\lambda_{min} = \pi d \quad \text{Eq(3.15)}$$

$$\lambda_{opt} = \sqrt{2}\pi d\left(1 + \frac{3\mu_L}{\sqrt{\rho_L \sigma d}}\right)^{0.5} \quad \text{Eq(3.16)}$$

Thus, for non viscous liquids the value of $\frac{\lambda}{d}$ required to produce maximum instability is 4.44, which is close to the value of 4.51 predicted by Rayleigh for this case. It is of interest to note that the minimum wavelength is the same for both viscous and non viscous liquids, but the optimum wavelength is greater for viscous liquids. Weber next examined the effect of air resistance on the disintegration of jets into drops. He found that air friction shortens both the minimum wavelength and the optimum wavelength for drop formation. Weber also considered the case where the air motion induces wave formation, as depicted in Figure 3.8, and showed that this can occur only at relative air velocities above a certain minimum value.

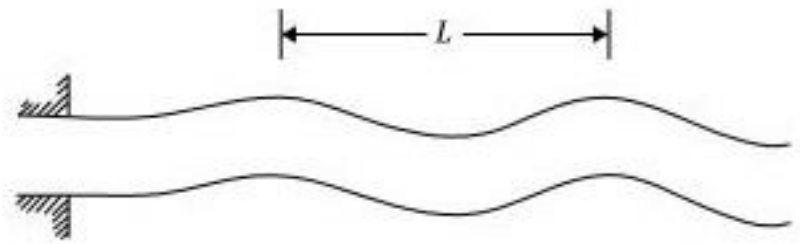

Figure 3.8: Jet disturbance causing wave formation

Haenlein [53] presented experimental evidence in support of Weber's theoretical analysis and identified four distinct regimes of breakup in the disintegration of a liquid jet:

- Drop formation without the influence of air:

This is the mechanism studied by Rayleigh. The term varicose is sometimes used to describe the appearance of the jet in this regime. Radially symmetric waves, as illustrated in Figure 3.9, are formed by the interaction of primary disturbances in the liquid and surface tension forces. This regime is characterized by a linear relationship between the length of the jet prior to breakup and the jet velocity. Weber calculated the breakup time to be proportional to $d_0^{1.5}$ for non viscous jets and proportional to d_0 for viscous jets.

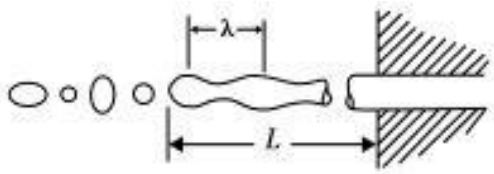

Figure 3.9: Oscillations cause jet breakup without air friction

- Drop formation with air influence:

As shown in Figure 3.10, when the jet velocity is increased, the aerodynamic forces of the surrounding air are no longer negligible and tend to accentuate the waves formed under the previous regime.

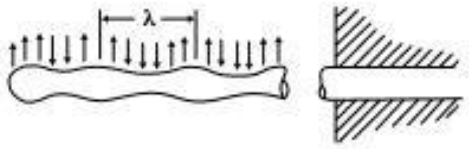

Figure 3.10: Oscillations with air friction

- Drop formation due to waviness of the jet:

As represented in Figure 3.11, this regime is associated with increasing effectiveness of aerodynamic forces and reduced relative influence of surface tension. The term sinuous has been used to describe the jet in this regime.

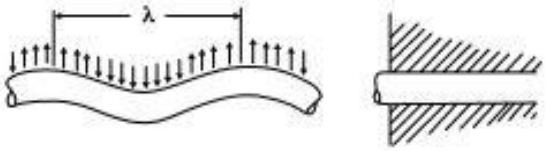

Figure 3.11: Wave like breakup caused by air friction

- Complete disintegration of the jet:

The liquid is broken up at the nozzle in a chaotic and irregular manner

Should be note that although these four separate regimes can be clearly identified, there is no sharp demarcation between them.

3.1.2.3 ADIMENSIONAL ANALYSIS

Both theoretical and experimental studies on jet and sheet disintegration have demonstrated the need to group all the variables involved into non dimensional parameters to clarify their effects on the atomization process.

As in most flow systems, the Reynolds grouping, which represents the ratio of momentum forces to viscous drag forces, usefully describes the flow state of the emerging jet in terms of both velocity profile and the magnitude of the radial velocity components that promote jet disintegration. Flow regimes represent typical flow patterns exhibited by fluids as they flow under differing conditions. Reynolds number is used to describe the boundaries of flow regimes.

$$Re_{liq} = \frac{v_{liq}\rho_{liq}d_{jet}}{\eta_{liq}} \qquad \text{Eq(3.17)}$$

$$Re_{liq} = \frac{v_{liq}\rho_{liq}d_{jet}}{\eta_{liq}} \qquad \text{Eq(3.18)}$$

Instead, the Ohnesorge number relates the viscous forces to inertial and surface tension forces. This group contains only the properties of the globules formed in primary atomization before they split up into smaller drops during secondary atomization. It is sometimes called a stability group because it provides an indication of the resistance of a globule to further disintegration [54].

$$Oh = \frac{\eta_{liq}}{\sqrt{\sigma_{liq}\rho_{liq}d_{jet}}} \qquad \text{Eq(3.19)}$$

Therefore, having been introduced these adimensional parameters, the most commonly quoted criterion for classifying the breakup mechanism of a jet is the one based on Oh versus Re map [55].

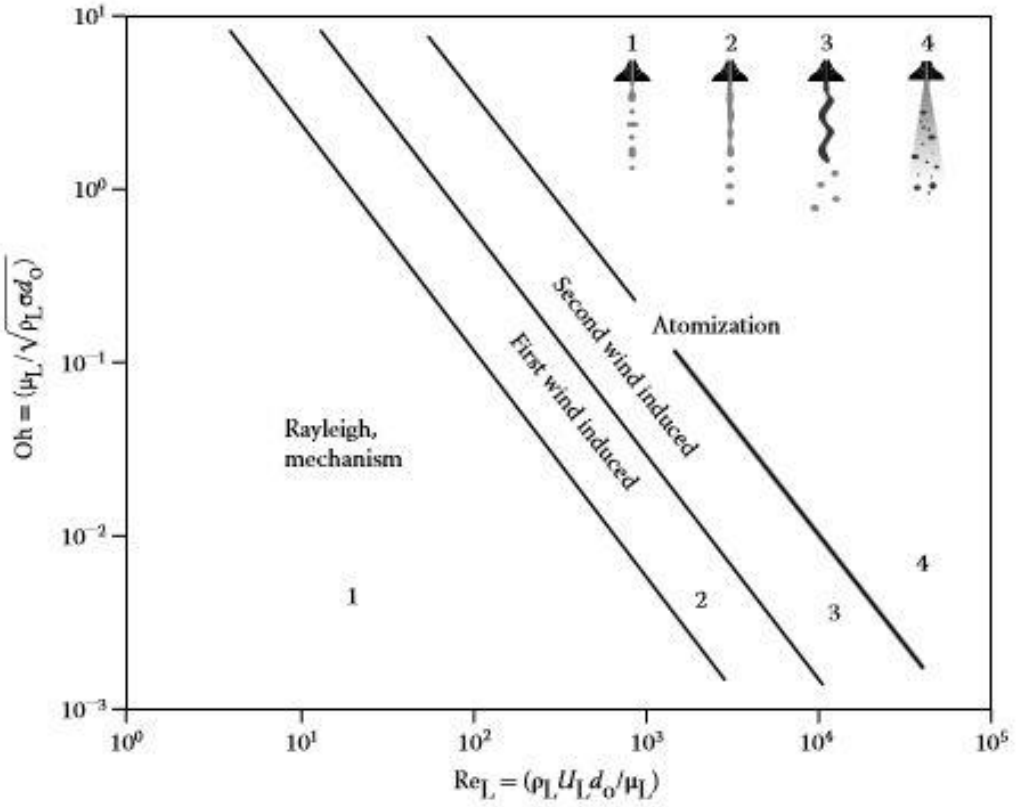

Figure 3.12: Disintegration modes classification

Furthermore, with increasing liquid velocity v_{liq} at the orifice of a circular tube shaped nozzle, still without any gas flow, the events of dripping, laminar jet breakup, wave breakup and finally atomisation follow one after the other consecutively. Neglecting the effect of gravity, transition to liquid column breakup into droplets is reached when the longitudinal contraction rate of the liquid jet is exactly equal to its rate of discharge. Thus, the liquid Weber number can be taken into consideration and can be thought of as a measure of the relative importance of the fluid's inertia compared to its surface tension [56].

$$We_{liq} = \frac{v_{air}^2 \rho_{liq} d_{orifice}}{\sigma_{liq}} \quad \text{Eq(3.20)}$$

Therefore, the flow characteristics most relevant to atomization is the velocity, which can contribute effectively to jet or sheet disintegration, especially under conditions where aerodynamic influences are relatively small. In reality, aerodynamic forces are seldom small, and the air Weber number, which represents the ratio of the disruptive aerodynamic forces to the restoring surface tension forces, becomes very significant.

$$We_{air} = \frac{v_{air}^2 \rho_{air} d_{orifice}}{\sigma_{liq}} \quad \text{Eq(3.21)}$$

In fact, if a gas impinges on a liquid surface with sufficiently high relative rate, the liquid accelerates and is broken up. Breakup takes place when the dynamic pressure of the gas exceeds the pressure inside the droplet to a considerable extent [56].

3.2 DROPLET DRYING KINETICS

The theoretical modelling of a spray drying process is based on the moisture and temperature history the spray droplets and wet particles undergo. Although a study of a single wet particle drying does not take into account many of the complex interactions encountered with sprays, it can be utilized as a practical and direct way of observing the rates of evaporation and morphological changes at the particulate level [57].

3.2.1 DROPLET DRYING HISTORY

The internal transport phenomena within the spray of droplet are described with the help of a two stage drying kinetics model [58] [59] [60], as illustrated in Figure 3.13.

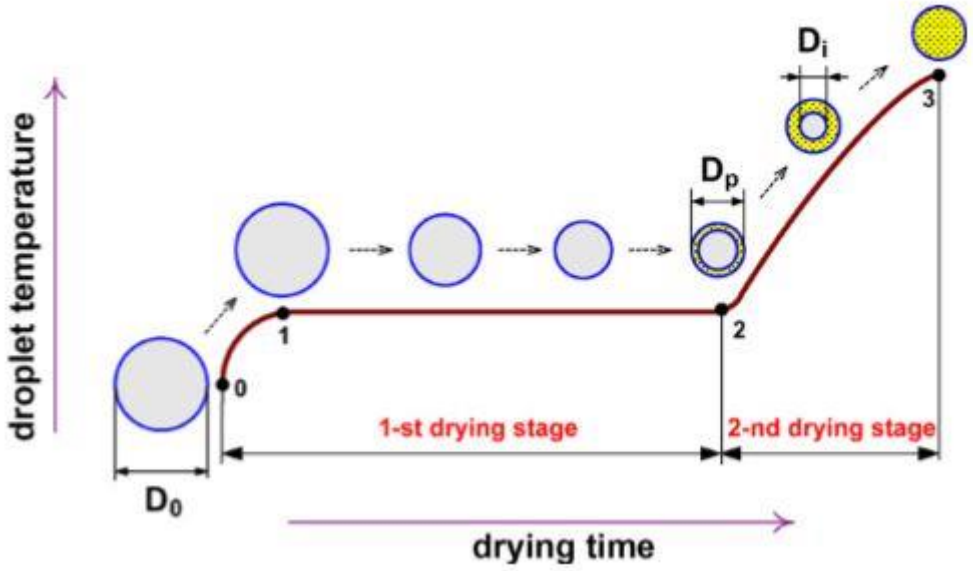

Figure 3.13: Two stage drying of droplet containing solids

During the sensible heating period, between the points 0 and 1 in Figure 3.13, the droplet temperature increases to its wet bulb temperature and no appreciable solvent evaporation takes place.

In the first stage of constant drying rate, between the points 1 and 2 in Figure 3.13, the droplet behaves like pure solvent and evaporation rate is dictated by wet bulb drying kinetics. This unhindered drying results in the shrinkage of the droplet diameter as the solvent is rapidly lost through evaporation. A scheme of droplet drying in the first drying stage is reported in Figure 3.14.

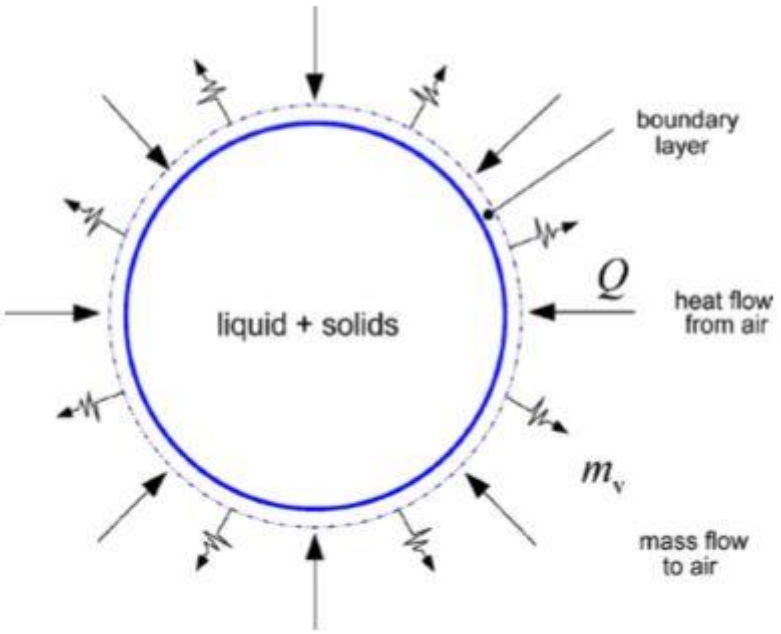

Figure 3.14: Scheme of droplet drying in the first drying stage

As evaporation progresses, solute molecules arrange themselves moving in such a way to homogenize the solution concentration within the droplet at a rate controlled by their diffusion rates. If particle migration is slow, the solute concentration close to the air/solution interface increases and solute precipitation may occur. When solidification, also called skin formation, occurs droplet turns into a wet particle, where can be identified two regions:

- Layer of dry porous skin;
- Internal wet core.

It is the beginning of falling rate drying period. In this condition, between the points 1 and 2 in Figure 3.13, solidification slows the transport of solvent to the surface for evaporation and drying becomes diffusion rate limited. As a result of the hindered drying, the particle wet core shrinks and the thickness of the crust region increases. The skin temperature increases as liquid boundary moves inward. The particle outer diameter is assumed to remain unchanged during the second drying stage, but the skin may collapse. A scheme of wet particle drying in the second drying stage is shown in Figure 3.15:

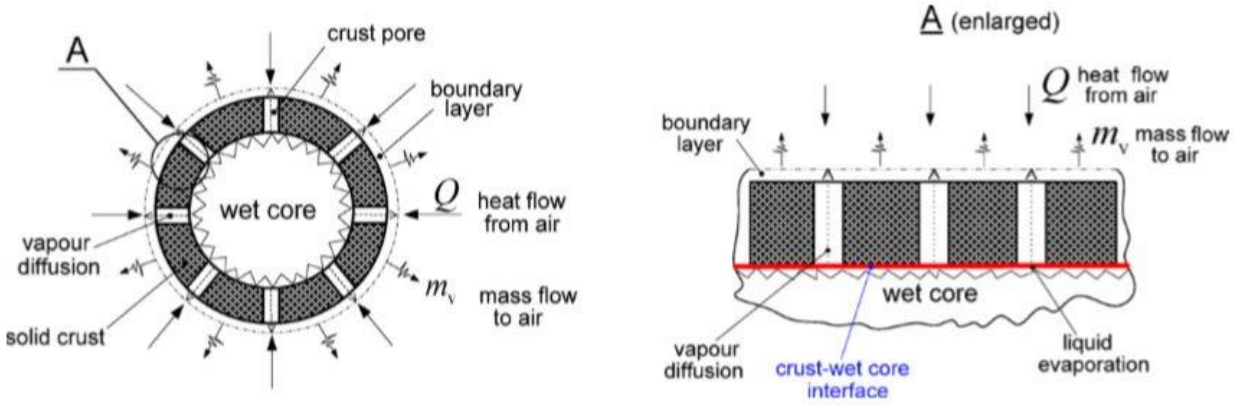

Figure 3.15: Scheme of wet particle drying in the second drying stage

After the point when the particle moisture content decreases to a minimal possible value, determined either as an equilibrium moisture content or as a bounded moisture that cannot be removed by drying, the particle is treated as a dry non evaporating solid sphere.

3.2.1.1 ANALYTICAL MODEL

The evaporation of a solution droplet during spray drying can be described as a coupled heat and mass transport problem. The difference between the vapour pressure of the solvents and their partial pressure in the gas phase is the driving force of the drying process. The rate of evaporation is determined by a balance of the energy flux causing vaporization at the surface and the energy flux convected to the surface of the droplet. The latter can be provided from the gas phase and from the heat capacity of the droplet through droplet cooling. The evaporation rate determines the surface recession rate of the droplet. The receding droplet surface causes a diffusional flux of the solutes

away from the surface towards the center of the droplet. In the absence of internal convection, the distribution of the chemical components in an evaporating droplet is described by the non linear diffusion equation which becomes Fick's second law of diffusion if no interactions between the solutes and constant diffusion coefficients are assumed [42].

$$\frac{\partial c_i}{\partial t} = D_i \frac{\partial^2 c_i}{\partial r^2} + \frac{2\partial c_i}{r\partial r} \quad \text{Eq(3.22)}$$

In the case of radial symmetry, using the normalized radial coordinate

$$R = \frac{r}{r_s} \quad \text{Eq(3.23)}$$

the equation (3.22) can be written as

$$\frac{\partial c_i}{\partial t} = \frac{D_i}{{r_s}^2}\left(\frac{\partial^2 c_i}{\partial R^2} + \frac{2\partial c_i}{R\partial R}\right) + \frac{R\partial c_i}{r_s \partial R}\frac{\partial r_s}{\partial t} \quad \text{Eq(3.24)}$$

where

- c_i denotes the concentration of solute i;
- D_i indicates the diffusion coefficient of solute i in the liquid phase;
- r_s represents the droplet radius.

Equation (3.24) has an analytical solution under the steady state condition, meaning the droplet surface is not receding,

$$r_s \frac{\partial r_s}{\partial t} = const \quad \text{Eq(3.25)}$$

The steady state evaporation of a liquid droplet of diameter d is proportional to the surface area of the droplet. The evaporation rate k is defined as

$$d^2(t) = d_0^2 - kt \quad \text{Eq(3.26)}$$

A constant evaporation rate fulfills condition (3.25), because

$$\frac{\partial d^2}{\partial t} = -k = 8 r_s \frac{\partial r_s}{\partial t} \quad \text{Eq(3.27)}$$

The solution to equation (3.24) under the assumption of constant evaporation is given by Leong [61]

$$c_i = c_{c,i} e^{-\frac{r_s \partial r_s}{2 D_i \partial t} R^2} \quad \text{Eq(3.28)}$$

Equation (3.28) expresses the concentration c as a function of the concentration at the center of the droplet c_c .

It is more useful to express the concentration as a function of the average concentration c_m in the droplet, because it can be calculated from the initial conditions at any time in the droplet history as

long as the evaporation rate is constant using a simple mass balance in combination with equation (3.26).

Hence, after equation (3.28) is integrated over the volume of the sphere to introduce the average concentration, rearrangement yields

$$c_i = c_{m,i} \frac{e^{Pe_i \frac{R^2}{2}}}{3 \int_0^1 R^2 e^{Pe_i \frac{R^2}{2}} dR} \quad \text{Eq(3.29)}$$

Here the dimensionless Peclet number Pe

$$Pe_i = -\frac{r_s \partial r_s}{D_i \partial t} = \frac{k}{8 D_i} \quad \text{Eq(3.30)}$$

has been introduced to simplify the equation.

For $R = 1$ it is possible to find the surface concentration

$$c_{s,i} = \frac{c_{m,i}}{3\beta_i} e^{\frac{Pe_i}{2}} \quad \text{Eq(3.31)}$$

with

$$\beta_i = \int_0^1 R^2 e^{Pe_i \frac{R^2}{2}} dR \quad \text{Eq(3.32)}$$

β must be integrated numerically for each Pe number to obtain the exact solution.

Alternatively, an approximate expression for the surface enrichment E_i

$$E_i = \frac{c_{s,i}}{c_{m,i}} = 1 + \frac{Pe_i}{5} + \frac{{Pe_i}^2}{100} - \frac{{Pe_i}^3}{4000} \quad \text{Eq(3.33)}$$

can be used with an accuracy of $\pm 1\%$ for $Pe < 20$.

This constant evaporation model assumes that during most of the evaporation the gas temperature and thus the droplet temperature are constant. It does not account for the non stationary evaporation at the beginning of the evaporation process, where the droplet temperature rapidly changes, nor does it account for any changes in the evaporation rate immediately prior to solidification of the particles. In general, the diffusion coefficients depend on the concentration of the solutes and change significantly during the drying process, especially when solute concentrations reach supersaturation or the liquid phase viscosity increases prior to solidification. This simplification prevents the application of the analytical model during the solidification of the particles.

3.2.1.2 NUMERICAL MODEL

The analytical model cannot correctly describe the non stationary phases of the evaporation, which are the initial temperature change of the droplet as it approaches the quasi steady equilibrium of the constant evaporation rate period, and more importantly, the solidification of the particle during the late stage of the evaporation. These processes must be described by coupled heat and mass transfer equations in the gas and the droplet. Because there is no analytical solution for this set of equations, a numerical treatment becomes necessary.

Many models for advanced two and three dimensional spray drying have been proposed by several academic and industrial groups. Most of the developed models were based on Computational Fluid Dynamics, an approach that utilizes numerical methods and algorithms to solve and analyze with the help of computers complicated problems that involve fluid flows. The usage of CFD technique allowed the researchers to reveal the complexity of flow fields of drying agent and droplets/particles as well as to establish the common features of spray drying processes like three dimensionality and unsteady character of the drying [62] [63] [64] [65] [66]. However, in spite of the performed extensive researches on comprehensive understanding of the main physical phenomena involved in the spray drying process and many detailed investigations devoted to the droplet drying kinetics [67], the existing spray drying models are lacking proper mathematical description of the complex internal transport phenomena within the dispersed phase. This disadvantage is attributed to an extreme difficulty of incorporating the comprehensive droplet drying kinetics models in commercially available CFD packages or individually developed numerical codes. Overcoming this challenge would open a way for the much more realistic theoretical modelling of the spray drying process and would give a reasonably reliable prediction of the quality and morphology of the obtained final product.

3.2.2 PARTICLE FORMATION MECHANISMS

The drying kinetics defines the resulting particle morphology and density. Due to the fact that these properties are strictly dependent on the film forming characteristics, the balance between the stiffness of the outer layer shell and evaporation of the enclosed solvent plays an essential role [68]. In absence of a detailed fluid dynamics model couplet to strict mechanics analysis, particle attributes can be related to process parameters using dimensionless correlations such as the Peclet number, that can define when a skin is likely to form at the particle surface during droplet drying [69] [70]. The Peclet number is influenced by a combination of material properties of the solute and the solvent and processing parameters that determine the evaporation rate [71].

For $Pe < 1$ the diffusional motion of the solutes is fast compared to the radial velocity of the receding droplet surface, due to the slow evaporation. The droplet shrinks while the solute molecules diffuse toward the center of the droplet, delaying the surface enrichment. Thus, the characteristic time for the solutes to reach saturation at the surface is close to the droplet lifetime. Under this circumstance,

the particle will form a dense structure close to the theoretical density of the material. Typical examples are solid saccharide particles dried at moderate to low drying gas temperatures [72].

Instead, when $Pe > 1$ the evaporation predominates and the surface becomes rapidly enriched in solutes that precipitate. The faster the evaporation rate, the sooner the surface reaches its critical supersaturation, causing early skin formation. This condition will lead to a larger size and lower density hollow particle, that may finally collapse or wrinkle depending on the thickness and mechanical properties of the skin. Typical examples that fall into the category of high Peclet number particle formation are proteins [73] and polymers [74].

The discussion in the preceding section is very simplified. It assumes a constant evaporation rate and a diffusion coefficient that does not change with time or location in the droplet. In reality, the diffusion coefficient of a component changes with concentration and composition of the solvent. Hence, the Peclet number changes as the droplet evaporation progresses, in particular in cosolvent systems, where one solvent evaporates faster than the other does.

The Peclet number associated with a component in a formulation system can also change drastically, when the component undergoes a phase transition, e.g. crystallizes once a critical concentration is reached. For instance if a molecule with low solubility is dried that has a large diffusion coefficient, so its Peclet number is low initially, the concentration increases without much surface enrichment until supersaturation is reached and precipitation of a separate phase is initiated at the surface or throughout the bulk of the droplet. At this point, the mobility of this component is no longer determined by the diffusion coefficient of the dissolved molecule, but rather by the much lower mobility of the phase separated domains. The Peclet number associated with this component is now very large and the phase separated domains accumulate at the surface and merge to form a shell which may deform in various ways, subsequently. Typical excipients that fall into this class are low solubility amino acids or small peptides that have a propensity to crystallize or form liquid crystals [42].

Although these mechanisms are well reported in the literature, in most pharmaceutical applications large polymers, proteins, carbohydrates and other large molecules are used resulting in viscous liquid feeds [75]. As a consequence, the diffusion movement of such solutes is limited. Studies on micro droplets have shown that even for molecules with low molecular weight, such as saccharides in water the evaporation is about 1000 times faster than the diffusion rate [76]. Therefore, it can be stated that pharmaceutical particles tend to be hollow. However, the plasticity of these materials during drying has resulted in greater morphology diversity [77]. Due to the low diffusivity, pharmaceutical particles form a shell earlier during drying and the rate of evaporation decays gradually as the shell becomes thicker. At this point the shell mobility is not only determined by the diffusion of the dissolved solids alone but also by their solubility and, more importantly, by the mechanical properties of the formed shell [42]. If the drying rate is high, the critical thickness for the mechanical stability of the particles is reached very early in the drying process and the resulting particles sustain the spherical form of the droplet. On the other hand, if the drying is slow the thin shell formed in the early stages of the drying will tend to follow the receding surface until its

thickness is stable enough to sustain the particle structure. Other feature throughout the formation of particles is the creation of an internal pressure when droplets are dried at temperatures close or above the boiling point of the solvent. In this case the vapor pressure inside the particles is higher than the outer surface and particles can, depending on the shell properties, inflate or break apart [75].

3.2.2.1 INFLUENCE OF PROCESSING PARAMETERS ON PARTICLE MORPHOLOGY

Spray droplets and wet particles passing through a spray dryer, whatever its mode of operation or method of atomization, may experience slightly different drying histories from one another. This depends upon their size, location within the dryer and possibly their close proximity to one another within the spray.

Sensitivity analysis on the equations of the most basic phenomena of solids diffusion and drying of droplets show that the most critical parameters influencing the kinetic of the drying are:

- Drying temperature;
- Droplet diameter: drying time is proportional to the square of initial diameter;
- Solvent volatility;
- Relative saturation of the drying gas.

Instead, the feed concentration has a major impact on the control of the solids diffusion and shell thickness. The flux of solids due to diffusion is mainly controlled by the concentration gradient that can be assumed to be present between saturation at the droplet surface and initial feed concentration. Moreover, the feed concentration has a second effect on the diffusion flux since increasing the solutes concentration normally implies that viscosity is also increased and so for high concentrations, close to saturation, the solids mobility is restricted.

Thus, as summarized in Figure 3.16, the adjustment of mass and heat transfer related parameters can be used to manufacture powders with the desired characteristics [75].

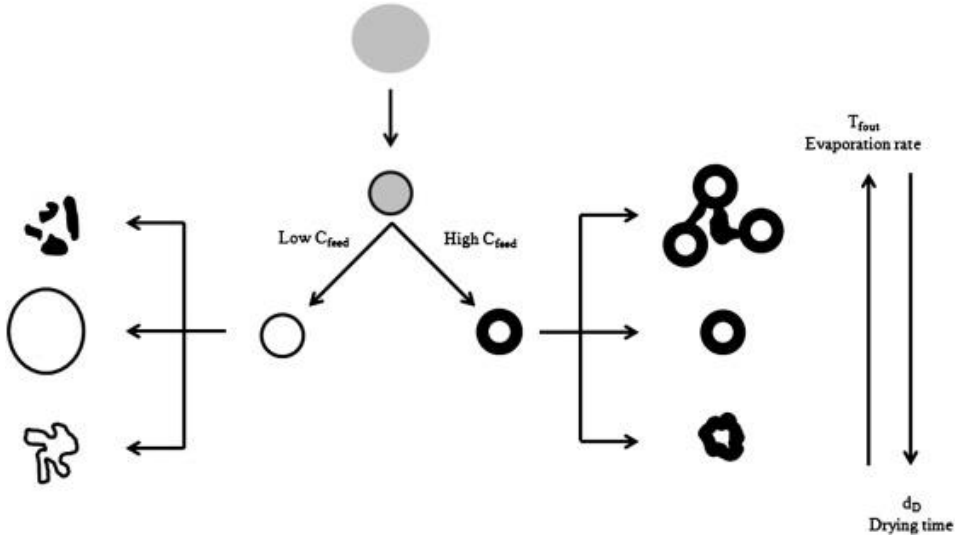

Figure 3.16: Effect of the drying time, solids concentration and outlet temperature on particle morphology

Chapter 4

The theory of extensional rheometry

The importance of elongational flow of polymer fluids arises from the observation that several industrially important processes involve a predominantly extensional mode of deformation. It is well known that the addition of a small amount of high molecular weight polymer in solutions greatly increases the resistance to flow in extension. This property of macromolecular fluids has been exploited in processes such as the prevention of the breakup of a jet of fluid emitting from a nozzle into droplets.

Thus in order to thoroughly understand the atomization process, it is necessary to examine the extensional rheological behavior of the solution. Extensional rheology studies the dynamic response of a fluid when an extensional deformation is applied. With the aim of investigating it, a filament stretching device, able to effectively isolate extensional effects from shear ones, has been proposed. In the last years, the filament stretching device has matured into a reliable method of measuring the rheological response of mobile liquids to a nearly ideal extensional deformation [78].

4.1 THEORETICAL BACKGROUND

Filament rheometers are becoming an increasingly common tool to extract information about the extensional rheological properties of fluids. Data are extracted from these devices through quantitative observations of the evolution of a thin fluid filament under the combined action of viscous, elastic and capillary forces. As shown in Figure 4.1, the technique relies on the generation of an instability in a thread and the following observation of this filament evolution to breakup.

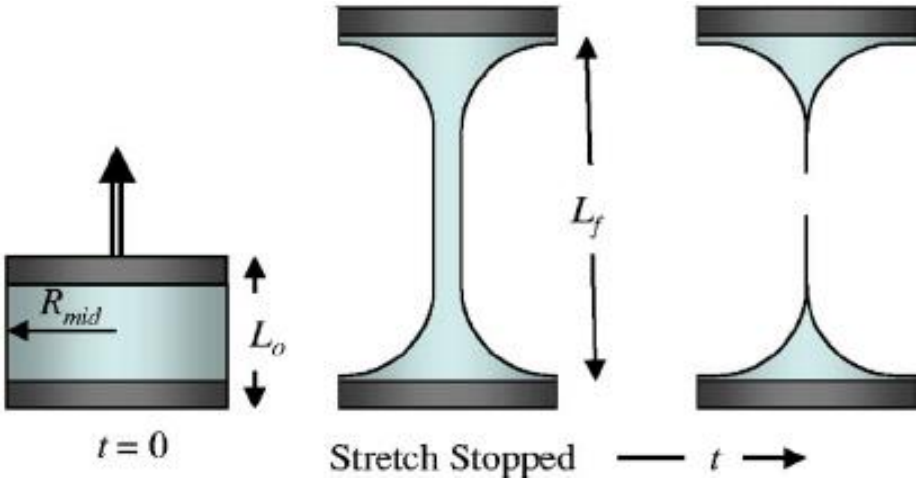

Figure 4.1: Evolution of liquid thread before break up

The sample is constrained axially between two smooth coaxial plates of radius R_0 and forms a liquid bridge configuration that is nominally cylindrical in shape. The precise shape is determined by satisfying the Young-Laplace equation and is a function of

- The aspect ratio:

$$\Lambda = \frac{L_0}{R_0} \qquad \text{Eq(4.1)}$$

  where L_0 is the initial gap;

- The volume of fluid contained between the plates;
- The gravitational body force;
- The surface tension σ [79] [80] .

The relative magnitudes of the latter quantities can be expressed in terms of the Bond number

$$Bo = \frac{\rho g R_0^2}{\sigma} \qquad \text{Eq(4.2)}$$

where ρ is the fluid density.

For $Bo = 0$, the maximum stable length of a cylindrical liquid bridge of volume $V_0 = \pi R_0^2 L_0$ is $L_{max} = 2\pi R_0$ as first noted by Plateau [81]. The maximum stable length decreases rapidly from this Plateau stability limit as the Bond number increases or the volume of fluid contained between the plates decreases [80][82].

In the CaBER 1, a commercial device exploiting the capillary breakup phenomenon, the plates separate rapidly over a short distance. A liquid bridge is therefore generated which has a distinctly necked but axisymmetric configuration. If inertial effects and viscous stresses in the extensional fluid are negligible then this necked configuration is symmetric about the midplan. However, if these effects become significant, then more complex shapes can arise [83] [84].

In this device the endplate motion is not controlled precisely but rather serves to provide a step displacement of the end plate to a new position L_1 which exceeds the the Plateau stability criterion L_{max} at a time $t_1 = t_0 + dt$. Once this new unstable necked configuration has been established the midpoint radius $R_{mid}(t)$ is monitored as a function of time using the laser micrometer.

The Plateau stability limit is determined from a quasi static energy balance and for a Newtonian fluid thus depends only on one material property, that is the surface tension. Instead, the dynamics of the drainage of the thin fluid column and the ultimate rupture of the liquid bridge into two or more droplets are governed by the viscous and elastic properties of the fluid. A complete understanding of this non linear dynamical process has only been developed over the past decade [85].

4.2 PROBLEM FORMULATION

In this device, a known homogeneous deformation profile is not imposed and the force is not measured. Instead, the system selects its own dynamics so that the viscous, elastic, gravitational and capillary forces balance each other. Thus, analysis of the resulting data is more complex since it is necessary to understand exactly what response the system selects, and also why it selects this, to recover accurate values for material parameters such as the fluid viscosity or characteristic relaxation time.

The appropriate system of equations for capillary driven breakup of a fluid thread with a time varying tensile force was first discussed and analysed by Renardy [86]. A generally accepted simplification is an adaptation to a one dimensional balance. This assumption is only valid in the center of the filament and not at the endplates. In reality, it means that each cylindrical slice of the filament is solely subjected to extensional flow [85][87] , as shown in Figure 4.2.

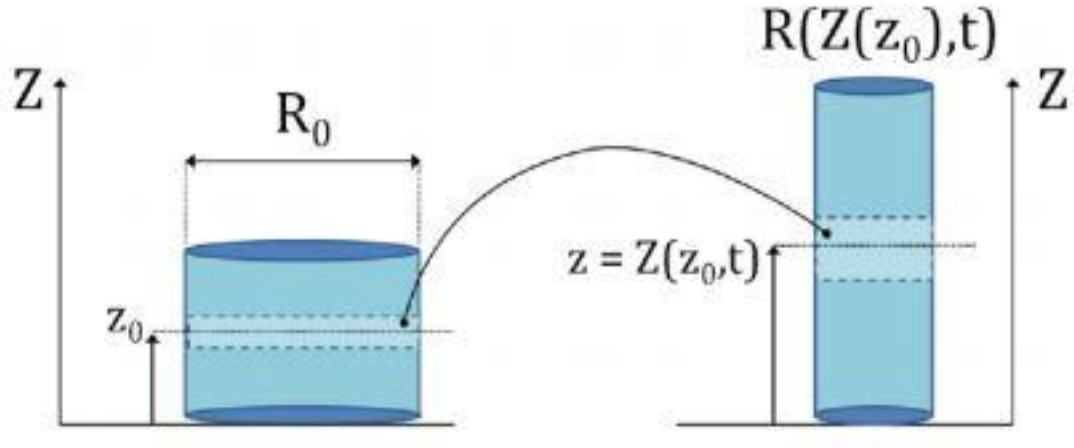

Figure 4.2: A fluid column at time t_0 before the stretch (on the left) and after the Lagrangian stretch (on the right): each part originally located at z_0 is moved to a new z axial position.

As originally formulated, the equation is written in terms of a Lagrangian stretch for each axial slice with radius R_0 and thickness d_z of the column defined as

$$S(Z_0, t) \equiv \frac{\partial z}{\partial Z_0} = \frac{R_0^2}{R(z(Z_0), t)^2} \quad \text{Eq(4.3)}$$

where $z(Z_0, t)$ denotes the Lagrangian position at time t of the one dimensional fluid slice located originally at axial position Z_0 at time t_0.

In experimental measurements of the midpoint radius or in digitized video images of liquid bridge shapes as a function of time, the radial profile $R(z(Z_0, t), t)$ is the primitive variable.

Considering the effects of higher order axial curvature χ [85] and axial gravity field, the axial and radial stress balances for a fluid segment of the filament are respectively

$$0 = \frac{F_z}{\pi R^2} - 2\eta_e \dot{\varepsilon} - \tau_{zz} + \frac{\rho g R_0^2 Z_0}{R^2} - p \quad \text{Eq(4.4)}$$

$$-\frac{\sigma}{R}\chi = -\eta_e \dot{\varepsilon} - \tau_{zz} - p \quad \text{Eq(4.5)}$$

Subsequently the definition of the Hencky strain

$$\varepsilon(Z_0, t) = 2 \ln \frac{R_0}{R(t)} = \ln(S) \quad \text{Eq(4.6)}$$

allows to calculate the strain rate

$$\dot{\varepsilon}(Z_0, t) = -\frac{2}{R}\left(\frac{dR}{dt}\right)_{z_0} \quad \text{Eq(4.7)}$$

To eliminate the hydrostatic pressure p, the axial and radial force balances, equations (4.4) and (4.5), are subtracted resulting in the following stress balance

$$\eta_e \left\{-\frac{2}{R}\left(\frac{dR}{dt}\right)_{z_0}\right\} = \frac{F_z}{\pi R^2} - \left[\tau_{p,zz} - \tau_{p,rr}\right] - \frac{\sigma}{R}\chi + \frac{\rho g R_0^2 Z_0}{R^2} \quad \text{Eq(4.8)}$$

where

- $\eta_e \left\{-\frac{2}{R}\left(\frac{dR}{dt}\right)_{z_0}\right\}$ is the viscous extensional stress contribution to the extensional stress of the fluid.
- $\frac{F_z}{\pi R^2}$ represents the force acting on each segment of the liquid filament, thus ensuring continuity. In the absence of fluid inertia, F_z is constant along the column axis but can vary in time.
- $\left[\tau_{p,zz} - \tau_{p,rr}\right]$ is the non Newtonian viscoelastic tensile stress contribution. This term is identically zero for a Newtonian fluid.

- $\frac{\sigma}{R}\chi$ represents the capillary pressure originating from the radial and axial curvature with

$$\chi = \left\{ \frac{1}{\left[1 + \left(\frac{dR}{dZ}\right)^2\right]^{\frac{1}{2}}} + \frac{R\frac{d^2R}{dZ^2}}{\left[1 + \left(\frac{dR}{dZ}\right)^2\right]^{\frac{3}{2}}} \right\} \quad \text{Eq(4.9)}$$

  In the original formulation of Renardy the higher order derivatives arising from axial curvature were omitted [86]; however, Eggers (1997) discusses how incorporation of these terms leads to more stable numerical methods [85].

- $\frac{\rho g R_0^2 Z_0}{R^2}$ describes the effect of gravity.

Solutions to this evolution equation have been found for a number of different type of fluids [87] [88] [89]. More complicated multimode constitutive models predict a spectrum of relaxation times, which is more realistic for real polymeric fluids. These models will usually capture the initial more rapid decay in radius during relaxation. This initial rapid drop is usually attributed to the relaxation of shorter time scales, after which point the longer time scales yield a more gradual radial decay.

For easy of use, some simplifications can be done:

- The radius R can be converted to the midpoint thread radius R_{mid}, through assumption of the fluid thread being estimated by an axially uniform cylindrical column of constant radius $R_{mid}(t)$, which is necking due to capillary pressure

$$p_{cap} = \frac{\sigma}{R_{mid}} \quad \text{Eq(4.10)}$$

  acting on it. Obviously this supposition well describes the entire axial length of the liquid bridge, except near the fixed endplates, where axial curvature becomes significant.

- The net tensile force can be described at the limit of filament evolution by the following equation caused by the surface tension

$$\lim_{R_{mid}\to 0} F_z(t) \to 2\pi\sigma R_{mid}(t) \quad \text{Eq(4.11)}$$

- The gravitational body force can be neglected.

Hence a simplified equation representing the capillary breakup of a generic fluid is obtained

$$-\eta_e \frac{2}{R_{mid}} \frac{dR_{mid}}{dt} \approx -\left[\tau_{p,zz} - \tau_{p,rr}\right] + \frac{\sigma}{R_{mid}} \quad \text{Eq(4.12)}$$

4.2.1 CAPILLARY THINNING OF VISCOUS FLUIDS

Experimental observations of the slenderness of the structures that develops during the breakup dynamics motivated the neglect of axial curvature along the necked fluid column. Therefore liquid bridge is approximated as an axially uniform thread that can be characterized simply by its midpoint radius $R_{mid}(t)$ [87]. For a Newtonian fluid of viscosity η_s and surface tension σ, a local force balance and elimination of the fluid pressure leads to the following evolution equation for the midpoint radius:

$$3\eta_s\left(-\frac{2}{R_{mid}}\frac{dR_{mid}(t)}{dt}\right)=\frac{\sigma}{R_{mid}(t)} \qquad \text{Eq(4.13)}$$

In developing this evolution equation, the total longitudinal stress along the fluid thread is assumed to be zero at all times since the column is connected to large quasi-static fluid reservoirs which are themselves attached to the rigid endplates of the device. The term in parentheses can be identified as the extensional deformation rate of the Lagrangian fluid element at the midplane of the column where the radius is measured.

Measurements of the rate of decrease in the measured filament radius thus predict a constant slope $-\frac{\sigma}{6\eta_s}$, and integration of equation (4.13) leads immediately to a linearly decreasing profile, which can be written in several useful forms:

$$R_{mid}(t)=R_1-\frac{\sigma}{6\eta_s}t=\frac{\sigma}{6\eta_s}(t_c-t) \qquad \text{Eq(4.14)}$$

where

- R_1 is the initial radius of the thread at time t = 0;
- t_c is the critical time of the breakup event, which is determined directly by the initial conditions to be

$$t_c=\frac{6\eta_s R_1}{\sigma} \qquad \text{Eq(4.15)}$$

In obtaining equation (4.14), it is assumed that the fastest growing mode determined from linear stability analysis of a cylindrical fluid jet remains dominant all the way to the final breakup event.

Liang and Mackley used the microfilament rheometer to study the breakup dynamics of a number of concentrated viscoelastic solutions of polyisobutylene in Decalin, plus a viscous Newtonian PDMS oil. For the Newtonian fluid, a linear decrease in radius with time was observed and they used the analysis above to obtain values of the ratio $\frac{\sigma}{\eta_s}$, which may be termed a capillary velocity and is a measure of the characteristic rate of necking in a Newtonian fluid thread. However, when they used this ratio with a separate rheometric measurement of the solvent viscosity they obtained a surface tension value that was approximately a factor of two below accepted literature values [90].

Kolte & Szabo presented a variant of a capillary breakup rheometer and attempted to recover values of the steady shear viscosity for a Newtonian polybutene oil. They also observed a linear decrease in the measured midpoint radius; however, when they used equation (4.14) to extract the solvent viscosity they found a very marked discrepancy with the value independently measured in a torsional rheometer. A full time dependent numerical simulation of the evolution of the fluid column undergoing capillary breakup showed excellent agreement with the experimental observations, and furthermore showed that the effects of a gravitational body force acting axially along the necked fluid column could not safely be neglected. The authors thus concluded that was not possible to use the simple analysis above to extract the Newtonian fluid viscosity [91].

This discrepancy between experimentally measured and theoretically expected values of $\frac{\sigma}{\eta_s}$ for a Newtonian fluid arises from the assumption of zero longitudinal fluid stress in the local force balance described by equation (4.13). In fact, the equation (4.14) is only valid at the later stages of fluid filament evolution, when gravitational influence is really negligible. This apparent inconsistency between the two results can be resolved if two criteria are satisfied:

- the axial gradients along the liquid bridge become increasingly negligible at later times so that

$$R(z,t) \rightarrow R_{mid}(t) \qquad \text{Eq(4.16)}$$

- the net tensile force in the thread approaches a specific value as the radius decreases which is given by

$$\lim_{R_{mid}\rightarrow 0} F_z(t) \rightarrow 2\pi\sigma R_{mid}(t) \qquad \text{Eq(4.17)}$$

Thus, a new dimensionless variable $X(t)$ is defined by

$$X(t) \equiv \frac{F_z(t)}{2\pi\sigma R_{mid}(t)} \qquad \text{Eq(4.18)}$$

where the non local effects arising from axial variations in the shape of the filament are encoded in the time evolving tensile force $F_z(t)$ acting on the thread.

If the value of X determined from these calculations is a constant, then substitution of $R(z,t) \rightarrow R_{mid}(t)$ plus equation (4.18) into equation (4.8) followed by integration in time leads to the following prediction for the time evolution in the midpoint radius:

$$R_{mid}(t) = R_1 - \frac{(2X-1)}{6}\frac{\sigma}{\eta_s}t \qquad \text{Eq(4.19)}$$

It is clear from equation (4.19) that the solution arising from a local force balance for a Newtonian fluid (4.14) corresponds to $X = 1$.

If an experiment is performed and the midpoint radius $R_{mid}(t)$ is indeed found to decrease linearly in time, then the value of the ratio $\frac{\sigma}{\eta_s}$ determined from regression of the data will depend critically

on what value of X it is appropriate to use in the analysis. The experimental results analyzed by Bazilevsky et al. [92], Liang and Mackley [90] and by Kolte and Szabo [91] have all assumed implicitly that $X = 1$ in accordance with the local force balance solution of equations (4.13) and (4.14).

Instead Papageorgiou, using an approach based on self similarity, determined numerically the value $X = 0.7127$ for the case of an inertialess viscous filament with a smoothly necked profile [93]. In this similarity solution to the unsteady Stokes equations, the similarity exponent characterizing the rate of contraction in the axial scale of the solution is much smaller, by a factor of 0.175, than the one for the radial scale and thus the filament rapidly becomes increasingly slender. However, it never becomes truly axially uniform as required by equations (4.13) and (4.14). On the other hand Eggers showed that in the very final stages of break up inertial effects can no longer be neglected and the time rate of change in the filament profile crosses over to a universal similarity solution that balances inertial, capillary and viscous effects, finding $X = 0.5912$ [85].

4.2.2 CAPILLARY THINNING OF VISCOELASTIC FLUIDS

The approximation of an axially uniform cylindrical thread is very good for a strongly strain hardening fluid such as a dilute solution of a high molecular weight polymer [94]. Theoretical work [95] [96] and subsequent numerical analysis [89] shows that following a rapid initial viscous dominated phase, there is an intermediate time scale in which the dynamics of the filament drainage are governed by a balance between surface tension and elasticity, rather than fluid viscosity. In this regime the filament radius decays exponentially at a rate of $(3\lambda_c)^{-1}$, according to the equation

$$\frac{R_{mid}}{R_0} = \left(\frac{1}{2}\frac{GR_0}{\sigma}\right)^{\frac{1}{3}} e^{-\frac{t}{3\lambda_c}} \qquad \text{Eq(4.20)}$$

where

- λ_c is the characteristic relaxation time governing the capillary breakup;
- G is the elastic modulus of the filament.

Physically, this corresponds to the radius at which occurs a balance of the elastic modulus $G = \frac{\eta_p}{\lambda}$ and the squeezing effects of capillary pressure [97], so the necking of the fluid.

Considering an Oldroyd-B model, Kolte and Szabo showed for a semi dilute PIB/PB Boger fluid that λ_c is closely related to the longest relaxation time λ_l of the fluid. They also elegantly discussed how the effects of a radial inhomogeneity in the stress distribution can account for the remaining discrepancy between λ_c and λ_l [91]. Numerical simulations for filament stretching rheometers demonstrated that this radial inhomogeneity is a strong function of the initial shape of the fluid sample and also the initial aspect ratio [98].

Instead, Entov and Hinch used the FENE-P model to provide a very approximate estimate of the corresponding critical time to breakup. They presented generalized expressions for elastocapillary

necking in a dilute solution of dumbbells with an arbitrary spectrum of relaxation times and showed that after a short transitional period, the column selects a necking rate so that only the mode with the longest time constant is liable for the response to extension [89]. Besides this, Anna & McKinley also exploited the multimode FENE-P model to predict the evolution of the transient filament diameter, considering the specific distribution of relaxation times expected for the Rouse-Zimm model, given by the equation

$$\lambda_i = \frac{\lambda}{i^m} \qquad \text{Eq(4.21)}$$

where

- $m = 1.5$ for the Zimm model;
- $m = 2$ for the Rouse model.

They noted that because the longest mode achieves an elastocapillary balance in which the Weissenberg number is

$$\lambda_l \dot{\varepsilon}_{mid} = \frac{2}{3} \qquad \text{Eq(4.22)}$$

all other modes experience a weak stretching flow with

$$\lambda_l \dot{\varepsilon}_{mid} = \frac{2}{3i^m} \qquad \text{Eq(4.23)}$$

Which for $i \geq 2$ is less then the critical value of 0.5 required for a coil stretch transition in a uniaxial extensional flow [99]. As the concentration or the molecular weight of polymer increases, the elastocapillary thinning process slows down as a consequence of the increase in the material relaxation time.

PART II

Pullulan performance as release enhancer

Chapter 5

The Pullulan was kindly provided by Hayashibara (Okayama, Japan). An overview on some interesting and relevant properties are listed in Table 5.1 [100].

Pullulan Definition	
C.A.S number	9057-02-7
Chemical formula	$(C_6H_{10}O_5)_x$
Description	White to off-white odorless powder

Pullulan Characteristics	
Solubility	Soluble in water, practically insoluble in ethanol
pH	5-7 (10% solution)
Loss on drying	Not more than 6%
Viscosity	100-180 $\frac{mm^2}{s}$ (10 wt% aqueous solution at 30°C)
Lead	Not more than 1 $\frac{mg}{kg}$
Microbiological criteria	Yeast and moulds: not more than 100 $\frac{CFU}{g}$
	Coliforms: Negative in 25 g
	Salmonella: Negative in 25 g

Table 0.1: Pullulan general properties

The Pullulan molecular weight and its distribution were investigated in literature using size exclusion chromatography [27]. The manufacturer's value for the Pullulan molecular weight is 300 KDa whereas from the analysis resulted to be lower than acclaimed. A high polydispersity index was noticed due to the large difference in weight and number average molecular weight, indicating a broad molecular weight distribution. All the data are reported in Table 5.2.

M_w	283500 Da
M_n	115100 Da
PDI	2.5

Table 0.2: Weight and number average molecular weight and polydispersity index of Pullulan

For the capsule matrix, the hydroxyl propyl methyl cellulose acetate succinate (AQUOT-LG®, HPMCAS) and the plasticizer polyethylene glycol (PEG), with a molecular weight of 8000 Da, were obtained respectively from Shin-Etsu (Tokyo, Japan) and Clariant Masterbatches (Milan, Italy). The filler, a polyvinyl alcohol polyethylene glycol graft copolymer (Kollicoat® IR, KIR), was supplied by BASF (Ludwigshafen am Rhein, Germany). The drug to be released, paracetamol, also known as acetaminophen or APAP, was purchased from Atabay (Istanbul, Turkey).

The pH dependent solubility of HPMCAS in aqueous media permits to investigate the release enhancer effect from different point of view. Indeed:

- Being water soluble in neutral environment:

  It allows a comparison between KIR and Pullulan behaviour.

- Being water insoluble in acidic environment:

  It allows assessing if the Pullulan alone is able to provide an acceptable performance even in the case neither the matrix itself nor the matrix containing KIR show release ability. Further, the possible effect of the pore former shape may be highlighted.

5.1 CAPSULE MATRIX PREPARATION

The neat methyl cellulose based matrix cannot be processed by microinjection molding without degradation, so the addition of a plasticizer is necessary to improve the flow behavior of the melts [101]. Using the polyethylene glycol the mechanical characteristics of the final product are also improved [25].

Regarding the release enhancers, as reported in literature [27], the powder mixture containing KIR was prepared first homogenizing the desired amount of HPMCAS in a small blade mixer, in order to reduce the particle size and avoid segregation, and next adding first the plasticizer and subsequently the filler, mixing them in a mortar with a pestle.

The same procedure was initially used to prepare the powder mixture containing Pullulan.

However, comparing the two release enhancers it is possible to notice their difference in size as well as structure. As shown in Figure 5.1, KIR particles result to be small, with a maximum diameter of the order of 50 μm, spherical and dense, while the Pullulan ones turn out to be large, about 200-300 μm, and porous.

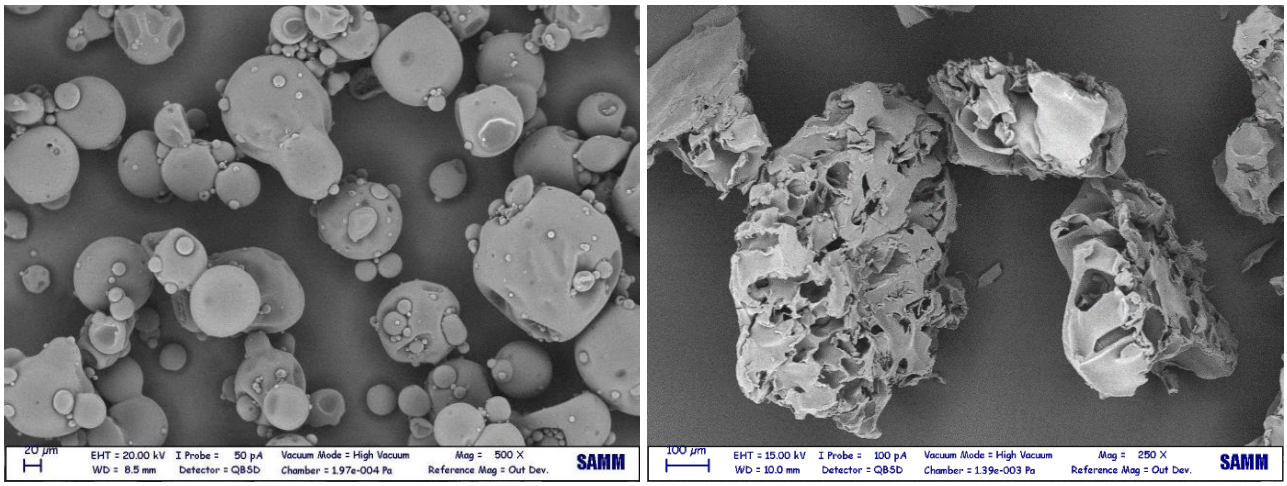

Figure 5.1: Morphology of KIR (on the left)
Magnification: 500x
and Pullulan particles (on the right)
Magnification: 250x

In previous literature [27], the diverse particle size and shape were shown to produce differences in processability. As a matter of fact, the replacement of KIR particles by Pullulan powder favoured the degradation of the system. Possible explanation could be the effect of temperature on processing time. Moreover, also mixing Pullulan and the matrix was difficult. Since the exact same production process was applied for both powders, it appeared that the KIR particles need less extensive mixing to ensure a homogeneous distribution of the particles.

Therefore, taking into account these considerations, a new protocol was developed for the preparation of capsule formulation in order to improve the results. Pullulan was previously desiccated at 40°C in an oven for 12 hours, as one of the causes for degradation might be the presence of humidity in the powder, and next co-milled with the HPMC AS in a pins mill, to grind the powders and improve its dispersion into the matrix. The polyethylene glycol was then added in the mortar.

The weight fractions of the final product are given in Table 5.3.

	Concentration (wt%)
HPMC AS	45.5
PEG	24.5
KIR/PUL	30

Table 5.3: Weight fractions of capsule components

5.2 EXTRUSION AND RHEOLOGICAL MEASUREMENTS

The Pullulan mixture rheology was investigated using an HAAKE Minilab II (Thermo Fisher Scientific, Karlsruhe, Germany). The system is based on a conical, twin screw compounder with an integrated backflow channel. Two pressure transducers are integrated in the backflow channel. They allow the measurement of melt viscosity when counter rotating screws are used. By measuring the applied rotation and the pressure in the backflow channel, the process can be monitored effectively. At the end of the test, the bypass valve can be opened and the sample is extruded as a strand. The device is shown in Figure 5.2 and the technical specifications in Appendix A.

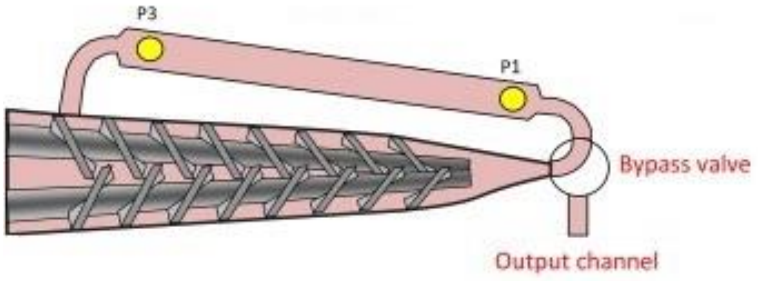

Figure 5.2: HAAKE Minilab II backflow channel with rheological slit capillary die

Two different analysis were executed, each test requiring small sample amounts of 5g or 7cm^3. First, the powder mixture was extruded without using the backflow channel at several temperatures for two different rotation speeds, as reported in Table 5.4.

Experimental conditions	
Temperature	160°C, 175°C, 185°C and 195°C
Rotation speed	30 rpm and 100 rpm

Table 5.4: Extrusion experimental conditions

Besides this, different rheological characterization tests were executed. First at temperatures of 160°C, 175°C, and 195°C, the powder mixture prepared without desiccation was backflushed and the shear rate history shown in Figure 5.3 was imposed to the sample, while the viscosity was measured. Using the same protocol, a test was done at 175°C analysing the powder mixture containing dried and co-milled Pullulan. Moreover, at 160°C and 175°C, measurements were performed starting the data collection 1 hour after the backflush of the Pullulan powder mixture prepared without desiccation.

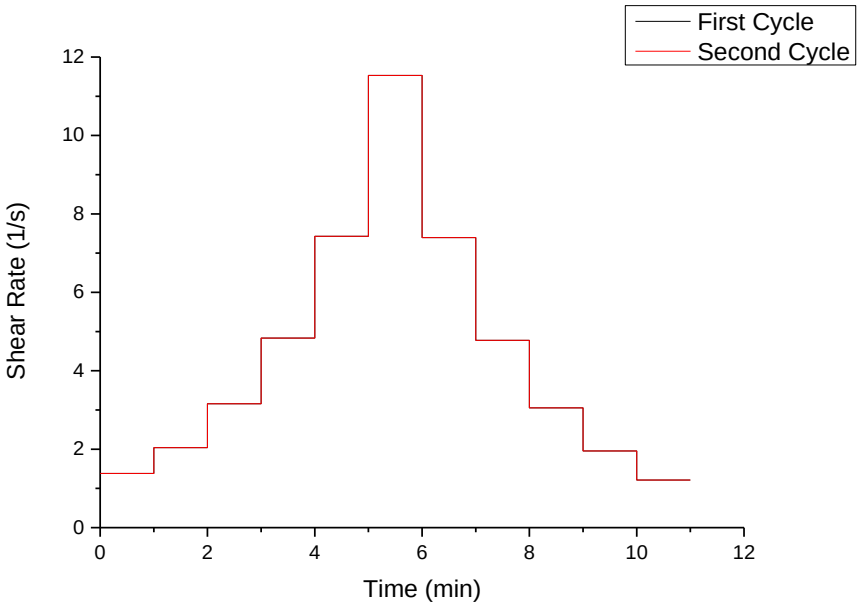

Figure 5.3: Extrusion shear rate profile

5.3 PRODUCTION AND CHARACTERIZATION OF SCREENING ITEMS

In order to accurately evaluate the drug release, as described later on, a geometry simpler than the capsules was chosen. Thus, circular disks were produced via microinjection moulding using a Babyplast® type 6/10P Standard (Cronoplast S.L, Rambaldi S.r.l, Italy). The device technical data are supplied in Appendix A.

The previously described polymeric formulations were used for the manufacturing of the moulded disks. Therefore, 50g of powder mixture were loaded into the plasticating chamber of the microinjection moulding press through the hopper and then conveyed by means of a first piston to the injecting chamber. By successively applying two distinct pressures, each for a defined period of time and at a selected rate, another piston, with a diameter of 10mm, injected a specific amount of melt through a 1mm diameter nozzle into the mould cavity. Prior to product ejection, the mould was kept closed by applying a clamping pressure to allow the injected melt to cool down and harden. The rate of each process stage was expressed as percentage of the maximum value. The process specifications for both the Pullulan and KIR powders mixture are reported in Table 5.5. The parameters for the KIR mixture were set based on a previous literature work [25].

	Process parameters	
	Pullulan	**KIR**
Plasticating chamber temperature	140°C	120-160°C
Injection temperature	150°C	130-170°C
Nozzle temperature	170°C	140-180°C
Charge	9mm	4.5-11mm
First injection pressure	40-55bar	20-90bar
First injection time	0.8s	0.8s
First injection rate (% of the max piston rate)	80%	40-90%
Second injection pressure	80bar	15-70bar
Second injection time	0.5s	0.3s
Second injection rate (% of the max piston rate)	70%	30-70%
Cooling temperature	15°C	15°C
Cooling time	3s	2.5s
Closing pressure	10bar	60bar
Opening rate (% of the max opening rate)	15%	20-40%

Table 5.5: Microinjection moulding process parameters

Moulded items were prepared by means of a 30mm diameter disk shaped mould provided with a central gate, which allowed manufacturing disks with thicknesses of 200, 400 and 600μm. Although varying the operating conditions within different ranges only the disks with thicknesses 400 and 600μm could be produced and their respective release behaviour were investigated further.

The injection moulded disks, 10 samples for each kind, were characterized based on weight using an analytical balance BP211 (Sartorius, Germany) and thickness employing a digimatic indicator ID-C112X (Mitutoyo, Japan).

5.4 DRUG RELEASE TEST

To evaluate the disks gastric resistance and release performance as a barrier is necessary to mimic the gastrointestinal pathway and thus the in vivo system behaviour. Therefore, according to the pharmaceutical guidelines [102], an in vitro approach was adopted and Method B USP34, that regulates the conditions of standard dissolution test for delayed release dosage forms, was implemented.

A pharmacopoeial apparatus II (Dissolution System 2100B, Distek, New Jersey, USA) was employed. It was composed by six cylindrical vessels with a hemispherical bottom. The vessels were partially immersed in a suitable heated water bath, which permitted holding the temperature inside the vessel at 37±0.5°C during the test and keeping the bath fluid in constant, smooth motion. No part of the assembly, including the environment in which the assembly was placed, contributed significant motion, agitation or vibration beyond that due to the smoothly rotating stirring element.

Each vessel contained a paddle formed from a blade and a shaft, used as stirring element. The shaft was positioned so that its axis was not more than 2mm from the vertical axis of the vessel at any point and rotates smoothly without significant wobble that could affect the results. A speed regulating device was used that allows the shaft rotation speed to be selected and maintained at the specific rate. Thus, the paddles were mixing continuously at a rotation speed of 100 rpm. The dissolution test apparatus is schematically represented in Figure 5.4.

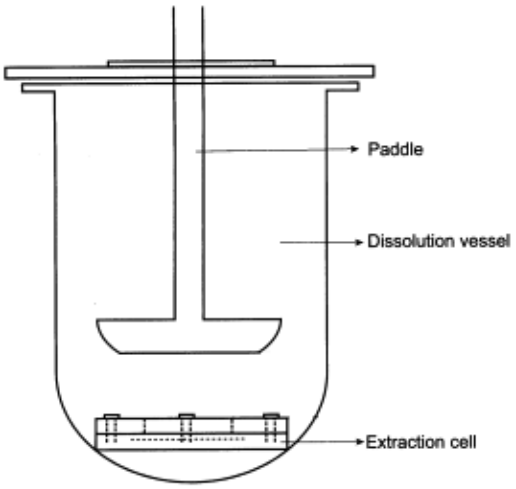

Figure 5.4: Dissolution test apparatus

Dissolution tests were performed for all the different type of available disks: both the powder mixture formulations, containing Pullulan or KIR as release enhancer, and their respective two thicknesses.

Six drug delivery cells for each set of test were set up as shown in Figure 5.5. The reservoir compartment was loaded with an amount of 70mg of drug tracer, paracetamol. Disks were positioned on manually assembled cells, which ensure that the drug cell is sealed off in order to avoid accidental drug release. The surface exposed to the acceptor fluid was 177 cm^2.

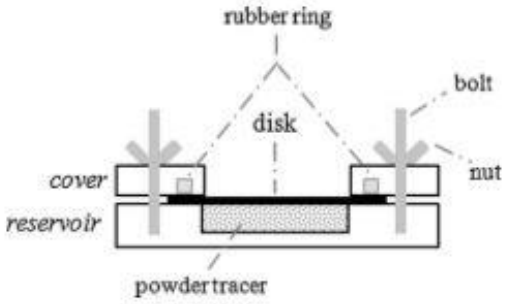

Figure 5.5: Schematic representation of drug release cell

Delivery cells were positioned in vessels filled with 500mL of a standard pharmaceutical buffer. Two buffer solutions with a pH of 1.2 and 6.8 were prepared, which compositions are reported in Table 5.6.

pH 1.2		**pH 6.8**	
KCl	0.25 vol%	K_2HPO_4	0.25 vol%
H_2O	0.325 vol%	H_2O	0.640 vol%
0.2M HCl	0.425 vol%	0.2M NaOH	0.110 vol%

Table 5.6: Volume fractions of buffers components

To mimic the residence in respectively the stomach and subsequently the small intestine, the procedure entailed for the reservoir device a residence time of 2 hours in the acidic buffer and thereafter the replacement with the one at pH 6.8, in which the drug would ideally be released as fast as possible. The pH profile during dissolution test is depicted in Figure 5.6.

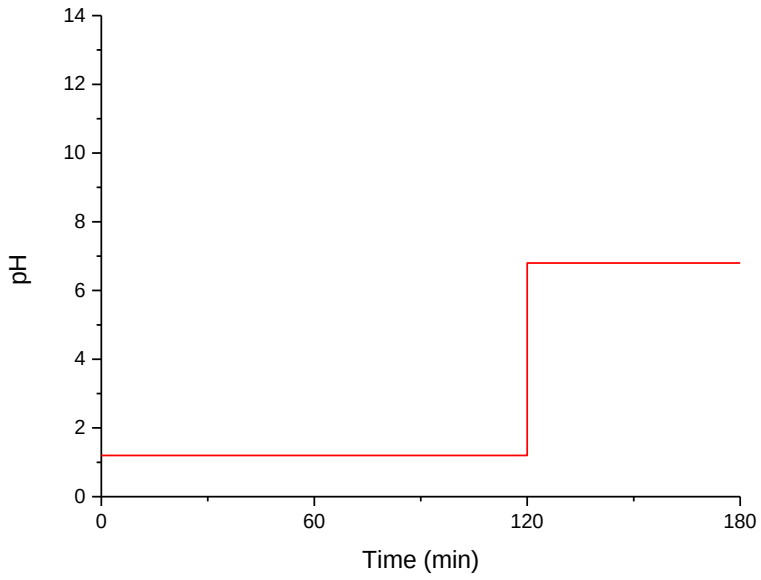

Figure 5.6: pH in the dissolution test

To monitor the release of drug, fluid samples were withdrawn every 5 minutes and assayed spectrophotometrically at 254 nm (Spectrophotometer LAMBDA 25 UV/Vis, Perkin Elmer, Massachusetts, USA). Hence, the concentration of the drug tracer is measured as a function of time, and the amount dissolved is then calculated.

Chapter 6

6.1 EXTRUSION AND RHEOLOGICAL MEASUREMENTS

The extrusion tests were executed in order to check the system stability to hot processing and evaluate the degradation phenomena in a quick and easy way. When increasing screws rotation speed as well as barrel temperature, differently coloured extruded ribbons were gathered, as displayed in Figure 6.1. The surface of these ribbons was quite rough, granular like. The roughness can be attributed to gas release during the extrusion process.

Figure 6.1: Extruded ribbons for temperatures ranging from 175 to 195°C and for rotation speeds of 30 (on the left) and 100 rpm (on the right)

Moreover, the cross section of ribbons extruded at 185°C at rotation speed of 30 rpm and 100 rpm was investigated. As shown in Figure 6.2 and Figure 6.3, it appears that the screws rotation improves the powders mixing.

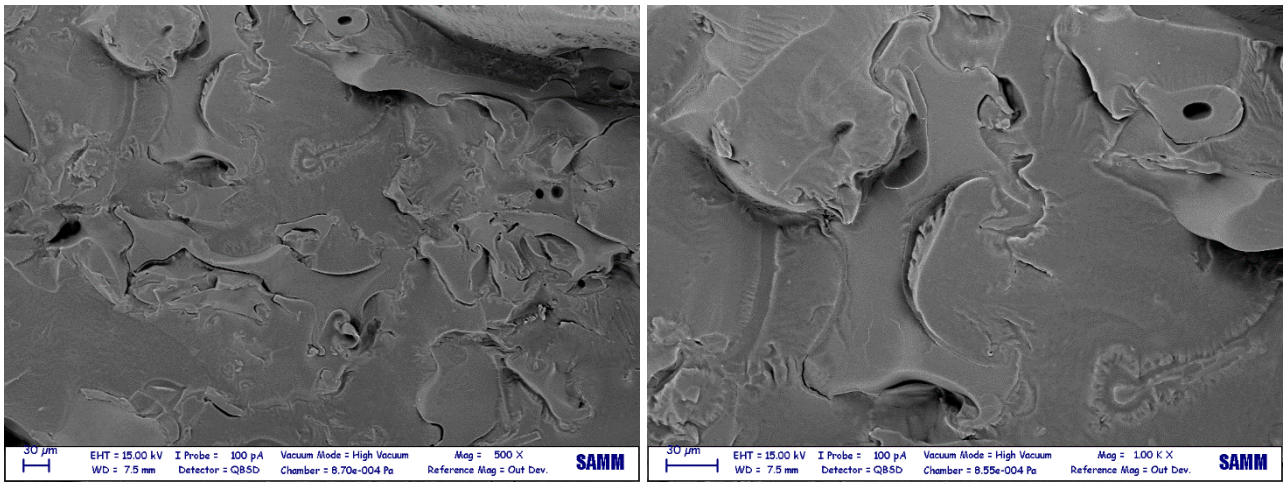

Figure 6.2: SEM images of the cross section of an extruded ribbon
at 185 °C and rotation speed of 30 rpm
Magnification: 500x (on the left)
Magnification: 1000x (on the right)

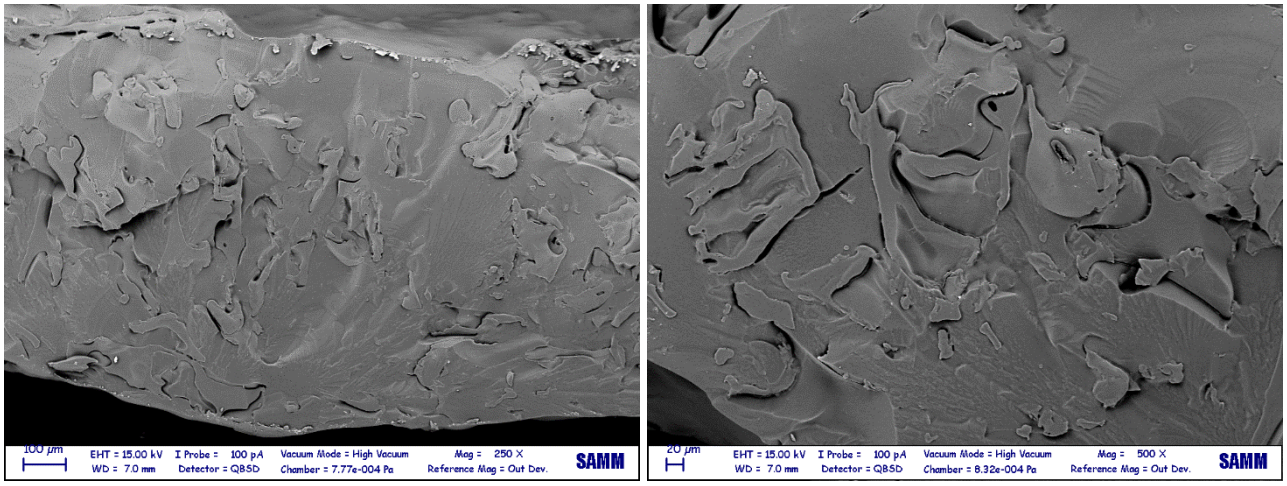

Figure 6.3: SEM images of the cross section of an extruded ribbon
at 185 °C and rotation speed of 100 rpm
Magnification: 250x (on the left)
Magnification: 500x (on the right)

The slit rheometer of the extruder was used to gain a quantitative measure of degradation by measuring the apparent viscosity when the shear rate history shown in Figure 5.3 in Section 5.2 was imposed on the sample. Both the powder mixtures, the first prepared following the procedure reported in literature [27] and the second according to the new developed protocol, were examined.

With regard to the first case, the experimental data concerning the measurements started immediately after the backflush of the material are displayed in Figure 6.4, while those concerning the measurements started 1 hour after the backflush of the material are reported in Appendix B. In all the implemented tests, shear thinning behaviour was detected.

At a temperature of 160°C a decrease in the viscosity in the second cycle may be noticed. This suggests that the Pullulan particles dimension was reduced during the mixing in the screws of the

extruder. Given the highly porous morphology, as proved in Figure 5.1 in Section 5.1, crushing the particles reduces their apparent volume fraction in the suspension, affecting the system rheology. Besides, the wall particle interaction should be reduced.

Instead, at higher temperatures, 175°C and especially 195°C, different results were obtained. Generally, low shear rates, situated at the beginning and the end of the cycle, show a higher shear viscosity for higher temperatures. Beyond that, after the first cycle, the shear viscosity seems to increase for the second cycle, starting and ending at a higher value. This increase in viscosity corresponds most likely to an increase in molecular weight or lengthening of the chains. This effect could be caused by crosslinking or gelification.

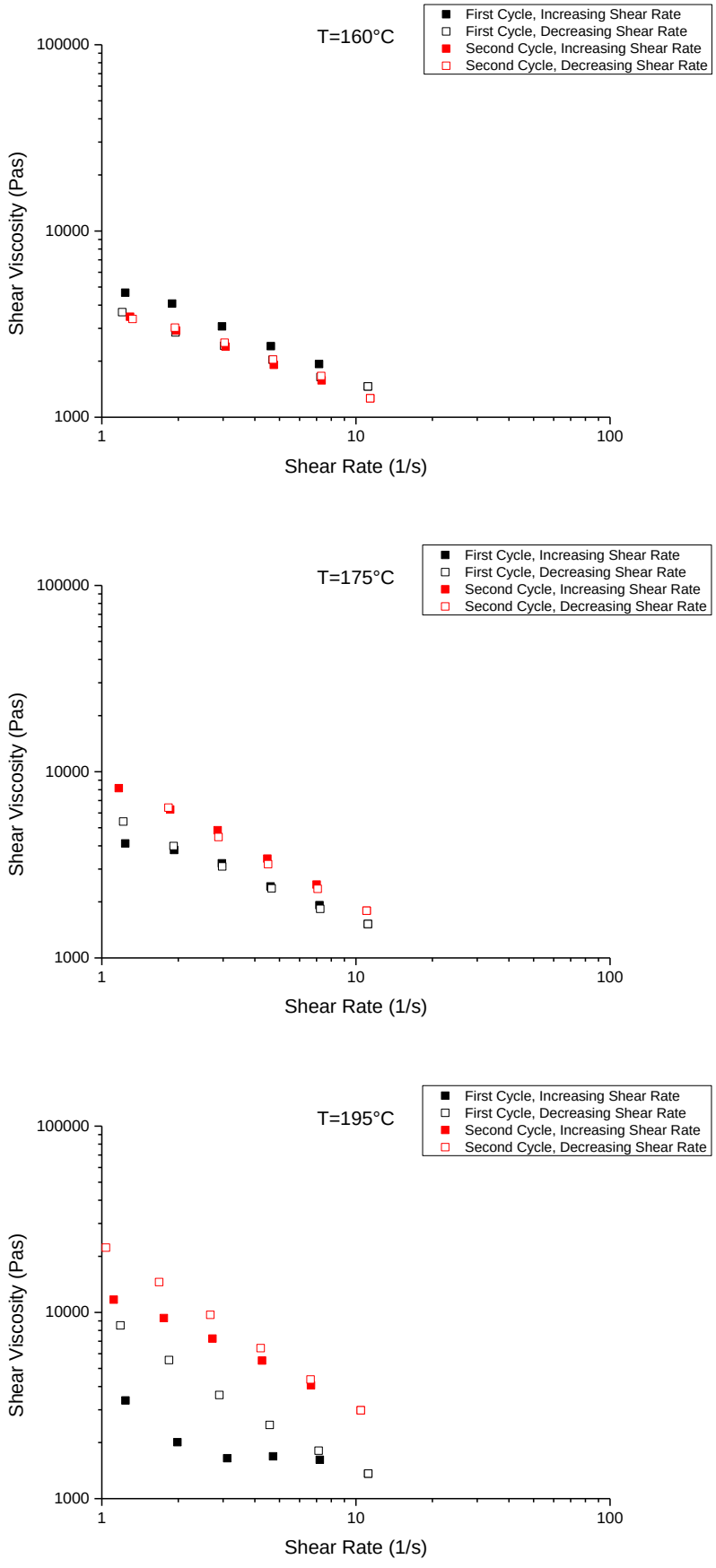

Figure 6.4: Shear viscosity of Pullulan mixture for extrusion shear rate cycles at different temperatures

As revealed in Figure 6.5, a comparison with co-milled Pullulan powder mixture at 175 °C, with the purpose of exploring the effect of water present in the powder, showed a larger difference in shear viscosity values at lower shear rates at the beginning versus the end of each cycle. Thus, degradation still takes place, even if to a minor extent with respect to the previous case.

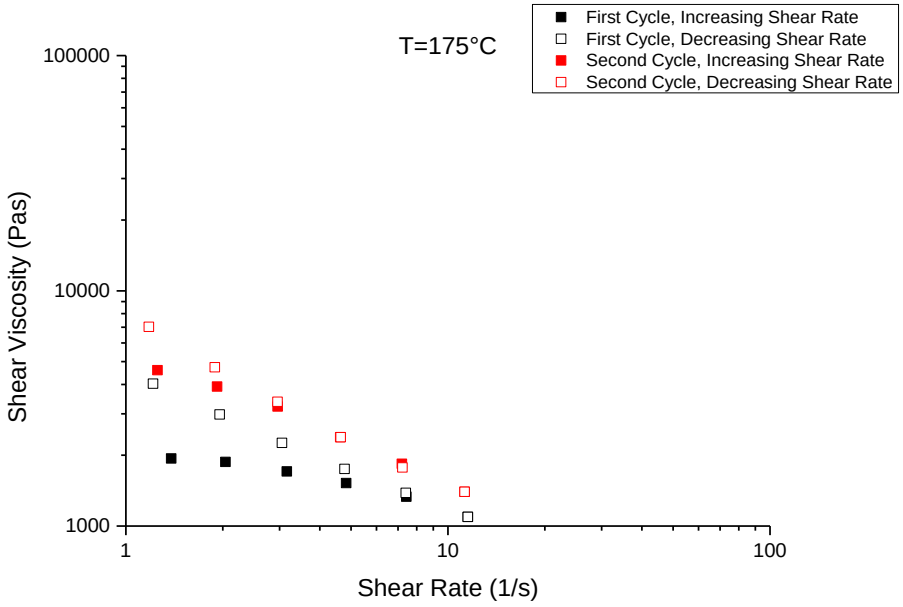

Figure 6.5: Shear viscosity of dried and co-milled Pullulan mixture for extrusion shear rate cycles at 175°C

6.2 EFFECTS OF THE TYPE OF RELEASE MODIFIER: COMPARISON BETWEEN KIR AND PULLULAN

Both the methylcellulose based matrix filled with KIR, as a reference material, and Pullulan were employed for the manufacturing of the moulded disks, which were used in the screening of release performance. In the case of Pullulan, both the preparation methods described in the Section 5.1 were considered. All the disks were subsequently characterized in terms of appearance, thickness and weight before drug release test were performed.

As a general remark, it is important to underline that ideally the release performance solely relies on the composition and thickness of the capsule shell itself and is independent on the drug preparation content. Hence, modification of the capsule thickness and composition, with possible use of different release enhancer particles shapes, results in a specific release rate and time, which thus can be adapted to the need of a certain medicine and therapeutic program.

6.2.1 PRODUCTION AND CHARACTERIZATION OF SCREENING ITEMS

Effectively, as anticipated in Section 5.1 and shown in Figure 6.6, comparing the disks containing KIR particles with the ones including Pullulan powder, obtained applying the first preparation method, dark spots and some brown coloration are noticed on the last one. Besides this, the dispersion of the Pullulan seems poor, as the appearance of the disk is not homogeneous, with brighter zone, attributable to Pullulan, on the edge of the disk. Instead, following the new protocol, brownish stains are not observed on injection moulded disks, which appear smooth and uniform, similarly to that containing the release modifier of reference.

Figure 6.6: Micro injection moulded disks of KIR (on the top), Pullulan (on the left) and dried and co-milled Pullulan (on the right)

Looking at the SEM micrographs of disks cross section, reported in Figure 6.7, the differences in particles dimension and shape are evident. Hence, depending on the selected release enhancer, different morphologies can be detected. In particular, in the case of:

- KIR, it is possible to notice the presence of spherical particles and holes, caused by the detachment from the matrix of the pore former particles.
- Pristine Pullulan, it results to be quite difficult to discern the matrix from the particles, which, however, appear to be similar to islands.
- Dried and co-milled Pullulan, particles are not observable, but in their place, cavities are observable. This is because to facilitate the recognition of the release enhancer particles, the disk cross section was immersed in the acidic buffer solution in which only Pullulan, and not matrix, is soluble, before SEM observation.

Indeed co-milling HPMC AS and Pullulan allows effectively grinding and successfully mixing the powders.

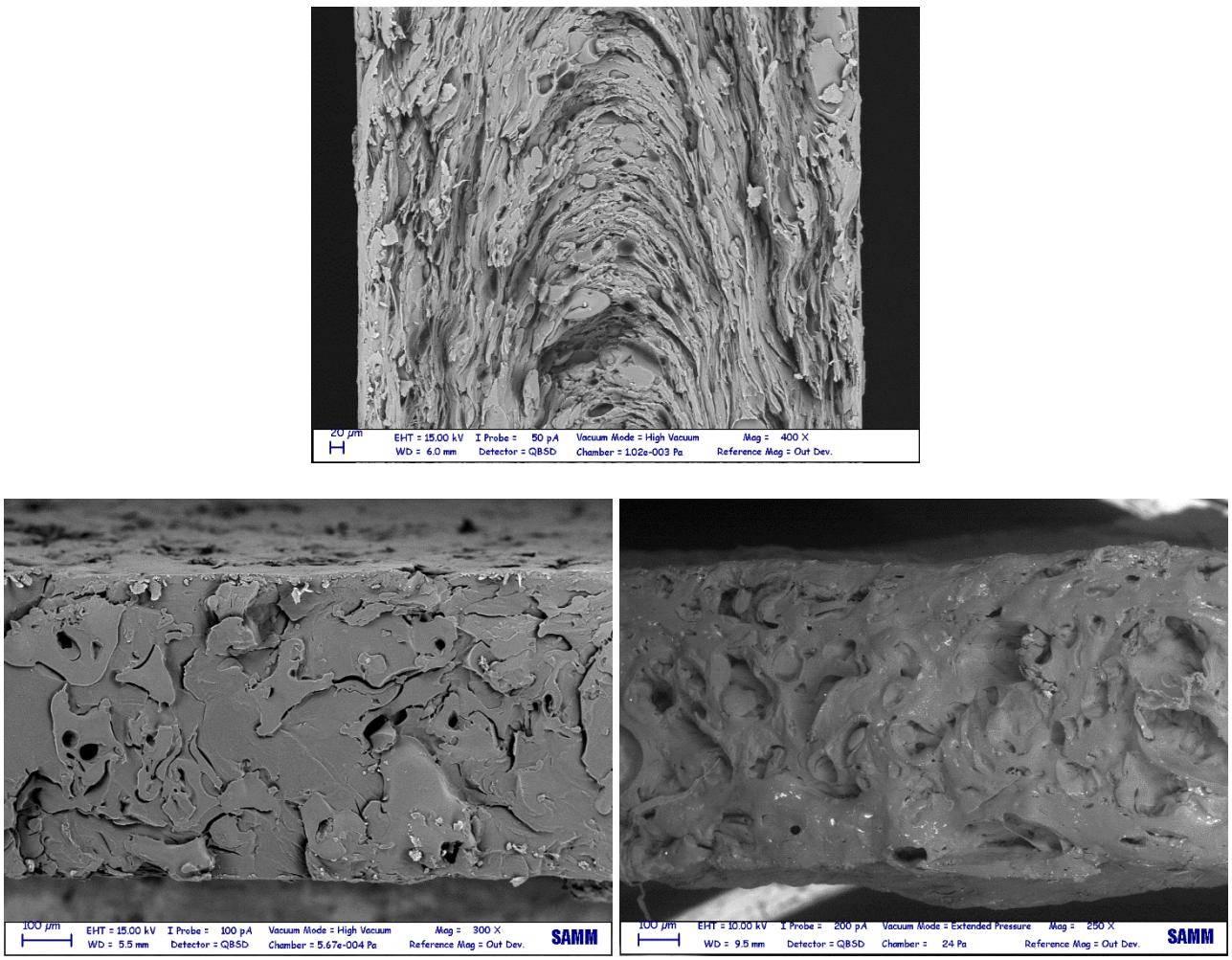

Figure 6.7: Cross section of disks with a thickness of 600µm containing
KIR (on the top, Magnification: 400x),
Pullulan (on the left, Magnification: 300x)
dried and co-milled Pullulan (on the right, Magnification: 250x)

By comparing in terms of thickness the injection moulded disks with those containing KIR particles, as illustrated in Figure 6.8, it is possible to point out that, while no difference are detectable when dried and co-milled Pullulan is used, in the case of Pullulan powder slightly thinner disks are manufactured. Instead, in terms of mass, as shown in Figure 6.9, the disks produced taking into account the new protocol result to be a little heavier, especially in the case of 400 μm nominal thickness. The interesting result is that the characteristics of the disks prepared with the new method are more repeatable.

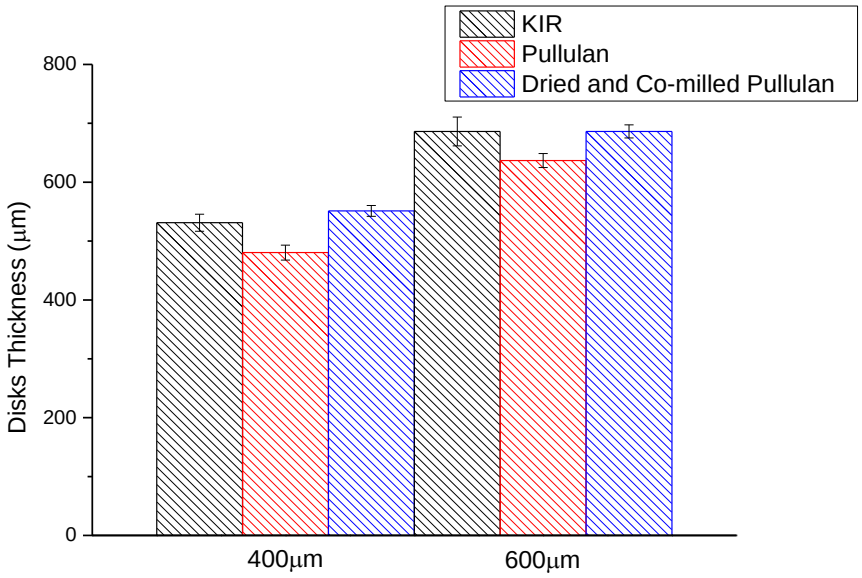

Figure 6.8: Disks thickness

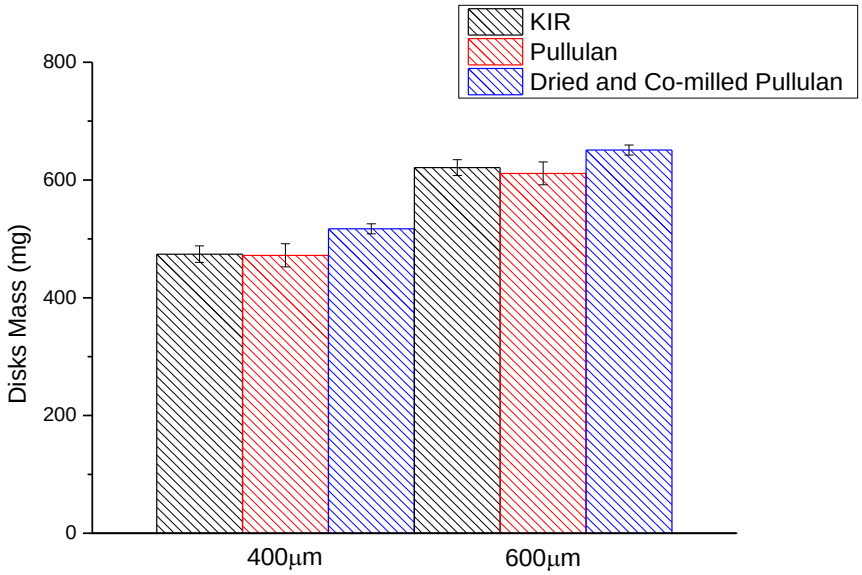

Figure 6.9: Disks mass

6.2.2 DRUG RELEASE PERFORMANCE

Pulsed drug release can be defined as the rapid release of a drug after a predetermined off release period. Lag time is defined as the time between the moment when a dosage form is immersed into an aqueous environment and the time at which the active ingredient begins to be released from the dosage form.

For the purpose of obtaining enteric release, a rapid release of the drug is desired when the capsule reaches the small intestine, after having passed through the stomach. Therefore, disks should resist the gastric pH values but rapidly dissolve/disintegrate at the intestinal pH values. Once this occurs, the release has to be immediate.

In vitro test demonstrate that disks are able to avoid drug permeation in the acidic environment and release their content after pH change. This behaviour suggests that, during the injection moulding process, the methyl cellulose based polymer upholsters and isolates efficaciously the pore former particles, soluble at any pH, that are therefore not reached by the medium. Only when, in basic environment, the methyl cellulose based polymer starts to dissolve, the medium can reach the release enhancer particles that, by dissolving, can improve the disintegration and dissolution rate of the entire matrix barrier.

The release profiles of 400 μm disks are exhibited in Figure 6.10, while those of 600 μm disks in Figure 6.11, where the red dashed line indicates the time at which pH change was carried out. In agreement with expectations, lag times were dependent on the disks wall thickness. Thus, disks with a thickness of 400 μm discharged their reservoir drug content before than those with a thickness of 600μm.

The disks containing Pullulan exhibited longer time spans before the drug was released. Some of them never even opened during the whole time span of the experiment. Besides this, their lag times distribution was broader. Instead, disks incorporating dried and co-milled Pullulan were characterized by replicable in vitro lag phases followed by an immediate drug release. The narrower time distribution guarantees a considerable in vitro reproducibility.

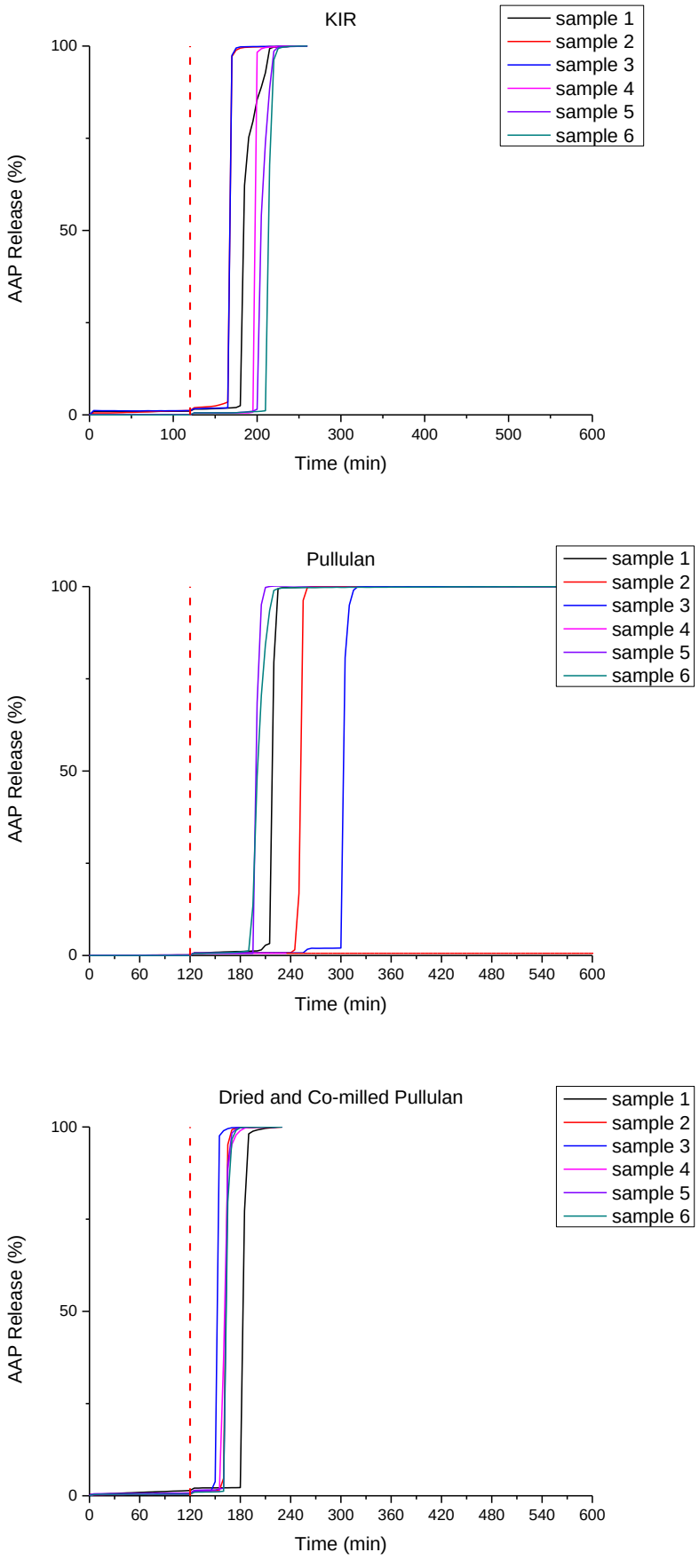

Figure 6.10: Drug release performance of 400 μm disks

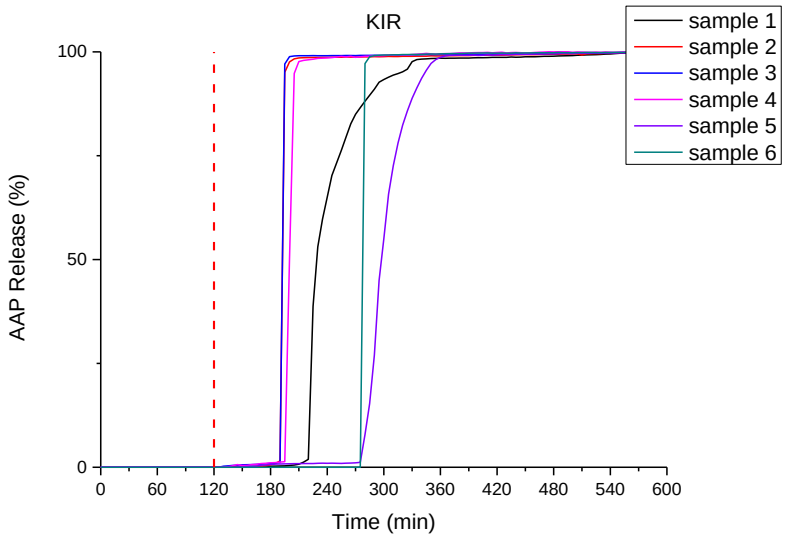

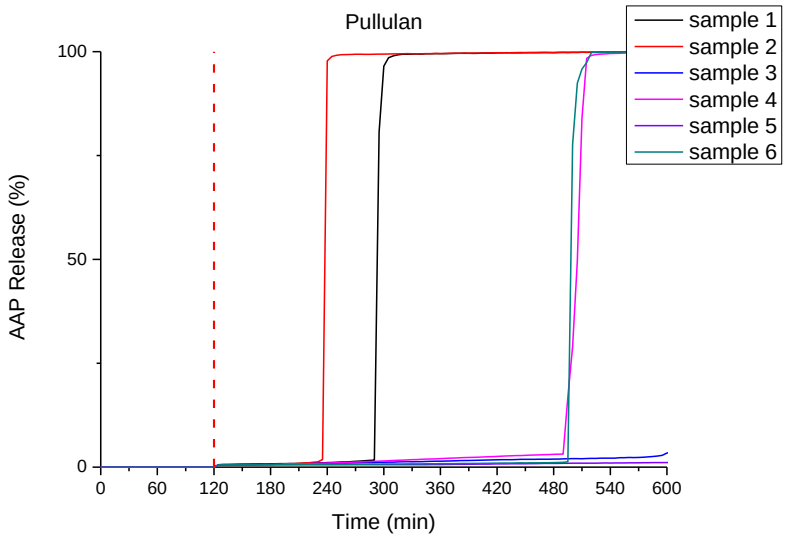

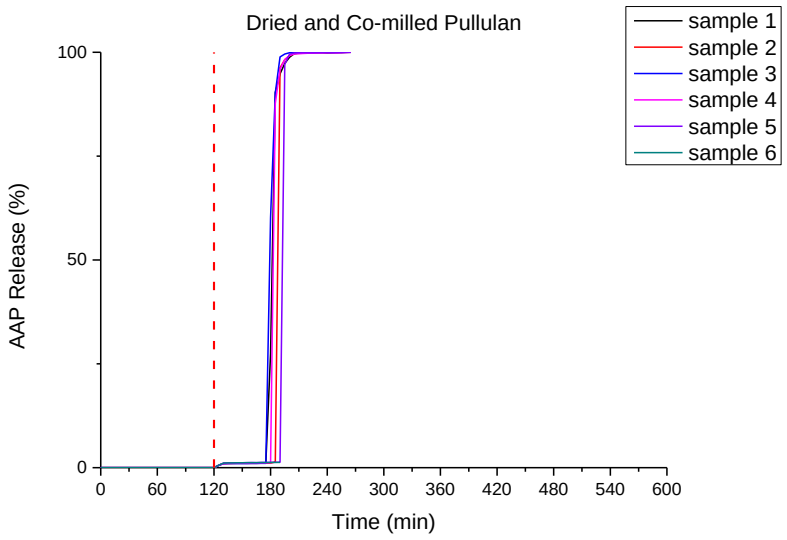

Figure 6.11: Drug release performance of 600 μm disks

A comparison between the disks mean release times, proposed in Figure 6.12, where the black dashed line indicates the time at which pH change was carried out, allows emphasizing the Pullulan not satisfactory behaviour. This could be conceivably ascribed to the fact that the particles were badly mixed, as discussed in Section 6.2.1, so most of them were located at the edge of the disk, which is not exposed to the medium and thus is not partaking in any release mechanism. Instead, as concerns the disks containing the dried and co-milled Pullulan, it is possible to note attractive and newsworthy results.

These improvements are of great importance because reveal that the developed protocol works well and absolutely better than the previous one. It allows reaching encouraging results, which incite to pursue the experimental research objective.

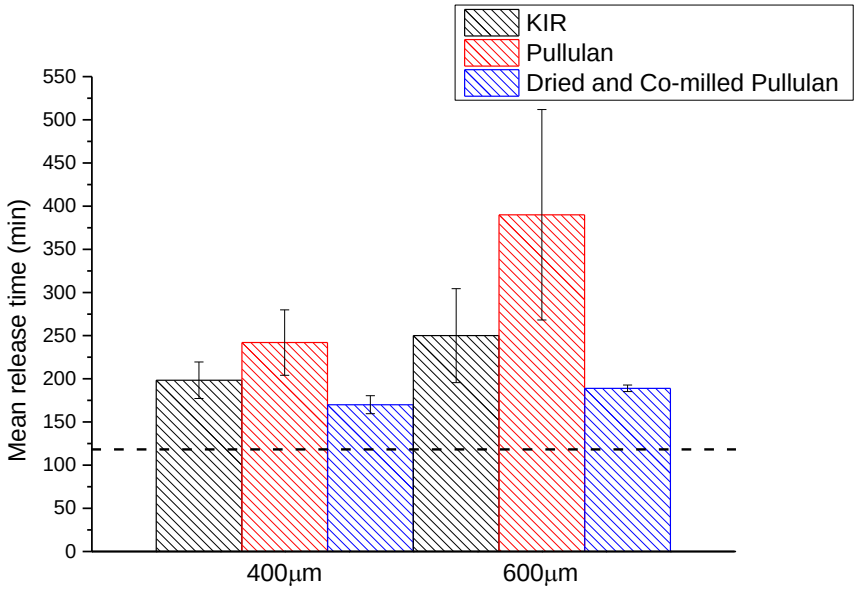

Figure 6.12: Disks mean release times

6.2.2.1 STATISTICAL ANALYSIS

In order to corroborate the obtained results and thus allege if the dried and co-milled Pullulan performs better than the KIR as release enhancer, a statistical analysis was carried out.

6.2.2.1.1 NORMALITY TEST

Many of the statistical procedures are based on the assumption that the data follows a normal, i.e. a Gaussian, distribution [103]. Due to the fact that the validity of many statistical procedures depends on the assumption of normality, in order to check it, two tests were performed using the software GraphPad.

The chosen test were:

- Kolmogorov-Smirnov test:

The Kolmogorov-Smirnov test is an empirical distribution function test in which the theoretical cumulative distribution function of the test distribution is contrasted with the empirical distribution function of the data [104]. This test compares the cumulative distribution of the data with the expected cumulative normal distribution, and bases its p value on the largest discrepancy. A limitation of the Kolmogorov-Smirnov test of normality without the Lilliefors correction is that it is very conservative and is sensitive to extreme values that cause tails in the distribution [105].

The test statistic is defined by

$$D = sup_x |F_n(x) - F(x, \mu, \sigma)| \quad \text{Eq(6.1)}$$

where

- $F_n(x)$ is the empirical distribution function of the data;
- $F(x, \mu, \sigma)$ is theoretical cumulative distribution function of the normal distribution function [106].

Large values of D indicate non normality.

- Shapiro-Wilk test:

The Shapiro-Wilk test has more statistical power to determine a non normal distribution than the Kolmogorov-Smirnov test. The Shapiro-Wilk test depends on the correlation between given data and their corresponding normal scores. The test statistic for this test is

$$W = \frac{(\sum_{i=1}^{n} a_i x_i)^2}{\sum_{i=1}^{n} (x_i - \bar{x})^2} \quad \text{Eq(6.2)}$$

where

- x_i is the i-th largest order statistic;
- $\bar{x}$ is the sample mean;
- n is the number of observation [107].

A significant W statistic causes the rejection of the assumption that the distribution is normal.

Therefore, in summary, the performed tests for normality calculate the probability that the sample is drawn from a normal population. The hypotheses used were:

- Ho: The sample data are not significantly different than a normal population.
- Ha: The sample data are significantly different than a normal population.

Thus, considering that, if the test is significant, the distribution is non normal:

- Probability > 0.05 means the data are normal

- Probability < 0.05 means the data are not normal.

The obtained results are summarized in Table 6.1 and Table 6.2.

400 μm disks		600 μm disks	
Statistic	**p Value**	**Statistic**	**p Value**
0,22268	0,96919	0,27464	0,68816
0,33333	0,42575	0,23051	1

Table 6.1: Kolmogorov-Smirnov test

400 μm disks		600 μm disks	
Statistic	**p Value**	**Statistic**	**p Value**
0,82557	0,09855	0,85413	0,16992
0,87934	0,26604	0,88104	0,31404

Table 6.2: Shapiro-Wilk test

In all the cases, the response at 5% level is that the normality cannot be rejected, which means that the data are drawn from a normally distributed population.

6.2.2.1.2 T TEST

Based on all checks of normality, the mean release time of each group of disks is normally distributed so a two sample t-test can be used to test between group differences.

A t-test for two means with unknown population variances and two independent samples is a hypothesis test that attempts to make a claim about the population means. More specifically, a t-test uses sample information to assess how plausible it is for the population means to be equal.

The test has two non overlapping hypotheses, the null and the alternative hypothesis. The null hypothesis is a statement about the population means, specifically the assumption of no effect, and the alternative hypothesis is the complementary hypothesis to the null hypothesis.

The following null and alternative hypotheses needed to be tested:

- Ho: $\mu_1 \geq \mu_2$
- Ha: $\mu_1 < \mu_2$

where μ_1 and μ_2 are the population means of dried and co-milled Pullulan and KIR disks, respectively.

The formula for a t-statistic for two population means with unknown population variances depends on whether the population variances are assumed to be equal or not. If the population variances are assumed to be equal, then the formula is

$$t = \frac{\overline{X_1} - \overline{X_2}}{\sqrt{\frac{s_1^2}{n_1} + \frac{s_2^2}{n_2}}} \qquad \text{Eq(6.3)}$$

On the other hand, if the population variances are assumed to be unequal, then the formula is

$$t = \frac{\overline{X_1} - \overline{X_2}}{\sqrt{\frac{(n_1 - 1)s_1^2 + (n_2 - 1)s_2^2}{n_1 + n_2 - 2}\left(\frac{1}{n_1} + \frac{1}{n_2}\right)}} \qquad \text{Eq(6.4)}$$

where

- $\overline{X_1}$ and $\overline{X_2}$ are the provided sample means;
- s_1 and s_2 are the provided standard deviations;
- n_1 and n_2 are the sample sizes.

The obtained results are listed in Table 6.3.

	400 µm disks	
	T statistic	**Prob >|t|**
Equal variance assumed	-2.688	0.0114
Equal variance not assumed	-2.688	0.015

	600 µm disks	
	T statistic	**Prob >|t|**
Equal variance assumed	-2.261	0.0251
Equal variance not assumed	-2.497	0,0271

Table 6.3: T-test

In all the cases, it is concluded that the null hypothesis Ho is rejected. Therefore, there is enough evidence to claim that population mean μ_1 is less than μ_2, at the 0.05 significance level.

6.2.2.1.3 F TEST

Many statistical procedures assume that although different samples can come from populations with different means, they have the same variance. The corresponding dispersion problem is of interest to confirm the validity of t-test, and for its own sake.

The following null and alternative hypotheses needed to be tested:

- Ho: $s_1^2 \geq s_2^2$
- Ha: $s_1^2 < s_2^2$

where s_1^2 and s_2^2 are the population variances of dried and co-milled Pullulan and KIR disks, respectively.

The equation for comparing two variances with the f-test is

$$F = \frac{s_1^2}{s_2^2} \qquad \text{Eq(6.5)}$$

The obtained results are reported in Table 6.4.

400 μm disks		**600 μm disks**	
F	**Prob > F**	**F**	**Prob > F**
4,12821	0,14581	203,42857	1,33737E-4

Table 6.4: F-test

While in the case of 400 μm disks, the null hypothesis is not rejected, and consequently there is not enough evidence to claim that the population mean μ_1 is less than μ_2, at the 0.05 significance level, in the case of 600 μm disks the null hypothesis is rejected. This means that there is enough evidence to claim that population mean μ_1 is less than μ_2, at the 0.05 significance level and thus that disks filled with dried and co-milled Pullulan release their content before than those containing KIR.

It is important emphasizing these newsworthy results, because they prove that the KIR can be well replaced by the Pullulan, which displays a behaviour comparable and, in the case of 600 μm, even better than that of KIR. Further, it was shown that the pretreatment, dimensions and dispersion route of particles in the matrix has a significant effect on the release performance of the moulded product. However, it was not possible to figure out the single contribution of the pretreatment, particle size distribution and dispersion. This was however out of the scope of the present research, but may be the subject of future work.

Finally, it must be observed that in the low pH environment, where the HPMCAS is insoluble, the Pullulan is ineffective in promoting drug release. In case of gastro resistant drug delivery system, this behaviour is desired, but the final aim of the work was check if the effectiveness of the pore formers could be pushed to a point that they may promote release also in case of limited matrix solubility. The present results show that particles with sphere like shape cannot hit this goal. Still, the possibility of creating percolating paths of soluble pore former, and then channels, is to be explored. The first step in this direction is being able to produce pore formers with fiber like structures, which are not available on the market at the moment. To do this, Pullulan is a very promising material, as its tendency to form fibres from solutions is reported in literature [27] and

because the fibrillary shape is expected to be preserved also when mixing them in the matrix melt, given Pullulan extremely high melting temperature.

The following parts of the thesis will deal with the characterization of Pullulan water and hydro alcoholic solutions and with the use of the spray drying technique to produce Pullulan fibres.

PART III

Pullulan solutions preparation and characterization

Chapter 7

Ethanol (EtOH) was provided by Sigma-Aldrich (Saint Louis, Missouri, USA).

7.1 POLYMER SOLUTIONS

Two different polymer solutions were prepared, consisted of:

- Pullulan and distilled water;
- Pullulan, distilled water and ethanol.

Pullulan and distilled water were weighted and then combined following the order:

- Half of the needed amount of water;
- Pullulan;
- Remaining quantity of water.

To promote a complete dissolution, the solution was smoothly stirred with a roll mixer. When required, ethanol was added to the polymer aqueous solution in a 6g solution : 1g EtOH proportion. This proportion was chosen arbitrarily and allowed to avoid the precipitation of Pullulan. Higher contents of ethanol indeed favoured the phase separation between the Pullulan and the liquid phase.

Solutions with different Pullulan contents were prepared, as reported in Table 7.1. The indicated values of concentration refer to the mass percentage of solute present in solution. However, for the sake of simplicity, when is useful and suitable, in the case of hydro alcoholic solutions the nominal concentration coinciding with the concentration of the equivalent aqueous solution before the ethanol addition will be indicated.

Pullulan concentration (wt%)	
H_2O solutions	**Pullulan H_2O + EtOH solutions**
20	17.143
15	12.857
10	8.571
7.5	6.428
5	4.286
1.5	1.286
0.5	0.428

Table 7.1: Considered solutions concentrations

The mass fraction of each component was chosen with an educated guess based on the calculation of the critical concentration for coil overlap c^* in water. In fact, knowing that the Pullulan mass average molecular weight is nominally 300 kDa, the Mark Houwink Sakurada equation was used to evaluate the intrinsic viscosity [η] [108] [109].

$$[\eta] = 1.956 * 10^{-4} M_w^{0.667} \quad \text{Eq(7.1)}$$

Then, as reported in literature [110],

$$[\eta] = \frac{0.77}{c^*} \quad \text{Eq(7.2)}$$

the critical overlap concentration for the Pullulan was calculated.

Moreover, considering that [111]

$$\frac{c_e}{c^*} \sim 10 \quad \text{Eq(7.3)}$$

also the entanglement concentration c_e was estimated.

The obtained results are listed in Table 7.2.

$[\boldsymbol{\eta}]$	$0.880\ \frac{\text{cm}^3}{\text{g}}$
$\boldsymbol{c^*}$	$0.875\ \frac{\text{g}}{\text{cm}^3}$
$\boldsymbol{c_e}$	$8.75\ \frac{\text{g}}{\text{cm}^3}$

Table 7.2: Evaluated intrinsic viscosity, critical concentration for coil overlap and entanglement concentration for Pullulan aqueous solutions

As discussed in literature [27], the density of the Pullulan aqueous solutions, measured with a glass pycnometer, is almost constant at a value slightly higher than $1\ \frac{\text{g}}{\text{cm}^3}$, with a very slight increase for increasing concentration. Diving the previous results for the density of the Pullulan aqueous solutions is possible to obtain the values reported in Table 7.3.

$\boldsymbol{c^*}$	0.875
$\boldsymbol{c_e}$	8.75

Table 7.3: Critical concentration for coil overlap and entanglement concentration for Pullulan aqueous solutions

Then, it was assumed that the coefficients of the Mark Houwink Sakurada equation, and consequently the critical concentration for coil overlap c^* and the entanglement concentration c_e values, are valid also for the hydro alcoholic solutions. Hence, the density of the Pullulan hydro alcoholic solutions was estimated, as a first approximation, with the rule of mixture. The evaluated

value was 0.963 $\frac{g}{cm^3}$. Dividing the results in Table 7.2 for the density of the Pullulan hydro alcoholic solutions is possible to obtain the values listed in Table 7.4.

c^*	0.909
c_e	9.09

Table 7.4: Critical concentration for coil overlap and entanglement concentration for Pullulan hydro alcoholic solutions

Therefore, as shown in Figure 7.1, for the considered concentrations the values

- Below $\frac{c}{c*} = 1$ are in the diluted regime;
- Between $\frac{c}{c*} = 1$ and $\frac{c}{c*} = 10$ are in the semidiluted regime;
- Above $\frac{c}{c*} = 10$ are in the semidiluted entangled regime.

The analysed concentrations were chosen in all the three different regimes in order to examine which interaction could have an interesting effect.

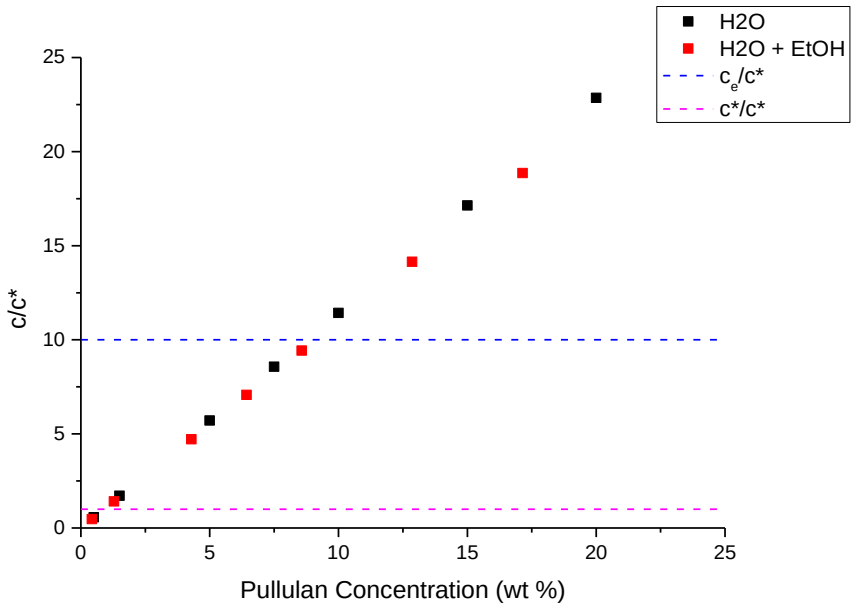

Figure 7.1: Comparison of polymer concentrations with respect to their critical concentration

As a general remark about the solution, it was observed that time stability seemed to be an issue, because considerable alterations of the samples were visually detected after two weeks. For this reason, each executed test required a new solution.

7.1.1 SURFACE TENSION

In literature [27], the surface tension of aqueous solutions was measured using the pendant drop method. The average values for the surface tension, as displayed in Table 7.5, were close to the relatively high one of water and approximately constant for all the considered solutions.

		Surface tension $\left(\frac{mN}{m}\right)$
Pullulan Concentration (wt%)	1	71.441
	5	71.424
	10	71.781
	15	71.761

Table 7.5: Surface tension of aqueous solutions

Taking into account these results, and in coherence with what done for hydro alcoholic solutions, the surface tension of the aqueous solutions was considered equal to that of water, thus 72.15 $\frac{\mathrm{mN}}{\mathrm{m}}$. Instead for the hydro alcoholic solutions, assuming always that the pullulan does not influence the surface tension value, it was calculated, as explained in literature [112], as a function of the ethanol mole fraction. Therefore the considered value was 43.71 $\frac{\mathrm{mN}}{\mathrm{m}}$.

7.1.2 SHEAR VISCOSITY

The shear viscosity measurements were conducted with a Modular Compact Rheometer MCR 502 (Anton Paar GmbH, Graz, Austria). The device technical specifications are displayed in Appendix A. The rheometer was controlled and data acquired using the RheoCompass software.

The experimental protocol for each sample consisted of measurement of shear stress and viscosity as a function of the applied shear rate. The experimental conditions are reported in Table 7.6.

Set value	
Variable	Shear Rate $\frac{d\gamma}{dt}$
Profile	Ramp logarithmic
Initial	0.01 $\frac{1}{s}$
Final	100 $\frac{1}{s}$

Data points	
Number	17
Duration	Ramp logarithmic
Initial	30 s
Final	1 s
Interval duration	152.436 s

Table 7.6: MCR 502 experimental setup

Tests were performed at 25°C, making use of a Peltier temperature device. The Peltier effect can be briefly described as the inverse thermo electrical effect. Depending on the voltage applied to both sides of a Peltier material it will immediately react with a temperature gradient from one side to the other. Thus, if one side is arranged to stay at a stable temperature, the other side can be controlled to the desired measuring temperature.

The measuring system was a Parallel Plate geometry. The chosen upper plate, PP 50, had a diameter of 50mm. This geometry has some advantages:

- High shear rate range;
- Small sample volume;
- Easy to fill and to clean;
- Quick temperature equilibration.

But also disadvantages:

- Gap leakage of the substance at too high shear rates;
- Sample drying effects:

  As regard as this point, polymer solutions containing ethanol were analyzed using a hood. In this way, the evaporation of the solvent was avoided and accurate results were obtained.

- The shear rate is not uniform within the gap:

$$\dot{\gamma} = \frac{\omega r}{h} \qquad \text{Eq(7.4)}$$

  where
  - ω is the angular velocity;
  - h is the sample gap height.

  For a parallel plate system the linear velocity increases with radius, but since the gap remains constant the shear rate then varies across the radius of the plate. Therefore, the shear rate varies from 0 at the center to a maximum at the at the outer edge, $r = R$.

  This does not matter for Newtonian liquids since both shear stress and shear rate are linearly related, and hence viscosity is constant, however, for non Newtonian liquids the shear stress

has a non linear dependence and the viscosity will thus vary at different radial locations. This can be largely corrected for by applying a non linear correction based on the local power law index n [113]. Otherwise, as implemented by the device, by calculating the viscosity at $\frac{3}{4}$ of the plate radius instead of the edge, since, as shown in Figure 7.2, the shear rate for non Newtonian and Newtonian materials have comparable values close to this point [114].

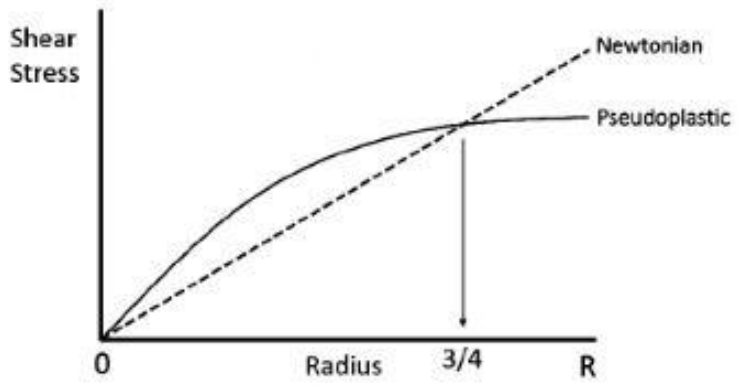

Figure 7.2: Schematic showing stress distribution across a parallel plate for Newtonian and pseudoplastic fluids having equivalent viscosity at $\frac{3}{4}$ R

Both the power law correction method and the single point method can give slight errors compared with measurements made on a cone plate configuration, especially in the transition region between Newtonian and non Newtonian behaviour. For the power law method, estimation of n by local differentiation of the torque versus angular velocity data can be a source of error, while for the single point correction, the radial position at which measured stresses are equivalent for Newtonian and non Newtonian materials can shift slightly from the $\frac{3}{4}$ position [115].

Each test was performed three times to verify the repeatability of the obtained experimental values.

7.1.3 ELONGATIONAL VISCOSITY

The elongational viscosity was measured with a Capillary Breakup Extensional Rheometer HAAKE CaBER 1 (Thermo Fisher Scientific, Karlsruhe, Germany). The instrument technical specifications are reported in Appendix A.

As examined in depth in Chapter 4, a small cylindrical plug of fluid, a liquid bridge, is generated between two flat disks of diameter D_0 and stabilized against gravitational sagging by capillarity. At time $t = 0$, the upper plate is rapidly set in motion, causing the formation of a filament which thins under capillary action. The time evolution of the midpoint diameter of the thinning filament is monitored by means of a laser. The basic operations of the device are shown in Figure 7.3.

The CaBER 1 uses a high precision laser micrometer to accurately track the filament diameter as it thins. Aside from its resolution, around 10μm, the micrometer is also immune to large ambient light

fluctuations and can resolve small filaments easily. This instrument is a class 1 laser, operating in the infrared, at a wavelength of 780nm.

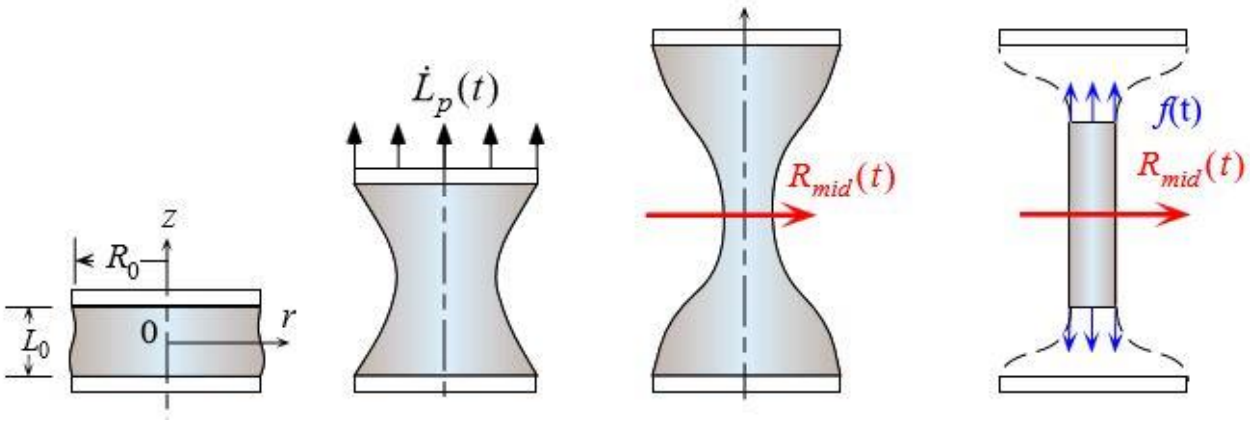

Figure 7.3: Schematic diagram of capillary breakup extensional rheometry

Data relating to the used geometry are summarized in Table 7.7.

Defined geometry		
Plate diameter	D_0	6 mm
Initial gap	L_0	3 mm
Initial aspect ratio	$\frac{L_0}{D_0}$	1
Final gap	L_1	7.6 mm
Final aspect ratio	$\frac{L_1}{L_0}$	2.5 mm

Table 7.7: CaBER 1 defined geometry

Note that it is recommended to use an initial plate gap of 3mm when using 6mm diameter plates, thus giving an aspect ratio of 1. If the initial gap is too large then the initial column of fluid takes on an hour glass shape due to the influence of gravity. This shape imposes a precondition on the fluid that distorts the final filament, and thus the measured properties. On the other hand, if the initial gap is too small then there is a strong shear flow in the initial stretch, which also preconditions the fluid in the flow. Neither of these effects are desirable.

The plate motion is controlled by a linear drive motor. This system allows fast response and reasonable control over the stretch profiles used. In the configuration supplied the linear motor of the CaBER 1 can be set to use three different stretch profiles. A linear stretch profile was chosen so that the final length could be reached in 30ms.

The testing protocol chosen was based on single measurement. The sampling mode was setted to high speed measurement, 1000 points per second, because, for fluids that break up quickly, less than

0.5s, this mode provides a sampling rate fast enough. Defined measurement options are reported in Table 7.8.

Acquisition parameters	
Acquisition rate	1000 Hz
Max acquisition duration	0.5 s

Table 7.8: CaBER 1 adopted measurement options

The sample was loaded pipetting the fluid in from the side, until a large enough mass was inserted to fill the gap. Is important to try to ensure that the gap between the plates is fully filled, but that the plate sides are completely dry. The theory assumes that the fluid is pinned at the plate edges, with a non slip boundary condition, and that there is no flow over the edges of the plates. Although in fact the CaBER can be remarkably tolerant of these influences, for consistency they are best avoided. It is also strictly necessary to make sure that there are no bubbles in the sample.

Tests were performed using a high speed megaPixel CMOS camera Mikrotron MC1310 (Mikrotron GmbH, Unterschleissheim, Germany) with Computar MC TV lens, characterized by a focal length of 50mm, to capture the filament evolution. An acquisition rate of 1000 frame per second was used along with a resolution of 1280 (H) × 512 (V) pixel.

Each test was performed five times to verify the repeatability of the obtained experimental values.

7.1.4 THERMOGRAVIMETRIC ANALYSIS

The thermogravimetric analysis was carried out with a Thermogravimetric Analyzer TGA Q500 (TA Instruments, New Castle, DE, USA). The experimental test monitored the amount and rate of mass variations of a material as a function of temperature or time as the sample specimen is subjected to a controlled temperature program in a controlled atmosphere. The device technical specifications are reported in Appendix A.

The test was performed with the aim of evaluating the solvent evaporation rate during the spray drying process, which occurred at 140°C. Therefore, the experimental protocol, that for each sample consisted of a ramp of 5 $\frac{^{\circ}C}{min}$ from 25°C to 140°C, followed by 35min of an isothermal test at 140°C, was selected to simulate the spray drying condition. Indeed the imposed ramp was a way to reach the spray drying temperature, 140°C, at which was of interest analyze the solutions behavior.

The chosen experimental conditions are reported in Table 7.9, while the applied temperature profile is illustrated in Figure 7.4.

Pan	Alumina: 500µL diameter: 10mm
Gas	Air

Table 7.9: TGA experimental conditions

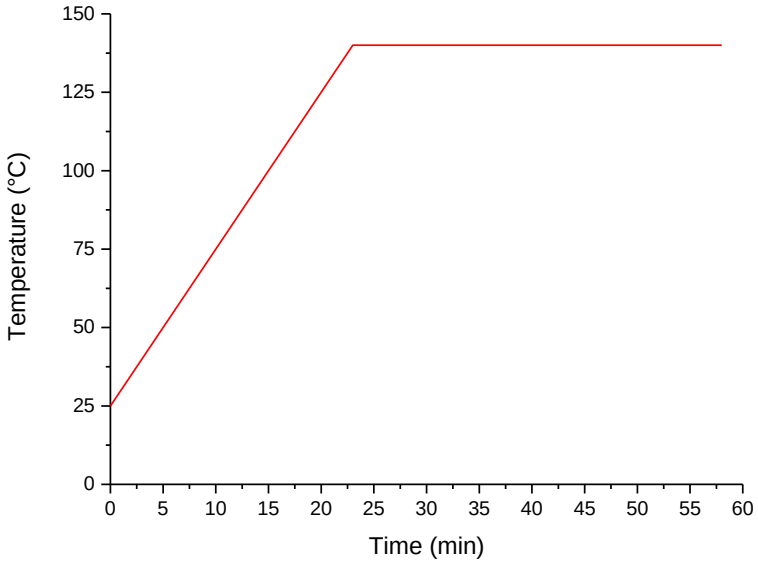

Figure 7.4: TGA temperature profile

Chapter 8

8.1 SHEAR VISCOSITY

Shear viscosity measurements were executed at 25°C. The flow curves attained from each of the three tests performed are represented in Figure 8.2 and Figure 8.3. The measured values result to be very repeatable, especially at higher shear rate. Only in the case of 0.5 wt% aqueous solution is possible to observe a higher dispersion of data.

Since the very low Pullulan concentration, this phenomenon can be related to the fact that this polymer solution consisted almost completely of water. Pure water is difficult to test because its surface tension can influence the rheological behaviour at low shear rates where the contribution from viscosity is comparable with the former.

Based on the idealized assumption of rotational symmetry, surface tension should not produce a torque in rotational rheometers. However, it is demonstrated that the rotational symmetry assumption can be violated easily. Finite deviations of contact line rotational symmetry, illustrated in Figure 8.1, allow surface tension to produce a torque, which impacts measurements of shear rheological material functions [116]. Torque in rotational rheometers is influenced by edge effects and non ideal conditions. Interfacial rheology and resistance to shear at the free surface can contribute to torque [117][118].

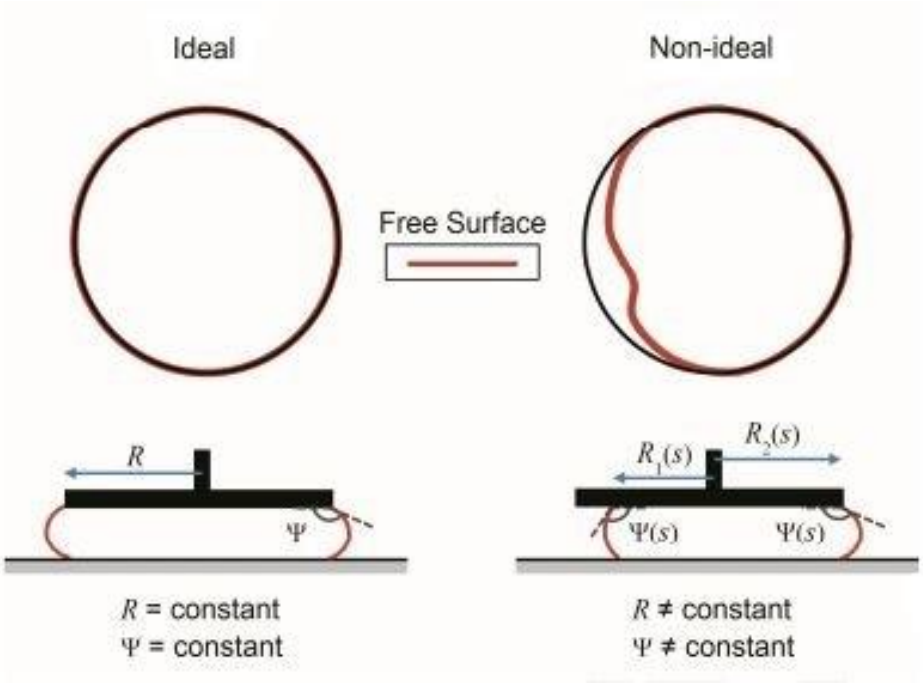

Figure 8.1: Contact line and interface angle: ideal versus non ideal.
Non ideal asymmetries are exaggerated compared to typical loading and can also occur as a result of over filling.

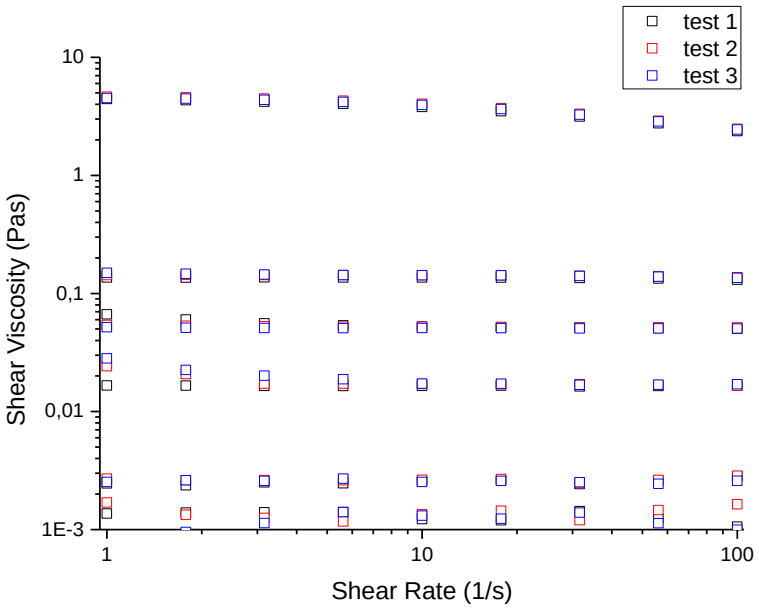

Figure 8.2: Shear viscosity versus shear rate of Pullulan aqueous solutions for nominal concentration of 20, 10, 7.5, 5, 1.5, 0.5 wt%

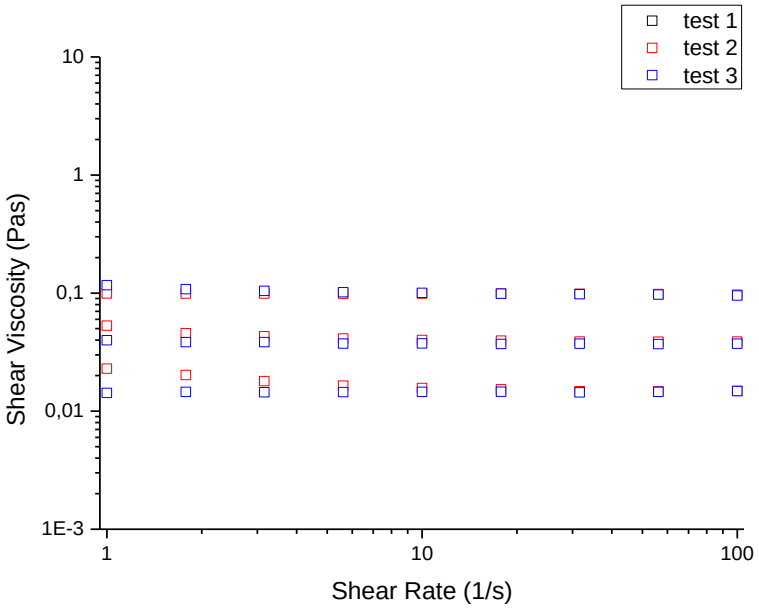

Figure 8.3: Shear viscosity versus shear rate of Pullulan hydro alcoholic solutions for nominal concentration of 10, 7.5, 5 wt%

A first evident consideration that can be made is that solutions with 10 wt% or lower Pullulan concentrations show Newtonian behavior, i.e. shear viscosity is independent of shear rate, in the shear rate range from 1 to 100 $\frac{1}{s}$. As Pullulan concentration increases beyond 10 wt% shear thinning become noticeable. However, the non Newtonian behavior is limited, since the viscosity decreases much less than one order of magnitude over two decades of shear rate.

Furthermore, comparing the flow curves of the aqueous and hydro alcoholic solutions, as reported in Figure 8.4, it appears that the presence of ethanol does not affect the shear behavior of the polymer

solution. Being equal the nominal concentration, the lower viscosity of the mixture containing the ethyl alcohol can be explained with its smaller real concentration. Thus, in this case, ethanol works just as a diluent.

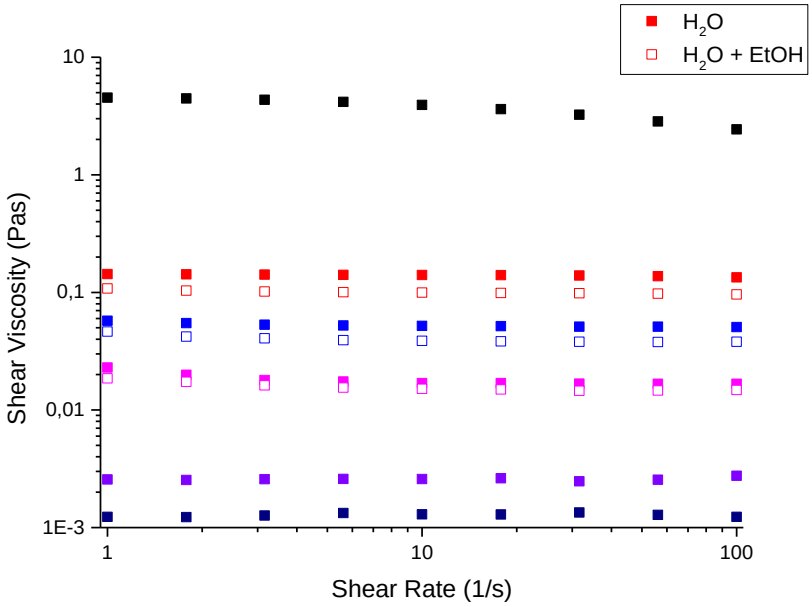

Figure 8.4: Shear viscosity versus shear rate of Pullulan solutions for nominal concentration of 20, 10, 7.5, 5, 1.5, 0.5 wt%

The previous assessment is also evident in Figure 8.5, where the solutions shear viscosity evaluated at shear rate equal to $1\,\frac{1}{s}$ is depicted. Even if it would be better to represent the data in volume fraction, it was not possible due to the lack of information regarding the specific volume. Independent on the way concentration is represented, it is clear that both aqueous and hydro alcoholic solutions follow the same trend.

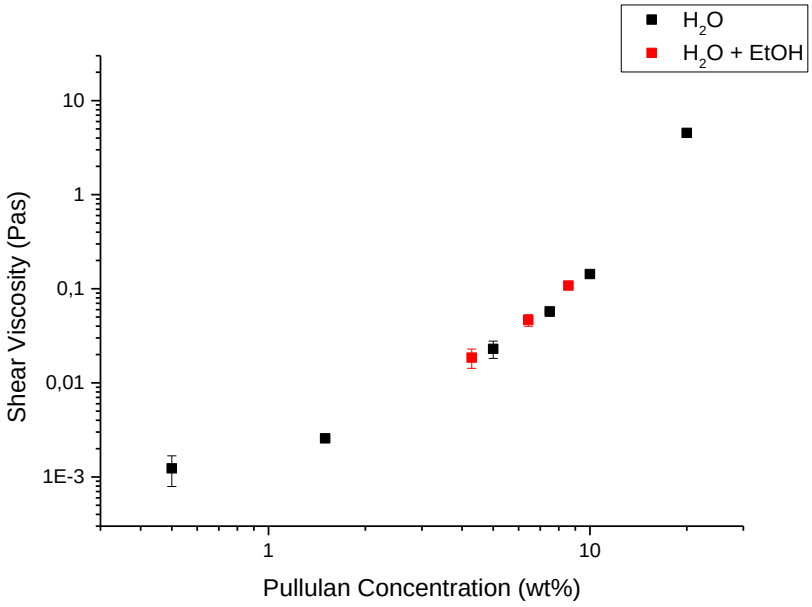

Figure 8.5: Shear viscosity versus Pullulan concentration

In literature [27], the shear viscosity of Pullulan aqueous solutions with concentrations of 15, 10, 5 wt% was measured with a stress controlled rheometer AR-G2 (TA Instruments, NewCastle, DE, USA), with a double wall coquette geometry and Peltier system. Comparing the literature data with those attained, as shown in Figure 8.6, it is possible to appreciate the consistency of the results.

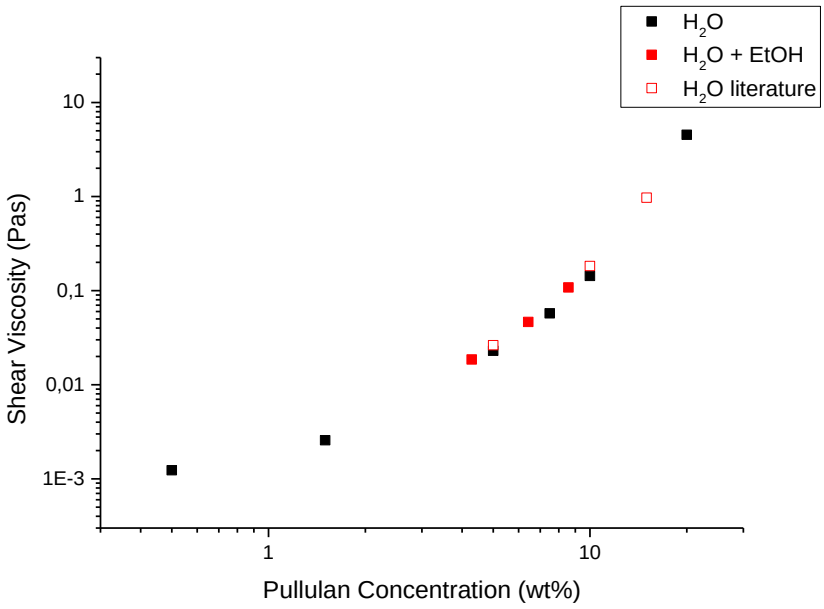

Figure 8.6: Comparison between the shear viscosity values reported in literature and those measured

Even if the solutions shear viscosity results to be independent of shear rate over the explored range, a shear thinning behavior is expected at higher shear rate. Hence, the constant value of viscosity can be considered as the zero shear viscosity. The measured values are listed in Table 8.1.

Nominal Concentration (wt%)	H_2O solutions (Pas)	H_2O + EtOH solutions (Pas)
20	4,531	
15	0,820	0,548
10	0,143	0,108
7.5	0,057	0,046
5	0,023	0,019
1.5	0,003	0,003
0.5	0,001	

Table 8.1: Zero shear viscosity

The value at a nominal Pullulan concentration of 15 wt% was interpolated, in the case of water solution, or extrapolated, in the case of mixture solution, by fitting, as illustrated in Figure 8.7, the trend in Figure 8.6 with the function

$$y = A_1 e^{\frac{x}{t_1}} + y_0 \qquad \text{Eq(8.1)}$$

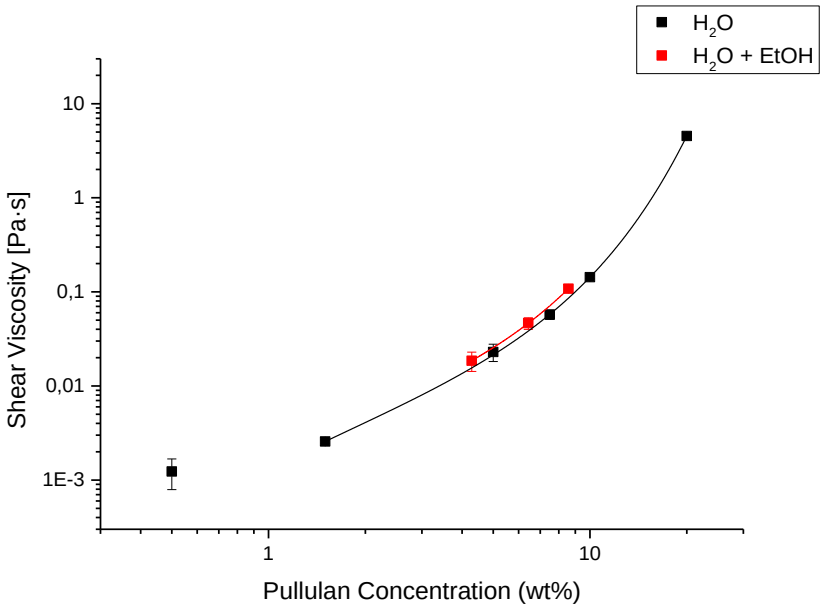

Figure 8.7: Fitting of the shear viscosity versus Pullulan concentration curves

As a general remark about the solution properties, it should be highlighted that little molecular weight variations were observed between different Pullulan batches. This has a visible effect on the rheological behaviour of the solutions, as demonstrated in Figure 8.8. Therefore is always important to carry out a complete characterization of new lots.

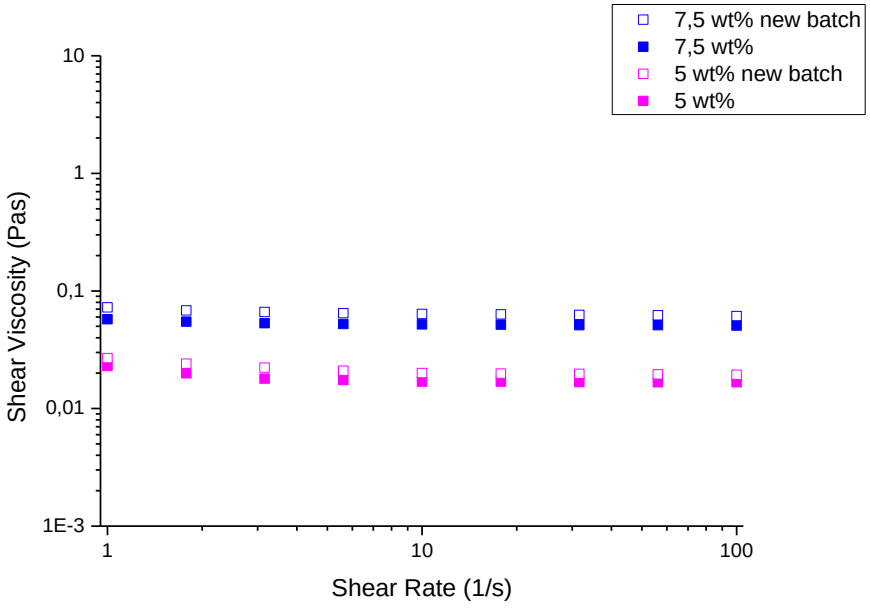

Figure 8.8: Comparison between the flow curves attained analyzing solutions prepared with Pullulan from different batches

8.2 ELONGATIONAL VISCOSITY

The principal experimental results obtained from the CaBER are the time evolution of the midpoint diameter of fluid capillaries. According to literature, the observed thinning of a filament of a semi dilute polymer solution can be separated into four regions [119], as depicted in Figure 8.9.

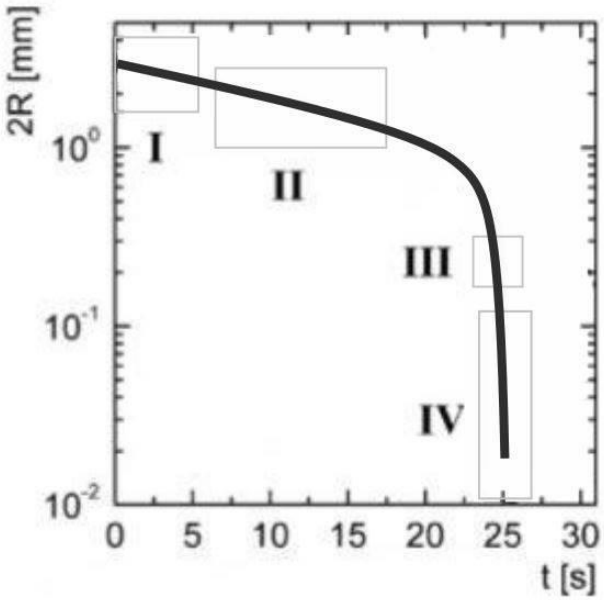

Figure 8.9: Evolution of the mid filament diameter as a function of time

- Regime I:

It is an ill defined regime that still contains strong contributions from gravitational sagging. Indeed, once the unstable bridge is formed, the forces acting on the midpoint of the filament during these initial instants are surface tension driven, which results in a flow away from the midpoint, and gravity driven, which determines a flow from the top to the bottom plate. It is only after the filament gets thin and sufficiently curved, and hence the surface tension generated capillary forces high enough, that gravity can no longer be deemed to be playing a part.

A local Bond number, introduced in Section 4.1, can be used to define a lower boundary to this regime

$$Bo^* = \frac{\rho g R^2}{\sigma} \qquad \text{Eq(8.2)}$$

where:

- ρ is the density;
- σ is the surface tension;
- $R(t)$ is the local filament radius that decreases with time.

By experience, gravitational effects can be neglected for local Bond number below ~0.2 which in the present case calculates to a radius of ~1mm.

- Regime II:

Sets in below this critical Bond number and is controlled by a visco-capillary balance of the capillary pressure $\frac{\sigma}{R}$ and the viscous stresses $\eta_E \dot{\varepsilon}$ in the filament. Since the filament radius is still large, the extension rate $\dot{\varepsilon}$ is low enough so that a Newtonian thinning regime with a constant Trouton ratio of the extensional viscosity η_E to the shear viscosity η_s of

$$\frac{\eta_E}{\eta_s} = 3 \qquad \text{Eq(8.3)}$$

is observed. The radius evolution can in this regime be described with the similarity solution of Papageorgiou [87] [93]

$$R = 0.0709 \frac{\sigma}{\eta_s}(t_b - t) \qquad \text{Eq(8.4)}$$

- Regime III

Is still showing a visco-capillary balance, however, the surface pressure and hence the extension rate $\dot{\varepsilon}$ is high enough so that the polymer solution is showing an extensional thinning, originating from the increased disentanglement and orientation of the polymer chains as described by Keunings [95]. For an extensional viscosity, that follows in this regime a power law of the form

$$\eta_E = K\dot{\varepsilon}^{n-1} \qquad \text{Eq(8.5)}$$

with a power law exponent n between 0 and 1, the filament diameter evolves as [120]

$$R = \Phi \frac{\sigma}{K}(t_b - t)^n \qquad \text{Eq(8.6)}$$

where the numerical front factor Φ is a function of n [94] [120][121].

In the transitional regime between II and III the viscosity is already decreasing, but has not reached the power law thinning yet.

- Regime IV

It occurs at the onset of an elasto-capillary balance where the surface pressure is balanced by the elastic stresses of the unravelling polymer chains. Within the elasto-capillary balance regime the filament is decaying exponentially with time [89][99][122][123]

$$R = R_0 \left(\frac{GR_0}{2\sigma}\right)^{\frac{1}{3}} e^{-\frac{t}{3\lambda_E}} \qquad \text{Eq(8.7)}$$

where

- R_0 is the midpoint radius following the cessation of stretching;
- λ_E is the longest relaxation time
- G is the elastic modulus of the material, defined as

$$G \equiv \frac{\eta_p}{\lambda_E} \quad \text{Eq(8.8)}$$

with η_p representing the polymeric contribution to the viscosity, given by

$$\eta_p = \eta_0 - \eta_s \quad \text{Eq(8.9)}$$

The exponential thinning in regime IV only takes place at small diameters close to breakup.

Considering Figure 8.10 and Figure 8.11, it is possible to distinguish these four zones especially in the case of the two highest concentrations. Data appears to be relatively repeatable. Samples of each solution follow the same trend and the deviation between the curves can be attributed to the different initial volume loaded. The red dashed line indicates the time at which plates stop moving, the desired nominal stretch has been reached and the self controlled capillary breakup starts taking place.

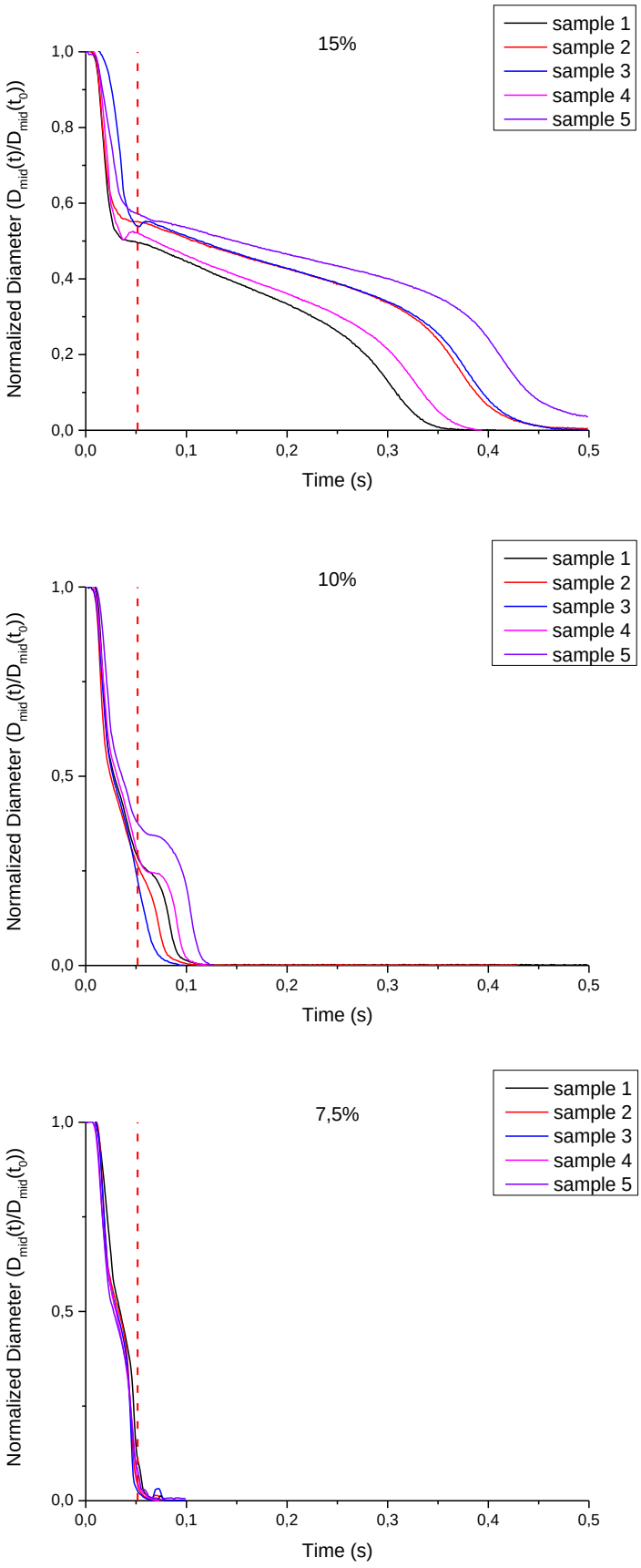

Figure 8.10: Normalized diameter versus time of Pullulan aqueous solutions

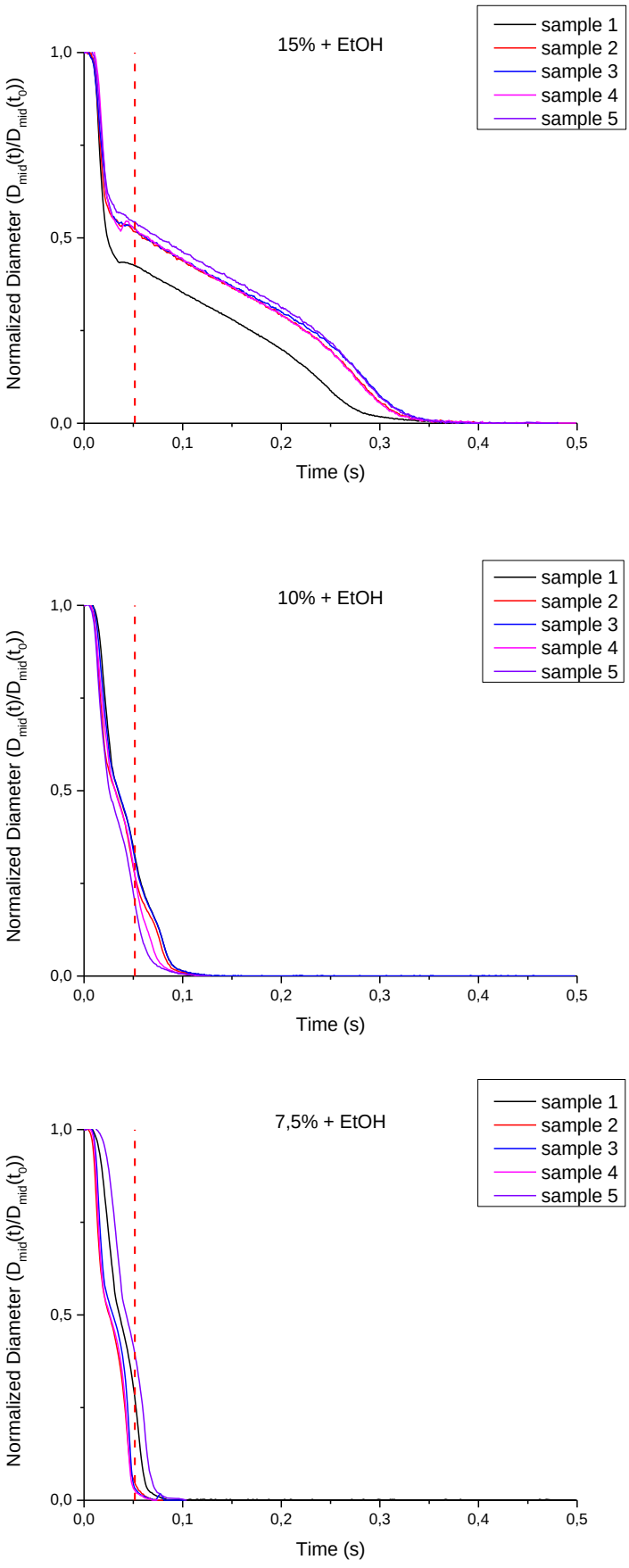

Figure 8.11: Normalized diameter versus time of Pullulan hydro alcoholic solutions

For the sake of clarity, just one representative sample for each solution was considered in order to examine the effect of concentration on thinning profile. As shown in Figure 8.12, it is possible to observe pronounced differences in the thinning dynamics of a polymer solution when increasing the concentration. Whereas for higher concentration the thinning is dominated by a long linear regime, corresponding to regime II, the time range for this regime is getting smaller for lower concentrations. Thus, the transition from a visco-capillary balance to an elasto-capillary balance is shifting with increasing concentrations to smaller filament radii.

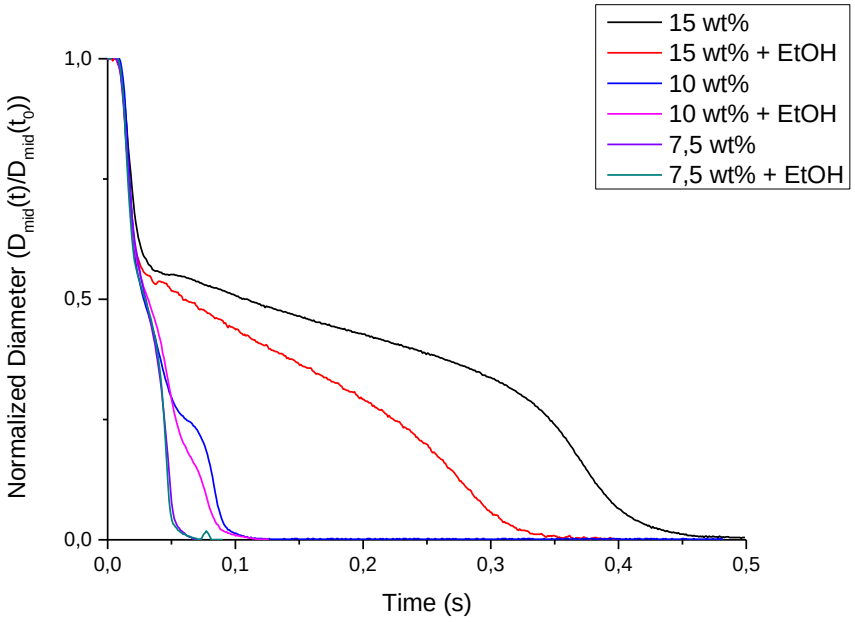

Figure 8.12: Normalized diameter versus time for different Pullulan concentrations

The critical time to breakup is not strictly a material property but depends on the properties of the fluid, the flow geometry and the surrounding medium. Although it is related to the capillary velocity $\frac{\sigma}{\eta_s}$ it also gives information about the non Newtonian behavior and evolution of the material. Obviously, for increasing concentration the time to breakup increases due to both the increase in viscosity and the more pronounced viscoelastic behavior. Thus, more diluted hydro alcoholic solutions display lower time to breakup than the water solutions with the same nominal concentration. Nevertheless, it is possible to note that the hydro alcoholic solutions, compared to aqueous solutions at the same real concentration, are characterized by a longer time to breakup. This phenomenon could be partly ascribed to the difference in surface tension, factor that, as previous analyzed, plays an important role during the thinning filament process.

These considerations are visible in Figure 8.13, where the time to breakup is obtained from the observation of all the videos recorded. The mean value between the five samples for each concentration is considered. Data are given in Table 8.2.

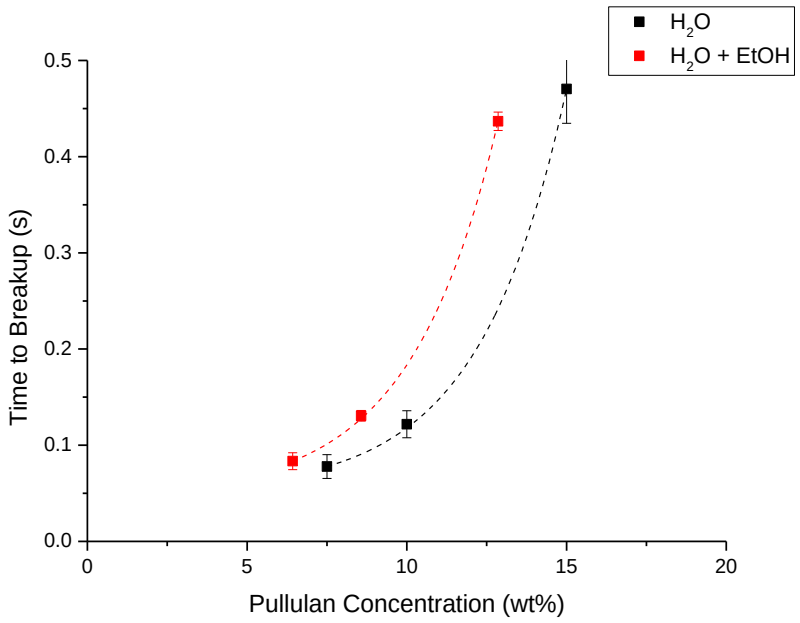

Figure 8.13: Time to breakup versus Pullulan concentration

		Time to breakup (s)			
		H_2O		H_2O + EtOH	
		Mean	St Dev	Mean	St Dev
Nominal Concentration (wt%)	15	0,470	0,036	0,437	0,010
	10	0,122	0,014	0,131	0,006
	7.5	0,078	0,012	0,083	0,009

Table 8.2: Time to breakup values

The determination of the longest relaxation time of a viscoelastic fluid in a uniaxial extensional flow field is one of the main applications of the capillary breakup extensional rheometry. Liquid elasticity is related to extension of the chains and to Brownian motion of the solvent. Brownian motion opposes the stretching and alignment of the chains because it acts to keep the chains in random configurations. In a flow, the degree of extension depends on how much viscous forces dominate those due to Brownian motion. When the applied stress is removed, the chains relax to their equilibrium state, which is visible at the microscopic level as elastic recoil. The rate of stress relaxation is dictated by the fluid's relaxation time. This time, which is zero for Newtonian fluids, is then a measure of fluid elasticity.

The polymer longest relaxation time was calculated fitting the exponential thinning regime. An example is reported in Figure 8.14, where the red dashed line, overlapped to the normalized diameter curve, represents the implemented fitting on the 15 wt% aqueous solution.

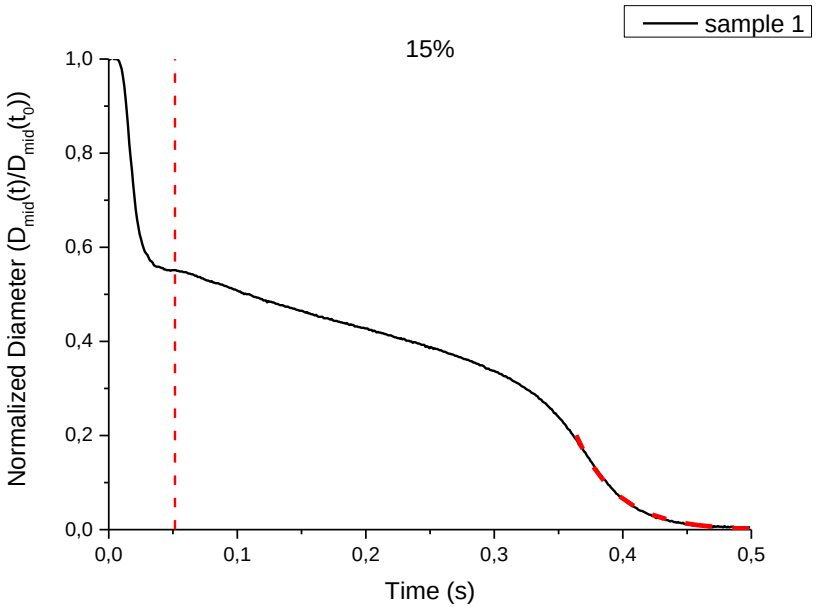

Figure 8.14: Fitting of the exponential thinning regime

All the curves were fitted and the mean value between the five samples for each concentration was calculated and considered. Obtained data are reported in Table 8.3. The relaxation times show a strong dependence on the concentration and decrease monotonically with decreasing concentration, as evidently depicted in Figure 8.15.

Furthermore, it appears that solutions containing ethanol are characterized by a higher degree of elasticity with respect to the water based ones at the same real concentration. The observed increase in relaxation time may be a second reason, along with surface tension reduction, for the increase of time to breakup at fixed pullulan concentration.

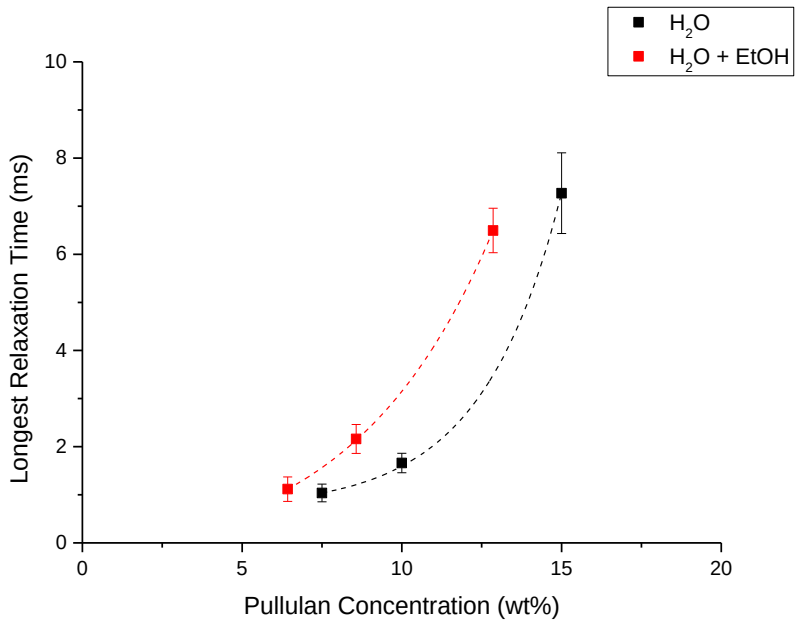

Figure 8.15: Longest relaxation time versus Pullulan concentration

		Longest relaxation time (ms)			
		H_2O		H_2O + EtOH	
		Mean	St Dev	Mean	St Dev
Nominal Concentration (wt%)	15	7,27	0,84	6,49	0,46
	10	1,66	0,20	2,16	0,30
	7.5	1,04	0,18	1,12	0,25

Table 0.3: Longest relaxation time values

In summary, the rheological characterization of the polymer solutions allows stating that the solutions exhibit a remarkable viscoelastic behavior, not noticed during the shear characterization. Therefore, the Pullulan solutions behave as a Boger fluid, an elastic liquid with a constant viscosity. Thus, because the viscosity is independent of shear rate or nearly so, elastic effects can be separated from viscous effects in viscoelastic flows because the latter effects can be determined with Newtonian fluids [124]. With respect of the behaviour of the solutions on the outcome of spray drying process, the difference in viscoelastic behavior, along with those in surface tension will have to be taken into account.

8.3 THERMOGRAVIMETRIC ANALYSIS

The analysis was performed with the aim of evaluating the solvent evaporation rate during the spray drying process and verifying if it is influenced by ethanol addition.

The curves showed in Figure 8.16 and Figure 8.17 represent the weight loss due to solvent evaporation for aqueous and hydro alcoholic solutions, respectively. At the end of each test, the volatile component completely evaporated and the remaining amount of solute was consistent with the amount added during the solution preparation. Only in the case of solution with 10 wt% concentration an inflated thin Pullulan film was observed in the pan. This phenomenon could be related to the fast evaporation detected for this sample.

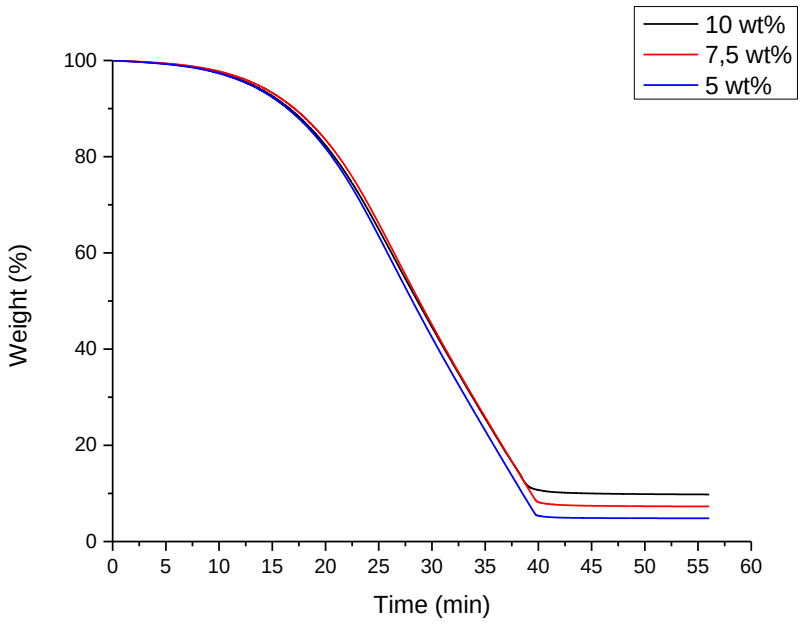

Figure 8.16: Thermogravimetric curves for Pullulan aqueous solutions

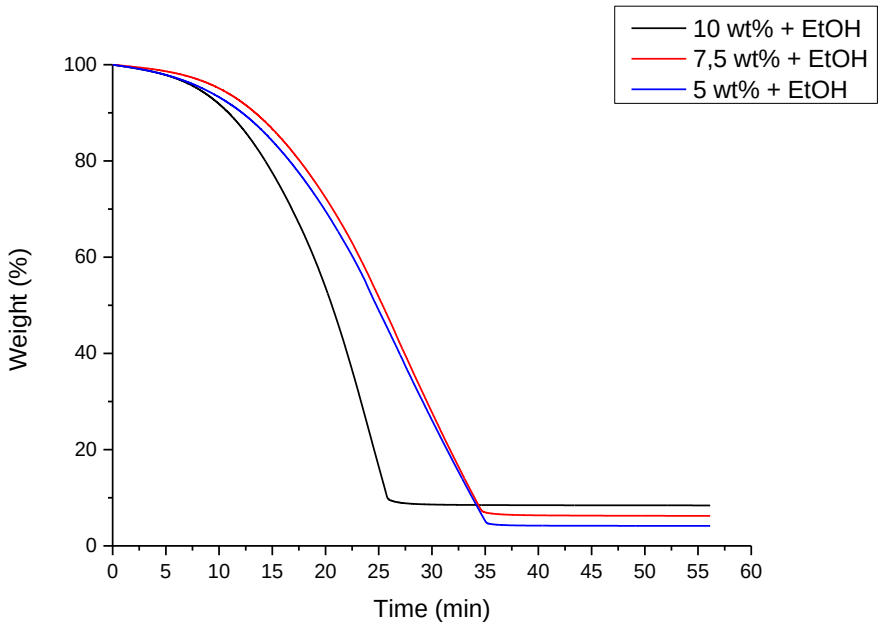

Figure 8.17: Thermogravimetric curves for Pullulan hydro alcoholic solutions

While, for small concentration of alcohol, the evaporation characteristic is globally close to that of the aqueous solutions, as its concentration increases, the mass variation trend differs significantly from the that of the aqueous solutions. This suggests that the evaporation mechanisms for the hydro alcoholic solutions differs from the water ones.

In ideal homogeneous solutions, vapour pressure is governed by Raoult's law, which predicts that the vapour pressure P_i of the ith component of the solution is reduced from the vapour pressure of the pure liquid P_i^0 in proportion to its mole fraction x_i:

$$P_i = x_i P_i^0 \quad \text{Eq(8.10)}$$

For a solution of two liquids, A and B, Raoult's law predicts then the total vapor pressure P above the solution is equal to the weighted sum of the pure vapor pressure of the two components P_A and P_B. Thus, the total pressure above the solution of A and B would be

$$P = P_A x_A + P_B x_B \quad \text{Eq(8.11)}$$

Given that, the sum of the mole fractions is equal to one

$$P = P_A(1 - x_B) + P_B x_B = P_A + (P_B - P_A)x_B \quad \text{Eq(8.12)}$$

This is a linear function of the mole fraction x_B.

Since vapor pressure of each solvent in the blend is different, as summarized in Table 8.4 for the investigated solvents, the composition of the solvents that evaporate is distinct from that of the initial solvent blend. Therefore, the partial vapor pressures change continuously as solvent evaporates from a mixture.

	Boiling Point (°C)	**Vapor pressure at 20°C (Pa)**
Water	100	2338
Ethanol	78	5950

Table 8.4: Water and ethanol chemical physical properties

However, when the cohesive forces between like molecules are greater than the adhesive forces between dissimilar molecules, the dissimilarities of polarity cause both components to escape solution more easily. Therefore, the vapor pressure is greater than expected from the Raoult's law, showing positive deviation. If the deviation is large, then the vapor pressure curve shows a maximum at a particular composition and form a positive azeotrope. This is the case of water and ethanol mixture.

Mixtures of ethanol and water form an azeotrope at about 89 mole% ethanol [125], i.e. a mixture of 95.6 wt% ethanol at normal pressure, which boils at 78 °C. This azeotropic composition is strongly temperature and pressure dependent and vanishes at temperatures below 30 °C [126].

The lifetime of the solutions decreases as the concentration of ethanol is increased, since the evaporation starts before. This evidence finds a further proof when comparing the percentage of weight loss evaluated at the beginning of the isothermal region, as reported in Figure 8.18. Consistently the amount of evaporated solvent is higher in hydro alcoholic solutions.

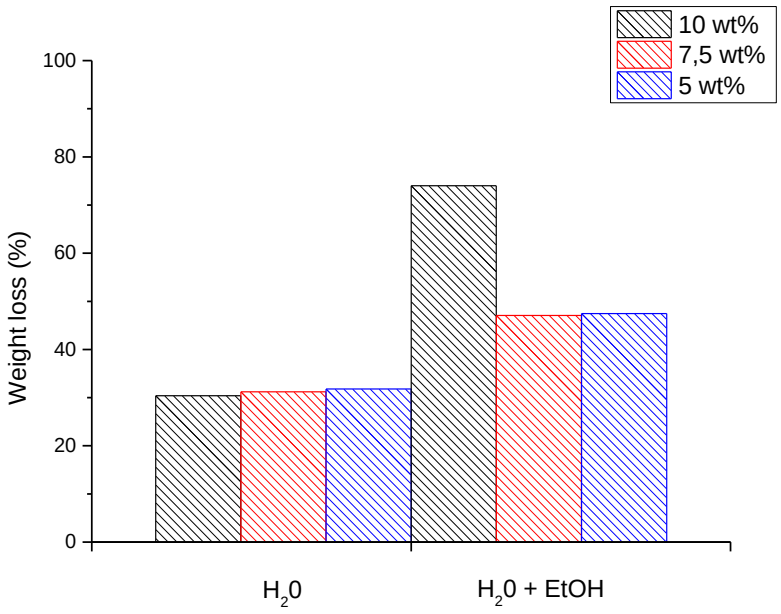

Figure 8.18: Comparison of weight loss at the beginning of the isothermal phase of the TGA

The solvent evaporation rate of each solution was estimated by fitting the respective thermogravimetric curve in the isothermal region, as clarified in Figure 8.19, where the red line overlapped to the thermogravimetric curve represents the linear fitting on the 10 wt% aqueous solution, and by multiplying the measured slope of the straight line by the area of the pan, having a diameter of 10mm.

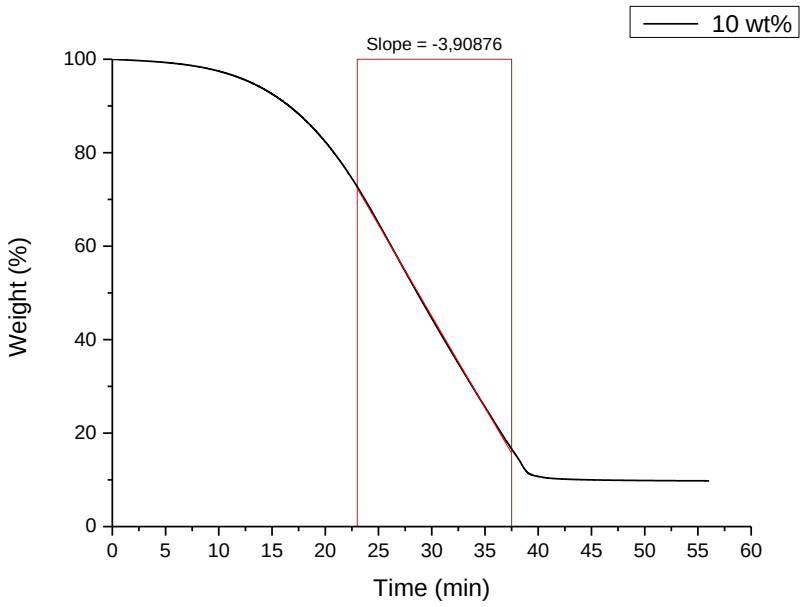

Figure 8.19: Fitting of the thermogravimetric curve

The obtained evaporation rate values are reported in Figure 8.20. As it is possible to note the presence of ethanol deeply influences the parameter under investigation.

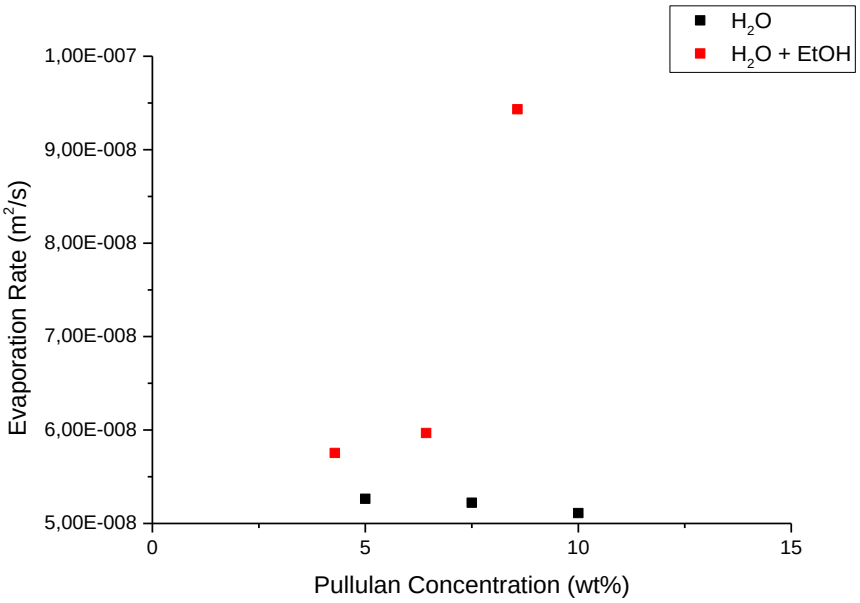

Figure 8.20: Evaporation rate versus Pullulan concentration

PART IV

Pullulan solutions spray drying

Chapter 9

9.1 SPRAY DRYING

Spray drying aims at engineering a particle and formulating it in a single step. As examined in depth in Chapter 3, this process consists of the atomization of the feedstock and the drying of droplet by the contacting of the spray with heated air. The atomization stage is designed to create the optimum conditions for evaporation and to lead to a dried product having the desired characteristics.

Experiments were carried out using a ForMate Spray Dryer 4M8 (ProCepT Processing Concept, Zelzate, Belgium). The instrument is sketched in Figure 9.1, where the red line indicates the path of the feed, while the blue one represents the supplied air. The technical specifications are reported in Appendix A.

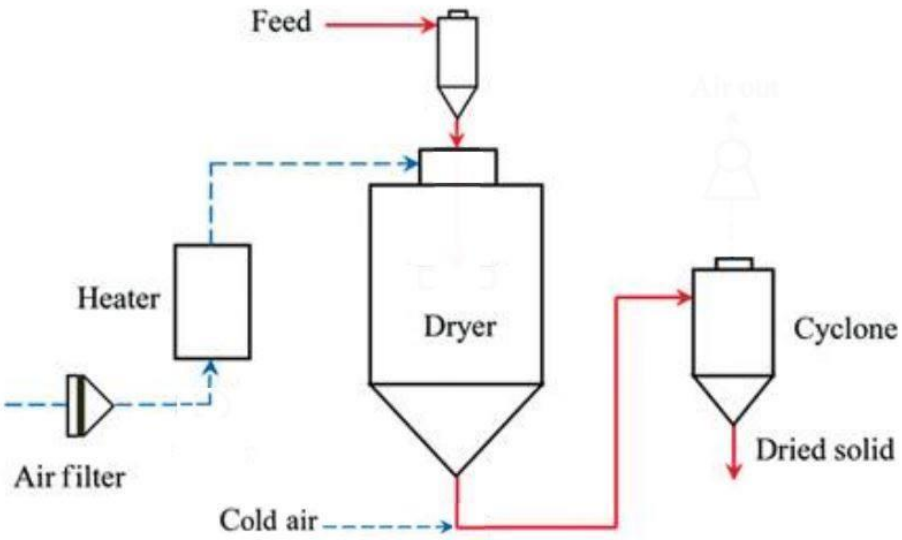

Figure 9.1: ForMate Spray Dryer 4M8 schematization

The instrument is an open cycle dryer, thus drying air is drawn from the atmosphere, heated, conveyed through the chamber and then exhausted to the atmosphere, and works in a single stage configuration, so the moisture is reduced to the target level in a single pass through the spray chamber.

The device operates with a laminar and concurrent flow, i.e. no turbulences are present in the chamber and sprayed product and hot gas have the same flow direction. In this arrangement, the atomized droplets entering the dryer are in contact with the hot inlet air, but their temperature is kept low due to a high rate of evaporation taking place and is approximately at the wet bulb temperature. The wet bulb temperature is the temperature a parcel of air would have if it were cooled to saturation by the evaporation of water into it, with the latent heat being supplied by the parcel. The removal of latent heat of vaporization from the air cools it. Thus, this phenomenon is

termed as evaporative cooling. This allows the particle to be maintained at a temperature below the outlet temperature of the drying air.

The contact time of the hot air with the spray droplets is very short, during which drying is achieved, and the air temperature drops instantaneously. To increase the residence time of particles, in order to assure a complete drying, a long chamber configuration, characterized by high height to diameter aspect ratios, was chosen. The cold air, in turn, pneumatically conveys the dried particles through the system.

Regarding the feed, it was loaded using a 5mL syringe and then pushed by a volumetric pump into the atomizing system, a two fluid nozzle, which utilizes the energy of compressed air to break up the liquid stream into droplets. The nozzle has a complete tips set, with orifice sizes ranging from 0.15mm to 1.2mm.

The two fluid nozzle has some advantages:

- Is capable of handling highly viscous feed;
- Produces much finer and more homogeneous spray when compared to pressure nozzles;
- Exerts better control over the droplet size.

But also limitations:

- Exhibits an higher tendency to clog;
- The requirement of compressed air adds to the cost of operation;
- The use of this atomizer introduces extra cold air into the spray chamber in the zone of atomization and, hence, reduces the temperature gradient that exists between the finely divided droplet and the surrounding drying medium. This impairs the effectiveness of heat transfer between the droplet and hot drying medium.

All sprayed solutions and utilized nozzle diameters are reported in Table 9.1.

		H_2O			H_2O + EtOH		
		0.6 mm	1 mm	1.2 mm	0.6 mm	1 mm	1.2 mm
Nominal Concentration (wt%)	20		✓			✓	
	10		✓	✓		✓	✓
	7.5	✓	✓	✓	✓	✓	✓
	5		✓	✓		✓	✓
	1.5		✓			✓	
	0.5		✓			✓	

Table 9.1: Sprayed solutions and utilized nozzle diameters

The spray drying chamber has a conical bottom to facilitate the collection of the dried powder. Indeed, following completion of drying, the particles of product must be separated from the drying air. Primary separation is accomplished by the particles simply falling to the bottom of the chamber. However, a small fraction of the particles remains entrained with the air and must be recovered in separation equipment. Cyclones, bag filters, and electrostatic precipitators may be used for the final separation stage.

A cyclone separator is a stationary mechanical device that utilizes centrifugal force to separate the solid particles from a carrier gas. It consists of an upper cylindrical part, referred to as the barrel, and a lower conical part, referred to as the cone. The gas stream, loaded with solid particles, leaving the spray dryer enters tangentially at the top of the barrel and travels downward into the cone, forming an outer vortex. The increasing air velocity in the outer vortex exerts a centrifugal force on the particles, separating them from the gas stream. When the gas stream reaches the bottom of the cone, an inner vortex is created. Thus, the gas reverses its direction and exits out at the top as clean gas. The particulates fall into the collection chamber attached to the bottom of the cyclone.

Same preliminary tests were done in order to tune the setup and find the best balance between the parameters. In this way it was possible to optimize the instrument performance and the output quality and amount. The evaluated variables were:

- The pump speed;
- The inlet temperature;
- The nozzle pressure.

Analysing these factors in the range of interest was noticed that:

- Decreasing the pump speed, powder sticking to the dryer walls could be avoided;
- A too low inlet temperature value did not assure a complete particle drying while a too high caused a yield reduction;
- The nozzle pressure did not influence the process.

Therefore, taking into account the previous considerations, the chosen experimental conditions are reported in Table 9.2.

Process parameters	
Nozzle pressure	2 bar
Inlet temperature	140 °C
Air flow rate	0.3 $\frac{m^3}{min}$
Feed flow rate	3 $\frac{mL}{min}$
Pressure chamber	3 mBar
Pressure cyclone	71 mBar

Table 9.2: Spray drying process parameters

9.2 PARTICLE SIZE ANALYSIS

Obtained powders were analyzed with an AccuSizer AD (Particle Sizing Systems, Santa Barbara, CA, USA), a single particle optical sensing technique. The instrument consists of five subsystems, as illustrated in Figure 9.2,

- Autodiluter;
- Optical sensor;
- Pulse height analyzer.

The Autodiluter performs a continuous dilution of a concentrated suspension of particles during to their passage through the optical sensor. The pulse height analyzer module continuously monitors the pulse rate during Autodilution. When the particle concentration falls below the coincidence limit of the sensor, typically between 7500 and 12000 particles/cc for particles smaller than 100μm, the pulse height analyzer unit begins collecting data.

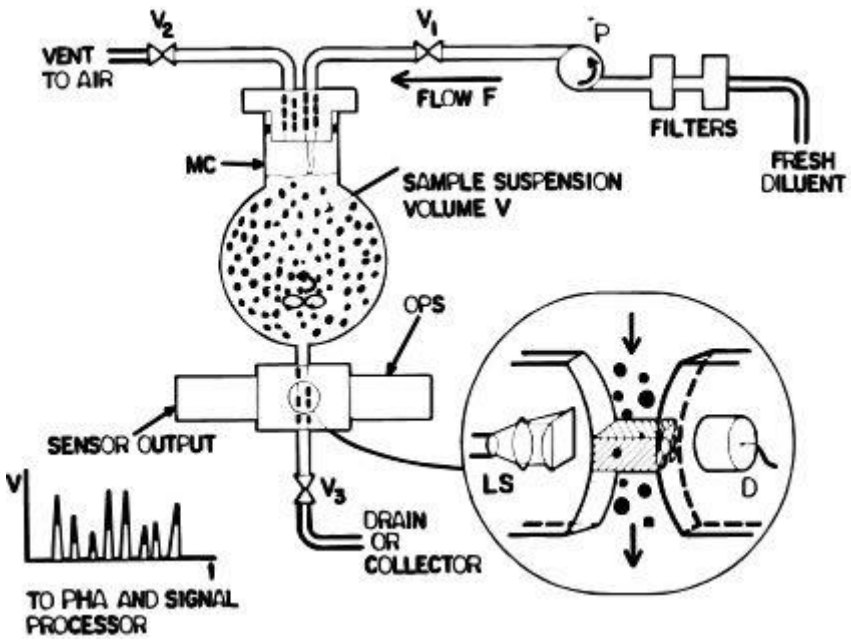

Figure 9.2: AccuSizer AD instrument system design

Because the Autodiluter was not used, it was important to dilute the sample before starting the analysis. Methanol was chosen as dispersing agent because of its characteristics:

- It is not a solvent for Pullulan;
- It is transparent at the light wavelength used for the measurement;
- It has a refractive index different from that of Pullulan.

Thus, a dispersion was prepared introducing approximately 1.25mg of powder into a clean sample cup using a sterile pipette and then adding 1mL of anhydrous methanol, filtered with a nylon strainer characterized by a nominal porosity of 0.2μm, employing a Gilson micropipette. A small amount of this liquid suspension was manually injected into the mixing chamber, consisting of a

dilution chamber automatically filled with filtered methanol. The sample particles were mixed with diluent in the mixing chamber by means of a magnetic stirrer.

The chosen experimental setup is reported in Table 9.3.

Experimental setup	
Vessel fluid volume	30mL
Injection volume	500μL
Detection time	10s

Table 9.3: AccuSizer AD experimental setup

Measurement of the diluted sample starts by gravity drain. Particles in liquid suspension flow through a small photo zone, a narrow slab like region of uniform illumination, produced by light from a laser diode. The particle suspension is sufficiently dilute when the particles pass, one at a time, through the illuminated region, avoiding overlapping.

The passage of a particle through the sensing zone causes a detected pulse, the magnitude of which depends on the mean diameter of the particle and the physical principle of detection, light scattering or obscuration (blockage). The extinction mode uses only light extinction to produce a signal from a lower to upper size limit. Typically, on a LE400-05 sensor this range is from 1 to 400 microns. The summation mode, the chosen one, uses a second detector in a patented configuration to extend the lower size limit by combining with the extinction signal a forward angle light scattering signal. In the case of the LE400-05 sensor, this extends the lower size limit of the sensor to 0.5 microns.

The illumination/detection system in the sensor is designed to provide a monotonic increase in pulse height with increasing particle diameter. The pulse height analyzer processes the signal pulses produced by the optical particle sensor and digitizes the sensor signal every 1 μs, with 14 bit resolution. A particle size distribution is constructed one particle at a time, by comparing the detected pulse heights with a standard calibration curve, obtained from a set of uniform particles of known diameters.

The resulting particle size distribution is displayed in real time: absolute counts versus diameter for each diameter channel, 8 to 512, logarithmically spaced over the total size range covered by the optical sensor. Additional derived distributions, both differential and cumulative, based on number, area and volume weighting, are calculated from the measured population distribution.

Pullulan tends to adhere to the cell walls, coating the cell windows and interfering with the sizing capabilities of the sensor through ruining the optical path. Therefore, after every run is mandatory to flush the system and make sure that it returns to a clean baseline.

9.3 POWDER OBSERVATION

Samples were analyzed with Scanning Electron Microscopy with Energy Dispersive Spectroscopy (SEM-EDS) on an Environmental SEM Zeiss EVO 50 EP equipped with spectrometer Oxford INCA 200-Pentafet LZ4. The samples were mounted on a stub of metal with adhesive, coated with 40 - 60 nm of Gold and then observed in the microscope in high vacuum condition.

Chapter 10

10.1 SPRAY DRIED POWDERS

All the solutions were sprayed according to the experimental conditions discussed in the previous Chapter. At the end of the process, the powders obtained from aqueous solutions result to be stuck on the walls of the product collection vessel. This behavior is just the opposite of that of the powder formulated from hydro alcoholic solutions.

In this regard, spray drying of sugar rich foods is difficult due to the presence of high content of sugars and organic acids. These compounds exhibit sticky behaviour. Stickiness is a term used to describe the phenomena of cohesion between particles and adhesion among particles and apparatus walls in the spray drying process. Stickiness depends not only on the properties of materials but also on the value of the inlet variables selected in a spray drying system [127].

Fast evaporation in spray drying hinders the particle crystallization. The high content of residual water depresses the glass transition temperature T_g of the material below the product temperature T_p even at the exit of the dryer. This leads to the existence of a liquid like amorphous material, which results in inter particle cohesion and particle adhesion to the dryer surfaces. The higher the temperature difference, $\Delta T_{ag} = T_{air} - T_g$ or $\Delta T_{pg} = T_p - T_g$ or in short ΔT, the higher is the degree of stickiness. Thus if the T_g of feed is increased, the ΔT is reduced and consequently the stickiness is reduced. In addition, when cold air is introduced at the bottom of the dryer or the walls temperature is reduced, the ΔT is decreased resulting in a lower stickiness.

Since, T_g of particles is a function of moisture content [128], the drying performance becomes a factor affecting its stickiness. In turn, the drying performance depends on the inlet variables and the interaction between the drying air and droplet properties.

The lower residual water content of dry particles when ethanol is added in feed solution is in accordance with the thermogravimetric analysis results and all the argumentations of Section 8.3, where it was remarked that the amount of evaporated solvent is higher in hydro alcoholic solutions.

10.1.1 POWDERS MORPHOLOGY

The SEM images of the powders produced reveal the presence, together with shrivelled particles, of numerous large spherical particles, captured as either swollen by an inner pressure or exploded. The phenomenon of particle inflation is associated with the increased vapor pressure that is created inside the particle. As soon as the particle shell is formed, the temperature of the particle approaches that of the outlet drying gas temperature. If that temperature is above the boiling point of one of the solvents, then the pressure inside the particle will exceed external pressure and the particle may expand as the result of the pressure gradient [69].

Some samples are characterized by the coexistence of particles and fibrous structures. Stringing refers to a bad atomization that happens in highly evaporating systems. A fine spray with high specific area is dried at high temperatures and with high content of solids. Consequently particles are formed before the spray is completely developed, string like particles are formed and particle agglomeration occurs [75].

Taking into account the purpose of this experimental section, i.e. the manufacturing of Pullulan elongated particle, the morphology of the obtained powders is summarized in Table 10.1, where:

- P indicates the presence of particles;
- F denotes the existence of fiber like structures.

		H_2O			**H_2O + EtOH**		
		0.6 mm	1 mm	1.2 mm	0.6 mm	1 mm	1.2 mm
Nominal Concentration (wt%)	20		P			P + F	
	10		P	P		P + F	P
	7.5	P + F	P	P	P + F	P + F	P + F
	5		P + F	P + F		P	P + F
	1.5		P			P	
	0.5		P			P	

Table 10.1: Powders morphology

As evident in Table 10.1, the nozzle size influences the powders morphology in a limited way. Thus, further investigations were carried out only on samples obtained using the nozzle with a diameter of 1mm.

A comparison between the powders morphology of these samples is proposed in Figure 10.1, Figure 10.2, Figure 10.3 and Figure 10.4. Further SEM images are reported in Appendix C.

Nominal Concentration: 10wt%

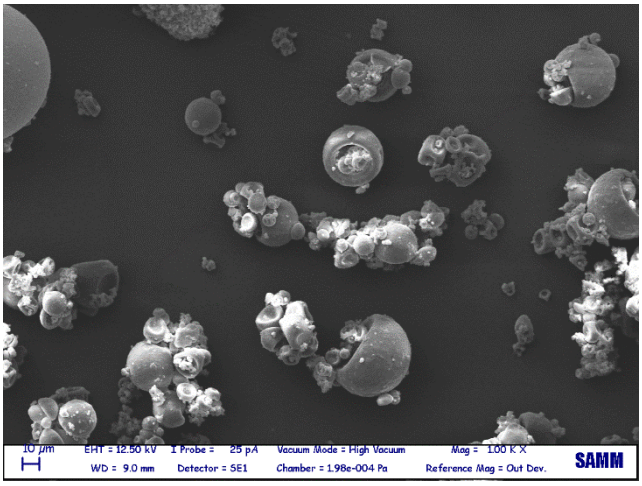

Nominal Concentration: 7.5wt%

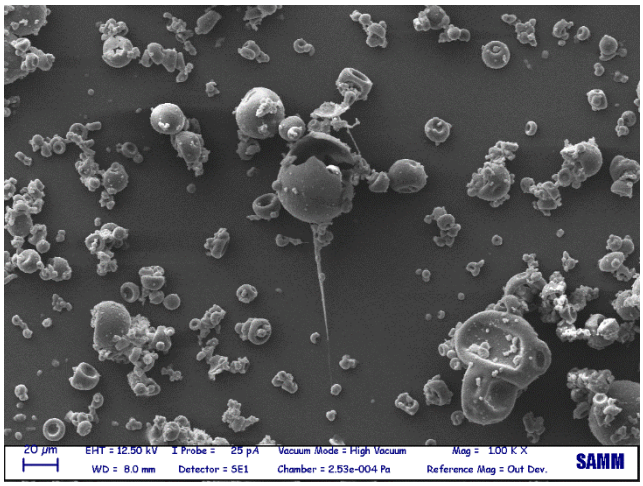

Nominal Concentration: 5wt%

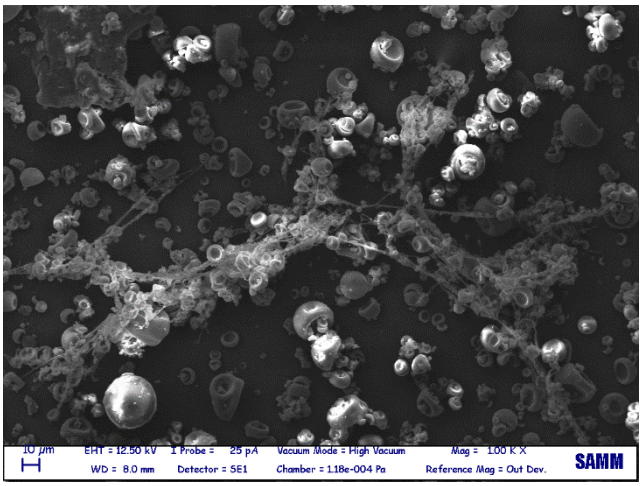

Nominal Concentration: 1.5wt%

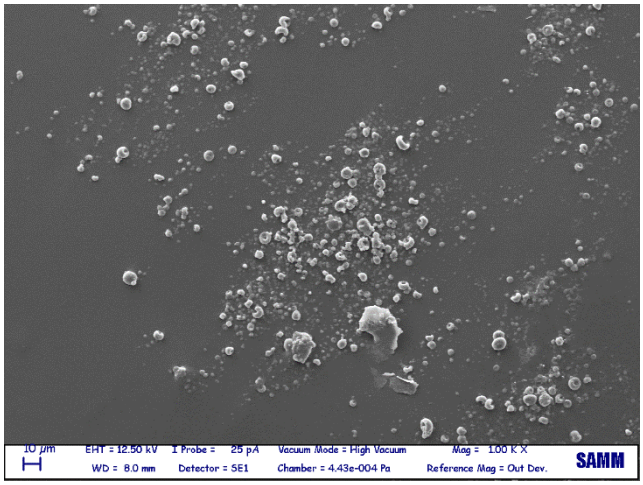

Nominal Concentration: 0.5wt%

Figure 10.1: Morphology of powders obtained from Pullulan aqueous solutions at different concentration using the nozzle with a diameter of 1mm
Magnification: 1kx

Nominal Concentration: 20wt%

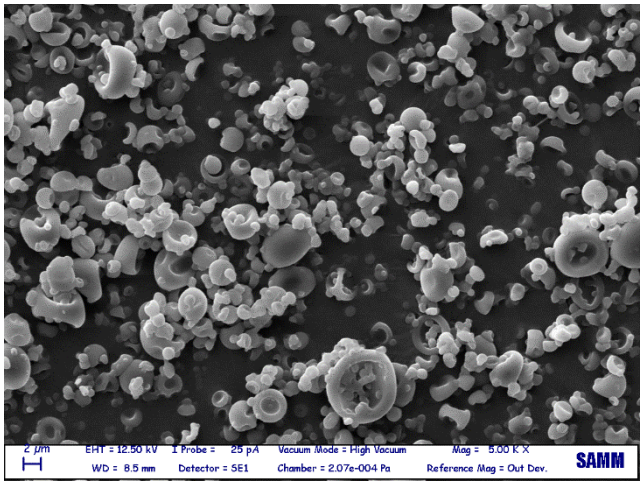

Nominal Concentration: 10wt%

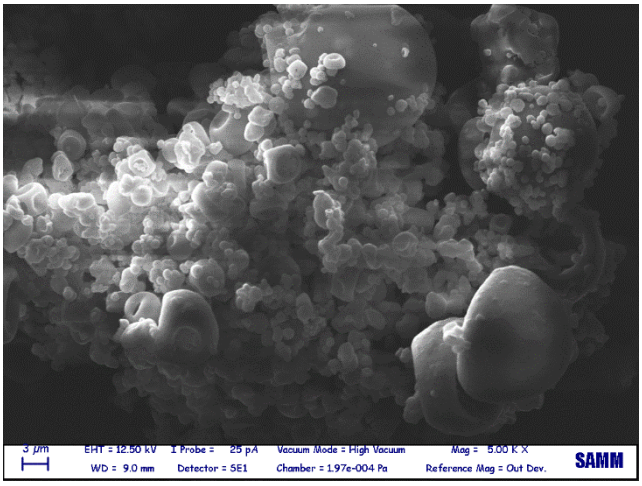

Nominal Concentration: 7.5wt%

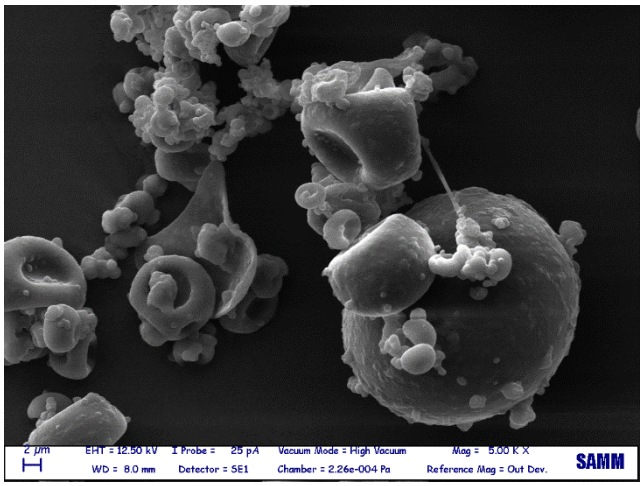

Nominal Concentration: 5wt%

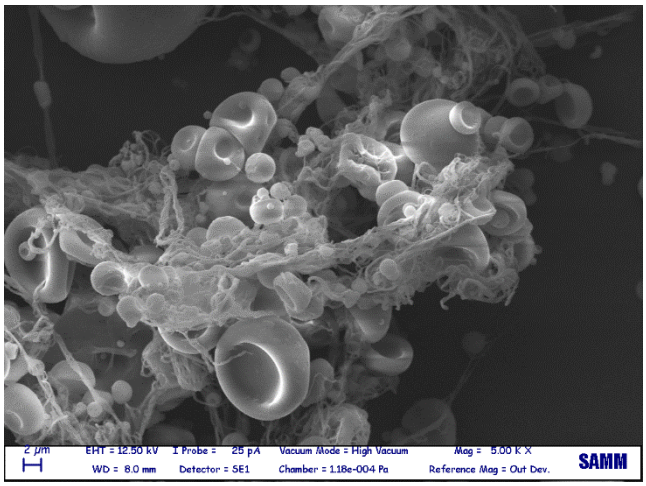

Nominal Concentration: 1.5wt%

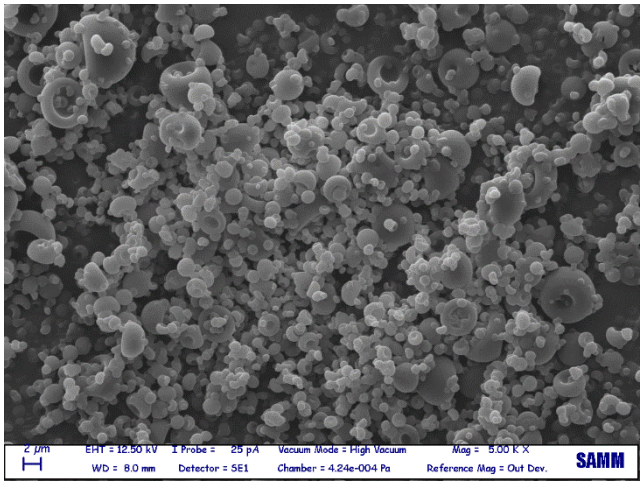

Nominal Concentration: 0.5wt%

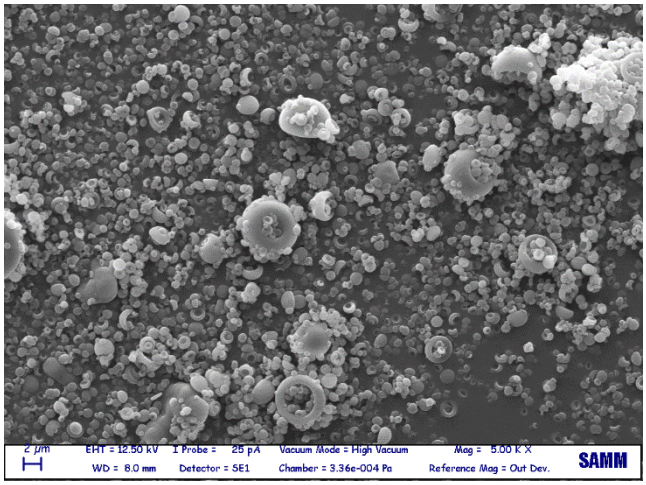

Figure 10.2: Morphology of powders obtained from Pullulan aqueous solutions at different concentration using the nozzle with a diameter of 1mm
Magnification: 5kx

Nominal Concentration: 20wt%

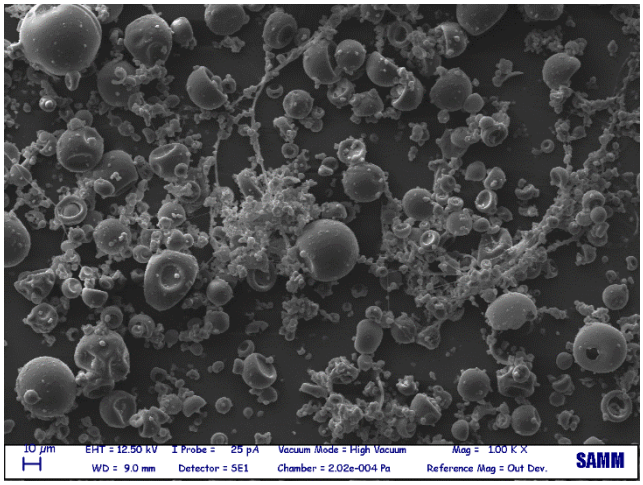

Nominal Concentration: 10wt%

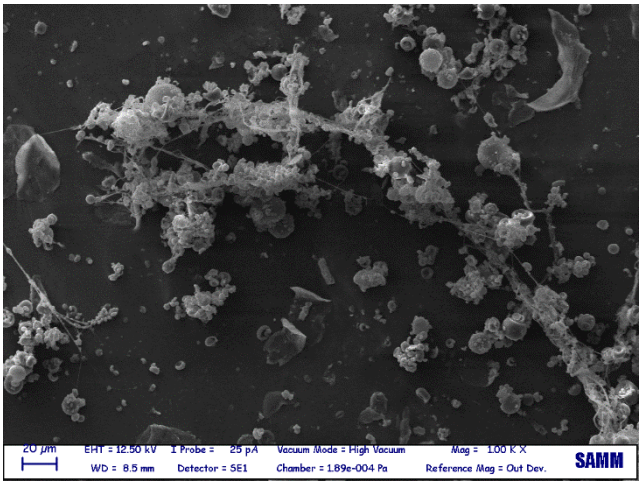

Nominal Concentration: 7.5wt%

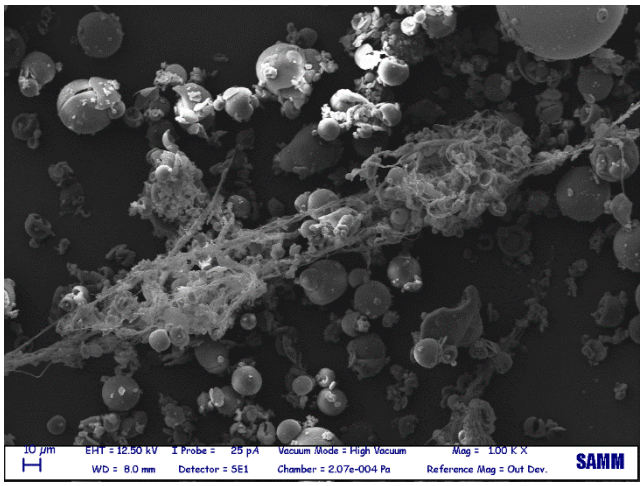

Nominal Concentration: 5wt%

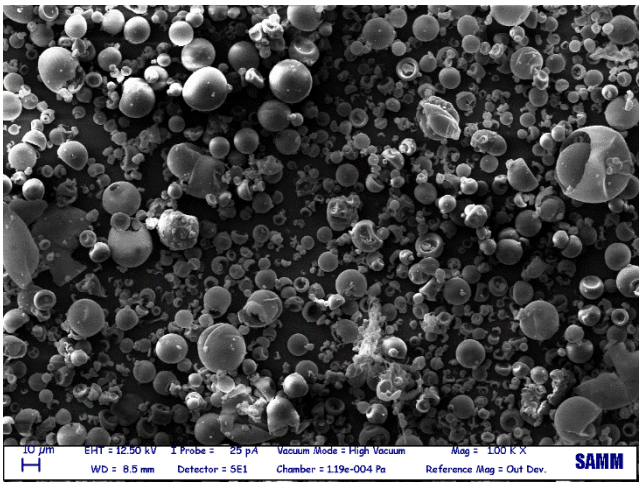

Nominal Concentration: 1.5wt%

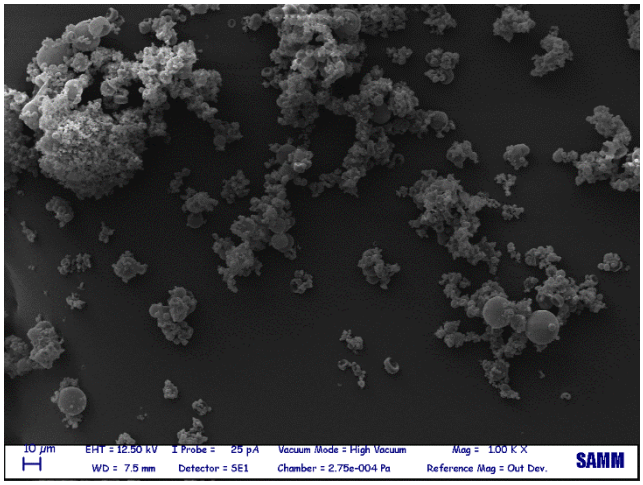

Nominal Concentration: 0.5wt%

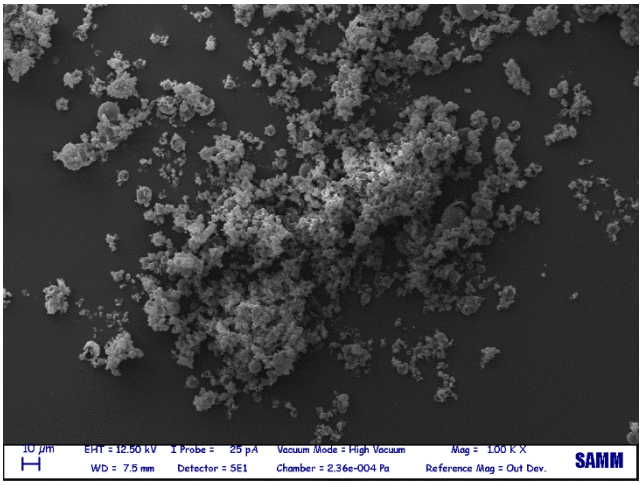

Figure 10.3: Morphology of powders obtained from Pullulan hydro alcoholic solutions at different concentration using the nozzle with a diameter of 1mm
Magnification: 1kx

Nominal Concentration: 20wt%

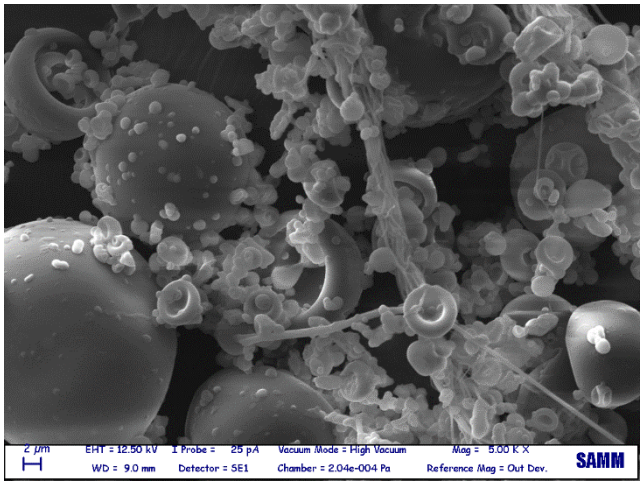

Nominal Concentration: 10wt%

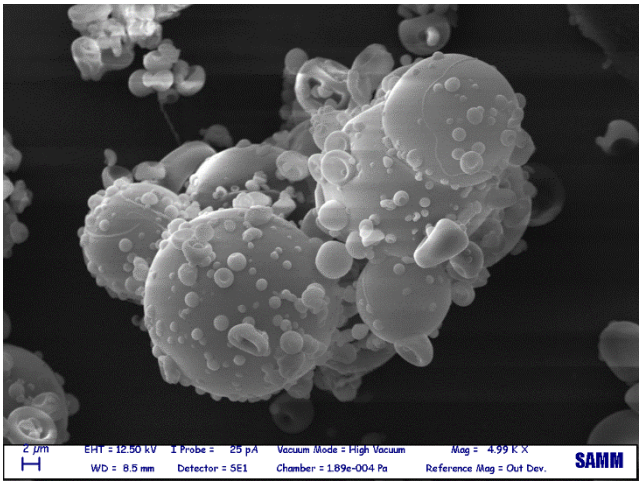

Nominal Concentration: 7.5wt%

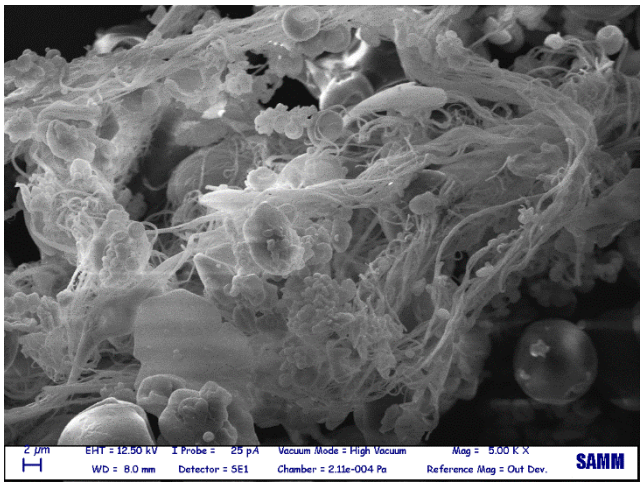

Nominal Concentration: 5wt%

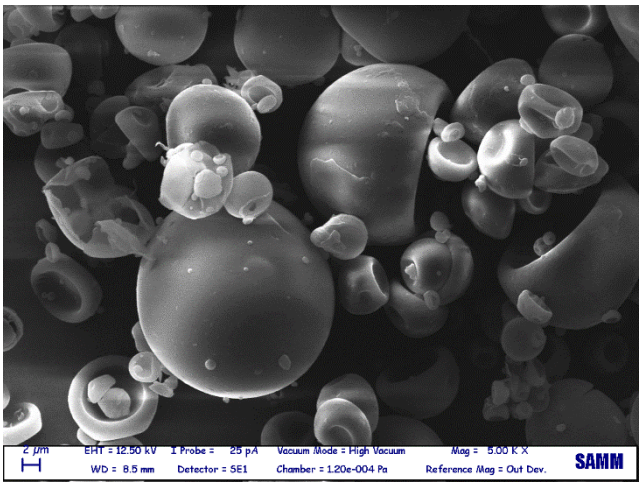

Nominal Concentration: 1.5wt%

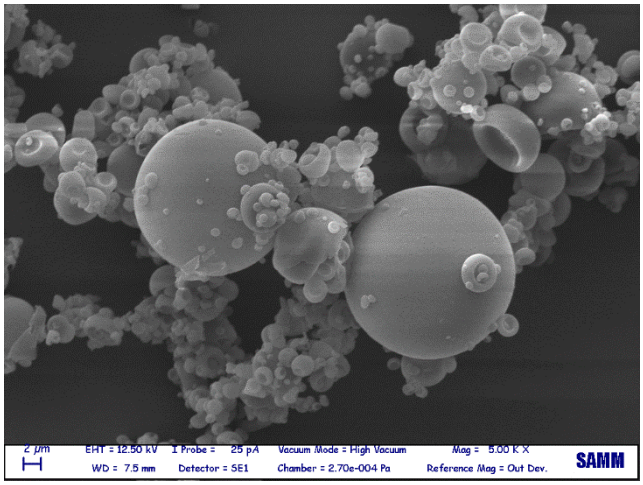

Nominal Concentration: 0.5wt%

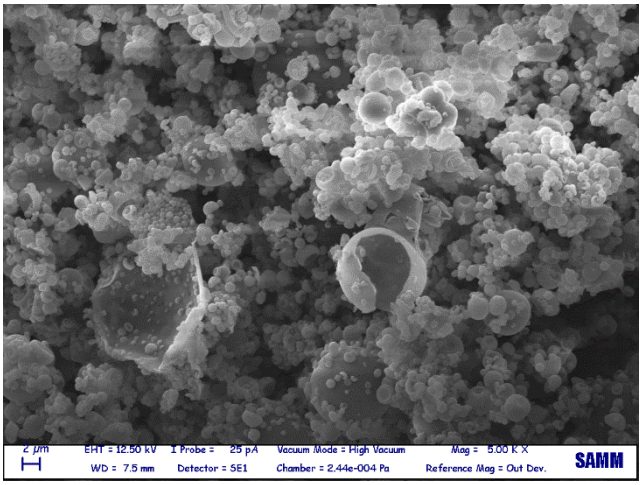

Figure 10.4: Morphology of powders obtained from Pullulan hydro alcoholic solutions at different concentration using the nozzle with a diameter of 1mm
Magnification: 5kx

10.1.2 PARTICLE SIZE

The particle size and shape can influence a large variety of important physical properties, manufacturing, processability and quality attributes, including:

- Dissolution rate;
- Powder flow properties;
- Packing properties;
- Mixing of powders.

The dissolution performance of matrix type controlled release capsules is highly influenced by excipients particle size [129]. Release enhancer percolation threshold, the critical porosity where the pore network just begins to span the whole matrix, is linearly correlated with filler particle size in matrix capsules. Percolation threshold increases when coarser drug particles are employed [130].

A reduction in particle size results in slower drug release [131]. Even if small particles dissolve more rapidly than large ones, lag time in matrix capsule designed for delayed delivery can increase with decreasing the particle size of channeling agent, as a consequence of the smaller pores formed by its dissolution. Large particles provide large channels in the matrix, facilitating the diffusion process of the drug toward the dissolution medium [132].

Assuming near saturation of the dissolved portion and a constant diffusion rate, when the diameter of channels is reduced, the flux through them must also be reduced. This fact is explained because of the smaller surface area through which the drug must diffuse. Therefore, the relationship between the drug diffusional path length and its effective dissolution area remains constant for a longer time, using smaller particle sizes, because of a more stable diffusion layer. As the particle size increases, the surface area exposed to the medium, and consequently the diffusion layer, is less stable and requires a more gradient concentration profile. Modulation of the lag time periods can be achieved by modifying the particle shape and size [133].

10.1.2.1 PARTICLE SIZE DISTRIBUTION

A spherical particle can be described using a single number, the diameter. Instead, non spherical particles should be represented using multiple length measures. Such a description provides greater accuracy, but it also adds greater complexity. Thus, techniques for the determination of particles size make the useful and convenient assumption that every particle may be approximated by a sphere. The reported value is not the direct measure of the geometric diameter, but rather an equivalent spherical diameter derived from the behavior of the particles in response to the probe used in the analysis. The reported diameters are often confused with geometric diameters, but are in fact equivalent diameters specific to the analytical technique.

10.1.2.1.1 REPRESENTATION OF RESULTS OF PARTICLE SIZE ANALYSIS

While it is tempting to use a single number to represent a particle size distribution, and thus the product specification, this is typically not a good idea. In nearly every case, a single data point cannot adequately describe a distribution of data points. This can easily lead to misunderstandings and provides no information about the width of the distribution.

A frequency distribution is an orderly arrangement of data classified according to the magnitude of the observations. A frequency distribution is determined when the data are grouped into classes of appropriate size indicating the number of observations in each class. Thus, frequency distribution indicates the percentage of particles existing within a specified particle size interval. A relative frequency distribution is a distribution in which relative frequencies are recorded for each class interval. Relative frequency of a class is the frequency obtained by dividing the number of particles in an interval, or class, by the total number of particles observed. Another important frequency distribution is the cumulative frequency distribution. In cumulative frequency distribution, the frequencies are shown in a cumulative manner. The cumulative frequency for each class interval is the frequency for that class interval added to the previous cumulative total. Cumulative frequency can also defined as the sum of all previous frequencies up to the current point. Indeed, cumulative distribution expresses the amounts of particles contained in the system that have a size below a specific value.

Median values are defined as the value below which half of the population resides. For particle size distributions, the median is called D50. D50 is the size, in μm, that splits the distribution with half above and half below this diameter. This value is one of the easier statistics to understand and also one of the most meaningful for particle size distributions.

The more common practice in analyzing distributions is to include other two significant information, which describe the coarsest and finest parts of the distribution. These are typically the D90 and D10. Using the same convention as the D50, the D90 describes the diameter below which 90% of particles can be observed. Instead, the D10 diameter indicates the size below which 10% of particles is grouped. A three point specification featuring the D10, D50, and D90 is considered complete and appropriate for most particulate materials.

Another important indicator is also the width of the distribution, which is determined as

$$Span = \frac{D_{90} - D_{10}}{D_{50}} \qquad \text{Eq(10.1)}$$

The span gives an idea of how far the 10% and 90% points are apart, normalized with respect to the midpoint. Therefore, it provides the basis to assess the homogeneity of the granules and their distribution in fractions of different sizes.

10.1.2.1.2 PARTICLE SIZE ANALYSER

In optical equivalent diameter where particles are probed by a light source, their scattering or absorption behavior is compared to that of a reference geometry, usually a homogeneous sphere. The geometric diameter of the reference sphere is only representative of the diameter of the sample particle if the optical properties of the sample are close to that of the reference. The optical particle size for these particles is in reality a function of their geometric diameter and their secondary morphological features.

The shapes of particles normally generated by spray drying processes are such that the spherical assumption is generally acceptable, even if not very accurate. Problems can arise, however, if the individual particles have a very large aspect ratio, such as fibers or needles.

The particle size analysis was carried on the powders obtained from both aqueous and hydro alcoholic solutions at different concentration using the nozzle with a diameter of 1mm. For each sample, the counted particles during the analysis were about 73000. While the number distribution curves are displayed in Appendix D, the evaluated percentiles are shown in Figure 10.5 and Figure 10.6.

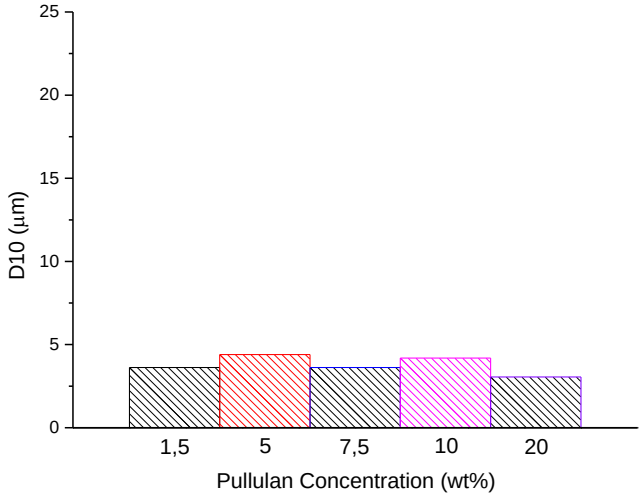

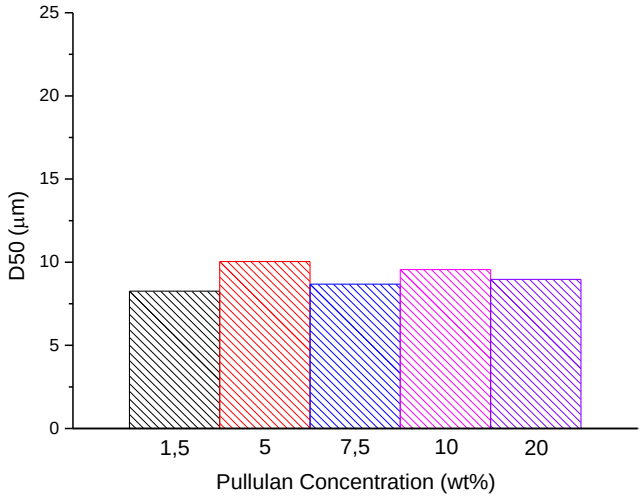

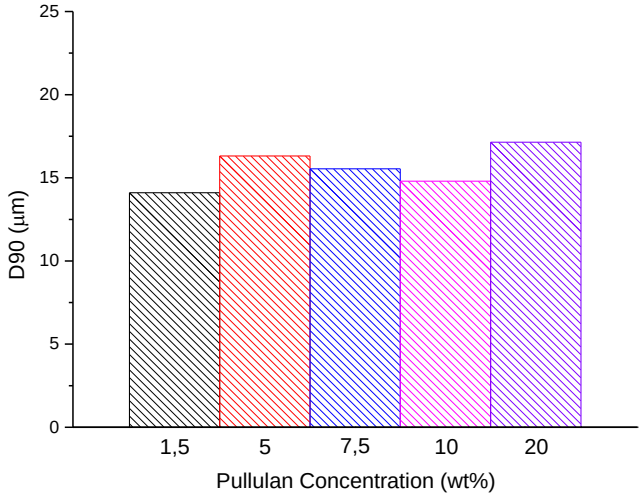

Figure 10.5: D10, D50, and D90 of powders obtained from Pullulan aqueous solutions at different concentrations measured by particle size analyser

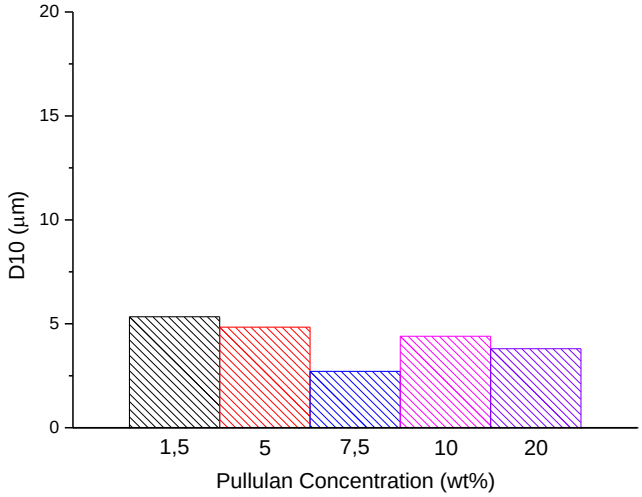

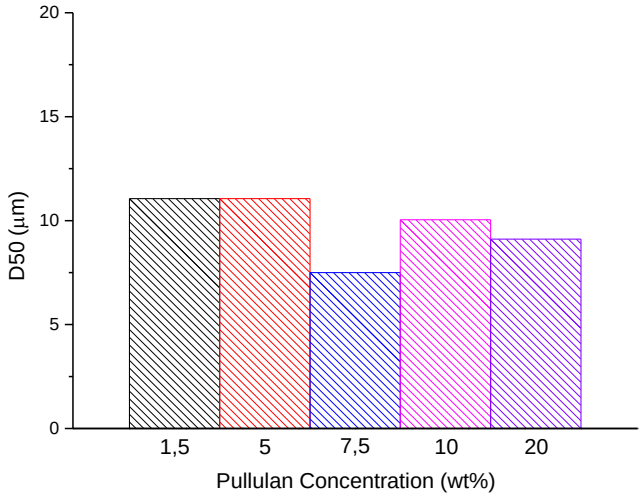

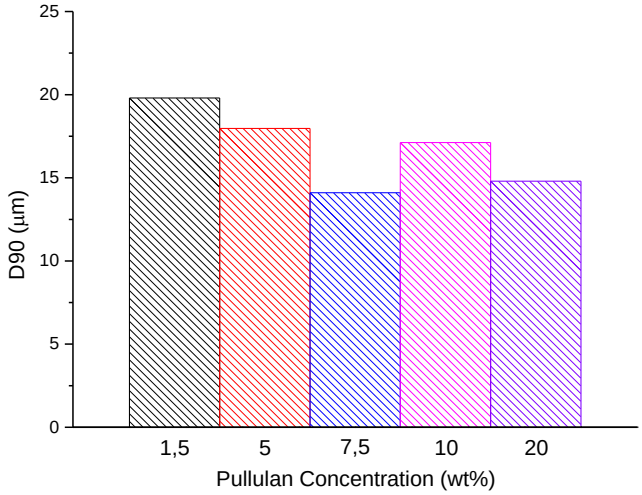

Figure 10.6: D10, D50, and D90 of powders obtained from Pullulan hydro alcoholic solutions at different concentrations measured by particle size analyser

Taking into account the limits of the analysis, it seems that there is not an evident correlation between the solution initial concentration and the diameters of the obtained particles, especially in the case of aqueous solutions. These particles have a rather narrow particle size distribution, as it is possible to ascertain considering the span values represented in Figure 10.7 and Figure 10.8.

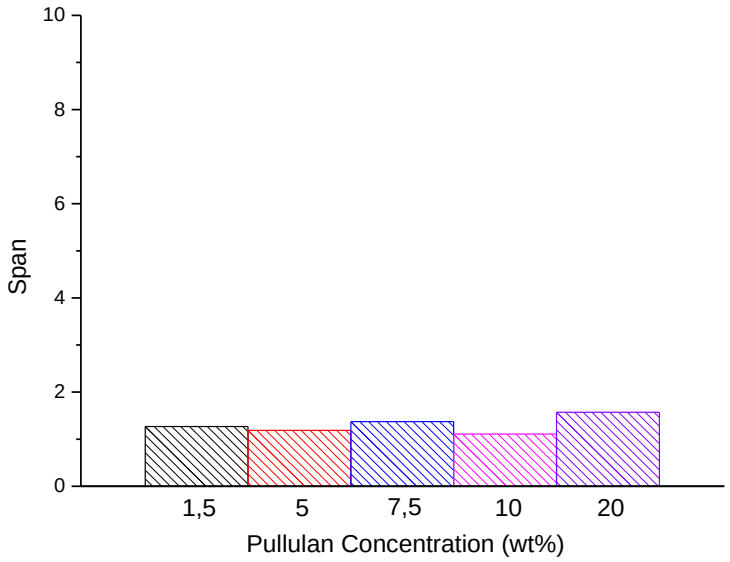

Figure 10.7: Span of powders obtained from Pullulan aqueous solutions at different concentrations measured by particle size analyser

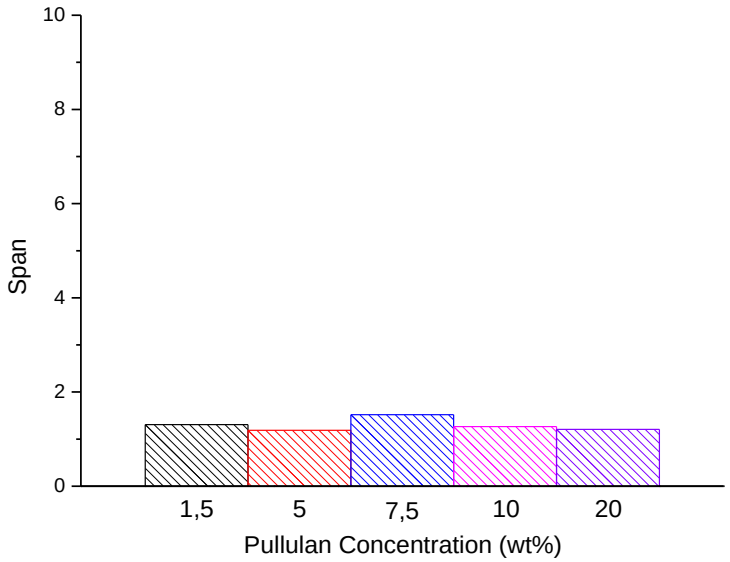

Figure 10.8: Span of powders obtained from Pullulan hydro alcoholic solutions at different concentrations measured by particle size analyser

10.1.2.1.3 IMAGE ANALYSIS

With few exceptions, spray dried particles are spherical and their size can be described by their geometric diameter. The geometric diameter is also often used as a reference, because it is in principle directly accessible by microscopic techniques. However, the measurement of geometric diameters by image analysis is not without difficulties. One is rarely interested in the size of just a single particle, but rather the size distribution of all particles in a product. This information can be obtained by image analysis of a sample of the dose, but care has to be taken to ensure that a representative, statistically relevant sample is analyzed.

The image analysis was performed on the same powders analyzed through the particle size technique. It is important to underline that in this investigation fibers were not considered, while they were in the automatic particle size analysis. Particles were approximated by an ellipse, as illustrated in Figure 10.9, and the major and minor axis were measured. In most cases, the aspect ratio between the two axes was nearly equal to 1. This is an evidence that, although some bumps are clearly visible from SEM images on their surface, the particles have a reasonably spherical shape. Therefore, only the major axis was taken into account as reference dimension. For each sample, the counted particles were about 150. While the number distribution curves are displayed in Appendix D, the evaluated percentiles are shown in Figure 10.10 and Figure 10.11.

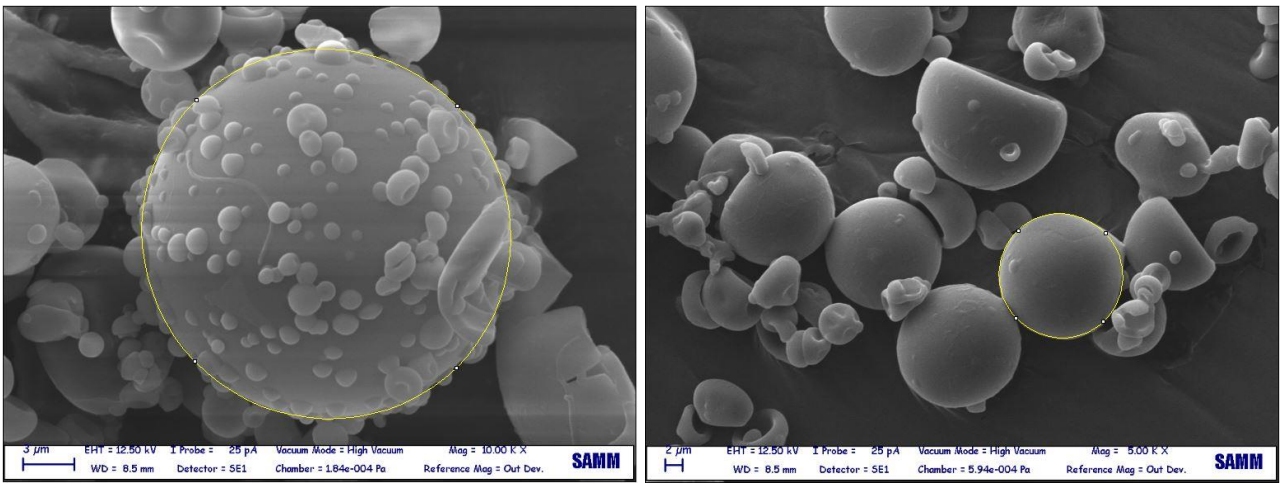

Figure 10.9: Particle size analysis
Morphology of powder obtained from 10 wt% Pullulan hydro alcoholic solution
using the nozzle with a diameter of 1mm (on the left)
Magnification: 10kx
Morphology of powder obtained from 5 wt% Pullulan hydro alcoholic solutions
using the nozzle with a diameter of 1.2mm (on the right)
Magnification:5kx

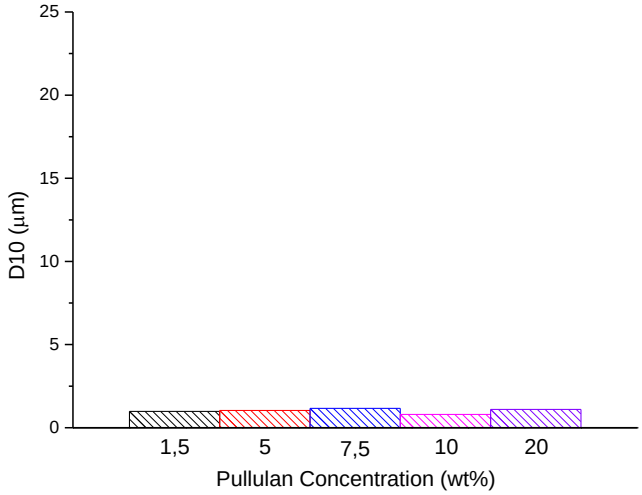

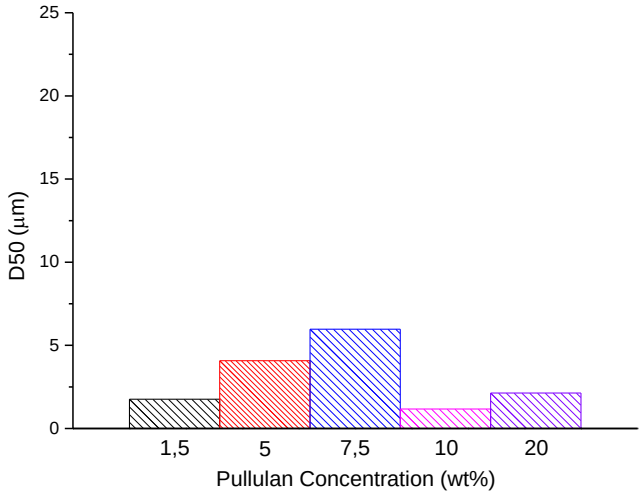

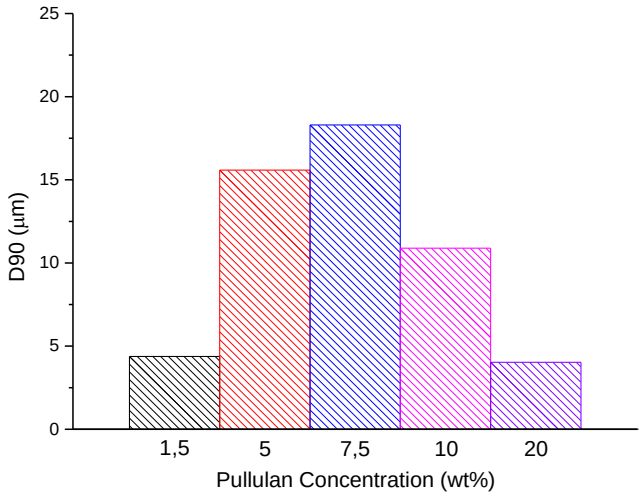

Figure 10.10: D10, D50, and D90 of powders obtained from Pullulan aqueous solutions at different concentrations measured by image analysis

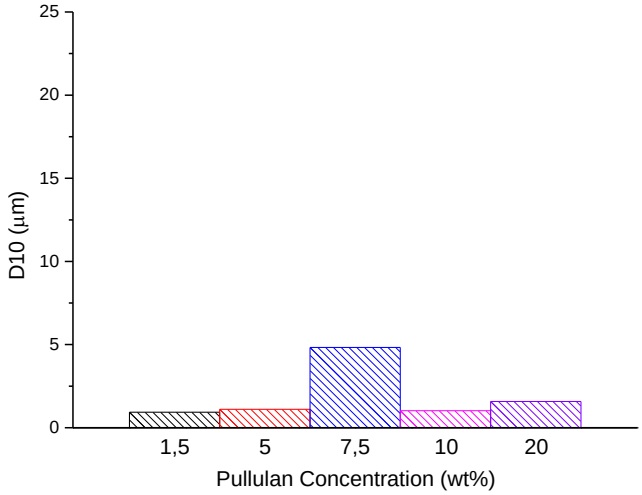

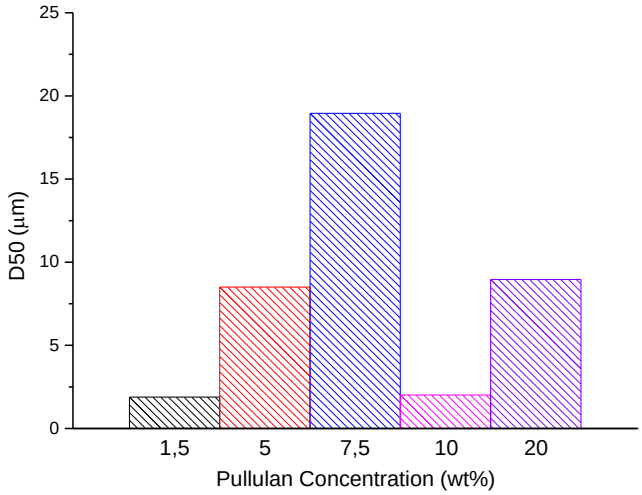

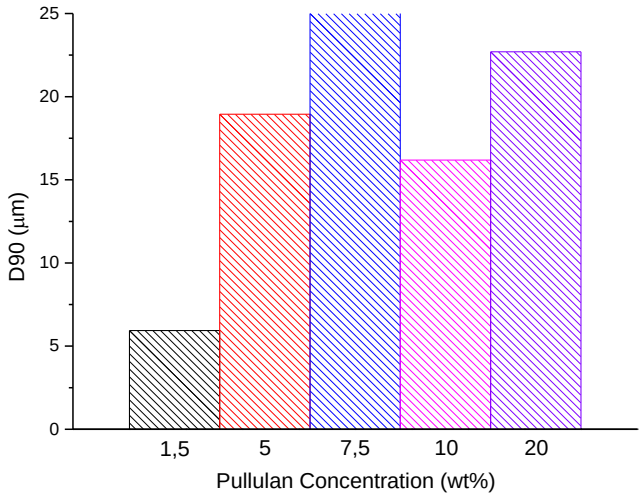

Figure 10.11: D10, D50, and D90 of powders obtained from Pullulan hydro alcoholic solutions at different concentrations measured by image analysis

Contrary to what emerge from the results of particle size analyser, correlation between the solution initial concentration and the diameters of the obtained particles may be observed. This is probably related with the fact that the image analysis technique allows to appropriately take into account the shape of the particles, not considering the fibers. Moreover, the particle size distribution seems to be broader, as it is possible to verify considering the span values represented in Figure 10.12 and Figure 10.13, especially when the sample relative to both the 10 wt% solution is considered.

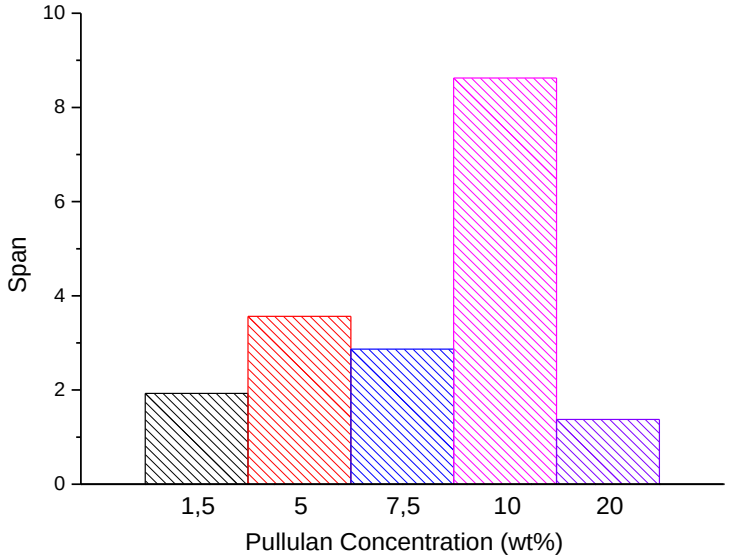

Figure 10.12: Span of powders obtained from Pullulan aqueous solutions at different concentrations measured by image analysis

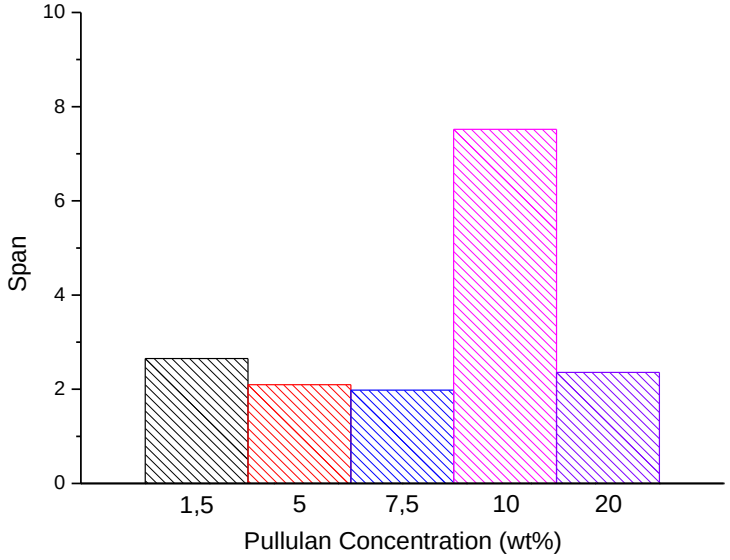

Figure 0.13: Span of powders obtained from Pullulan hydro alcoholic solutions at different concentrations measured by image analysis

10.1.2.1.4 COMPARISON BETWEEN THE PARTICLE SIZE ANALYSER AND THE IMAGE ANALYSIS RESULTS

The task of setting a particle size specification for a material requires knowledge of which technique will be used for the analysis and how size affects product performance. Sources of error must be investigated and incorporated into the final specification. Be aware that, in general, different particle sizing techniques will produce different results for a variety of reasons including:

- The physical property being measured;
- The algorithm used;
- The basis of the distribution (number, volume, etc.);
- The dynamic range of the instrument.

Therefore, a specification based on using laser diffraction is not easily compared to measurements from other techniques such as particle counting or sieving. Nevertheless, a comparison between the D10, D50 and D90 values from the two techniques used in the present work is proposed in Figure 10.14.

As expected, differences are noticeable. However, taking into account the way through which the measurements are carried out by the two techniques, data obtained from image analysis are in our opinion more reliable. This is due especially to the fact that, since the analysis was not done in an automated manner, the information that can be deduced are surely concerning the particles and not the fibres or fibres/particles aggregates.

Obviously is possible to note a higher data dispersion as compared to the one obtained from the particle size analyser, which can be ascribed to the significant difference in the number of the analysed particles. Moreover, it should be considered that the image analysis was made possible thanks to SEM images, which were taken observing the powder placed on just one stub, for each sample. Therefore, only a relatively small portion of the powder was investigated. Furthermore, the images were taken with the intent to assess the presence of the fibres, the original aim of the project. Thus, at the moment of sampling, no great attention was paid to choose a large sample. As a consequence, the images available are relatively few and not all images allow to distinguish clearly the particle shapes.

For sure, the comparison between the two techniques highlights the significant difference in the case of the powders from hydro alcoholic solution with a nominal Pullulan concentration of 7.5 wt%. Looking at the images this sample is characterized by the presence of big swollen particles and a great amount of fibres noodles.

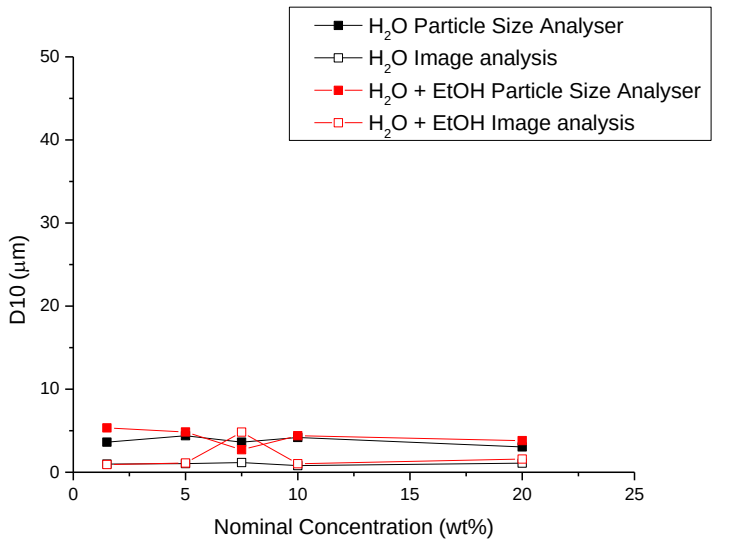

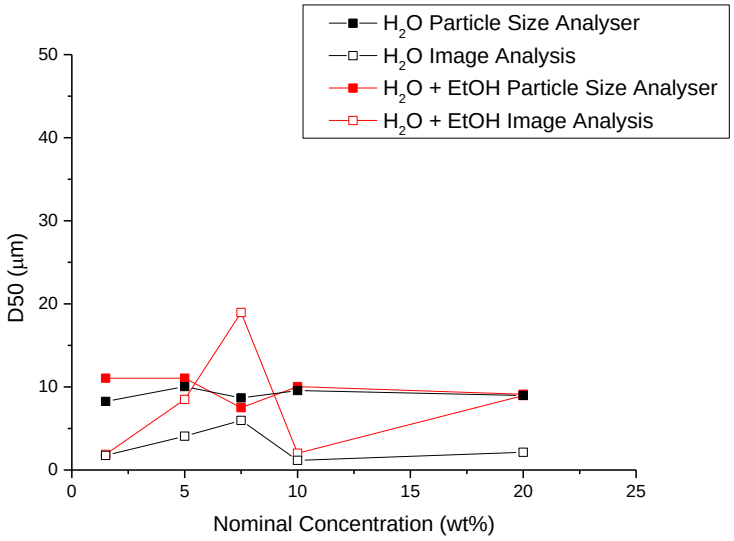

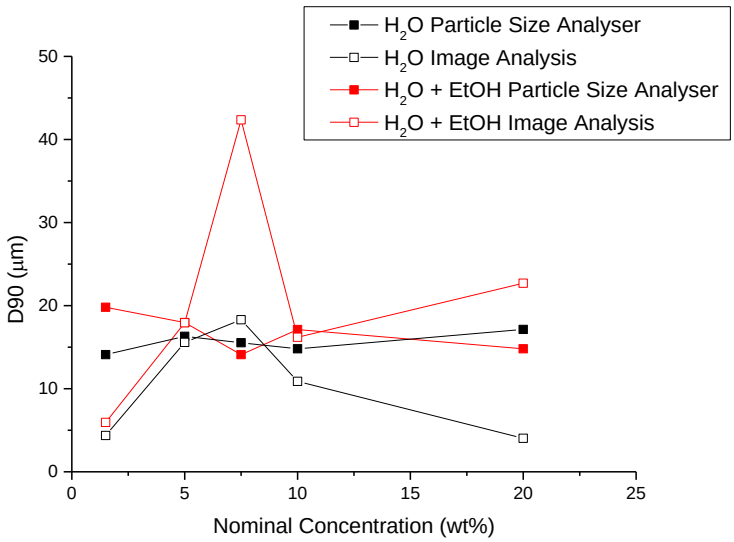

Figure 10.14: Comparison between the D10, D50 and D90 measured by the different techniques

10.1.2.2 SAUTER MEAN DIAMETER

Another approach to characterize the particles size distribution is considering a specific average value, the Sauter mean diameter. The Sauter mean diameter of a collection of spherical objects of different diameters is equal to the diameter of identical spherical objects forming an equivalent collection of spheres. The systems have different number of spherical objects, identical total surface area, and identical total volume.

Therefore, the Sauter mean diameter is also called the surface volume mean, D_{32}, which means that the average of particulate matter is calculated as the volume to surface ratio. The D_{32} is the diameter of a droplet having the same volume to surface area ratio as the total volume of all the droplets to the total surface area of all the droplets [134]. Thus, the Sauter mean diameter is defined as

$$D_{32} = \frac{\int_{2r_{min}}^{2r_{max}} (2r)^3 q(2r) d(2r)}{\int_{2r_{min}}^{2r_{max}} (2r)^2 q(2r) d(2r)} \qquad \text{Eq(10.2)}$$

where

- $2r_{max}$ represents the maximum value of diameter of the frequency curve $q(2r)$;
- $2r_{min}$ represents the minimum value of diameter of the frequency curve $q(2r)$

For the particulate matter characterized by size fractions, the Sauter mean diameter can be calculated using formula:

$$D_{32} = \frac{\sum_{i=1}^{n} n_i d_i^3}{\sum_{i=1}^{n} n_i d_i^2} \qquad \text{Eq(10.3)}$$

where

- n_i is the number of particulate matter in a particulate size fraction;
- d_i is the diameter of particulate matter in a particulate size fraction.

Therefore, using equation (10.3), the Sauter mean diameter of the powders was calculated taking into account the data obtained from both particle size analyser and image analysis. The results are shown in Figure 10.15 and Figure 10.16. As previously underlined in Section 10.1.2.1.4, differences are again noticeable between the obtained D_{32} values. Indeed, while in the first case it appears that the evaluated Sauter mean diameter is not influenced by the solution initial concentration, in second case, it emerges that there could be a correlation between the feed concentration and solvent and the powder characteristics. Thence, this is a further proof of the fact that the shape factor causes disagreements when particles are measured with different techniques.

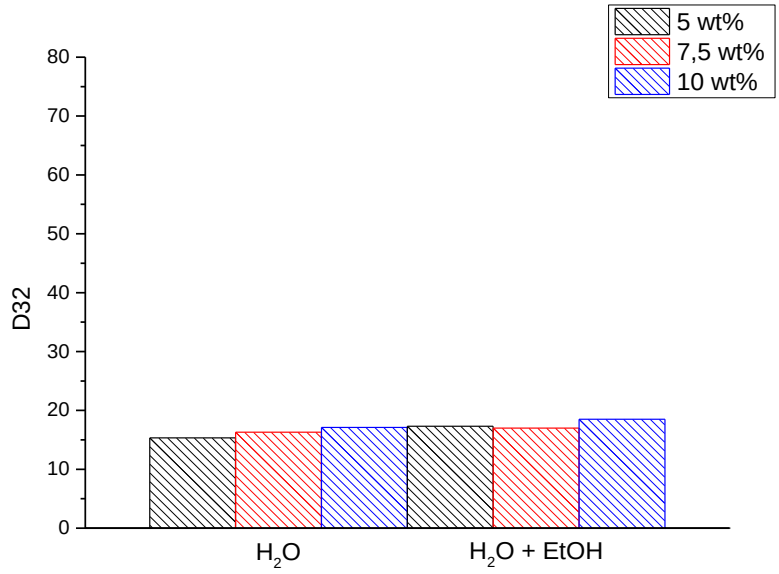

Figure 10.15: Sauter mean diameter of powders obtained from Pullulan solutions at different concentrations evaluated from particle size analyser data

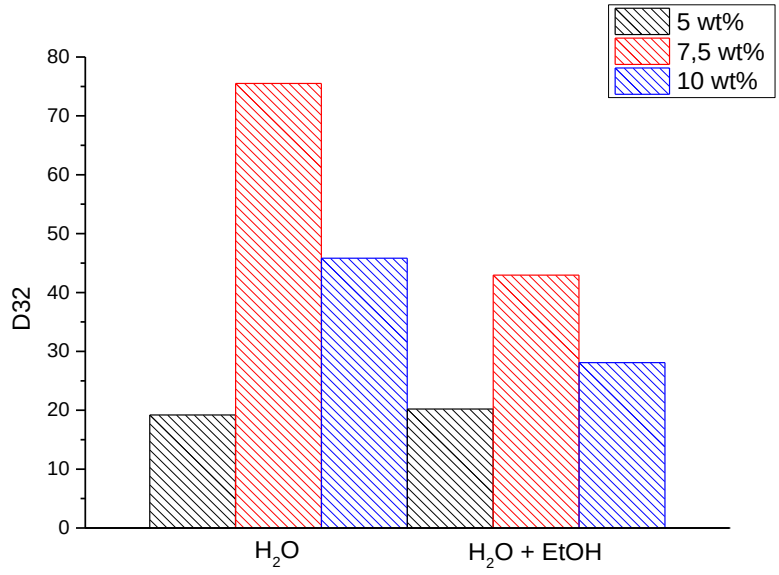

Figure 10.16: Sauter mean diameter of powders obtained from Pullulan solutions at different concentrations evaluated from image analysis data

10.1.2.2.1 COMPARISON WITH SEMI EMPIRICAL EQUATION

In order to verify if it is possible to predict the Sauter mean diameter, the drop size relation formulated by Dombrowski and Johns [135], based on the analysis of the aerodynamic instability and disintegration of viscous sheets, was taken into consideration.

Considering a realistic case where the liquid has finite viscosity and where the thickness of the liquid sheet diminishes as it moves away from the orifice, a semi empirical equation for the approximation of the mean droplet size has been suggested according to equations

$$D_{32} = C_1(\delta_{sheet}x)^{\frac{1}{3}}\left(\frac{\sigma_{liq}}{\rho_{air}v_{rel\_sheet}^2}\right)^{\frac{1}{3}}\left(\frac{\rho_{liq}}{\rho_{air}}\right)^{\frac{1}{6}} \quad \text{Eq(10.4)}$$

$$D_{32} = C_1 d_{orifice}\left(\frac{\chi_{sheet}\pi}{4We_{air}}\right)^{\frac{1}{3}}\left(\frac{\rho_{liq}}{\rho_{air}}\right)^{\frac{1}{6}} \quad \text{Eq(10.5)}$$

where

- C_1 is a constant between 1.2 and 1.7;
- δ_{sheet} is the liquid sheet thickness, which become thinner with increasing the distance from the nozzle outlet;
- x is the distance measured from the liquid orifice;
- v_{rel_sheet} is the difference between the velocity of the nozzle atomizing air and the liquid sheet, thus in practice close to v_{air} ;
- We_{air} is the air Weber number;
- χ_{sheet} is the liquid sheet coefficient.

The product of the liquid sheet thickness δ_{sheet} and the distance x measured from the liquid orifice is constant over a certain range of distances and is called the sheet thickness parameter defined as K_{sheet} , given by

$$K_{sheet} = \delta_{sheet}x \quad \text{Eq(10.6)}$$

In studies with nozzles having round liquid orifices, it is chosen to normalize K_{sheet} with respect to the round cross sectional area of the nozzle outlet. Hereby, the liquid sheet coefficient sheet is obtained according to equation

$$\chi_{sheet} = \frac{4\delta_{sheet}x}{\pi d_{orifice}^2} \quad \text{Eq(10.7)}$$

Therefore, the semi empirical equation (10.4) was used to calculate the Sauter mean diameter of the powders. However, due to the fact that a complete evaluation was not possible because of the lack of data, the results were normalized respect to the 10 wt% aqueous solution. This value was chosen arbitrarily.

The obtained Sauter mean diameters are represented in Figure 10.17. It appears that the D_{32} decreases in presence of ethanol, even if it is not influenced by the initial solutions concentration. This trend is not in agreement with the ones observed in Section 10.1.2.2, where the D_{32} was evaluated using its definition. This discrepancy can be explained by the fact that the theoretical model proposed by Dombrowski and Johns does not take into account the solution viscosity. However, as deeply investigated in Section 3.1.2, this parameter plays a crucial role during the atomization process. Hence, due to its relevance, it cannot be neglected.

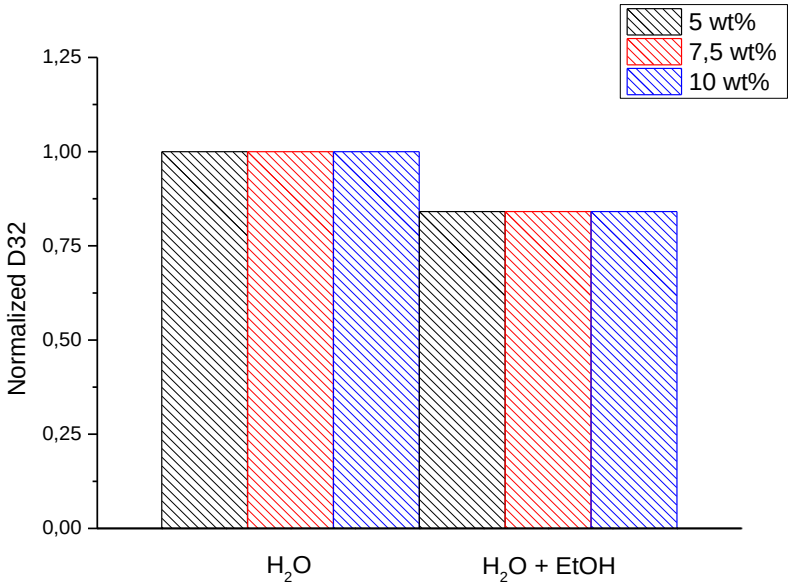

Figure 10.17: Normalized D32 of powders obtained from Pullulan solutions at different concentrations resulted from semi empirical equation

10.2 ADIMENSIONAL ANALYSIS

The non dimensionalization of the governing equations of fluid flow is important for both theoretical and computational reasons. Non dimensional scaling provides a method for defining dimensionless groups that can provide physical insight into the relative importance of various effects in the system of governing equations. Computationally, dimensionless forms have the added benefit of providing numerical scaling of the system of discrete equations, thus providing a physically linked technique for improving the ill conditioning of the system of equations.

Considering the previous results, only the powders of interest, 5 wt%, 7.5 wt% and 10 wt%, were further investigated. As introduced in Section 3.1.2.3, Section 3.2.2 and Section 4.1 some of the important dimensionless numbers used in fluid mechanics and heat transfer are evaluated below.

10.2.1 ATOMIZATION

10.2.1.1 BOND NUMBER

The Bond number is a measure of the importance of surface tension forces compared to gravity. A high Bond number indicates that the system is relatively unaffected by surface tension whereas a low Bond number, typically less than 1, indicates that surface tension dominates.

$$Bo = \frac{\rho g R_{orifice}^2}{\sigma} \qquad \text{Eq(10.8)}$$

Using the previous equation (10.8) the Bond number values were evaluated. As shown in Figure 10.18, it results to be unaffected by concentration for either Pullulan solutions, aqueous or hydro alcoholic. Even if the Bond number is higher for hydro alcoholic solutions, in both cases the effect of gravitational forces is negligible with respect to that of surface tension.

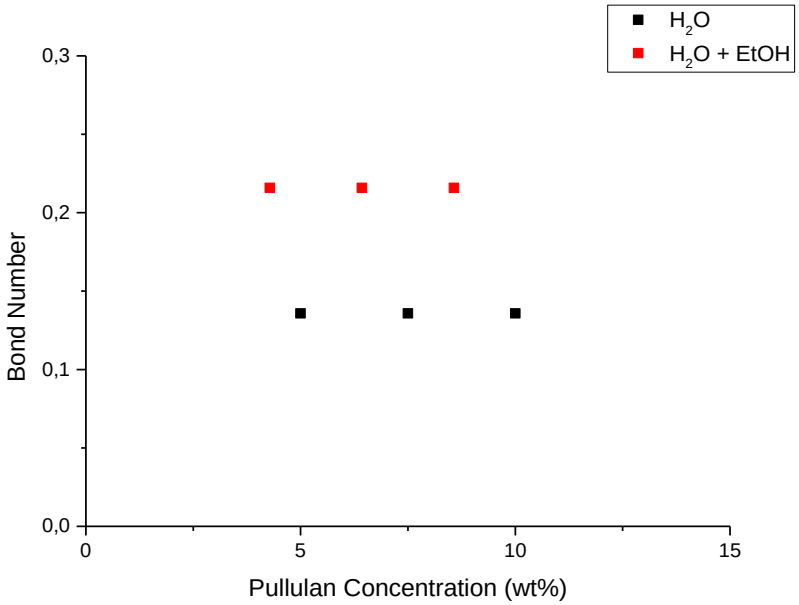

Figure 10.18: Bond number versus Pullulan concentration

10.2.1.2 OHNESORGE NUMBER

The Ohnesorge number relates the viscous forces to inertial and surface tension forces. The higher the Ohnesorge number, the more dominant is the internal viscous dissipation. This means that most of the energy provided to the system converts into internal viscous dissipation, i.e., that a droplet formation is critical or even impossible. Instead, the lower the Ohnesorge number, the weaker are the friction losses due to viscous forces. As a consequence, a droplet can form [136].

$$Oh = \frac{\eta_{liq}}{\sqrt{\sigma_{liq}\rho_{liq}d_{jet}}} \qquad \text{Eq(10.9)}$$

Taking into account the previous equation (10.9), where d_{jet} was approximated with the nozzle diameter, the Ohnesorge number values were calculated. The results are reported in Figure 10.19, where the blue dashed line represents the critical Ohnesorge value, 0.2077, above which viscosity dominates and under which the inertia prevails.

Except the solutions with the lower concentration, the others have an Ohnesorge number above the critical value, indicating a greater influence of the viscosity and thus meaning that viscous forces prevailed on the inertial ones. A general remark can be made concerning this non dimensional number, which is increasing for increasing concentrations, so the relative magnitude of the respective viscous effects grows relative to the inertial ones. Again, hydro alcoholic solutions are characterized by values higher than aqueous solutions at the same concentration, mainly due to their lower surface tension.

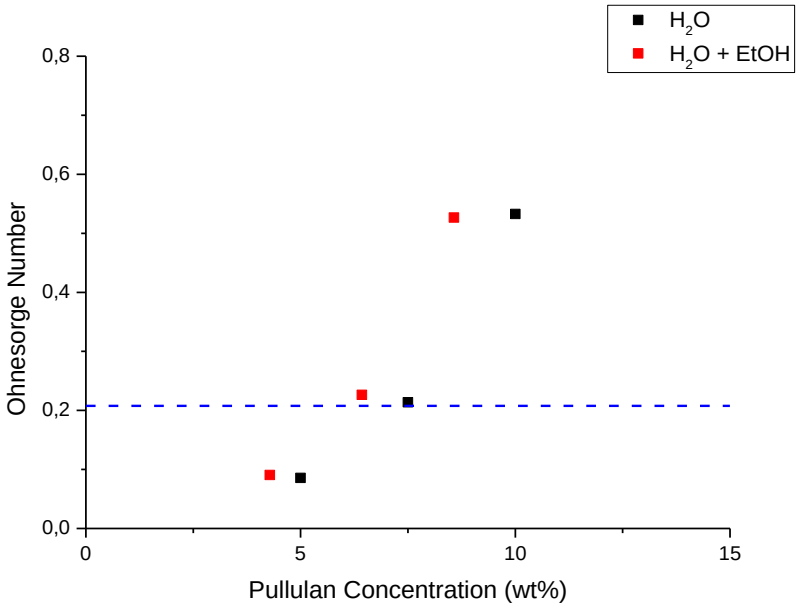

Figure 10.19: Ohnesorge number versus Pullulan concentration

The Ohnesorge number allows obtaining further information regarding the liquid sheet formation and breakup. As deeply discussed in Section 3.1.2.2, at higher rates of flow, laminar liquid jets or threads are formed that breakup into droplets beyond a certain distance from the nozzle. Such liquid threads are intrinsically unstable. On their surface centrally symmetrical surface waves are formed which grow fast for wavelengths

$$\lambda > \pi d_{jet} \qquad \text{Eq(10.10)}$$

The fastest growing wave disturbance on the ligament surface corresponds to the optimum wavelength λ_{opt} given by the following equation (10.11)

$$\lambda_{opt} = \pi d_{jet}\sqrt{2 + 6\,Oh} \qquad \text{Eq(10.11)}$$

The evaluated data are shown in Figure 10.20.

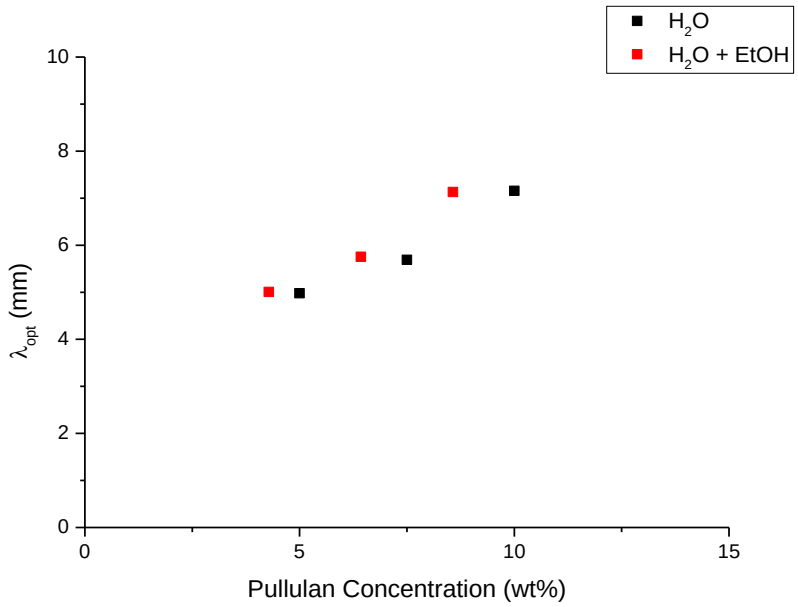

Figure 10.20: Optimum wavelength versus Pullulan concentration

Moreover, following the theories by Rayleigh, presented in Section 3.1.2.2, it was argued that it is reasonable to assume that the droplet diameter relates directly to the jet diameter at the jet break up position [137]. Under this assumption, it was shown that the droplet diameter might be determined according to the following equation (10.12)

$$d_{droplet} = d_{jet}(44 + 133\ Oh)^{\frac{1}{6}} \qquad \text{Eq(10.12)}$$

Figure 10.21 reports the value for the droplet diameter and it is possible to note that, in the investigated range, variations in fluid properties have a limited effect on the droplet diameters.

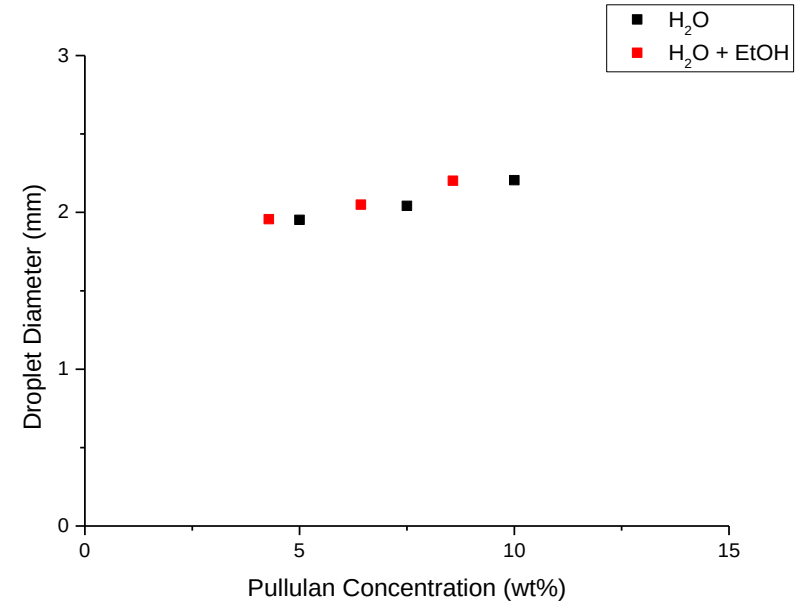

Figure 10.21: Droplet diameter versus Pullulan concentration

The diameters reported do not compare with those determined by image analysis. This is not surprising, due to the fact that, as anticipated in Section 3.1.2.3, should be considered that the Ohnesorge group allow the prediction of the globules formed in primary atomization before they split up into smaller drops during secondary atomization [54]. Moreover, the Ohnesorge number is independent of the air velocity, which plays an essential role in determining the atomization during the spray drying process, and so it is not sufficient to conduct a complete assessment of the phenomenon. Therefore, the Ohnesorge number is only adequate to describe droplet ejection in conjunction with the Weber number, which is analyzed later.

10.2.1.3 REYNOLDS NUMBER

The Reynolds number can be defined as the ratio of inertial forces to viscous forces and interpreted as the ratio of dynamic pressure to shearing stress. It is a convenient parameter for predicting if a flow will be laminar or turbulent. High values of the parameter indicate that viscous forces are small and the flow is essentially inviscid. Low values of the parameter indicate that viscous forces must be considered.

The Reynolds number of the liquid, also referred to as liquid Reynolds number, was evaluated using the equation

$$Re_{liq} = \frac{v_{liq}\rho_{liq}d_{jet}}{\eta_{liq}} \qquad \text{Eq(10.13)}$$

where v_{liq} was computed dividing the feed flow rate by the orifice area. As reported in Figure 10.22, it is possible to observe that an increase in viscosity lowers the Reynolds number.

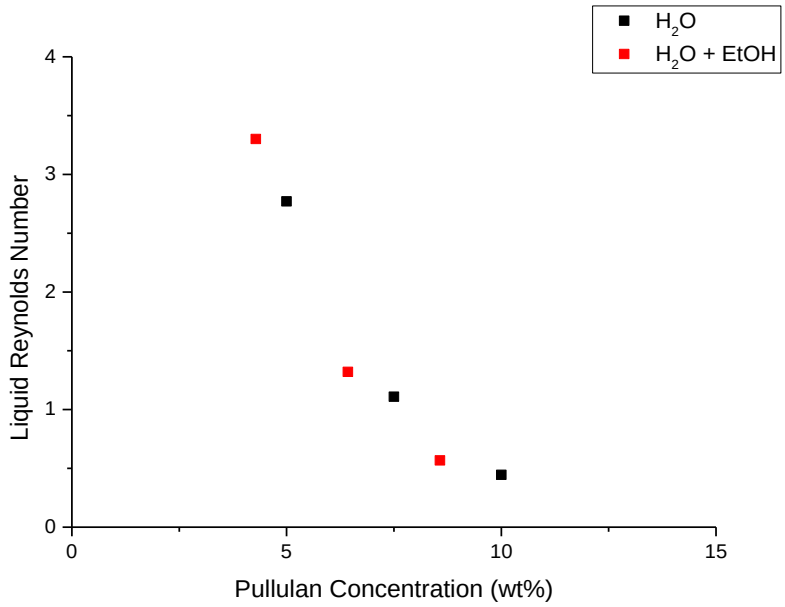

Figure 10.22: Liquid Reynolds number versus Pullulan concentration

Having been introduced the Ohnesorge number and the liquid Reynolds number, as anticipated in Section 3.1.2.3, the most commonly quoted criterion for classifying the breakup mechanism of a jet is the one based on Oh versus Re map [55]. Considering the chart, see Figure 3.12, it is possible to note that the obtained values correspond to the mechanism of disintegration studied by Rayleigh. Thus, without any gas flow, dripping occurs.

This is a further proof of the fact that the air velocity has a crucial and pivotal role in giving rise to high frictional forces over liquid surfaces, causing liquid disintegration into spray droplets. Thereby, also the air Reynolds number should be considered in order to provide an exhaustive description of the phenomenon.

This adimensional number was evaluated according to equation

$$Re_{air} = \frac{v_{air}\rho_{air}d_{jet}}{\eta_{air}} = 345245 \qquad \text{Eq(10.14)}$$

where v_{air} was computed dividing the air flow rate by the rim around the orifice area.

At a relatively high value of the air Reynolds number and a relative low value of sheet velocity, the sheet deformation and breakup is greatly affected by air friction [138]. As the air Reynolds number is increased, local disturbances in the sheet become more predominant until holes are caused to form near the orifice, giving rise to a perforated sheet. Consequently, the predominant disturbances are a function of both air Reynolds number and sheet velocity [48].

In Figure 10.23, it is showed a map to predict the way the liquid sheet disintegrates as a function of its velocity and air Reynolds number. From figure, below a Reynolds number of about 20000 and a sheet velocity below 750 $\frac{cm}{s}$, disintegration is caused mainly by air friction producing waves in the sheet. At a higher number, as it occurs in the present work, disintegration starts earlier through the formation of perforation in the sheet.

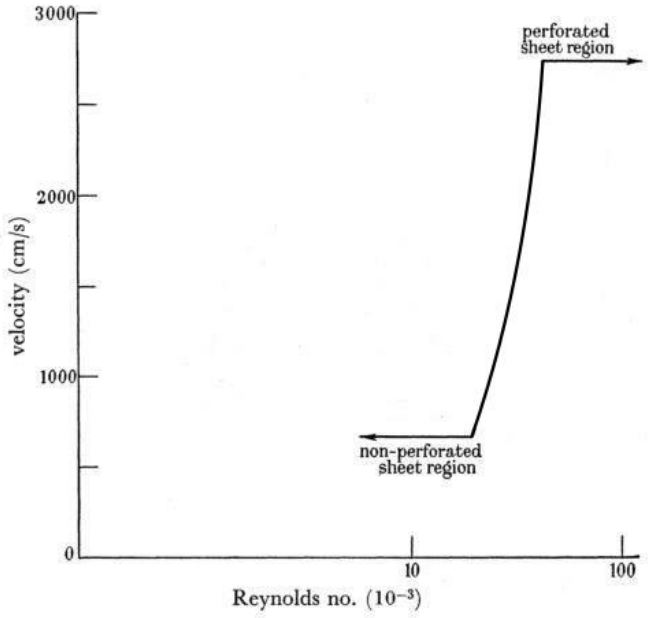

Figure 10.23: Relation between velocity of flow and air Reynolds number

Furthermore, the influence of the Reynolds number on discharge coefficient C_D, i.e. the ratio of actual flow rate to theoretical flow rate, has been investigated in literature [139][140]. Figure 10.24, reporting C_D as a function Re, can be divided into three distinct regions. In the first stage, corresponding to laminar flow, C_D increases almost linearly with $\sqrt{Re}$. During the second stage, corresponding to semi turbulent flow, C_D at first increases with Re up to a maximum value, beyond which further increase in Re causes C_D to decline. In the fully turbulent stage, which is of most practical interest, C_D remains sensibly constant.

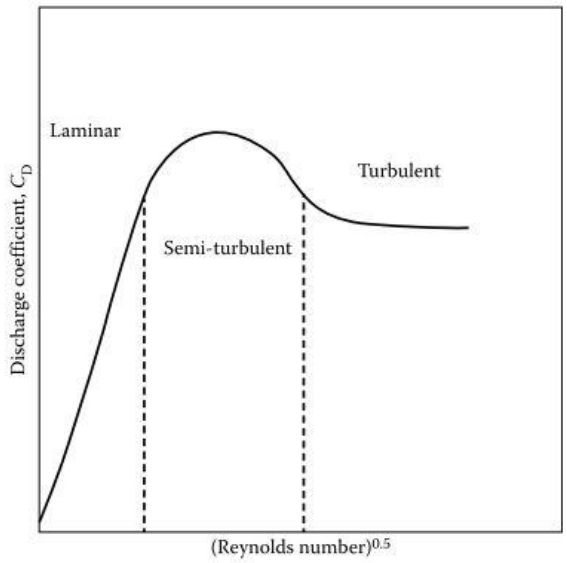

Figure 10.24: Variation in discharge coefficient with Reynolds number

The characteristic peak in the curve of C_D against Re for a sharp edged orifice diminishes rapidly as the orifice length to diameter ratio is increased from 0.5 to unity, as reported in Figure 10.25, which is based on literature experimental data [141].

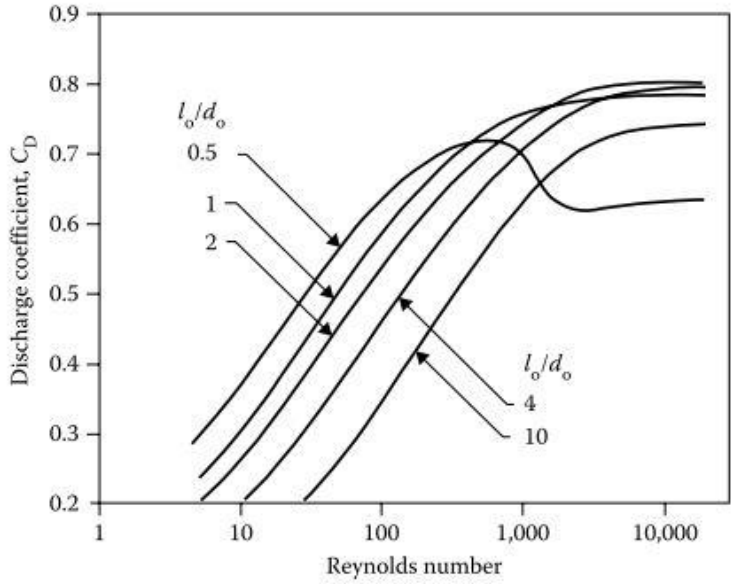

Figure 10.25: Variation of discharge coefficient with Reynolds number for various orifice length to diameter ratios

Indeed, it is possible to note that for $\frac{l_0}{d_0} = 0.5$ the passage is similar to a simple plate orifice, as illustrated in Figure 10.24. The discharge coefficient is low because the liquid jet forms a vena contracta, which, as is depicted in Figure 10.26, in the short length available, has no time to re-expand and fill the nozzle. With increase in $\frac{l_0}{d_0}$ the jet expands in the passage and C_D increases, reaching a maximum at a value of $\frac{l_0}{d_0}$ of around 2. Further increase in $\frac{l_0}{d_0}$ reduces C_D due to increase in frictional losses. The discharge coefficients generally increase with increase in Reynolds numbers until a maximum value is attained at Reynolds number of around 10,000. Beyond this point, as it occurs in the present work, the value of CD remains sensibly constant and independent of Reynolds number.

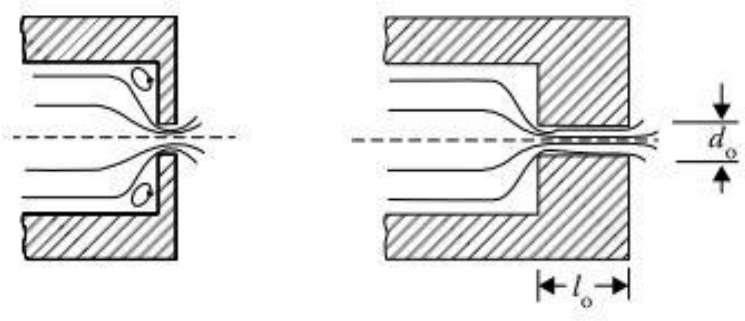

Figure10.26: Influence of final orifice length to diameter ratio on flow pattern

10.2.1.4 WEBER NUMBER

As discussed up to this point, the magnitude of the first stage of the atomization process depends partly on the Reynolds number, which provides a measure of the disruptive forces present within the liquid sheet. These forces are enhanced by increases in air velocity and are reduced by an increase in liquid viscosity.

However, the first stage of the atomization process is also influenced by the Weber number, which governs the development of capillary waves, or ripples, on the liquid surface. The rate of growth of these perturbations into projections large enough to break off and form ligaments is dependent on the ratio of the aerodynamic forces at the liquid air interface to the consolidating surface tension forces in the liquid, that is, on Weber number.

Considering the following equation (10.15), the liquid Weber number values were evaluated.

$$We_{liq} = \frac{v_{air}^2 \rho_{liq} d_{orifice}}{\sigma_{liq}} \qquad \text{Eq(10.15)}$$

The obtained results, shown in Figure 10.27, reveal that the liquid Weber number seems not to be not influenced by concentration variations of Pullulan solution, both aqueous and hydro alcoholic. However, even if in the case of hydro alcoholic solution the Weber number results to be higher, it is

generally low, meaning that the inertial forces acting on the droplets at the interface are generally small and, in absence of any other effect, only capillary pressure will be responsible for jet breakup.

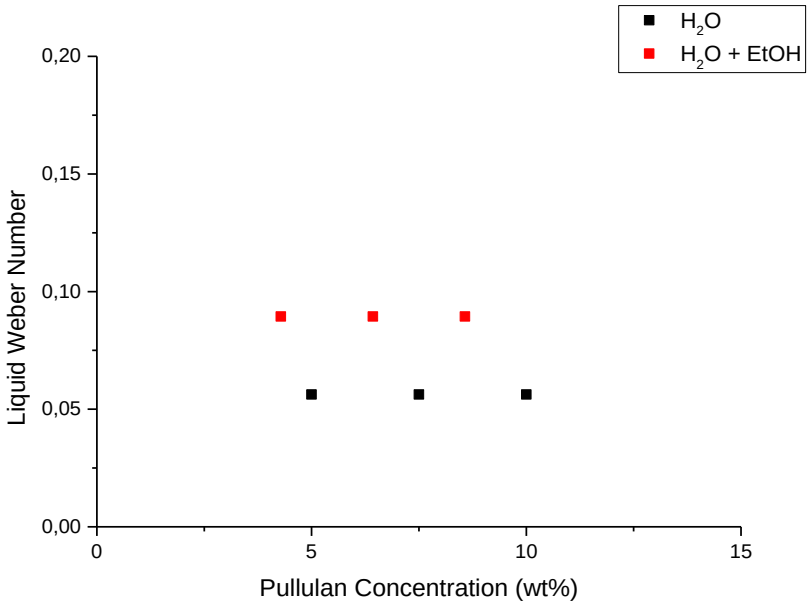

Figure 10.27: Liquid Weber number versus Pullulan concentration

Neglecting the effect of gravity, transition from dripping to liquid column breakup into droplets is reached when the longitudinal contraction rate of the liquid jet is exactly equal to its rate of discharge.

This condition is given by the following relation [45]

$$We_{liq} = \frac{v_{liq}^2 \rho_{liq} d_{orifice}}{\sigma_{liq}} = 4 \qquad \text{Eq(10.16)}$$

Comparing the calculated liquid Weber number with the critical value suggested by the previous condition, it is possible to draw a conclusion coherent with that extracted considering the Ohnesorge number versus Reynolds number map, in Figure 3.12, which is that without any gas flow the events of dripping occurs and, therefore, the effect of air velocity has to be taken into account.

Shape change and aerodynamic thinning forms an integral part of the breakup process for high speed drops [142]. Indeed, during the first stage of the drop breakup process, the drops experience a shape change. Under the action of aerodynamic pressure, the drops become distorted from their undisturbed spherical shapes and become flattened, or disk shaped, normal to the airflow direction.

The distortion of a drop prior to its breakup is controlled by the air Weber number. The air Weber number represents a measure of the importance of the gas pressure compared to the liquid capillary pressure. The higher the Weber number, the larger are the deforming external pressure forces compared with the reforming surface tension forces. Breakup takes place when the dynamic pressure of the gas exceeds the pressure inside the droplet to a considerable extent, so it occurs at a critical value of the Weber number that depends on the continuous flow field. According to the equation (10.17), the air Weber numbers were calculated.

$$We_{air} = \frac{v_{air}^2 \rho_{air} d_{orifice}}{\sigma_{liq}} \qquad \text{Eq(10.17)}$$

Considering the obtained data, reported in Figure 10.28, it is possible to ascertain that the real cause for atomization is the air pressure that overcome any other effect. Further, the action seems more relevant for hydro alcoholic solutions, given their lower surface tension.

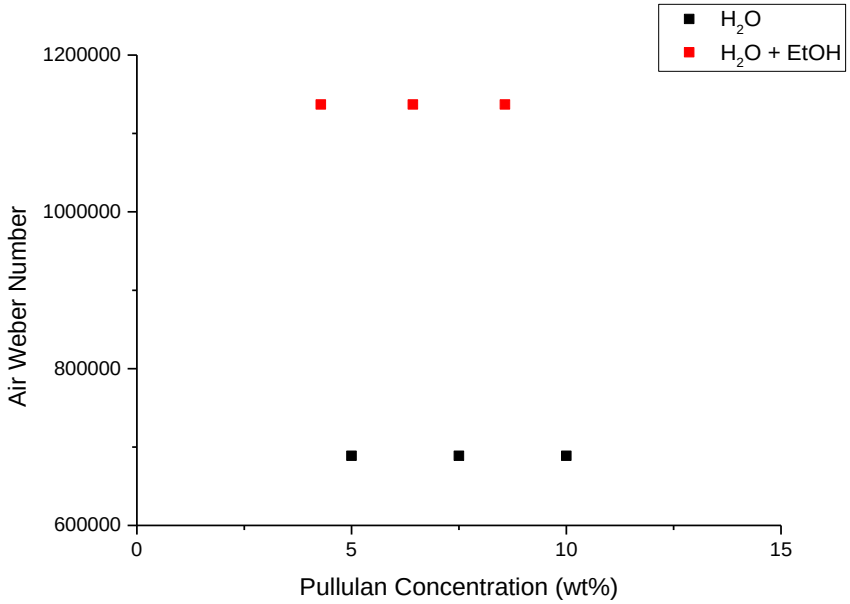

Figure10.28: Air Weber number versus Pullulan concentration

10.2.1.5 DEBORAH NUMBER

All the adimensional numbers considered until now are the typical parameters analyzed in literature to group all the variables involved in the spray drying process and to clarify their effects on the atomization. However, the previous considerations and models consider only viscous systems. In the case of interest, the solutions showed a significant degree of elasticity. Therefore, in order to assess the importance of elastic effect relative to the others, the Deborah number and the Elastocapillary number were examined.

To characterize the breakup process it is then necessary to seek a different set of dimensionless parameters that do not depend on the velocity scale. Such capillary thinning and breakup processes are governed by, at least, three characteristic time scales [143]:

- The viscous time scale

$$t_{visc} \sim \frac{\eta R}{\sigma} \qquad \text{Eq(10.18)}$$

- The polymeric time scale

$$t_{poly} \sim \lambda \qquad \text{Eq(10.19)}$$

- The inertial time scale

$$t_R \sim \sqrt{\frac{\rho R^3}{\sigma}} \qquad \text{Eq(10.20)}$$

The Deborah number corresponds to the ratio of the polymeric relaxation time to the inertial time scale, representing a balance between the elastic and inertial forces. Hence, the greater the Deborah number, the more solid like, which in the present case can be interpreted as more resistant to breakup, is the material. The smaller the Deborah number, the more fluid like it is [144].

$$De = \frac{t_{poly}}{t_R} = \frac{\lambda}{\sqrt{\frac{\rho R_{orifice}{}^3}{\sigma}}} \qquad \text{Eq(10.21)}$$

Taking into account the equation (10.21), where λ is the longest relaxation time, the Deborah number values were calculated. As revealed in Figure 10.29, in which the blue dashed line represents the critical Deborah number, equal to 0.9766, the Pullulan solutions with the lower concentrations exhibited values below this threshold, while the Pullulan solutions with the higher concentrations present values above it. Therefore in the first case the inertia effects dominate, whereas in the second case the elastic forces prevail.

A general remark can be made concerning this adimensional number, which is increasing for increasing concentrations, so the relative magnitude of the elastic effects grows relative to the inertial ones. Moreover, it is interesting to note that the hydro alcoholic solutions are characterized by a sharper rise than the aqueous solutions, which, according to the rheological characterization debated in Section 8.2, can be ascribed to their higher degree of elasticity. With respect to the tendency of forming fibers, the result suggest that fiber should form at the highest concentration, but not at 7.5 wt% Pullulan concentration. This is in contrast with the experimental observations where in case of aqueous solutions fibers are observed only at 7.5%. In the case of hydro alcoholic concentrations, instead, fibers form at both the concentrations. However, remembering the results for Reynolds and Ohnesorge numbers, it was observed that surface tension and viscosity dominated over inertia. Therefore, also the relative importance of elasticity with respect to these effects, expressed by the elastocapillary number, deserves consideration.

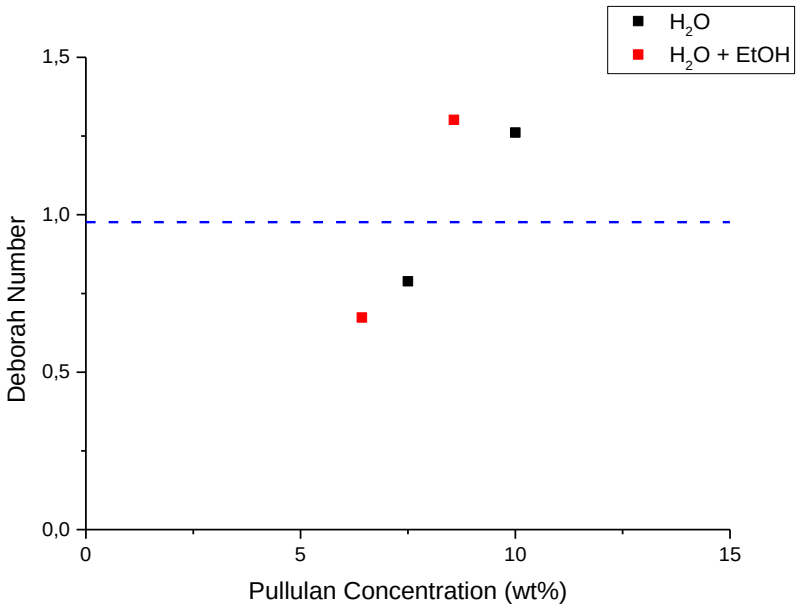

Figure 10.29: Deborah number versus Pullulan concentration

10.2.1.6 ELASTOCAPILLARY NUMBER

The Elastocapillary number Ec, instead, balances the viscous and elastic effects. In particular, the elastic effects dominate for $Ec > 4.7015$, while viscous effects prevail for $Ec < 4.7015$.

$$Ec = \frac{t_{poly}}{t_{visc}} = \frac{\lambda\sigma}{\eta R_{orifice}} \qquad \text{Eq(10.22)}$$

Using the equation (10.22), the Elastocapillary numbers were evaluated. As shown in Figure 10.30, even if all the values are below the critical threshold, meaning that the viscous effects govern, it appears that for increasing the solutions concentration, the viscous forces are proportionally larger than the elastic ones, with a decreasing Ec as result. Therefore, the increase in viscous effects is larger compared to the increase in elastic properties of the polymer solution when the concentration is rising. It is important to remember that an increase in the Elastocapillary number results in strong stabilization of the jet, and this could explain the presence of fibers at 7.5 wt% for both the type of solutions considered in the present work.

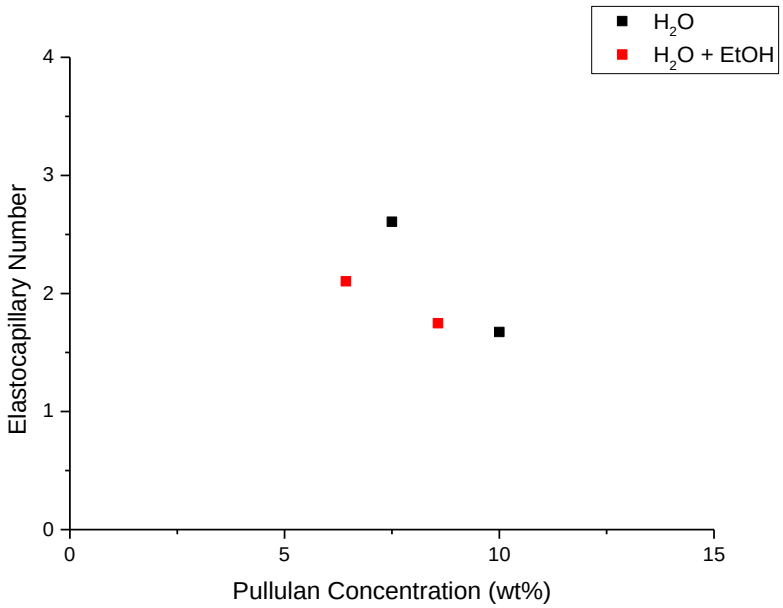

Figure 10.30: Elastocapillary number versus Pullulan concentration

In summary, considering all the adimensional number discussed until this point, it is possible to point out that the atomization process is for sure favoured by the high frictional forces generates by the air impinging on the liquid surface, causing liquid disintegration into spray droplets.

However, as regard liquid property, in many respects, the viscous and elastic forces are the most important parameter and concentration controls which of the two is dominating. Further, adimensional analysis was carried out using the nozzle dimension as reference dimensions, and therefore it holds only very close to the nozzle. However, evidences exist that as reported in Figure 10.31, even if close to the nozzle the viscoelastic effects are negligible, and jets initially evolve consequently, far from the nozzle, the polymeric component increases the elongational viscosity. The enhanced extensional resistance withstands the fast nonlinear deformations that occur during the capillary breakup process, leading to the formation of ligaments and much poorer atomization for the viscoelastic jet. Therefore, the large scale features remain unchanged, but the viscoelastic behaviour results in finer scale structures such as atomized droplets that remain connected to the core jet by thin viscoelastic ligaments. The lifetime of these ligaments depends on the extensional viscosity of the fluid [145].

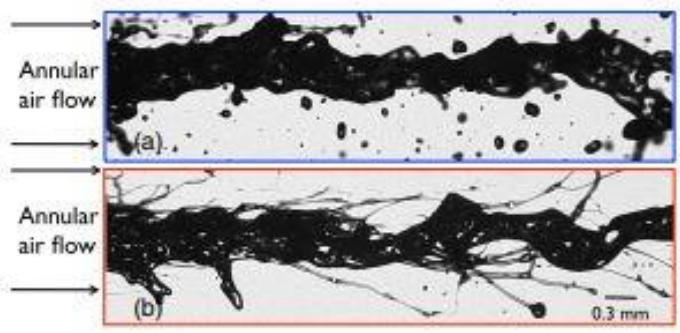

Figure 10.31: Snapshot of the liquid jet for (a) the Newtonian solvent and (b) the viscoelastic solution

The other factor to take into account is the feed viscosity. Although in an absolute sense its influence on atomization is no greater than that of surface tension, its importance stems from the fact that it affects not only the drop size distributions in the spray but also the nozzle flow rate and spray pattern. An increase in viscosity lowers the Reynolds number and also hinders the development of any natural instability in the jet or sheet. The combined effect is to delay disintegration and increase the size of the drops in the spray.

Finally, all models reported in literature do not take into consideration the possibility that threads, instead of droplets, may be stabilized by premature drying of the fluid due to solvent evaporation. In order to complete the topic dissertation, it could be of future interest the comparison between the characteristic time scale for solvent evaporation and those for inertial, viscous and elastic breakup in order to attempt if liquid ligament drying occurs before the secondary atomization phase, thus trying to explain the fibres formation. Physically, viscous and elastic forces may delay the capillary necking and breakup of the filament long enough for significant solvent evaporation to occur. In this regard, a valid starting point may be the analysis of Tripathi [146], concerning industrial coating process, in which filaments life time was compared with a characteristic residence time. In this way, it was possible to demonstrate that if the residence time of a fluid element in the flow is of the same order as, or greater than, the filament lifetime the formation and growth of strands, also referred to as stringiness, is likely.

10.2.2 DROPLET DRYING KINETICS

10.2.2.1 PECLET NUMBER

As explained in Section 3.2.2, the Peclet number describes the surface accumulation due to comparison between the evaporation rate of the solvent and the diffusional motion of the solute.

According to literature, while the evaporation rates were determined from thermogravimetric curves as calculated in Section 8.3, the diffusion coefficients are usually evaluated using the Stokes Einstein equation

$$D = \frac{K_B T}{6\pi\eta r} \qquad \text{Eq(10.23)}$$

where:

- K_B is the Boltzmann's constant;
- T is the absolute temperature;
- η is the dynamic viscosity;
- r is the gyration radius.

However, this equation is valid for diffusion of spherical particles through a liquid diluted dispersion with low Reynolds number. This is not the present case, in which a semi diluted polymer

solution is taken into account. Therefore, the free volume theory should be considered in this circumstance.

In the free volume theory, the volume of a liquid is viewed as consisting of two parts [147][148]:

- The volume occupied by the molecules themselves;
- The empty space between the molecules.

The empty space is commonly referred to as the free volume, of which only that portion which is continuously redistributed by thermal fluctuations is available for molecular transport. This part of the free volume is denoted the hole free volume, while the remainder is termed the interstitial free volume. Molecular transport, as perceived by current free volume theory, is consequently governed by the probable occurrence of two events:

- The appearance of a hole of sufficient size adjacent to a molecule
- The overcoming of attractive forces by the molecule with enough energy.

The diffusion free volume theory assumes molecular transport in a liquid consisting of hard spheres. In this type of system molecules move with the gas kinetic velocity but most of the time are confined to a cage bounded by their immediate neighbors. Occasionally, a fluctuation in density opens up a hole in a cage large enough to permit a considerable displacement, giving rise to diffusive motion if a molecule jumps into the hole before the first can return to its original position [149].

Based on the free volume theory, an expression for the solvent tracer diffusion coefficient was proposed, in which the following assumptions are implicit:

- Molecular transport may occur only when a void with a volume greater than a given critical value is formed by the redistribution of the free volume
- No energy is required for free-volume redistribution.

The temperature and concentration dependence of the solvent tracer diffusion coefficient, D_s, can be determined using the following equation

$$D_s = D_0 e^{-\frac{E}{RT}} e^{-\frac{\gamma(w_s V_s + w_p \xi V_p)}{V_{FH}}} \qquad \text{Eq(10.24)}$$

where

- V_i is the specific critical hole-free volume of component i required for a jump;
- w_i is the mass fraction of component i;
- D_0 is a pre exponential factor;
- E is the energy per mole that a molecule needs to overcome attractive forces that keep it close to its neighbors;
- γ is an overlap factor which is introduced because the same free volume is available to more than one molecule;
- T is the system absolute temperature;
- R is the gas constant;

- ξ is the ratio of molar volumes for the solvent and polymer jumping units.

Due to the complexity of the theory and above all the lack of data, a simpler approximated approach was adopted in the present work and the Peclet number was estimated considering a diffusion coefficient for Pullulan in aqueous solution at infinite dilution available in literature [150]. The reported value is

$$D = 2.21 * 10^{-7}\ \frac{cm^2}{s} \qquad \text{Eq(10.25)}$$

Recalling that the Peclet number is evaluated according to the following equation

$$Pe = \frac{k}{8D} \qquad \text{Eq(10.26)}$$

it is clear that as this diffusion coefficient certainly overestimates the value in a concentrated solution, the Peclet numbers determined underestimate the real value. Nevertheless, as shown in Figure 10.32, they are well above unity, meaning that evaporation dominates and the surface becomes rapidly enriched in solutes that precipitate.

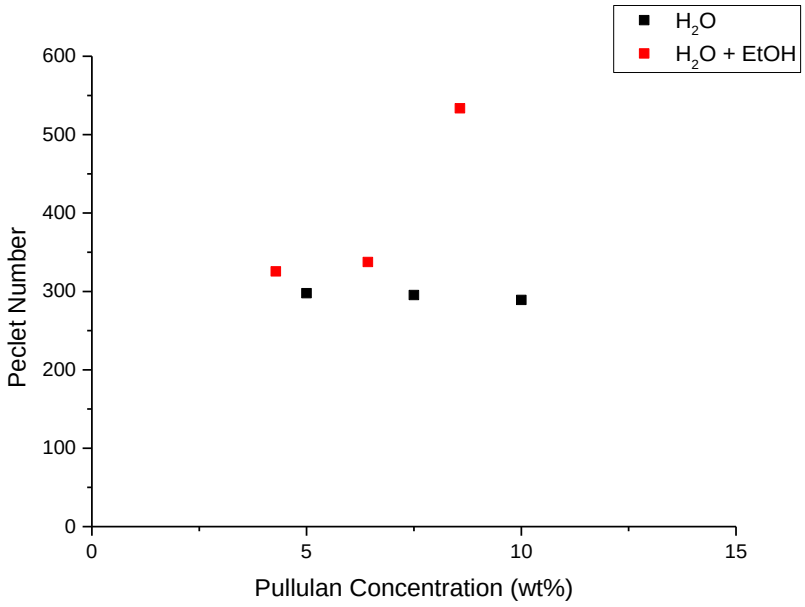

Figure10.32: Peclet number versus Pullulan concentration

Recalling that the faster the evaporation rate the sooner the surface reaches its critical supersaturation causing early skin formation, the surface enrichment of each solution, as illustrated in Figure 10.33, was calculated using the following equation (10.27), where β was integrated numerically to obtain the exact solution.

$$E_i = \frac{e^{Pe_i \frac{R^2}{2}}}{3\int_0^1 R^2 e^{Pe_i \frac{R^2}{2}} dR} \qquad \text{Eq(10.27)}$$

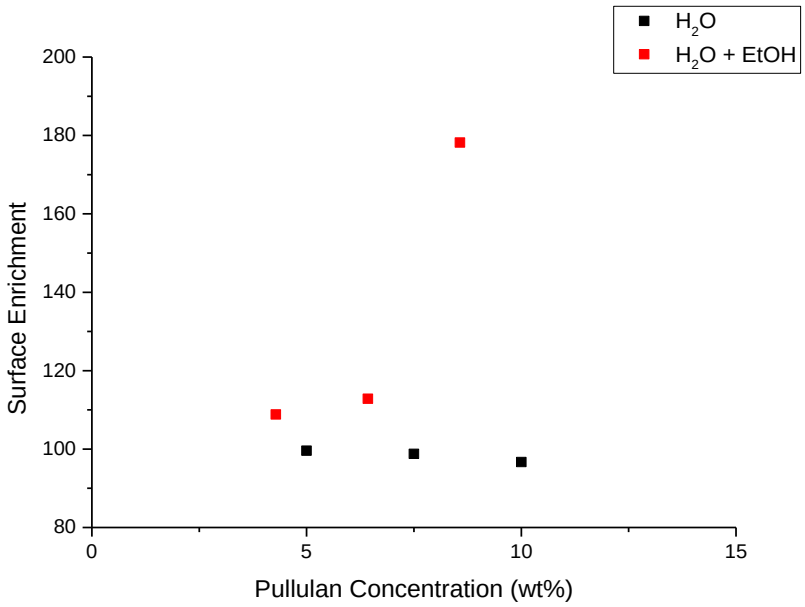

Figure 10.33: Surface enrichment versus Pullulan concentration

Moreover, remembering that this condition leads to the formation of larger size and lower density hollow particles, is possible to confirm this statement referring to various SEM images, in which, being depicted broken particles, it is evident the internal void. Some examples are exhibited in Figure 10.34.

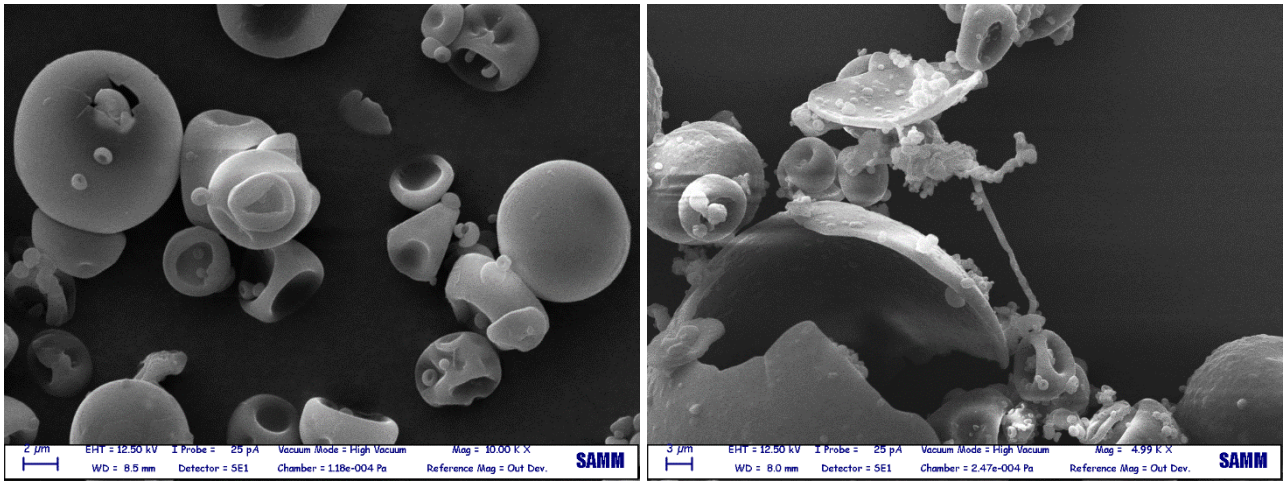

Figure 10.34: Hollow particles
Morphology of powder obtained from 5 wt% Pullulan hydro alcoholic solution
using the nozzle with a diameter of 1mm (on the left)
Magnification: 10kx
Morphology of powder obtained from 7.5 wt% Pullulan aqueous solution
using the nozzle with a diameter of 1mm (on the right)
Magnification: 5kx

Chapter 11

Conclusion

An appropriately designed controlled release drug delivery system can be a major advance towards solving problems concerning the targeting of a drug to a specific organ or tissue and controlling the rate of drug delivery to the target sites. Injection moulded matrix type drug delivery systems are an interesting and promising option when developing oral controlled release system.

If gastro resistance is desired, HPMCAS is a very good candidate, given its insolubility at the low pH typical of stomach environment and soluble at those typical of the intestine. However, even if the selected bulk material dissolves at pH typical of the intestinal tract, an immediate drug release is not feasible. Therefore, a novel solution to reduce the lag time and enhance the dissolution rate of the capsular devices is the addition of release modifiers in the capsule matrix.

In this context, the aim of the present work was to improve the release performance of injection moulded capsules, in order to attain the drug discharge almost immediately after leaving the stomach and entering the small intestine. An even more ambitious goal was to modify the release performance of the drug delivery system in such a way that release is possible even if the matrix solubility is very limited. To achieve both purposes, the idea was to use particles of elongated shape to ensure the creation of percolation paths, allowing the formation of more effective networks throughout the capsule thickness. Thus, complying with all the necessary requirements, Pullulan was chosen as candidate material.

The spray drying technique was implemented and Pullulan fibres, together with shrivelled and large spherical particles, were obtained. The viscoelastic properties of the polymer solution were found to be crucial. An overview of the different forces acting on the fluid ligaments was presented and an adimensional analysis, a method to qualitatively asses the physical insight into the relative importance of various effects in the system of governing equations, was conducted.

As a first step, release performance of Pullulan powders was assessed and a new protocol was developed for the preparation of the capsule matrix. In order to accurately examine the Pullulan behaviour as pore former, a methylcellulose based matrix filled with dried and co-milled Pullulan was employed for the manufacturing of the moulded disks, which were used in the screening of release performance.

Remarkable results were achieved, revealing that the developed protocol is efficacious and proving that the Pullulan can be employed with great success as release enhancer. However, the ultimate aim of the research is not yet reached. Therefore, the influence of the shape factor, and thus the creation of a percolation path, still resulted essential.

Of course, the encouraging achievements incite to pursue the experimental research objective and are a definitive incentive for further investigation.

To produce Pullulan fibres the spray drying technique was implemented. Water and hydro alcoholic solutions containing different concentration of Pullulan were prepared and both their rheology and evaporation behaviour were investigated. Spray drying was performed on all the systems and depending on the concentration, spherical particles alone or Pullulan fibres, together with shrivelled and large spherical particles, were obtained. Finally, the study of the relative importance of the different forces acting on the fluid during droplets formation and drying was conducted showing that both the evaporation behaviour and the elastic properties of the polymer solution were crucial for fibres formation.

To conclude, the spray drying revealed fit for the production of Pullulan fibres, and its potential for high productivity makes it promising in view of the preparation of the amount of Pullulan required for the production of injection moulded screening items.

Appendix A

Technical data

	Unit	MCR 502
Bearing		Air
Min. torque rotation	nNm	1
Max. torque	mNm	200
Max. speed	$\frac{rad}{s}$	314
Normal force range	N	0.005 to 50
Normal force resolution	N	0.5

Table A.1: Modular Compact Rheometer MCR 502 technical data

	Unit	CaBER 1
Hencky strain		Up to $\varepsilon_0 = 10$
Imposed strain rate	$\frac{1}{s}$	$0.0<\varepsilon_0<300$
Fluid strain rate	$\frac{1}{s}$	$10^{-5}<\varepsilon_0<10$
Shear viscosity range	mPas	$10\text{-}10^6$
System response time	ms	10

Table A.2: Capillary Breakup Extensional Rheometer HAAKE CaBER 1 technical data

	Unit	TGA Q500
Maximum sample weight	G	1
Weighing precision	%	+/-0.01
Sensitivity	Mg	0.1
Temperature range	°C	Ambient to 1000
Isothermal temperature accuracy	°C	+/-1
Isothermal temperature precision	°C	+/-0.1
Controlled heating rate	$\frac{°C}{min}$	0.01 to 100

Table A.3: Thermogravimetric Analyzer TGA Q500 technical data

	Unit	4M8
Air flow rate	$\frac{m^3}{min}$	0.20-1
Temperature air inlet	°C	0-180
Feed flow rate	$\frac{mL}{min}$	0.1-150
Compressed air	Bar	3-6

Table A.4: ForMate Spray Dryer 4M8 technical data

	Unit	HAAKE Minilab II
Extruder design		Conical co and counter rotating
Extruder pressure	bar	up to 200
Drive speed range	$\frac{1}{min}$	1 to 360
Drive max torque per screw	Nm	5

Table A.5: HAAKE Minilab II technical data

	Unit	Babyplast 6/10P Standard
Piston diameter	mm	10, 12, 14, 16, 18
Volume	cm^3	4, 6.5, 9, 12, 15
Injection pressure	bar	2650, 1830, 1340, 1030, 815
Clamp force	KN	62.5
Opening force	KN	4
Opening stroke	mm	30-110
Ejection force	KN	7.5
Ejection stroke	mm	45

Table A.6: Babyplast 6/10P Standard technical data

Appendix B

Extrusion and rheological measurements

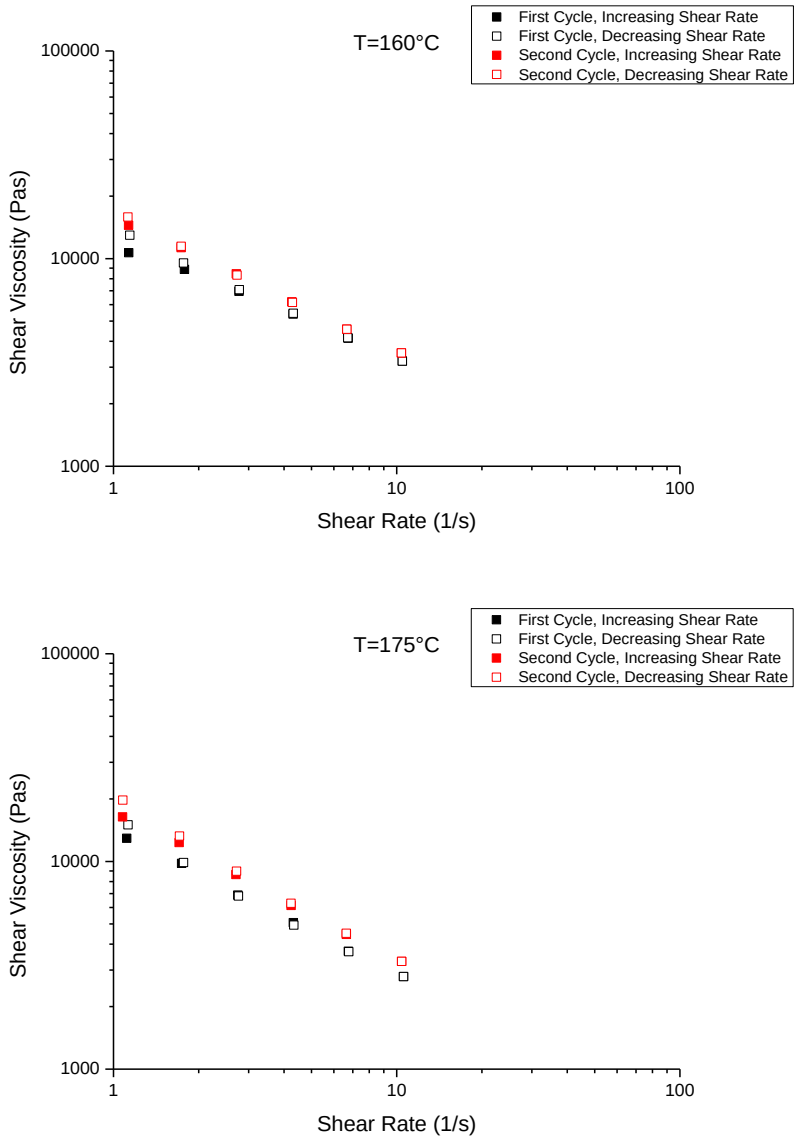

Figure B.1: Shear viscosity of Pullulan mixture at extrusion shear rate cycles

Appendix C

Powders morphology

Nominal Concentration: 10 wt%

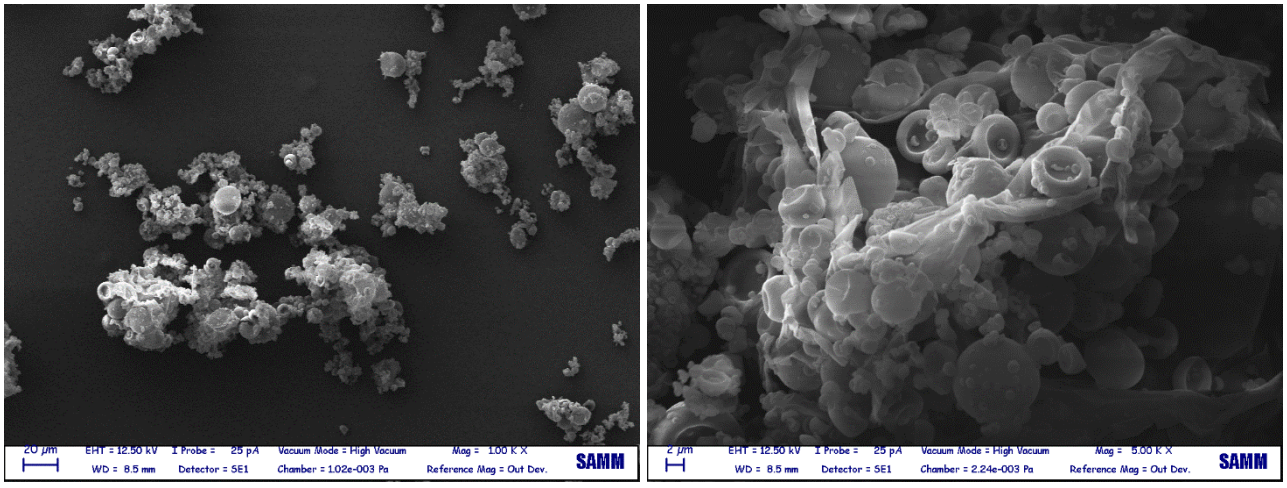

Nominal Concentration: 7.5 wt%

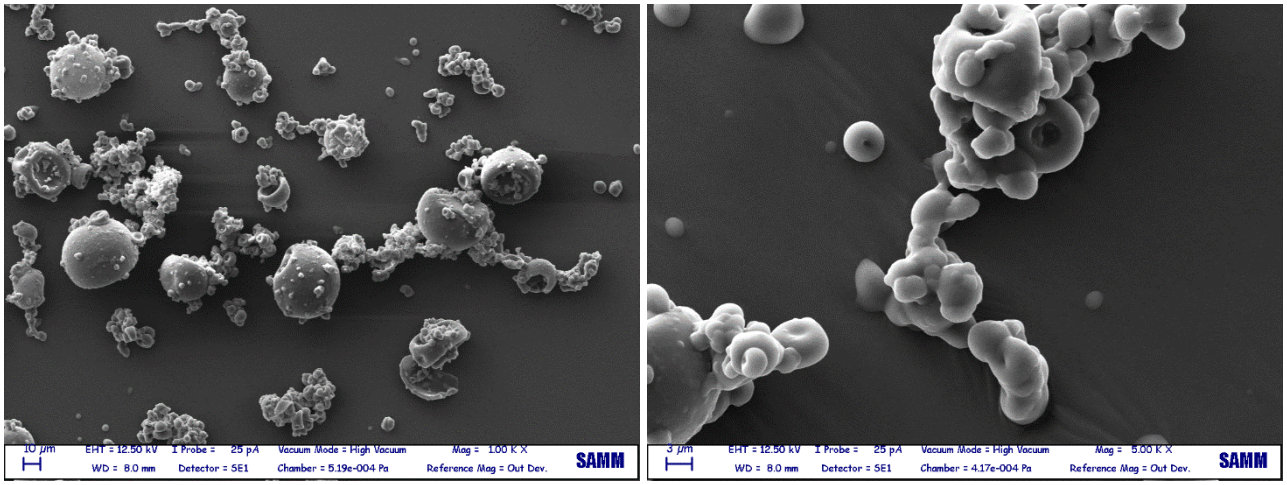

Nominal Concentration: 5 wt%

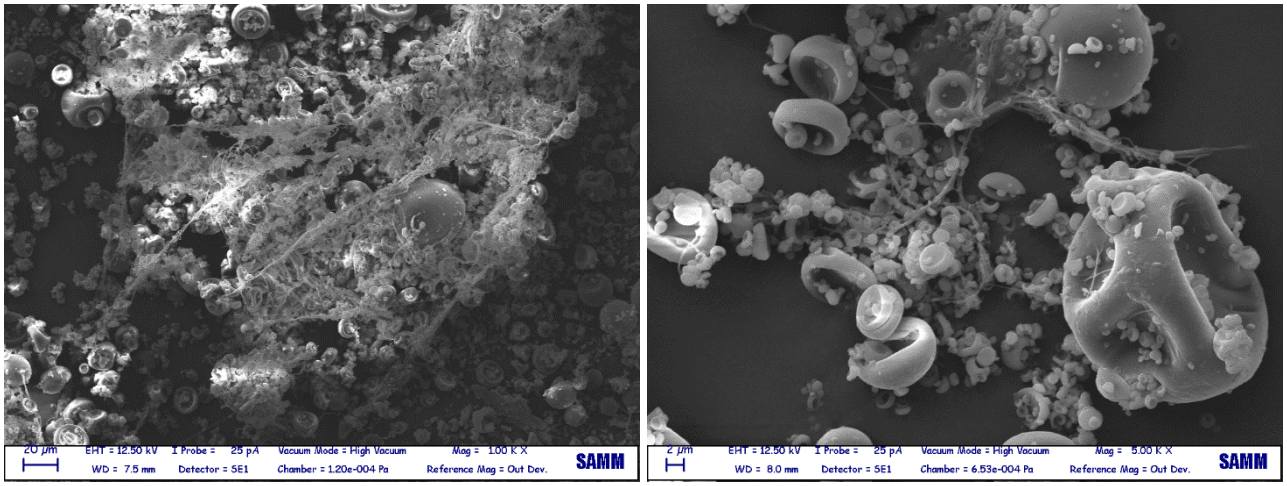

Figure C.1: Morphology of powders obtained from Pullulan aqueous solutions at different concentration using the nozzle with a diameter of 1.2mm
Magnification: 1kx (on the left)
Magnification: 5kx (on the right)

Nominal Concentration: 10 wt%

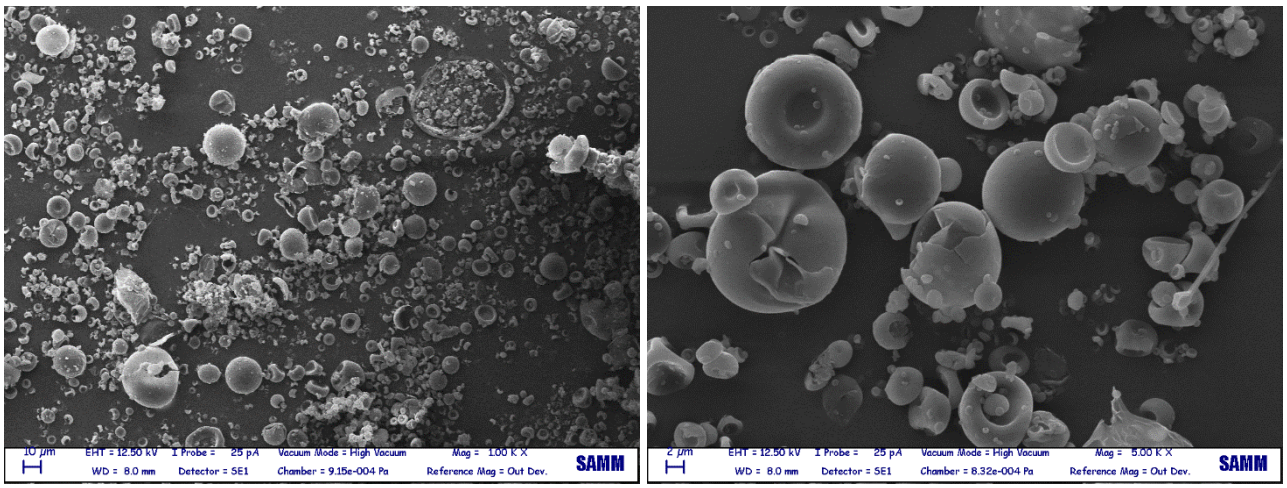

Nominal Concentration: 7.5 wt%

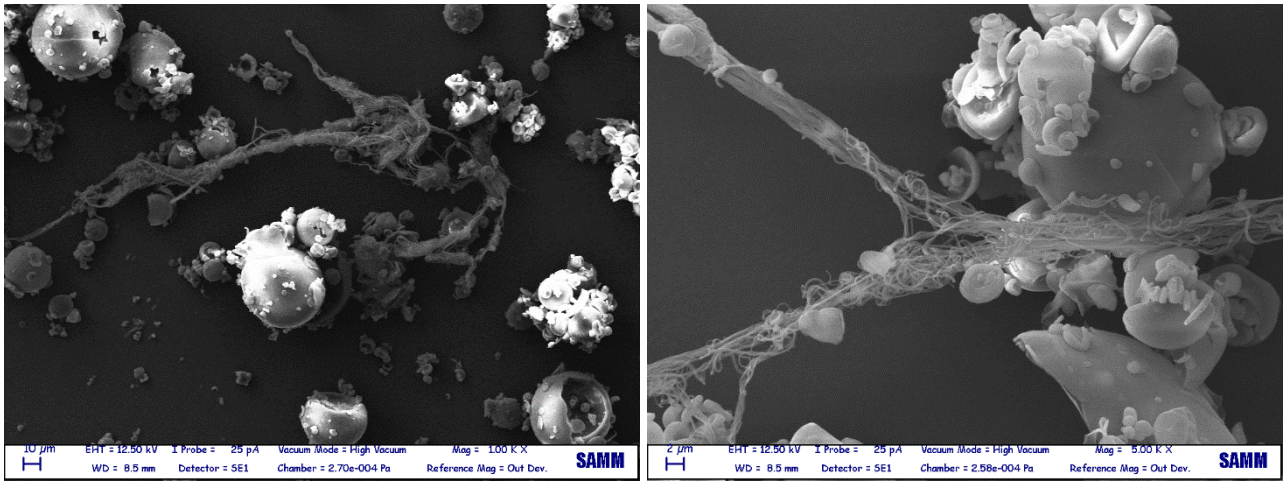

Nominal Concentration: 5 wt%

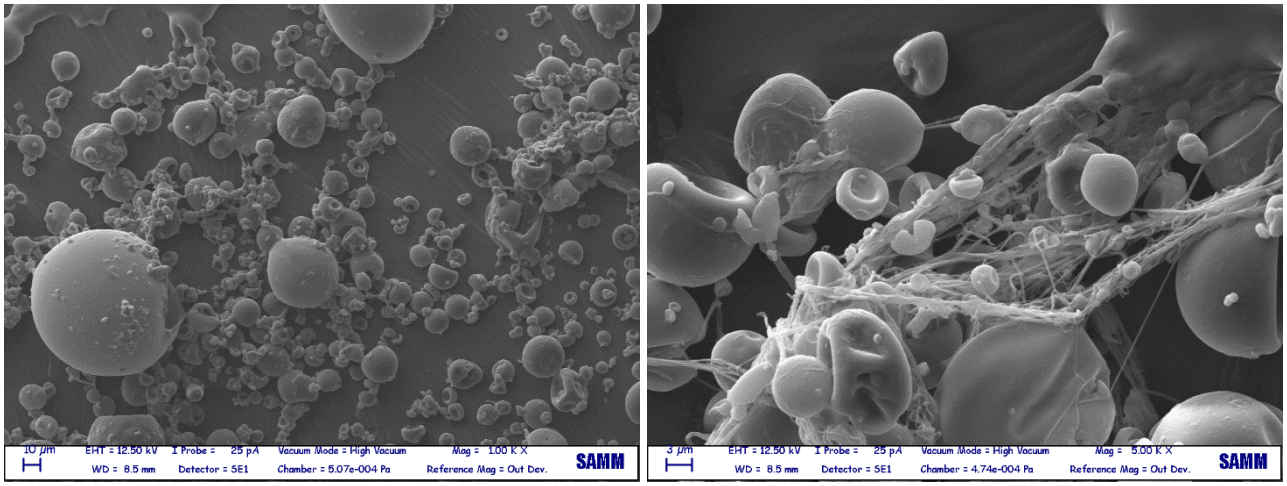

Figure C.2: Morphology of powders obtained from Pullulan hydro alcoholic solutions at different concentration using the nozzle with a diameter of 1.2mm
Magnification: 1kx (on the left)
Magnification: 5kx (on the right)

Nozzle 1.2mm

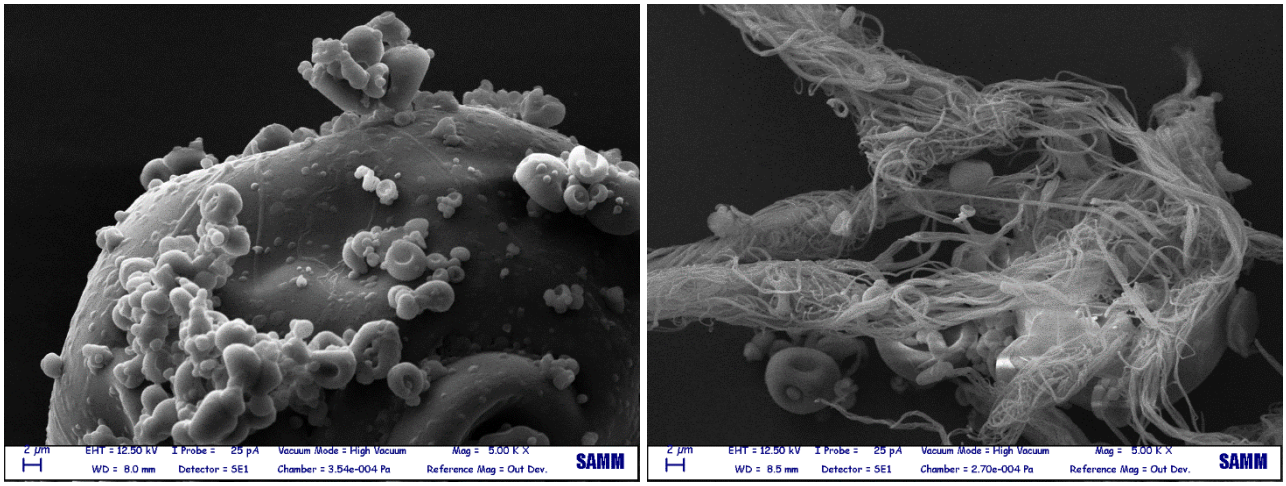

Nozzle 1mm

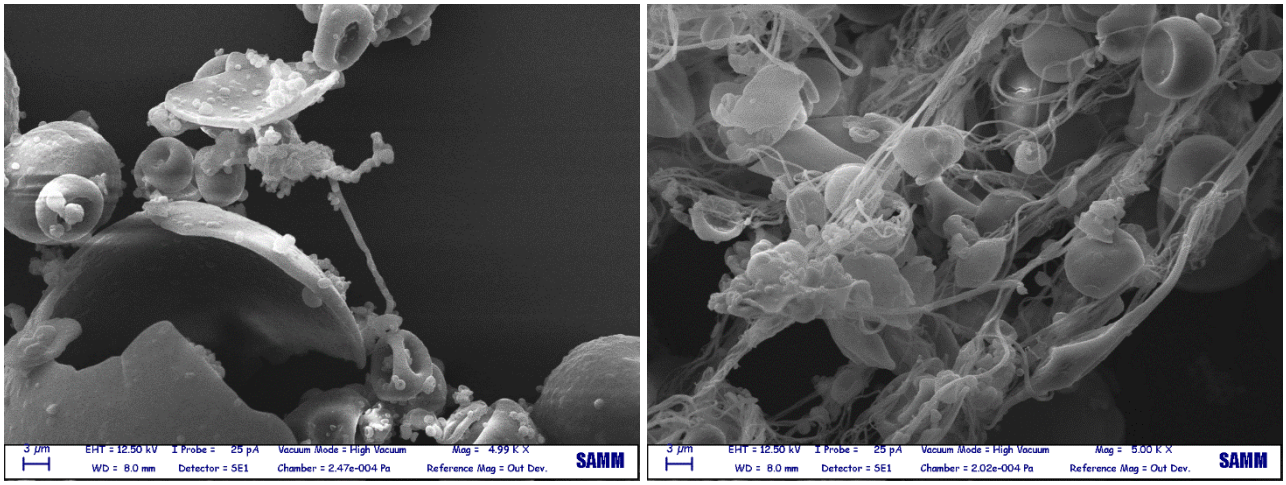

Nozzle 0.6mm

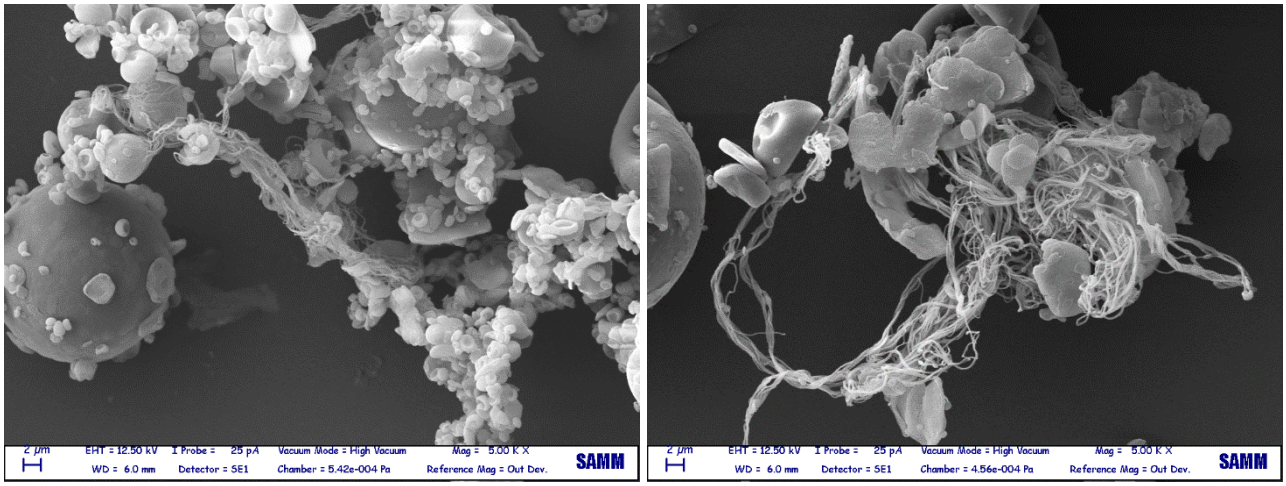

Figure C.3: Morphology of powders obtained from 7.5 wt% Pullulan aqueous (on the left) and hydro alcoholic (on the right) solutions
Magnification: 5kx

Particle size distribution

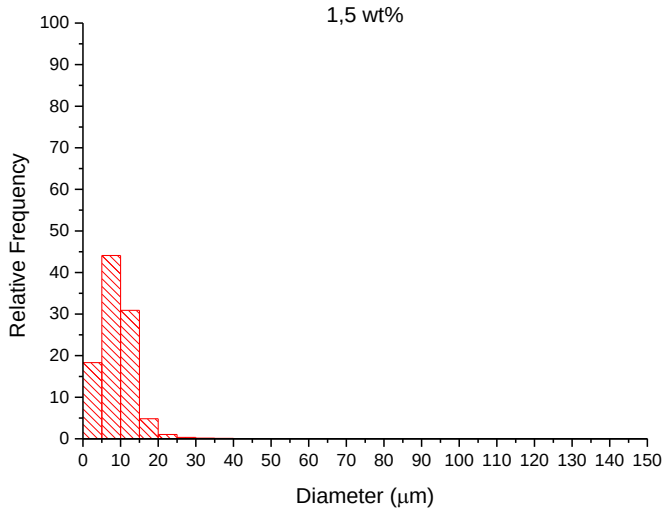

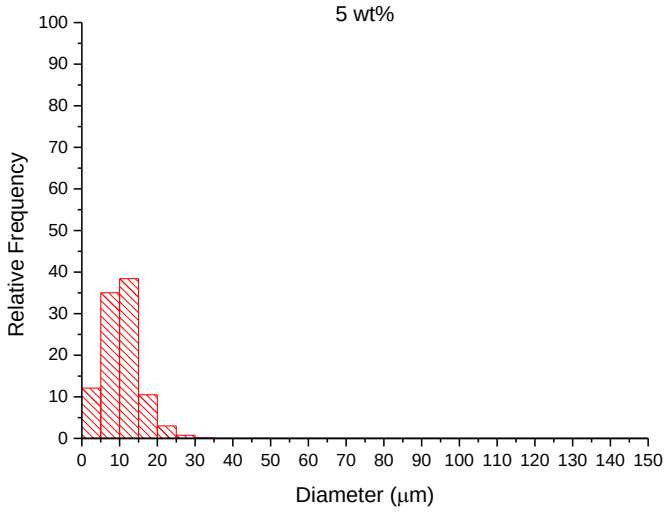

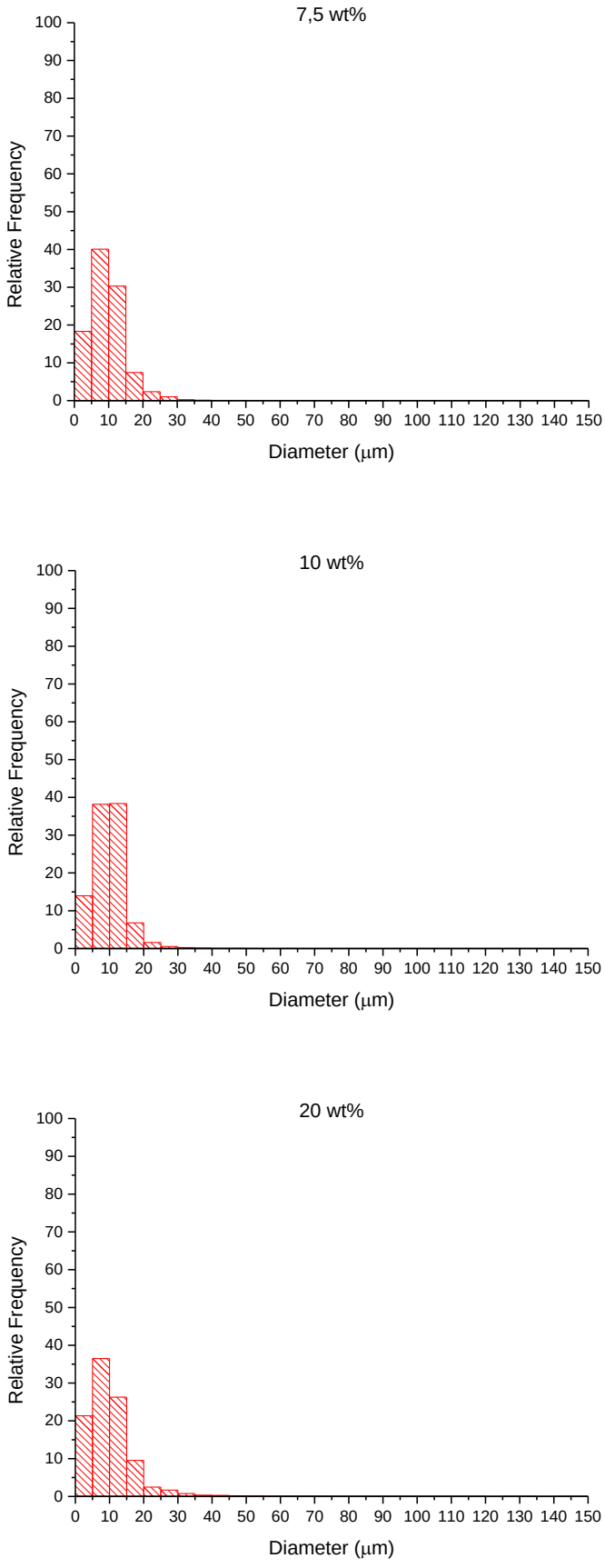

Figure D.1: Relative frequency distribution of powders obtained from aqueous solutions resulted from particle size analyser

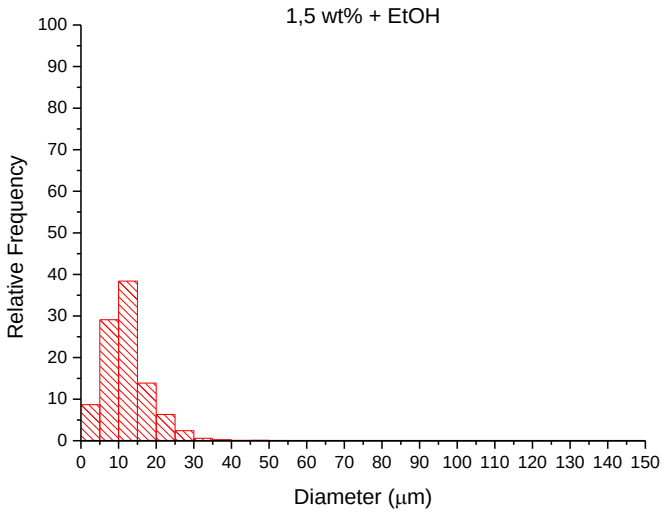
1,5 wt% + EtOH
Relative Frequency
Diameter (μm)

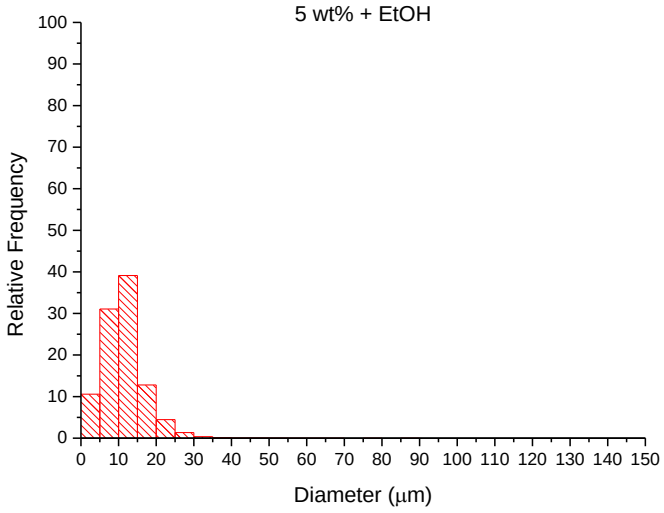
5 wt% + EtOH
Relative Frequency
Diameter (μm)

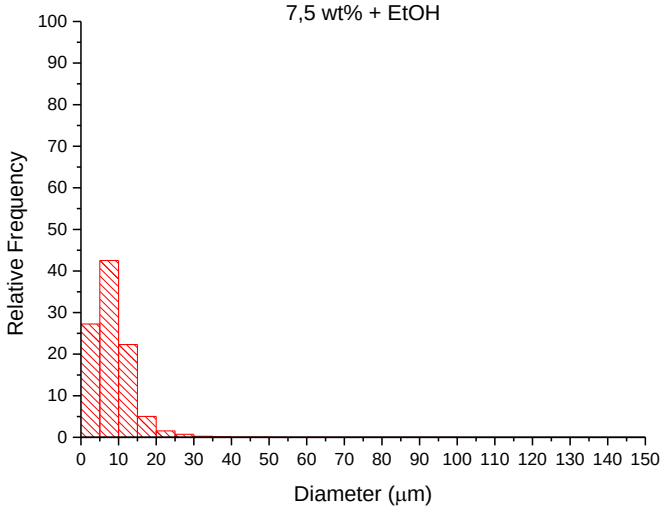
7,5 wt% + EtOH
Relative Frequency
Diameter (μm)

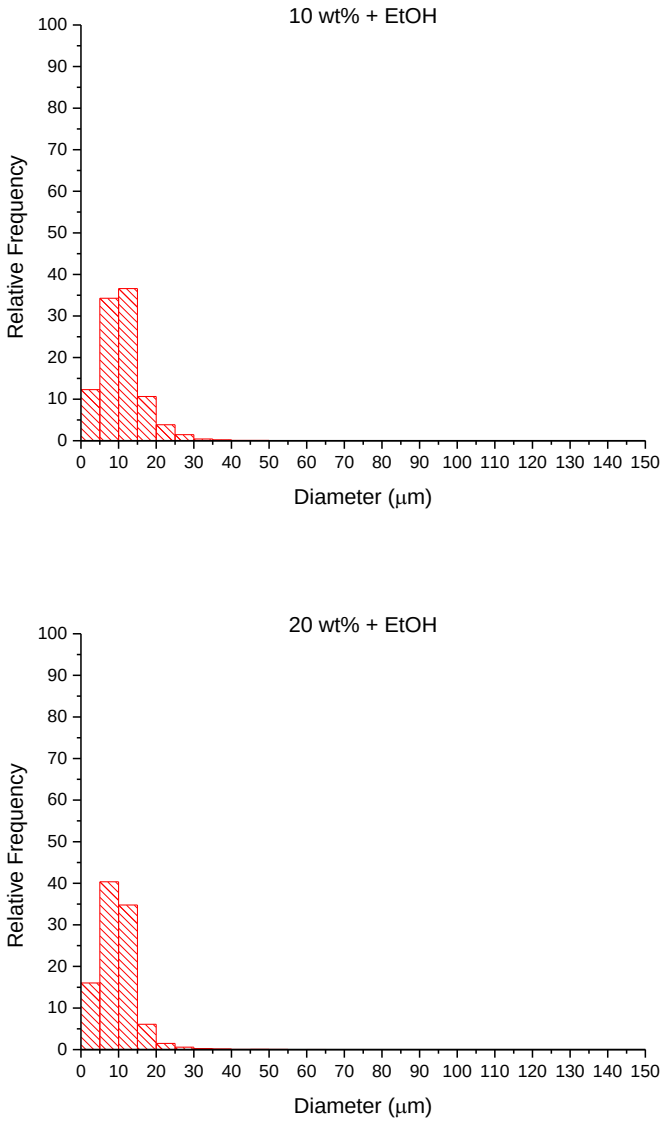

Figure D.2: Relative frequency distribution of powders obtained from hydro alcoholic solutions resulted from particle size analyser

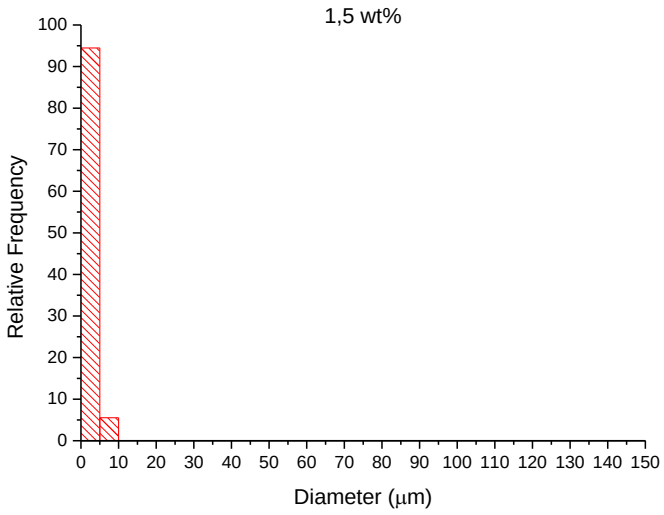
1,5 wt%
Relative Frequency
Diameter (μm)

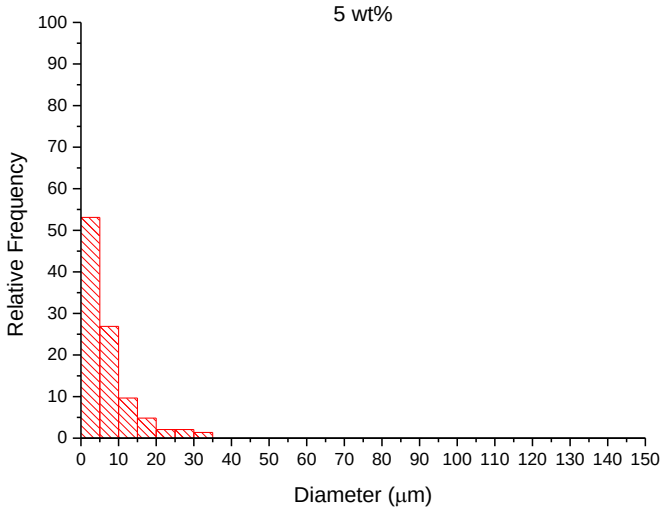
5 wt%
Relative Frequency
Diameter (μm)

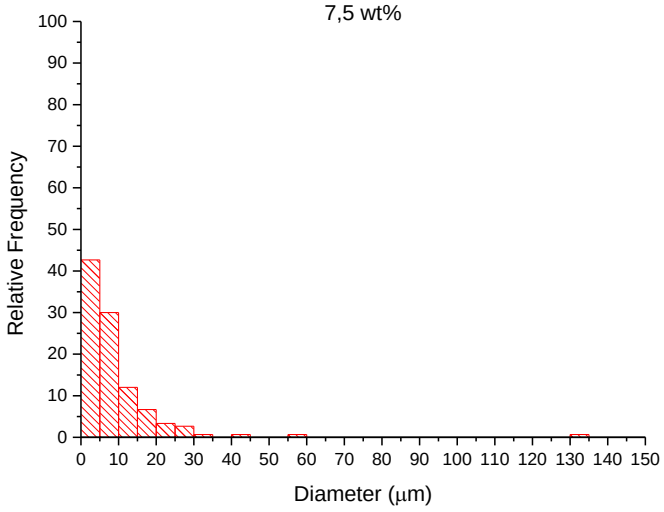
7,5 wt%
Relative Frequency
Diameter (μm)

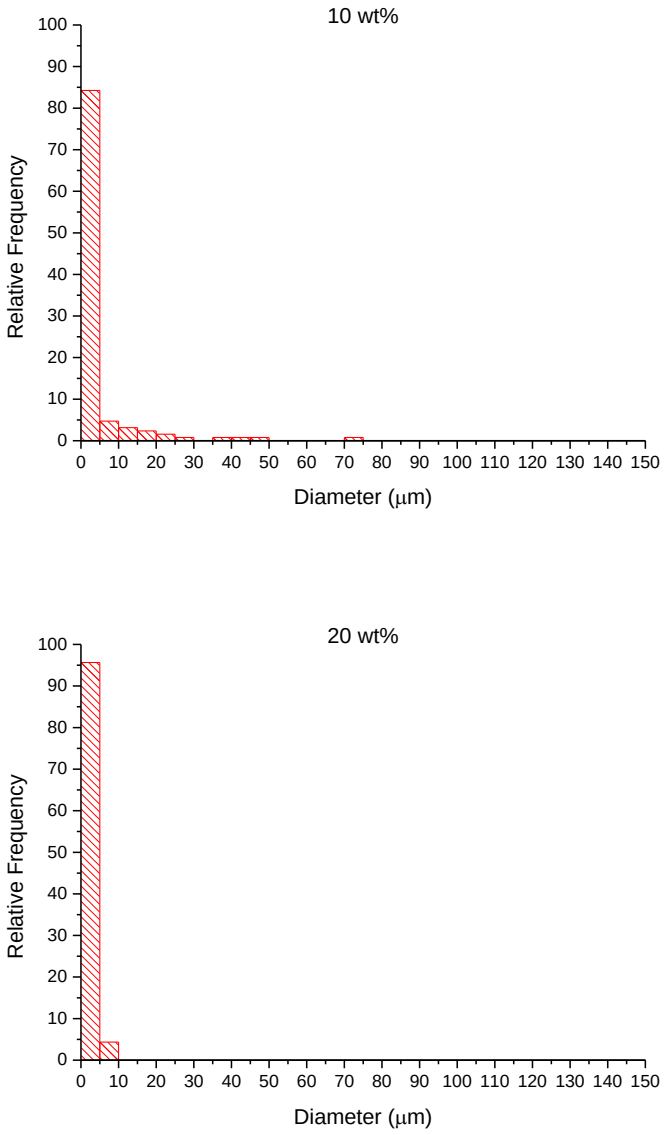

Figure D.3: Relative frequency distribution of powders obtained from aqueous solutions resulted from image analysis

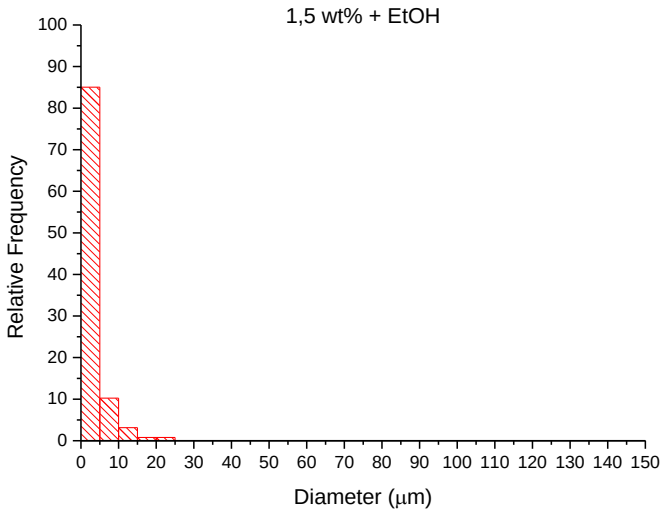
1,5 wt% + EtOH
Relative Frequency
Diameter (μm)

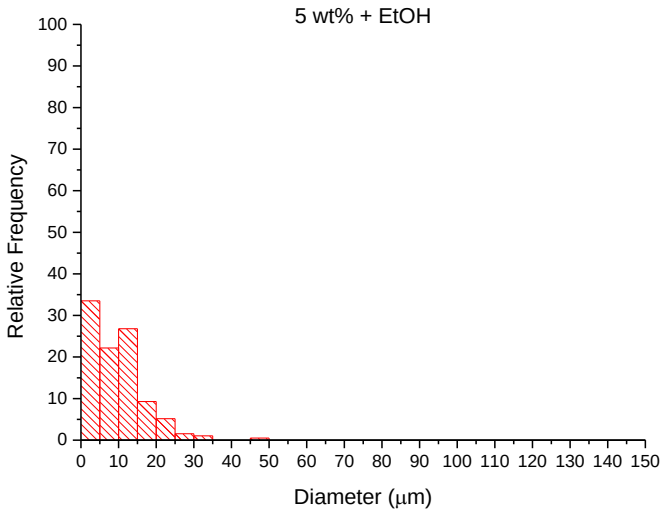
5 wt% + EtOH
Relative Frequency
Diameter (μm)

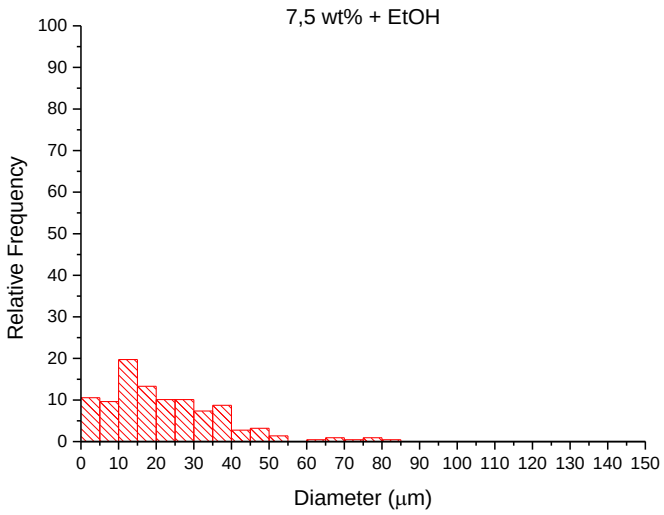
7,5 wt% + EtOH
Relative Frequency
Diameter (μm)

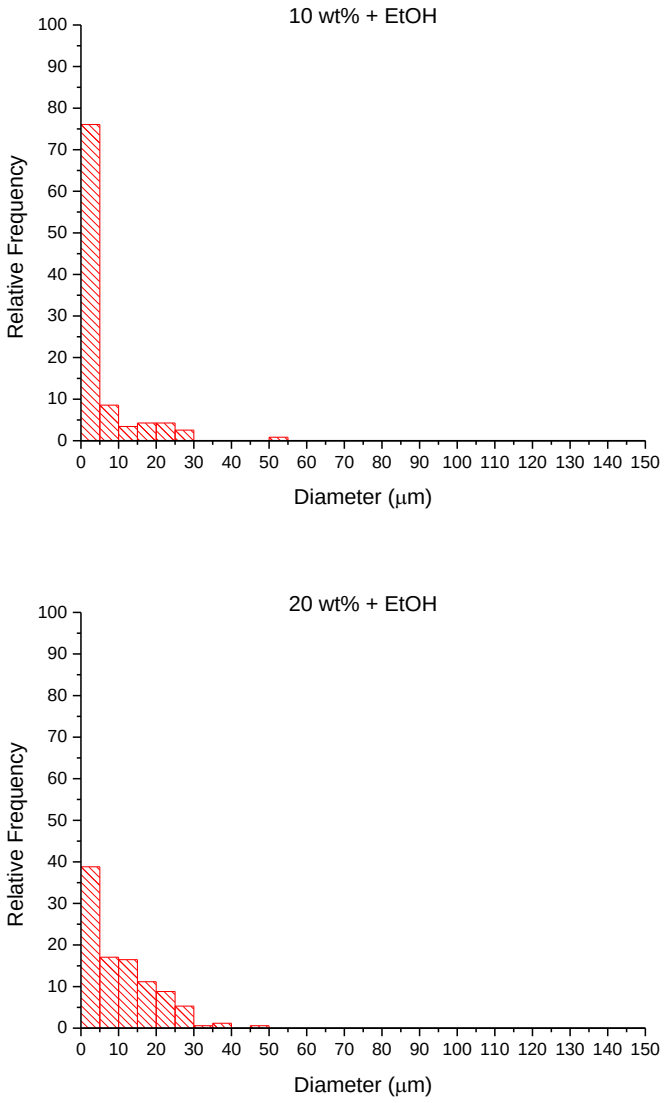

Figure D.4: Relative frequency distribution of powders obtained from hydro alcoholic solutions resulted from image analysis

Bibliographic References

[1] G. Tiwari *et al.*, "Drug delivery systems: An updated review," *Int. J. Pharm. Investig.*, vol. 2, no. 1, p. 2, 2012.

[2] N. A. Kshirsagar, "Drug Delivery Systems," *Indian J. Pharmacol.*, vol. 32, pp. S54–S61, 2000.

[3] P. Tyle, *Drug delivery devices : fundamentals and applications*. New York: M. Dekker, 1988.

[4] V. V. Ranade and J. B. Cannon, *Drug Delivery Systems*, Third Edit. CRC Press, 2011.

[5] K. K. Jain, *Drug Delivery System*, Second Edi. Springer, 2014.

[6] D. Paolino, M. Fresta, P. Sinha, and M. Ferrari, "Drug Delivery Systems," *Encycl. Med. Devices Instrum.*, pp. 437–495, 2006.

[7] E. Tomlinson, "Biological opportunities for site-specific drug delivery using particulate carriers.," *ELLIS HORWOOD Ser. Biomed.*, pp. 32–65, 1987.

[8] L. Shargel, A. Yu, and S. Wu-Pong, *Applied Biopharmaceutics & Pharmacokinetics*, Sixth Edit. McGraw Hill, 2012.

[9] Y. Perrie and T. Rades, *Pharmaceutics: Drug Delivery and Targeting*. Pharmaceutical Press, 2009.

[10] M. M. Al-Tabakha, "HPMC Capsules: Current Status and Future Prospects," *J. Pharm. Pharm. Sci.*, vol. 13, no. 3, pp. 428–442, 2010.

[11] D. Murachanian, "Two piece hard capsules for pharmaceutical formulations.pdf," *Pharm. Process.*, vol. 14, no. 3, pp. 31–41, 2010.

[12] A. Maroni, L. Zema, M. D. Del Curto, G. Loreti, and A. Gazzaniga, "Oral pulsatile delivery: Rationale and chronopharmaceutical formulations," *Int. J. Pharm.*, vol. 398, no. 1–2, pp. 1–8, 2010.

[13] K. Thoma and K. Bechtold, "Enteric coated hard gelatin capsules," *Capsugel Tech. Bull.*, pp. 1–17, 1992.

[14] P. Speiser, "Injection-moulded oral medicament in solid form," *US Pat.*, vol. 3,432,592, pp. 3–6, 1969.

[15] L. Zema, G. Loreti, A. Melocchi, A. Maroni, and A. Gazzaniga, "Injection Molding and its application to drug delivery," *J. Control. Release*, vol. 159, no. 3, pp. 324–331, 2012.

[16] L. Eith, R. F. T. Stepto, and I. Tomka, "Injection-moulded drug-delivery systems," *Manuf. Chem.*, vol. 58, no. 1, pp. 21–25, 1987.

[17] C. König, K. Ruffieux, E. Wintermantel, and J. Blaser, "Autosterilization of biodegradable implants by injection molding process," *J. Biomed. Mater. Res.*, vol. 38, no. 2, pp. 115–119, 1997.

[18] S. Wacker, M. Soliva, and P. Speiser, "Injection molding as a suitable process for manufacturing solid dispersions or solutions," *Pharm. Ind.*, vol. 53, no. 9, pp. 853–856, 1991.

[19] M. A. Repka, S. Majumdar, S. K. Battu, R. Srirangam, and S. B. Upadhye, "Applications of hot-melt extrusion for drug delivery," *Expert Opin. Drug Deliv.*, vol. 5, no. 12, pp. 1357–1376, 2008.

[20] A. Maroni, L. Zema, M. Cerea, A. Foppoli, L. Palugan, and A. Gazzaniga, "Erodible drug delivery systems for time-controlled release into the gastrointestinal tract," *J. Drug Deliv. Sci. Technol.*, vol. 32, pp. 229–235, 2016.

[21] M. E. Sangalli, A. Maroni, L. Zema, C. Busetti, F. Giordano, and A. Gazzaniga, "In vitro and in vivo evaluation of an oral system for time and / or site-specific drug delivery," *J. Control. Release*, vol. 73, pp. 103–110, 2001.

[22] A. Gazzaniga, M. Cerea, A. Cozzi, A. Foppoli, A. Maroni, and L. Zema, "A novel injection-molded capsular device for oral pulsatile delivery based on swellable/erodible polymers.," *AAPS PharmSciTech*, vol. 12, no. 1, pp. 295–303, 2011.

[23] L. Zema, G. Loreti, E. Macchi, A. Foppoli, A. Maroni, and A. Gazzaniga, "Injection-Molded Capsular Device for Oral Pulsatile Release: Development of a Novel Mold," *J. Pharm. Sci.*, vol. 102, no. 2, pp. 489–499, 2013.

[24] A. L. Sarodea, S. Obara, F. K. Tanno, H. Sandhuc, R. Iyer, and N. Shahd, "Stability assessment of hypromellose acetate succinate (HPMCAS) NF for application in hot melt extrusion (HME)," *Carbohydr. Polym.*, vol. 101, pp. 146–153, 2014.

[25] L. Zema, G. Loreti, A. Melocchi, A. Maroni, L. Palugan, and A. Gazzaniga, "Gastroresistant capsular device prepared by injection molding," *Int. J. Pharm.*, vol. 440, no. 2, pp. 264–272, 2013.

[26] Joint FAO/WHO Expert Committee on Food Additives, "Polyvinyl alcohol (PVA)-polyethylene glycol (PEG) graft co-polymer," in *COMPENDIUM OF FOOD ADDITIVE SPECIFICATIONS*, 2015, pp. 47–57.

[27] L. Vanthienen, "Novel Percolation Paths in Capsular Devices for Oral Prolonged Drug Release," KU Leuven, 2017.

[28] R. P. Babu, K. O'Connor, and R. Seeram, "Current progress on bio-based polymers and their future trends," *Prog. Biomater.*, vol. 2, no. 8, pp. 1–16, 2013.

[29] R. S. Singh and G. K. Saini, "Biosynthesis of Pullulan and Its Applications in Food and Pharmaceutical Industry," in *Microorganisms in Sustainable Agriculture and Biotechnology*, T. Satyanarayana, B. Johri, and A. Prakash, Eds. Springer, 2012, pp. 509–553.

[30] K. C. Cheng, A. Demirci, and J. M. Catchmark, "Pullulan: Biosynthesis, production, and applications," *Appl. Microbiol. Biotechnol.*, vol. 92, no. 1, pp. 29–44, 2011.

[31] J. K. Park and T. Khan, *Other microbial polysaccharides: Pullulan, scleroglucan, elsinan, levan, alternant, dextran*. Woodhead Publishing Limited, 2009.

[32] T. D. Leathers, "Biotechnological production and applications of pullulan," *Appl. Microbiol. Biotechnol.*, vol. 62, no. 5–6, pp. 468–473, 2003.

[33] I. Bataille and A. Meddahi-pellé, "Pullulan for Biomedical Uses," *Book*, pp. 35–39, 1982.

[34] R. F. Childers, P. L. Oren, and W. M. K. Seidler, "Film coating formulations," 5,015,480, 1991.

[35] Y. Izutsu and K. Sogo, “Pullulan and Sugar Coated Pharmaceutical Composition,” 4,650,666, 1987.

[36] H. Matsunaga, K. Tsuji, and T. Saito, “Foamed Plastics of Resin Compositions Comprising Pullulan Type Resins and Thermoplastic Resins and Process for Producing the Same,” 3,976,605, 1976.

[37] H. Matsunaga, K. Tsuji, and T. Saito, “Resin composition of hydrophilic pullulan, hydrophobic thermoplastic resin, and plasticizer,” 4,045,388, 1977.

[38] Y. Miyamoto, H. Goto, H. Sato, H. Okano, and M. Iijima, “Process for sugar-coating solid preparation,” 4,610,891, 1986.

[39] S. H. Leung, R. Leone, L. D. Kumar, and A. F. Sorg, “Fast dissolving orally consumable films,” US 7,025,983 B2, 2006.

[40] S. Nakashio, N. Sekine, N. Toyota, and F. Fujita, “Paint containing pullulan,” 3,888,809, 1975.

[41] S. Nakashio, K. Tsuji, N. Toyota, and F. Fujita, “Novel cosmetics containing pullulan,” 3,972,997, 1976.

[42] R. Vehring, W. R. Foss, and D. Lechuga-Ballesteros, “Particle formation in spray drying,” *J. Aerosol Sci.*, vol. 38, no. 7, pp. 728–746, 2007.

[43] A. Sosnik and K. P. Seremeta, “Advantages and challenges of the spray-drying technology for the production of pure drug particles and drug-loaded polymeric carriers,” *Adv. Colloid Interface Sci.*, vol. 223, pp. 40–54, 2015.

[44] V. Lefebvre, A., McDonell, *Atomization and Sprays*, Second. CRC Press, 2017.

[45] P. D. Hede, P. Bach, and A. D. Jensen, “Two-fluid spray atomisation and pneumatic nozzles for fluid bed coating/agglomeration purposes: A review,” *Chem. Eng. Sci.*, vol. 63, no. 14, pp. 3821–3842, 2008.

[46] A. H. Lefebvre, *GAS Turbine Combustion, Second Edition*, Second. Taylor & Francis, 1998.

[47] A. H. Lefebvre, “Airblast atomization,” *Prog. Energy Combust. Sci.*, vol. 6, no. 3, pp. 233–261, 1980.

[48] N. Dombrowski and R. P. Fraser, “A Photographic Investigation into the Disintegration of Liquid Sheets,” *R. Soc.*, vol. 247, no. 924, pp. 101–130, 1954.

[49] R. P. Fraser, “Liquid fuel atomization,” *Symp. Combust.*, vol. 6, no. 1, pp. 687–701, 1957.

[50] L. Rayleigh, “On the instability of jets.pdf,” *Proceedings of the London mathematical society*, vol. 10. pp. 4–13, 1878.

[51] E. Tyler, “XL. Instability of liquid jets,” *London, Edinburgh, Dublin Philos. Mag. J. Sci.*, vol. 16, no. 105, pp. 504–518, Aug. 1933.

[52] C. Weber, “Disintegration of liquid jets,” *ZAMM - J. Appl. Math. Mech. / Zeitschrift für Angew. Math. und Mech.*, vol. 11, no. 2, pp. 136–154, 1931.

[53] A. Haenlein, *Disintegration of a liquid jet*, Technical. National Advisory Committee for

Aeronautics, 1932.

[54] W. Ohnesorge, "Formation of drops by nozzles and the breakup of liquid jets," *J. Appl. Math. Mech.*, vol. 16, pp. 355 – 358, 1936.

[55] R. D. Reitz, "Atomization and other breakup regimes of a liquid jet," 1978.

[56] P. Walzel, "Liquid atomization," *Int. Chem. Eng.*, vol. 33, no. 1, pp. 46–60, 1993.

[57] D. E. Walton, "The Evaporation of Water Droplets. A Single Droplet Drying Experiment," *Dry. Technol.*, vol. 22, no. 3, pp. 431–456, 2004.

[58] D. Huang, "Modeling of Particle Formation during Spray Drying," *Eur. Dry. Conf. - EuroDrying'2011*, no. October, pp. 26–28, 2011.

[59] M. Mezhericher, A. Levy, and I. Borde, "Spray drying modelling based on advanced droplet drying kinetics," *Chem. Eng. Process. Process Intensif.*, vol. 49, no. 11, pp. 1205–1213, 2010.

[60] M. Mezhericher, A. Levy, and I. Borde, "Modelling of particle breakage during drying," *Chem. Eng. Process. Process Intensif.*, vol. 47, no. 8, pp. 1410–1417, 2008.

[61] K. H. Leong, "Morphological control of particles generated from the evaporation of solution droplets: Theoretical considerations," *J. Aerosol Sci.*, vol. 18, no. 5, pp. 511–524, 1987.

[62] D. B. Southwell, T. A. G. Langrish, and D. F. Fletcher, "Use of computational fluid dynamics techniques to assess design alternatives for the plenum chamber of a small spray dryer," *Dry. Technol.*, vol. 19, no. 2, pp. 257–268, 2001.

[63] D. F. Fletcher, B. Guo, D. J. E. Harvie, T. A. G. Langrish, J. J. Nijdam, and J. Williams, "What is important in the simulation of spray dryer performance and how do current CFD models perform?," *Appl. Math. Model.*, vol. 30, no. 11, pp. 1281–1292, 2006.

[64] I. Zbiciński and X. Li, "Conditions for accurate CFD modeling of spray-drying process," *Dry. Technol.*, vol. 24, no. 9, pp. 1109–1114, 2006.

[65] M. Mezhericher, A. Levy, and I. Borde, "Modeling of droplet drying in spray chambers using 2D and 3D computational fluid dynamics," *Dry. Technol.*, vol. 27, no. 3, pp. 359–370, 2009.

[66] T. A. G. Langrish, "New engineered particles from spray dryers: Research needs in spray drying," *Dry. Technol.*, vol. 25, no. 6, pp. 971–983, 2007.

[67] M. Mezhericher, A. Levy, and I. Borde, "Theoretical models of single droplet drying kinetics: A review," *Dry. Technol.*, vol. 28, no. 2, pp. 278–293, 2010.

[68] J. D. Ormes *et al.*, "Design of experiments utilization to map the processing capabilities of a micro-spray dryer: Particle design and throughput optimization in support of drug discovery," *Pharm. Dev. Technol.*, vol. 18, no. 1, pp. 121–129, 2013.

[69] D. E. Dobry, D. M. Settell, J. M. Baumann, R. J. Ray, L. J. Graham, and R. A. Beyerinck, "A model-based methodology for spray-drying process development," *J. Pharm. Innov.*, vol. 4, no. 3, pp. 133–142, 2009.

[70] S. Belotti *et al.*, "Spray-dried amikacin sulphate powder for inhalation in cystic fibrosis patients: The role of ethanol in particle formation," *Eur. J. Pharm. Biopharm.*, vol. 93, pp. 165–

172, 2015.

[71] R. Vehring, "Pharmaceutical particle engineering via spray drying," *Pharm. Res.*, vol. 25, no. 5, pp. 999–1022, 2008.

[72] K. Mosén, K. Bäckström, K. Thalberg, T. Schaefer, H. G. Kristensen, and A. Axelsson, "Particle formation and capture during spray drying of inhalable particles," *Pharm. Dev. Technol.*, vol. 9, no. 4, pp. 409–417, 2004.

[73] Y. F. Maa, H. R. Costantino, P. A. Nguyen, and C. C. Hsu, "The effect of operating and formulation variables on the morphology of spray-dried protein particles," *Pharm. Dev. Technol.*, vol. 2, no. 3, pp. 213–223, 1997.

[74] B. Bittner and T. Kissel, "Ultrasonic atomization for spray drying: a versatile technique for the preparation of protein loaded biodegradable microspheres," *J. Microencapsul.*, vol. 16, no. 3, pp. 325–341, 1999.

[75] J. Vicente, J. Pinto, J. Menezes, and F. Gaspar, "Fundamental analysis of particle formation in spray drying," *Powder Technol.*, vol. 247, pp. 1–7, 2013.

[76] H. Schiffter and G. Lee, "Single-Droplet Evaporation Kinetics and Particle Formation in an Acoustic Levitator. Part 2: Drying Kinetics and Particle Formation from Microdroplets of Aqueous Mannitol, Trehalose, or Catalase," *J. Pharm. Sci.*, vol. 96, no. 9, pp. 2284–2295, 2007.

[77] D. E. Walton, "The morphology of spray-dried particles: a qualitative view," *Dry. Technol.*, vol. 18, no. 9, pp. 1943–1986, 2000.

[78] G.McKinley, "Filament stretching rheometry of complex fluids," *Annu. Rev. Fluid Mech.*, vol. 34, no. 1, pp. 375–415, 2002.

[79] P. Szabo, "Transient Filament Stretching Rheometer I: Force Balance Analysis," *Rheol. Acta*, vol. 36, pp. 277–284, 1997.

[80] L. A. Slobozhanin and J. M. Perales, "Stability of liquid bridges between equal disks in an axial gravity field," *Phys. Fluids A Fluid Dyn.*, vol. 5, no. 6, pp. 1305–1314, 1993.

[81] J. Plateau, "Experimental and Theoretical Researches on the Figures of Equilibrium of a Liquid Mass Withdrawn from the Action of Gravity," *Philos. Mag.*, vol. 14, no. 90, pp. 431–451, 1857.

[82] R. D. Gillette and D. C. Dyson, "Stability of fluid interfaces of revolution between equal solid circular plates," *Chem. Eng. J.*, vol. 2, no. 1, pp. 44–54, Jan. 1971.

[83] S. Gaudet, G. H. McKinley, and H. A. Stone, "Extensional deformation of Newtonian liquid bridges," *Phys. Fluids*, vol. 8, no. 10, pp. 2568–2579, 1996.

[84] S. Berg, R. Kroger, and H. Rath, "Measurement of Extensional Viscosity by Stretching Large Liquid Bridges in Microgravity," *J. Nonnewton. Fluid Mech.*, vol. 55, pp. 307–319, 1994.

[85] J. Eggers, "Nonlinear dynamics and breakup of free-surface flows," *Rev. Mod. Phys.*, vol. 69, no. 3, pp. 865–930, 1997.

[86] M. Renardy, "A numerical study of the asymptotic evolution and breakup of Newtonian and viscoelastic jets," *J. Nonnewton. Fluid Mech.*, vol. 59, no. 2–3, pp. 267–282, 1995.

[87] G. H. McKinley and A. Tripathi, "How to extract the Newtonian viscosity from capillary breakup measurements in a filament rheometer," *J. Rheol. (N. Y. N. Y).*, vol. 44, no. 3, pp. 653–670, 2000.

[88] A. V Bazilevskii, V. M. Entov, M. M. Lerner, and A. N. Rozhkov, "Failure of Polymer Solution Filaments1," no. March 1997, pp. 316–324, 1996.

[89] V. M. Entov and E. J. Hinch, "Effect of a spectrum of relaxation times on the capillary thinning of a filament of elastic liquid," *J. Nonnewton. Fluid Mech.*, vol. 72, no. 1, pp. 31–53, 1997.

[90] R. F. Liang and M. R. Mackley, "Rheological characterization of the time and strain dependence for polyisobutylene solutions," *J. Nonnewton. Fluid Mech.*, vol. 52, no. 3, pp. 387–405, 1994.

[91] M. I. Kolte and P. Szabo, "Capillary thinning of polymeric filaments," *J. Rheol. (N. Y. N. Y).*, vol. 43, no. 3, pp. 609–625, 1999.

[92] A. Nikolaevich, R. Russian, and A. N. Rozhkov, "Third European Rheology Conference and Golden Jubilee Meeting of the British Society of Rheology," no. January, 1990.

[93] D. T. Papageorgiou, "On the Breakup of Viscous-Liquid Threads," *Phys. Fluids*, vol. 7, pp. 1529–1544, 1995.

[94] G. H. McKinley, "Visco-Elasto-Capillary Thinning and Break-Up of Complex Fluids," *Polymer (Guildf).*, no. 5, pp. 1274–1277, 2005.

[95] D. W. Bousfield, R. Keunings, G. Marrucci, and M. M. Denn, "Nonlinear analysis of the surface tension driven breakup of viscoelastic filaments," *J. Nonnewton. Fluid Mech.*, vol. 21, no. 1, pp. 79–97, 1986.

[96] M. Renardy, "Some comments on the surface-tension driven break-up (or the lack of it) of viscoelastic jets," *J. Nonnewton. Fluid Mech.*, vol. 51, no. 1, pp. 97–107, 1994.

[97] H. C. Chang, E. A. Demekhin, and E. Kalaidin, "Iterated stretching of viscoelastic jets," *Phys. Fluids*, vol. 11, no. 7, pp. 1717–1737, 1999.

[98] M. Yao, G. H. McKinley, and B. Debbaut, *Extensional deformation, stress relaxation and necking failure of viscoelastic filaments*, vol. 79, no. 2–3. 1998.

[99] S. L. Anna and G. H. McKinley, "Elasto-capillary thinning and breakup of model elastic liquids," *J. Rheol. (N. Y. N. Y).*, vol. 45, no. 1, pp. 115–138, 2001.

[100] F. Uses, "Synonyms definition," *Test*, vol. 4, no. 1986, pp. 1–4, 2004.

[101] F. Baldi *et al.*, "Rheological Characterization of Ethylcellulose-Based Melts for Pharmaceutical Applications," *AAPS PharmSciTech*, no. 8, pp. 1–12, 2016.

[102] United States Pharmacopeial Convention, *U.S. Pharmacopeial guidelines <711> Dissolution*. 2011.

[103] A. Ghasemi and S. Zahediasl, "Normality tests for statistical analysis: A guide for non-statisticians," *Int. J. Endocrinol. Metab.*, vol. 10, no. 2, pp. 486–489, 2012.

[104] P. Armitage and T. Colton, *Encyclopedia of biostatistics*, Second. John Wiley & Sons, 2005.

[105] J. Peat and B. Barton, *Medical Statistics: A Guide to Data Analysis and Critical Appraisal*, First. Blackwell Publishing, 2005.

[106] D. Öztuna, A. H. Elhan, and E. Tüccar, "Investigation of four different normality tests in terms of type 1 error rate and power under different distributions," *Turkish J. Med. Sci.*, vol. 36, no. 3, pp. 171–176, 2006.

[107] M. Mendes and A. Pala, "Type I Error Rate and Power of Three Normality Tests," *Pakistan J. Inf. Technol.*, vol. 2, no. 2, pp. 135–139, 2003.

[108] M. R. Kasaai, "Intrinsic viscosity-molecular weight relationship and hydrodynamic volume for pullulan," *J. Appl. Polym. Sci.*, vol. 100, no. 6, pp. 4325–4332, 2006.

[109] K. Kawahara, K. Ohta, H. Miyamoto, and S. Nakamura, "Preparation and solution properties of pullulan fractions as standard samples for water-soluble polymers," *Carbohydr. Polym.*, vol. 4, no. 5, pp. 335–356, 1984.

[110] L. Palangetic, N. K. Reddy, S. Srinivasan, R. E. Cohen, G. H. McKinley, and C. Clasen, "Dispersity and spinnability: Why highly polydisperse polymer solutions are desirable for electrospinning," *Polym. (United Kingdom)*, vol. 55, no. 19, pp. 4920–4931, 2014.

[111] R. H. Colby, "Structure and linear viscoelasticity of flexible polymer solutions: Comparison of polyelectrolyte and neutral polymer solutions," *Rheol. Acta*, vol. 49, no. 5, pp. 425–442, 2010.

[112] I. S. Khattab, F. Bandarkar, M. A. A. Fakhree, and A. Jouyban, "Density, viscosity, and surface tension of water+ethanol mixtures from 293 to 323K," *Korean J. Chem. Eng.*, vol. 29, no. 6, pp. 812–817, 2012.

[113] C. W. Macosko, *Rheology: Principles, Measurements, and Applications*, Advances i. Vch Pub, 1994.

[114] M. M. Cross and A. Kaye, "Simple procedures for obtaining viscosity/shear rate data from a parallel disc viscometer," *Polymer (Guildf).*, vol. 28, no. 3, pp. 435–440, 1987.

[115] J. J. Duffy, A. J. Hill, and S. H. Murphy, "Simple method for determining stress and strain constants for non-standard measuring systems on a rotational rheometer," *Appl. Rheol.*, vol. 25, no. 4, pp. 1–6, 2015.

[116] M. T. Johnston and R. H. Ewoldt, "Precision rheometry: Surface tension effects on low-torque measurements in rotational rheometers," *J. Rheol. (N. Y. N. Y).*, vol. 57, no. 6, pp. 1515–1532, 2013.

[117] M. Kaibara, "Rheology of blood coagulation," *Biorheology*, vol. 33, no. 2, pp. 101–117, 1996.

[118] V. Sharma, A. Jaishankar, Y.-C. Wang, and G. H. McKinley, "Rheology of globular proteins: apparent yield stress, high shear rate viscosity and interfacial viscoelasticity of bovine serum albumin solutions," *Soft Matter*, vol. 7, no. 11, p. 5150, 2011.

[119] C. Clasen, "Capillary breakup extensional rheometry of semi-dilute polymer solutions," *331 Korea-Australia Rheol. J.*, vol. 22, no. 4, pp. 331–338, 2010.

[120] P. Doshi, R. Suryo, O. E. Yildirim, G. H. McKinley, and O. A. Basaran, "Scaling in pinch-off of generalized Newtonian fluids," *J. Non-Newton. Fluid Mech.*, vol. 113, no. 1, pp. 1–27, 2003.

[121] R. Suryo and O. A. Basaran, "Local dynamics during pinch-off of liquid threads of power law fluids: Scaling analysis and self-similarity," *J. Nonnewton. Fluid Mech.*, vol. 138, no. 2–3, pp. 134–160, 2006.

[122] C. Clasen, J. Eggers, M. A. Fontelos, J. Li, and G. H. McKinley, "The beads-on-string structure of viscoelastic threads," *J. Fluid Mech.*, vol. 556, pp. 283–308, 2006.

[123] C. Clasen *et al.*, "How dilute are dilute solutions in extensional flows?," *J. Rheol. (N. Y. N. Y).*, vol. 50, no. 6, pp. 849–881, 2006.

[124] D. F. James, "Boger Fluids," *Annu. Rev. Fluid Mech.*, vol. 41, no. 1, pp. 129–142, 2009.

[125] Z. Lei, H. Wang, R. Zhou, and Z. Duan, "Influence of salt added to solvent on extractive distillation," *Chem. Eng. J.*, vol. 87, no. 2, pp. 149–156, 2002.

[126] R. C. Pemberton and C. J. Mash, "Thermodynamic properties of aqueous mixtures II . Vapour pressuresand excessGibbsenergies for water + ethanol at 303 . 15 to 363 . 15 K determined by an accurate static method," *J. Chem. Thermodyn.*, vol. 10, pp. 867–888, 1978.

[127] V. Truong, B. R. Bhandari, and T. Howes, "Optimization of co-current spray drying process of sugar-rich foods. Part I-Moisture and glass transition temperature profile during drying," *J. Food Eng.*, vol. 71, no. 1, pp. 55–65, 2005.

[128] H. Levine and L. Slade, "Water as a plasticizer: physico-chemical aspects of low-moisture polymeric systems," in *Water Science Reviews 3: Water Dynamics*, F. Franks, Ed. Cambridge University Press, 1988, pp. 79–185.

[129] B. Y. Shekunov, P. Chattopadhyay, H. H. Y. Tong, and A. H. L. Chow, "Particle size analysis in pharmaceutics: Principles, methods and applications," *Pharm. Res.*, vol. 24, no. 2, pp. 203–227, 2007.

[130] I. Caraballo, M. Millan, and A. M. Rabasco, "Relationship between drug percolation threshold and particle size in matrix tablets," *Pharmaceutical Research*, vol. 13, no. 3. pp. 387–390, 1996.

[131] C. V. Liew, L. W. Chan, A. L. Ching, and P. W. S. Heng, "Evaluation of sodium alginate as drug release modifier in matrix tablets," *Int. J. Pharm.*, vol. 309, no. 1–2, pp. 25–37, 2006.

[132] M. L. González-Rodríguez, F. Maestrelli, P. Mura, and A. M. Rabasco, "In vitro release of sodium diclofenac from a central core matrix tablet aimed for colonic drug delivery," *Eur. J. Pharm. Sci.*, vol. 20, no. 1, pp. 125–131, 2003.

[133] M. L. González-Rodríguez, J. I. Pérez-Martínez, S. Merino, A. Fini, and A. M. Rabasco, "Channeling agent and drug release from a central core matrix tablet," *Drug Dev. Ind. Pharm.*, vol. 27, no. 5, pp. 439–446, 2001.

[134] P. B. Kowalczuk and J. Drzymala, "Physical meaning of the Sauter mean diameter of spherical particulate matter," *Part. Sci. Technol.*, vol. 34, no. 6, pp. 645–647, 2016.

[135] N. Dombrowski and W. . Johns, "The aerodynamic instability and desintegration of viscous liquid sheets," *Chem. Eng. Sci.*, vol. 18, pp. 230–242, 1963.

[136] D. Li, *Encyclopedia of Microfluidics and Nanofluidics*, Second. Springer Science & Business Media, 2015.

[137] R. P. A. Hartman, D. J. Brunner, D. M. A. Camelot, J. C. M. Marijnissen, and B. Scarlett, "Jet break-up in electrohydrodynamic atomization in the cone-jet mode," *J. Aerosol Sci.*, vol. 31, no. 1, pp. 65–95, 2000.

[138] P. H. Schweitzer, "Mechanism of Disintegration of Liquid Jets," *J. Appl. Phys.*, vol. 8, pp. 513–521, 1937.

[139] A. G. Gelalles, "Effect of orifice length-diameter ratio on fuel sprays for compression-ignition engines," 1931.

[140] M. Shimizu, M. Arai, and H. Hiroyasu, "Measurements of Breakup Length in High Speed Jet," *Bull. JSME*, vol. 27, no. 230, pp. 1709–1715, 1984.

[141] A. Lichtarowicz, R. K. Duggins, and E. Markland, "Discharge Coefficients for Incompressible Non-Cavitating Flow through Long Orifices," *J. Mech. Eng. Sci.*, vol. 7, no. 2, pp. 210–219, Jun. 1965.

[142] Z. Liu and R. D. Reitz, "An analysis of the distortion and breakup mechanisms of high speed liquid drops," *Int. J. Multiph. Flow*, vol. 23, no. 4, pp. 631–650, 1997.

[143] G. H. McKinley, "Dimensionless groups for understanding free surface flows of complex fluids," *Soc. Rheol. Bull*, vol. 2005, no. July, pp. 6–9, 2005.

[144] M. Reiner, "The Deborah Number," *Phys. Today*, vol. 17, no. 1, p. 62, 1964.

[145] B. Keshavarz, E. C. Houze, J. R. Moore, M. R. Koerner, and G. H. McKinley, "Ligament Mediated Fragmentation of Viscoelastic Liquids," *Phys. Rev. Lett.*, vol. 117, no. 15, pp. 1–6, 2016.

[146] A. Tripathi, P. Whittingstall, and G. H. McKinley, "Using filament stretching rheometry to predict strand formation and 'processability' in adhesives and other non-Newtonian fluids," *Rheol. Acta*, vol. 39, no. 4, pp. 321–337, 2000.

[147] J. S. Vrentas and J. L. Duda, *Diffusion in polymer—solvent systems. I. Reexamination of the free-volume theory*, vol. 15. 1977.

[148] J. S. Vrentas and J. L. Duda, *Diffusion in polymer–solvent systems. II. A predictive theory for the dependence of diffusion coefficients on temperature, concentration, and molecular weight*, vol. 15. 1977.

[149] M. H. Cohen and D. Turnbull, "Molecular Transport in Liquids and Glasses," *J. Chem. Phys.*, vol. 31, no. 5, 1959.

[150] K. Nishinari, K. Kohyama, P. A. Williams, G. O. Phillips, W. Burchard, and K. Ogino, "Solution Properties of Pullulan," *Macromolecules*, vol. 24, no. 20, pp. 5590–5593, 1991.